Dissertations, Theses, and Masters Projects   Theses, Dissertations, & Master Projects

2002

Proton form factors: Measurement of the proton form factors ratio up to Q(2) = 5.6 GEV(2) by recoil polarimetry

Olivier Gayou

College of William & Mary - Arts & Sciences

Follow this and additional works at: https://scholarworks.wm.edu/etd

Recommended Citation

PROTON FORM FACTORS

MEASUREMENT OF THE PROTON FORM FACTORS RATIO $\mu_P G_{E_P}/G_{M_P}$ UP TO $Q^2 = 5.6$ GEV^2 BY RECOIL POLARIMETRY

A Dissertation

Presented to

The Faculty of the Department of Physics

The College of William and Mary in Virginia

In Partial Fulfillment

Of the Requirements for the Degree of

Doctor of Philosophy

---

by

Olivier Gayou

2002

APPROVAL SHEET

This dissertation is submitted in partial fulfillment of

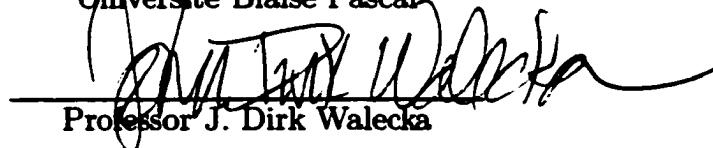the requirements for the degree of

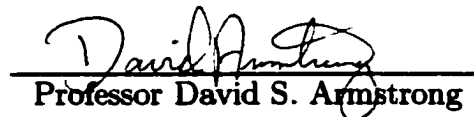Doctor of Philosophy

Olivier Gayou

Approved, April 2002

Professor Charles F. Perdrisat (co-advisor)

Docteur Hélène Fonvieille (co-advisor)
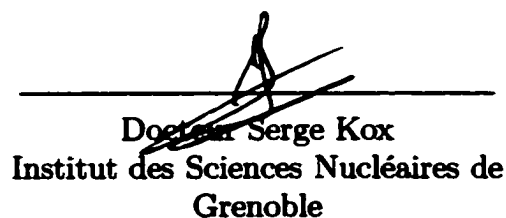Université Blaise Pascal

Professor J. Dirk Walecka

Professor David S. Armstrong

Professor Todd Averett

Docteur Serge Kox
Institut des Sciences Nucléaires de
Grenoble

ii

A la mémoire de mon grand-père,
A ma nièce, qui naitra dans trois mois.

iii

CONTENTS

ACKNOWLEDGMENTS

Whatever a physics PhD student learns during his research years, he always learns it from the many people he comes to work with. I therefore have myself a lot of individuals to thank. First, my advisor Charles Perdrisat, who accepted me in the William and Mary program less than four years ago, allowed me to work on this beautiful experiment, producing such an important result. I thank him for always making me feel like his colleague more than his student. I learned a lot working with him. This thesis was the first "joint" thesis between the College of William and Mary and the Université Blaise Pascal in Clermont-Ferrand, France. I hope the collaboration was a success that will see others following it. Hélène Fonvieille kindly accepted to be my co-advisor for the French part, and I owe her many readings and corrections to the manuscript. Thank you for the time given the last three years, and especially at the end.

I also thank the four other members of my committee, Dirk Walecka, Serge Kox, of the Institut des Sciences Nucléaires de Grenoble in France, David Armstrong and Todd Averett, for their enthusiasm for my work. Special thanks to Serge Kox and Dirk Walecka for writing reports on my thesis for the Université Blaise Pascal.

I very much enjoyed working with the small "GEp" group, Charles Perdrisat, Vina Punjabi, Mark Jones, Lubomir Pentchev, Ed Brash, Sasha Kozlov and Ron Gilman. I want to specially mention Mark, whose knowledge of Hall A seems infinite, and without whom many experiments in this Hall might have taken longer to analyze, and Lubomir, for his considerable work on the systematic uncertainties. I

would also like to thank Steffen Strauch, for his help and many useful discussions on his polarization analysis code.

Like all other experiments in Hall A, E99-007 would not have been possible without the support of Kees de Jager and the Hall A physics staff members, as well as the technical team led by Ed Folts. I specially thank Jack Segal for organizing the swap of the detector packages during the summer before the experiment.

I would also like to thank all the friends I met since I live in the US, either at the Physics Department of the College of William and Mary or at Jefferson Lab. Julie, Paul, Dan, Liz, Kevin, Mina, Lei, Bryan, Joe, Maud, Kathy, Alexandre $\cdots$ and of course all the others, thank you for all the things we have done together in the past four years.

I also wish to thank my family, my parents, Philippe and Christine, my brother Benoît and his wife Valérie (and their baby in a few months !), my sister Delphine, and my dear friends Adrien and Lætitia, Fred and Béatrice, Jean-Luc and Rachel, for always supporting me in what I did, and always staying close to me despite the distance.

Last but not least, I would like to thank Rikki, for her presence and love this past year, and for recently accepting my love for the rest of my life.

LIST OF TABLES

LIST OF FIGURES

xvii

xviii

ABSTRACT

In this thesis, we present the results of the experiment E99-007, which measured the ratio of the electric to magnetic form factors of the proton to the four momentum transfer square $Q^2 = 5.6$ GeV^2, by recoil polarimetry. Data were taken in 2000 at the Thomas Jefferson National Accelerator Facility in Virginia, USA. A 4.6 GeV polarized electron beam was scattered off a cryogenic hydrogen target. The polarization of the recoil proton was measured in the Focal Plane Polarimeter, located after one of the two High Resolution Spectrometers in the hall. The ratio of the transverse to longitudinal components of the recoil proton polarization is proportional to the ratio of the form factors. Elastic events were selected by detecting the scattered electron in a large acceptance lead-glass calorimeter.

The main result of this experiment is the linear decrease of the form factor ratio with increasing Q^2, corresponding to different spatial distributions of the electric charge and the magnetization. Numerous theoretical calculations show that relativistic effects, such as mixing of spin states due to Lorentz boosts, are important to account for the observed data in this critical intermediate kinematic region.

PROTON FORM FACTORS

MEASUREMENT OF THE PROTON FORM FACTORS RATIO $\mu_P G_{E_P}/G_{M_P}$

UP TO $Q^2 = 5.6$ GEV^2 BY RECOIL POLARIMETRY

Introduction

Gravitation, electromagnetism, strong, and weak interactions are the four fundamental forces we know to describe the universe. Theories involving these four forces are expected to ultimately explain all phenomena, from cosmology and the first minutes of our universe, to the infinitely small scale of quantum physics. The strong interaction, responsible for binding the components of the nucleus of all atoms that form visible matter, is certainly the least understood of all. This force constitutes the focus of hadronic physics, which is studied in electron accelerators of the type of the Thomas Jefferson National Accelerator Facility. Jefferson Lab's scientific goal is to *"study the structure of the nuclear many-body system (B $\geq$ 1), its quark substructure, and the nature of the strong and electroweak interactions governing the behavior of this fundamental form of matter"* [1, p.vii].

When the proton and the neutron, which form the building blocks of nuclei in their fundamental state, were discovered in 1919 and 1931 respectively, they were thought as being Dirac particles, just as the electron. In particular, they were expected to be point-like, without any internal structure. As a consequence, they should have a Dirac magnetic moment, expressed by:

$$\mu_D = \frac{q}{mc}|\vec{s}|$$ (0.1)

where q, m and s are the electric charge, mass and spin of the particle, respectively. In particular, the neutron magnetic moment should be 0 ($q = 0$). However, later measurements of these nucleons magnetic moments led to $\mu_p = 2.79\mu_B$ and $\mu_n =$

2

$-1.91\mu_B$, where μ_B is the Bohr magneton. This was the first evidence of a nucleon substructure.

Electron scattering experiments in the 1950's revealed a charge and magnetization distribution inside the proton and the neutron. Two form factors, called the electric and magnetic elastic form factors G_E and G_M were introduced to account for these distributions. Used to describe electromagnetic scattering of electrons off the nucleon, they contain the information about the internal structure responsible for the deviation from the scattering off point-like particles.

Fifty years later, as many other types of experiments study hadronic systems more complicated than the simple nucleon, these form factors remain difficult to measure, and only high intensity electron beams can measure these fundamental quantities at high momentum transfer, corresponding to a deep probing of the nucleon. The advent of highly polarized beams at Jefferson Lab, which use the spin degree of freedom of the particles to further study the nucleon structure, has allowed a great step forward in this understanding.

In 1964, a theory was suggesting that nucleons were actually composed of elementary particles called quarks. The existence of these quarks was confirmed experimentally in 1968, at the Stanford Linear Accelerator, where high energy electrons scattered off protons behaved as if bouncing off smaller hard cores. The search for all expected quark flavors extended to 1995 when the top quark was finally detected at Fermilab. The discovery of quarks led to the development of the Quantum ChromoDynamics field theory (QCD) of the strong interaction, in which quarks interact strongly by exchanging gluons, the force carriers. The very complex nature of this theory does not allow us to simply calculate all strong interaction phenomena. A complete understanding of the strong force relies on the collection of more experimental data.

This thesis presents the motivation, analysis and result of experiment E99-007,

which was conducted in 2000 in Hall A at Jefferson Lab. In this experiment, the ratio of the electric to magnetic form factors G_E/G_M of the proton was measured, to the relatively high four-momentum transfer squared $Q^2 = 5.6$ GeV^2. This experiment was the second phase of a series of measurements which started in 1998 with experiment E93-027, and will continue in the next few years with experiment E01-109. These experiments use the powerful, newly available, technique of recoil polarization to measure the form factor ratio.

This thesis is separated into seven chapters. The first chapter presents the powerful tool of electron scattering to study the nucleon, and discusses the formalism of nucleon form factors. It gives a detailed description of the two methods to measure these form factors, the Rosenbluth separation and the recoil polarimetry. It concludes with a presentation of the available experimental data prior to E99-007. The second chapter motivates the need of further measurements of the nucleon form factors, by presenting theoretical calculations and predictions.

The next four chapters focus on experiment E99-007. Chapter 3 describes the kinematics and the experimental equipment used, and chapters 4 and 5 discuss the analysis method. The sixth chapter presents the results of the measurements, and discusses the systematic errors.

The last chapter concludes by comparing these new data with theoretical models. Future experiments measuring nucleon form factors at Jefferson Lab are discussed.

CHAPTER 1

Nucleon form factors

1.1 Definitions and formalism

1.1.1 Exclusive electron scattering

When scattered off a nuclear target, the electron can exchange a virtual photon with the target nucleus, which probes the electromagnetic structure of this nucleus. The first advantage of electron scattering is that the electromagnetic coupling constant is small enough ($\alpha = 1/137$) to work only at the leading order of perturbation theory. The leading order diagram of elastic scattering reaction off a proton. Eq. 1.1, is shown on Fig. 1.1. We have:

$$e(k) + P(p) \to e(k') + P(p') \tag{1.1}$$
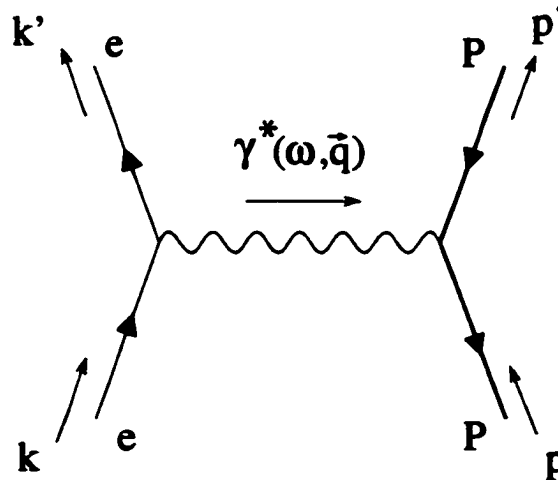
Figure 1.1: Leading order Feynman diagram of elastic scattering of an electron off a proton.

where the initial and final electrons have four-momenta $k = (E, \vec{k})$ and $k' = (E', \vec{k}')$ respectively, and the initial and final proton $p = (E_p, \vec{p})$ and $p' = (E'_p, \vec{p}')$ respectively. The virtual photon has a four-momentum $q = (\omega, \vec{q})$. We define the important Lorentz-invariant four-momentum transfer squared Q^2:

$$Q^2 = -q^2 = -\left(\omega^2 - \vec{q}^2\right) = -(k - k')^2 \sim 4EE' \sin^2 \frac{\theta_e}{2} \qquad (1.2)$$

where the last expression, true in the Lab frame, neglects the electron mass, which is justified when the electron is ultra-relativistic. Since a large Q^2 value is associated with a very short wavelength, the virtual photon will probe the short-scale structure of the proton.

In exclusive elastic scattering, where the recoil proton is also detected, the kinematics can be defined by either one of the final state particles, so that Q^2 can also be defined from the proton momenta:

$$Q^2 = -(p' - p)^2 = -\left[\left(E'_p - E_p\right)^2 - (\vec{p}' - \vec{p})^2\right] \qquad (1.3)$$

In the Lab frame, the initial proton is at rest, $\vec{p} = 0$ and $E_p = m$, and Eq. 1.3 becomes:

$$Q^2 = -\left[E'^2 + m^2 - 2E'_p m - \vec{p}^2\right] = -\left[2m^2 - 2mE'_p\right] = 2mT_p \qquad (1.4)$$

where m is the mass of the proton and $T_p = E'_p - m$ is the kinetic energy of the final proton in the Lab frame.

The second advantage of the electromagnetic probe lies in the fact that the leptonic vertex $e(k) \rightarrow e(k') + \gamma^*(q)$ is fully described by the theory of the electromagnetic interaction, Quantum ElectroDynamics (QED), so that only the hadronic vertex $\gamma^*(q) + P(p) \rightarrow P(p')$ contains new information, related to the unknown electromagnetic structure of the proton.

One disadvantage in using electrons as a probe of the nucleon and nucleus is that due to the small mass of the electron, one has to take radiative corrections

into account. Another disadvantage is that the electron does not interact with the gluon, which is a fundamental piece of the strong interaction puzzle. Finally, the small cross sections associated to electron scattering require higher beam intensities.

1.1.2 Formalism

Reading off the diagram in Fig. 1.1, the amplitude for elastic scattering can be written as:

$$
\begin{aligned}
i\mathcal{M} &= [ie\bar{v}(p')\Gamma^\mu(p',p)v(p)]\frac{-ig_{\mu\nu}}{q^2}[ie\bar{u}(k')\gamma^\nu u(k)] \\
&= \frac{-i}{q^2}[ie\bar{v}(p')\Gamma^\mu(p',p)v(p)][ie\bar{u}(k')\gamma_\mu u(k)]
\end{aligned}
\tag{1.5}
$$

where γ^μ, $\mu = 0,1,2,3$ with the 0-th component as the time component, are the Dirac 4×4 matrices:

$$
\gamma_0 = \begin{pmatrix} 0 & 1 \\ 1 & 0 \end{pmatrix} \ , \quad \vec{\gamma} = \begin{pmatrix} 0 & \vec{\sigma} \\ -\vec{\sigma} & 0 \end{pmatrix}
\tag{1.6}
$$

and $\vec{\sigma}$ is the set of standard Pauli matrices:

$$
\sigma_1 = \begin{pmatrix} 0 & 1 \\ 1 & 0 \end{pmatrix} \ , \quad \sigma_2 = \begin{pmatrix} 0 & -i \\ i & 0 \end{pmatrix} \ . \quad \sigma_3 = \begin{pmatrix} 1 & 0 \\ 0 & -1 \end{pmatrix}
\tag{1.7}
$$

For convenience, let's define:

$$
\sigma^\mu \equiv (1,\vec{\sigma}), \bar{\sigma}^\mu \equiv (1,-\vec{\sigma}).
\tag{1.8}
$$

$u(k)$ and $\bar{u}(k')$ in Eq. 1.5 are four-component Dirac spinors for the initial and final electrons respectively, and $v(p)$ and $\bar{v}(p')$ are spinors for the initial and final protons respectively. In particular, the proton spinors enter in the plane-wave solution for a spin 1/2 particle $\psi(x) = v(p)e^{-ip\cdot x}$ which satisfies the Dirac equation:

$$
(-i\gamma^\mu\partial_\mu - m)\psi(x) = 0
\tag{1.9}
$$

One can write [2]:

$$v(p) = \begin{pmatrix} \sqrt{p \cdot \sigma}\chi \\ \sqrt{p \cdot \bar{\sigma}}\chi \end{pmatrix} \tag{1.10}$$

where χ is a two-component spinor, normalized to $\chi^\dagger\chi = 1$.

As noted earlier, in the amplitude Eq. 1.5, the leptonic current $j_\mu = ie\bar{u}(k')\gamma_\mu u(k)$ is fully described by QED. On the other hand, the hadronic current $\mathcal{J}^\mu = ie\bar{v}(p')\Gamma^\mu v(p)$ involves the factor Γ^μ, which contains the information about the internal electromagnetic structure of the proton. In general, Γ^μ is some expression that involves p, p', γ^μ and constants such as the proton mass m, the electric charge e, and pure numbers. Since it transforms as a vector, Γ^μ must be a linear combination of these vectors, where the coefficients can only be function of q^2. It is convenient to write the current in the following way:

$$\mathcal{J}^\mu = ie\bar{v}(p')\Gamma^\mu v(p) = ie\bar{v}(p')\left[\gamma^\mu F_1(q^2) + \frac{i\sigma^{\mu\nu}q_\nu}{2m}\kappa F_2(q^2)\right]v(p) \tag{1.11}$$

where $\sigma^{\mu\nu} = \frac{i}{2}[\gamma^\mu, \gamma^\nu]$, and $F_1(q^2)$ and $F_2(q^2)$ are called the proton elastic form factors. They contain the information about the electromagnetic structure of the proton, which the virtual photon probes without modifying it. κ is the anomalous magnetic moment of the proton.

$F_1(q^2)$, or equivalently $F_1(Q^2)$, is the Dirac form factor; it conserves helicity in the hadron current. $F_2(q^2)$, or $F_2(Q^2)$ is the Pauli form factor; attached to the $\sigma^{\mu\nu}$ term, it is responsible for the spin flip in the current. F_1 and F_2 can be defined in a similar way for the neutron. The form factors are normalized to their value at $Q^2 = 0$. For the proton:

$$F_{1p}(0) = 1 \quad , \quad F_{2p}(0) = 1 \tag{1.12}$$

and for the neutron:

$$F_{1n}(0) = 0 \quad , \quad F_{2n}(0) = 1 \tag{1.13}$$

1.1.3 Sachs form factors

These form factors can also be written in the Sachs formalism [3], where the electric (G_E) and magnetic (G_M) form factors are defined as:

$$
\begin{aligned}
G_E &= F_1 - \tau \kappa F_2 \\
G_M &= F_1 + \kappa F_2
\end{aligned}
\tag{1.14}
$$

where $\tau = \frac{Q^2}{4m^2}$ is a kinematic factor. The Sachs form factors have the particular values at $Q^2 = 0$ of the electric charge and magnetic moment of the corresponding nucleon:

$$
\begin{aligned}
G_{Ep}(0) &= 1 \quad , \quad G_{Mp}(0) = \mu_p \\
G_{En}(0) &= 0 \quad , \quad G_{Mn}(0) = \mu_n
\end{aligned}
\tag{1.15}
$$

where $\mu_p = 2.79$ and $\mu_n = -1.91$ in units of nuclear magneton.

1.1.4 Hadronic current in the Breit frame

Following Refs. [2] and [4], we can express the current $\mathcal{J}^\mu$ in the Breit frame, also called the brick-wall frame. This frame is defined as the frame where the initial and final nucleon momenta are equal and opposite. The transformation from the Lab frame to the Breit frame is a boost along the transferred momentum. A definition of variables in the Breit frame, which are noted with a subscript B, can be found in Appendix A. In this frame, the form factors have an intuitive meaning, and are simply related to the current. Using the Gordon identity [5, p.72]:

$$
\bar{v}(p')\gamma^\mu v(p) = \bar{v}(p') \left[\frac{p'^\mu + p^\mu}{2m} + \frac{i\sigma^{\mu\nu}q_\nu}{2m} \right] v(p)
\tag{1.16}
$$

we can write:

$$
\Gamma^\mu = ie\bar{v}(p') \left[(F_1 + \kappa F_2)\gamma^\mu - \frac{(p + p')^\mu}{2m} \kappa F_2 \right] v(p)
\tag{1.17}
$$

In the Breit frame, the explicit expression of this current $\mathcal{J}^\mu = (\mathcal{J}^0, \vec{\mathcal{J}})$ is simplified:

$$\mathcal{J}^0 = ie\bar{v}(p') \left[(F_1 + \kappa F_2)\gamma^0 - \frac{E_{pB}}{m}\kappa F_2 \right] v(p)$$

$$\vec{\mathcal{J}} = ie(F_1 + \kappa F_2)\bar{v}(p')\vec{\gamma}v(p) \tag{1.18}$$

Using $\bar{v}(p') = v^\dagger(p')\gamma^0$, we can express the time component $\mathcal{J}^0$:

$$\mathcal{J}^0 = ie \left[(F_1 + \kappa F_2)v^\dagger(p')v(p) - \kappa F_2 \frac{E_{pB}}{m} v^\dagger(p')\gamma^0 v(p) \right] \tag{1.19}$$

and with $v(p)$ and γ^0 defined by Eqs. 1.10 and 1.6 respectively, we have:

$$\mathcal{J}^0 = ie(F_1 + \kappa F_2)\chi'^\dagger \left(\sqrt{p' \cdot \sigma}, \sqrt{p' \cdot \bar{\sigma}} \right) \begin{pmatrix} \sqrt{p \cdot \sigma} \\ \sqrt{p \cdot \bar{\sigma}} \end{pmatrix} \chi$$

$$-ie\kappa F_2 \frac{E_{pB}}{m}\chi' \left(\sqrt{p' \cdot \sigma}, \sqrt{p' \cdot \bar{\sigma}} \right) \begin{pmatrix} 0 & 1 \\ 1 & 0 \end{pmatrix} \begin{pmatrix} \sqrt{p \cdot \sigma} \\ \sqrt{p \cdot \bar{\sigma}} \end{pmatrix} \chi \tag{1.20}$$

We then must use the expressions:

$$\sqrt{p' \cdot \sigma}\sqrt{p \cdot \sigma} = \sqrt{p' \cdot \bar{\sigma}}\sqrt{p \cdot \bar{\sigma}} = m$$

$$\sqrt{p' \cdot \sigma}\sqrt{p \cdot \bar{\sigma}} + \sqrt{p' \cdot \bar{\sigma}}\sqrt{p \cdot \sigma} = 2E_{pB} \tag{1.21}$$

and

$$\tau = \frac{Q^2}{4m^2} = \frac{\vec{q}_B^2}{4m^2} = \frac{E_{pB}^2 - m^2}{m^2} \tag{1.22}$$

to finally get the simple relation:

$$\mathcal{J}^0 = ie2m\chi'^\dagger\chi(F_1 - \tau\kappa F_2) = ie2m\chi'^\dagger\chi G_E \tag{1.23}$$

In a similar way, we can express the vector current $\vec{\mathcal{J}}$ in the Breit frame:

$$\vec{\mathcal{J}} = -e\chi'^\dagger(\vec{\sigma} \times \vec{q}_B)\chi(F_1 + \kappa F_2) = -e\chi'^\dagger(\vec{\sigma} \times \vec{q}_B)\chi G_M \tag{1.24}$$

Notice the particularly simple relation between the Sachs form factors and the electromagnetic current at the hadronic vertex in the Breit frame: the electric form

factor G_E is directly responsible for the electric part of the interaction of the virtual photon with the nucleon, and the magnetic form factor G_M gives the magnetic part of this interaction. In the Breit frame, the electric and magnetic form factors can be identified with the Fourier transforms of the electric charge and magnetic current distributions, following the small Q^2 development:

$$
\begin{aligned}
G_E(Q^2) &= \int \rho(\vec{r}) e^{i\vec{q}\cdot\vec{r}} d^3\vec{r} \\
&= \int \rho(\vec{r}) d^3\vec{r} - \frac{\vec{q}^2}{6} \int \rho(\vec{r}) \vec{r}^2 d^3\vec{r} + \cdots
\end{aligned}
\tag{1.25}
$$

where the first integral in this small Q^2 expansion yields the total charge in units of e, and the second integral defines the square of the electric rms radius of the nucleon.

1.2 Rosenbluth cross section

This section presents a detailed derivation of the unpolarized elastic scattering cross section, and shows how measurements of this cross section allow to separate the electric and the magnetic form factors presented in the previous section.

1.2.1 Cross section calculation

The differential cross section can be written in any frame, and in particular in the lab frame, as:

$$
d\sigma = \frac{(2\pi^4)|\mathcal{M}|^2}{4(k\cdot p)}\delta^4(k + p - k' - p')\frac{d^3\vec{k}'}{(2\pi^3)2E'}\frac{d^3\vec{p}'}{(2\pi^3)2E'_p}
\tag{1.26}
$$

where we have neglected the electron mass, and where $\mathcal{M}$ is the amplitude defined in Eq .1.5. This can be reduced, integrating over $\vec{k}'$ and then $\vec{p}'$, to:

$$
\frac{d\sigma}{d\Omega_e} = \frac{|\mathcal{M}|^2}{64\pi^2}\frac{1}{m^2}\left(\frac{E'_p}{E_p}\right)^2
\tag{1.27}
$$

where Ω_e is the solid angle in which the electron is scattered, and $|\mathcal{M}|^2$ has the form:

$$|\mathcal{M}|^2 = \left[\mathcal{J}^\mu \frac{-i}{q^2} j_\mu\right]\left[\mathcal{J}^\nu \frac{-i}{q^2} j_\nu\right]^* = \left(\frac{1}{q^2}\right)^2 [\mathcal{J}^\mu \mathcal{J}^{\nu*}][j_\mu j_\nu^*] = \left(\frac{e^2}{q^2}\right)^2 W^{\mu\nu} L_{\mu\nu} \quad (1.28)$$

We define the hadronic and leptonic tensor respectively:

$$W^{\mu\nu} = \frac{1}{e^2}\mathcal{J}^\mu \mathcal{J}^{\nu*}$$

$$L_{\mu\nu} = \frac{1}{e^2}j_\mu j_\nu^* \quad (1.29)$$

where, for the unpolarized cross section, $W^{\mu\nu}$ and $L_{\mu\nu}$ are averaged over the incident particle spin states, and summed over the final particle spin states. Because the contraction of these two tensors is a Lorentz invariant, they can be calculated in any frame, as long as they are both calculated in the same frame.

Leptonic tensor

From Eq. 1.29, one can write:

$$L_{\mu\nu} = \bar{u}(k')\gamma_\mu u(k)\,[\bar{u}(k')\gamma_\nu u(k)]^* = \bar{u}(k')\gamma_\mu u(k)\bar{u}(k)\gamma_\nu u(k') \quad (1.30)$$

which is averaged over the polarization states of the incident electron and summed over the polarization states of the scattered electron. Recalling that u and $\bar{u}$ have spinor indices $(1,2)$, we can write the product in Eq. 1.30 as:

$$\begin{aligned} L_{\mu\nu} &= \bar{u}^a(k')\gamma_\mu^{ab}u(k)^b\bar{u}^c(k)\gamma_\nu^{cd}u^d(k') = u^d(k')\bar{u}^a(k')\gamma_\mu^{ab}u(k)^b\bar{u}^c(k)\gamma_\nu^{cd} \\ &= Tr\,[u(k')\bar{u}(k')\gamma_\mu u(k)\bar{u}(k)\gamma_\nu] \end{aligned} \quad (1.31)$$

The spinors disappear when summing and averaging over the spin states, using the completeness relation [5, p.49]:

$$\sum_{s=1,2} u^s(k)\bar{u}^s(k) = \gamma \cdot k - m_e \quad (1.32)$$

The tensor then becomes:

$$L_{\mu\nu} = \frac{1}{2}Tr\left[(\gamma \cdot k' - m_e)\gamma_\mu(\gamma \cdot k - m_e)\gamma_\nu\right] \tag{1.33}$$

This can be further simplified, using the trace technique of γ-matrices, in particular the fact that the trace of a product of an odd number of γ-matrices is null, and:

$$Tr\left[\gamma_\mu\gamma_\nu\right] = 4g_{\mu\nu}$$

$$Tr\left[\gamma_\mu\gamma_\nu\gamma_\rho\gamma_\sigma\right] = 4\left(g_{\mu\nu}g_{\rho\sigma} - g_{\mu\rho}g_{\nu\sigma} + g_{\mu\sigma}g_{\nu\rho}\right) \tag{1.34}$$

where $g_{\mu\nu}$ is the Minkowski metric. The leptonic tensor then takes the form:

$$L_{\mu\nu} = 2k_\mu k'_\nu + 2k_\nu k'_\mu - 2g_{\mu\nu}k \cdot k' \tag{1.35}$$

where $2k \cdot k' = Q^2$ if we neglect the electron mass. It is important to note here that the unpolarized leptonic tensor is symmetrical under permutation of indices μ and ν.

Hadronic tensor

Let us write the hadronic tensor $W^{\mu\nu}$ in the Breit frame, since this is where the current has a particularly simple expression. Summarizing Eqs. 1.23 and 1.24, we can write the current (in the system shown in Fig. A.1, $q_{B1} = q_{B2} = 0$ and $q_{B3} = \sqrt{Q^2}$) as:

$$J^\mu = ie\chi'^\dagger \mathcal{F}^\mu \chi \tag{1.36}$$

with:

$$\mathcal{F}^0 = 2mG_E$$

$$\mathcal{F}^1 = i\sqrt{Q^2}G_M\sigma^2$$

$$\mathcal{F}^2 = -i\sqrt{Q^2}G_M\sigma^1$$

$$\mathcal{F}^3 = 0 \tag{1.37}$$

so that:

$$W^{\mu\nu} = \frac{1}{e^2} \mathcal{J}^\mu \mathcal{J}^{\nu*} = \chi'^\dagger \mathcal{F}^\mu \chi \left[\chi'^\dagger \mathcal{F}^\nu \chi \right]^* = \chi'^\dagger \mathcal{F}^\mu \chi \chi^\dagger \mathcal{F}^{\nu\dagger} \chi' \qquad (1.38)$$

In a similar way as for the derivation of the leptonic tensor, we average over initial proton spin states and sum over final proton spin states and use the completeness relation:

$$\sum_{s=1,2} \chi^s \chi^{\dagger s} = 1 \qquad (1.39)$$

to get:

$$W^{\mu\nu} = \frac{1}{2} Tr \left[\mathcal{F}^\mu \mathcal{F}^{\nu\dagger} \right] \qquad (1.40)$$

We can derive explicitly each term. First it is trivial to note that:

$$W^{3\mu} = W^{\mu 3} = 0 \qquad (1.41)$$

for $\mu = 0, 1, 2, 3$. Then let's use the fact that $Tr\left[\sigma^i\right] = 0$ ($i = 1, 2, 3$) to get:

$$W^{0i} = W^{i0} = 0 \qquad (1.42)$$

for $i = 1, 2, 3$. Finally $Tr\left[\sigma^1 \sigma^2\right] = Tr\left[\sigma^2 \sigma^1\right] = 0$ leads to:

$$W^{12} = W^{21} = 0 \qquad (1.43)$$

Only three terms are non-zero:

$$W^{00} = 4m^2 G_E^2$$
$$W^{11} = Q^2 G_M^2$$
$$W^{22} = Q^2 G_M^2 \qquad (1.44)$$

It is important to note that all the interference terms involving the product $G_E G_M$, which can come from W^{01} or W^{02}, have disappeared, therefore the unpolarized cross section will not contain any of these interference terms.

Amplitude in the Breit frame

We are now ready to derive the unpolarized cross section for elastic scattering of an electron off the proton. We first have to contract the leptonic and the hadronic tensors. Using only the three non-zero terms, we have:

$$
\begin{aligned}
W^{\mu\nu}L_{\mu\nu} &= W^{00}L_{00} + W^{11}L_{11} + W^{22}L_{22} \\
&= 4m^2 G_E^2 L_{00} + Q^2 G_M^2 (L_{11} + L_{22})
\end{aligned}
\tag{1.45}
$$

We need to derive the corresponding terms of the leptonic tensor. Using Eq. 1.35, we get:

$$
\begin{aligned}
L_{00} &= 4E_B^2 - Q^2 = Q^2 \cot^2 \frac{\theta_B}{2} \\
L_{11} &= 4k_{1B}^2 + Q^2 = Q^2 \left(1 + \cot \frac{\theta_B}{2}\right) \\
L_{22} &= Q^2
\end{aligned}
\tag{1.46}
$$

where the subscript B again denotes variables in the Breit frame. We can then calculate the square of the amplitude, according to Eq. 1.28:

$$
\begin{aligned}
|\mathcal{M}|^2 &= \left(\frac{e^2}{Q^2}\right)^2 \left[4m^2 G_E^2 Q^2 \cot^2 \frac{\theta_B}{2} + Q^2 G_M^2 \left(2Q^2 + Q^2 \cot^2 \frac{\theta_B}{2}\right)\right] \\
&= \left(\frac{e^2}{Q^2}\right)^2 4m^2 Q^2 \left[2\tau G_M^2 + \cot^2 \frac{\theta_B}{2} \left(G_E^2 + \tau G_M^2\right)\right]
\end{aligned}
\tag{1.47}
$$

where τ is the usual factor $\tau = \frac{Q^2}{4m^2}$.

Back to the Lab frame

At this point it is more interesting to convert this expression to the Lab frame, since this is where we can perform experiments. Using Eq. A.14, we can express the amplitude squared Eq. 1.47 in the Lab frame:

$$
|\mathcal{M}|^2 = \left(\frac{e^2}{Q^2}\right)^2 4m^2 Q^2 \left[2\tau G_M^2 + \frac{\cot^2 \frac{\theta_e}{2}}{1 + \tau} \left(G_E^2 + \tau G_M^2\right)\right]
\tag{1.48}
$$

Plugging this relation into Eq. 1.27 leads to the cross section in the Lab frame:

$$\frac{d\sigma}{d\Omega_e} = \frac{\alpha^2}{Q^2}\left(\frac{E'}{E}\right)^2\left[2\tau G_M^2 + \frac{\cot^2\frac{\theta_e}{2}}{1+\tau}\left(G_E^2 + \tau G_M^2\right)\right] \qquad (1.49)$$

where $\alpha = e^2/4\pi \sim 1/137$ is the fine structure constant. This expression of the cross section is known as the Rosenbluth formula [6]. Note that this formula describes only the leading order in perturbation theory, with one-photon exchange.

1.2.2 Rosenbluth separation

The Rosenbluth cross section has two contributions: the electric term G_E and the magnetic term G_M. As noted earlier, there is no interference term, so that the two contributions can be separated. We can define the "reduced cross section" as:

$$\sigma_{red} = (1+\tau)\tan^2(\theta_e/2)\frac{\frac{d\sigma}{d\Omega_e}}{\frac{\alpha^2}{Q^2}\left(\frac{E'}{E}\right)} = G_E^2 + \frac{\tau}{\epsilon}G_M^2 \qquad (1.50)$$

where $1/\epsilon = 1 + 2(1+\tau)\tan^2(\theta_e/2)$ is a term that represents the polarization of the virtual photon. This relation is the basis of the Rosenbluth separation technique, used to measure the elastic form factors of the nucleon separately. The quantity $1/\epsilon$ can be varied at a given Q^2, by changing the incident electron energy and the scattering angle. Therefore, if at the same Q^2, but different values of $1/\epsilon$, one measures the elastic scattering cross section, one can separate the two contributions, as shown in Fig. 1.2. A linear fit to the cross section measurements leads to a slope that is equal to τG_M^2 and an intercept equal to G_E^2.

This method has been extensively used in the last 40 years to measure the elastic form factors, and proved to be very powerful to measure the proton and the neutron magnetic form factor up to a large Q^2, and the proton electric form factor to $Q^2 = 1$ GeV^2. However, its efficiency is limited for the neutron electric form factor, since this quantity is normalized to the electric charge of the neutron, which is 0, so that the cross section is immediately completely dominated by the magnetic term.
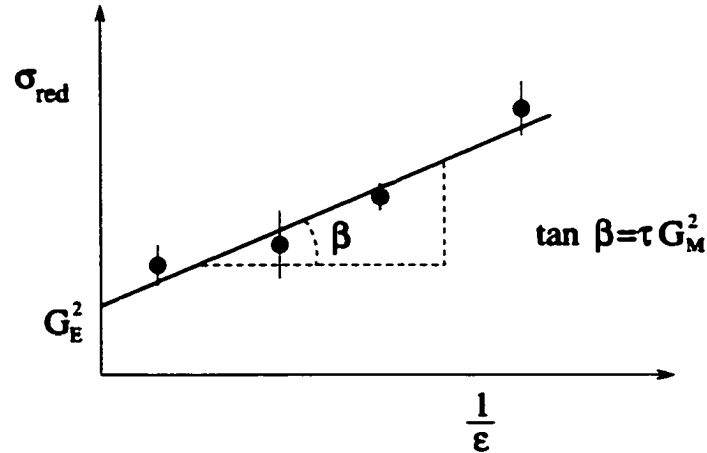
Figure 1.2: Rosenbluth separation: σ_{red} vs. $1/\epsilon$, at a given Q^2. The slope is τG_M^2 and the intercept is G_E^2 (the data points do not correspond to any existing measurement; they are here just to illustrate the method).

For the proton, as Q^2 increases, the magnetic term will also dominate, for two reasons: first, the normalization factor of the magnetic form factor is $\mu_p = 2.79$ times larger than the one of the electric form factor, which makes its contribution already $\mu_p^2 \sim 7.7$ times larger; second, the factor $\tau \propto Q^2$ in the magnetic term increases as Q^2 gets bigger. In fact, at $Q^2 = 2$ GeV^2, the magnetic term contributes already about 95% of the total cross section.

1.3 Recoil polarization technique

A practical way to measure a small term in the presence of a dominating larger term, is to measure the interference between the two. As we have seen in the previous section, the unpolarized elastic cross section of an electron off a nucleon has no interference term between G_E and G_M. However, this term can be measured using the spin degree of freedom of the incident electron and of either the initial or final nucleon. This section describes the recoil polarization technique, which allows the determination of the ratio G_E/G_M by measuring the polarization of the recoil

nucleon, in the scattering of a polarized beam off an unpolarized target. Another way of measuring this interference term would be to look for asymmetries in the scattering of a polarized beam off a polarized target. This method is not discussed here.

1.3.1 Polarized tensors

If we measure the polarization $P_{\hat{u}}$ of the recoil nucleon along a unit vector $\hat{u}$, we measure a preferential orientation, pointing one way or the other, of the spin along $\hat{u}$. In this case, the completeness relation Eq. 1.39 does not hold anymore. Instead, we have to use:

$$\sum_{s=1,2} \chi'^s \chi'^{\dagger s} = 1 + \vec{\sigma} \cdot \hat{u} \tag{1.51}$$

so that the hadronic tensor becomes:

$$W^{\mu\nu} = \frac{1}{2} Tr \left[\mathcal{F}^\mu (1 + \vec{\sigma} \cdot \hat{u}) \mathcal{F}^{\nu\dagger} \right] = W_u^{\mu\nu} + W_p^{\mu\nu} \tag{1.52}$$

where $W_u^{\mu\nu}$ is the unpolarized hadronic tensor Eq. 1.40, and $W_p^{\mu\nu}$ is the polarized one:

$$W_p^{\mu\nu} = \frac{1}{2} Tr \left[\mathcal{F}^\mu \mathcal{F}^{\nu\dagger} \vec{\sigma} \cdot \hat{u} \right] \tag{1.53}$$

There are three directions to consider: along the three axis of the coordinate system shown in Fig. A.1 in Appendix A: u_3 along the nucleon momentum, u_1 in the transverse direction in the scattering plane, and u_2 normal to the scattering plane.

Apart from the measurement of the recoil proton polarization measurement, the recoil polarization method requires the use of a longitudinally polarized beam, *i.e.* a beam in which the spin of the electron along the momentum is preferentially in one direction: parallel (right-handed) or anti-parallel (left handed) to the momentum. The polarization of the beam is then defined as the asymmetry:

$$h = \frac{N_{par} - N_{antipar}}{N_{par} + N_{antipar}} \tag{1.54}$$

where N_{par} and $N_{antipar}$ are the number of electrons with their spin parallel and anti-parallel to their momentum respectively. Therefore, to express the fact that the electron beam is polarized, one must also modify the leptonic tensor. For this, we introduce a new γ matrix:

$$\gamma_5 = i\gamma_0\gamma_1\gamma_2\gamma_3 = \begin{pmatrix} -1 & 0 \\ 0 & 1 \end{pmatrix} \tag{1.55}$$

In this representation, one can see that the operator:

$$\frac{1 - \gamma_5}{2} = \begin{pmatrix} 1 & 0 \\ 0 & 0 \end{pmatrix} \tag{1.56}$$

projects the spin along the momentum in a preferential direction, therefore describes a right-handed polarized beam. If the beam polarization is h, the leptonic tensor becomes:

$$\begin{aligned}
L_{\mu\nu} &= \frac{1}{2}Tr\left[(\gamma \cdot k' - m_e)\gamma_\mu (1 - h\gamma_5)(\gamma \cdot k - m_e)\gamma_\nu\right] \\
&= 2k_\mu k'_\nu + 2k_\nu k'_\mu - 2g_{\mu\nu}k \cdot k' + 2ih\epsilon_{\mu\nu\alpha\beta}k_\alpha k'_\beta \\
&= L^u_{\mu\nu} + L^p_{\mu\nu}
\end{aligned} \tag{1.57}$$

neglecting the electron mass, and where $\epsilon_{\mu\nu\alpha\beta}$ is the Levi-Civita symbol. It is 0 if any two indices are identical, -1 under an even number of permutations and $+1$ under an odd number of permutations. Note that $L^p_{\mu\nu}$ is anti-symmetrical.

1.3.2 Polarized amplitude

When we contract the leptonic and the hadronic tensors to form the amplitude squared, we get:

$$W^{\mu\nu}L_{\mu\nu} = W^{\mu\nu}_u L^u_{\mu\nu} + W^{\mu\nu}_u L^p_{\mu\nu} + W^{\mu\nu}_p L^u_{\mu\nu} + W^{\mu\nu}_p L^p_{\mu\nu} \tag{1.58}$$

where

- $W_u^{\mu\nu} L_{\mu\nu}^u$ is the amplitude squared of the unpolarized process, derived in the previous section,

- $W_u^{\mu\nu} L_{\mu\nu}^p = 0$ because it is the product of a symmetrical and an anti-symmetrical tensors,

- $W_p^{\mu\nu} L_{\mu\nu}^u$ represents the polarization state of the recoil proton after scattering of an unpolarized beam off an unpolarized target, or **induced polarization**,

- $W_p^{\mu\nu} L_{\mu\nu}^p$ represents the polarization state of the recoil proton after scattering of a polarized beam of polarization h, or **transferred polarization**.

The recoil polarizations (induced and transferred) along the vector $\hat{u}$ are then given by:

$$P_{\hat{u}}^{ind} = \frac{W_p^{\mu\nu} L_{\mu\nu}^u}{W_u^{\mu\nu} L_{\mu\nu}^u}$$

$$h P_{\hat{u}}^{transf} = \frac{W_p^{\mu\nu} L_{\mu\nu}^p}{W_u^{\mu\nu} L_{\mu\nu}^u} \tag{1.59}$$

Using these definitions, the amplitude can be written:

$$W^{\mu\nu} L_{\mu\nu} = W_u^{\mu\nu} L_{\mu\nu}^u \left(1 + P_{\hat{u}}^{ind} + h P_{\hat{u}}^{transf}\right) \tag{1.60}$$

1-component

Let's first suppose we measure the polarization along the 1-direction. We can derive each term of the hadronic tensor:

$$W_{p,1}^{\mu\nu} = \frac{1}{2} Tr\left[\mathcal{F}^\mu \mathcal{F}^{\nu\dagger} \sigma^1\right] \tag{1.61}$$

Using $\sigma^1 \sigma^2 = i\sigma^3$, $\sigma^3 \sigma^1 = i\sigma^2$ and $\sigma^2 \sigma^3 = i\sigma^1$, we get:

$$\mathcal{F}^{0\dagger} \sigma^1 = 2mG_E \sigma^1$$

$$\mathcal{F}^{1\dagger} \sigma^1 = -\sqrt{Q^2} G_M \sigma^3$$

$$\mathcal{F}^{2\dagger} \sigma^1 = i\sqrt{Q^2} G_M$$

$$\mathcal{F}^{3\dagger} \sigma^1 = 0 \tag{1.62}$$

which we multiply on the left by $\mathcal{F}^\mu$ and take the trace, using the same trace properties of the $\vec{\sigma}$ matrices noted in Section 1.2.1. The only non-zero terms arising are:

$$W_{p,1}^{02} = i\sqrt{Q^2} 2mG_EG_M$$

$$W_{p,1}^{20} = -i\sqrt{Q^2} 2mG_EG_M \tag{1.63}$$

We note here, and this will be also true for the other components, that the polarized tensor is anti-symmetrical, so that when it is multiplied by the symmetrical unpolarized leptonic tensor, the terms will vanish. **In electromagnetic elastic scattering, which is a parity conserving process, in the one-photon exchange approximation, there is no induced polarization.**

Let us now derive the corresponding polarized terms of the leptonic tensor in the Breit frame. This part is anti-symmetrical, so it obeys:

$$L_{02}^p = -L_{20}^p \tag{1.64}$$

According to Eq. 1.57:

$$L_{02}^p = 2ih\epsilon_{02\alpha\beta}k_\alpha k'_\beta$$

$$= 2ih(k_{1B}k'_{3B} - k_{3B}k'_{1B}) = -ihQ^2 \cot\frac{\theta_B}{2} \tag{1.65}$$

If we contract Eqs. 1.65 and 1.63, we get the transfered polarization amplitude:

$$W_{p,1}^{\mu\nu}L_{\mu\nu}^p = 4hmQ^2\sqrt{Q^2}\cot\frac{\theta_B}{2}G_EG_M \tag{1.66}$$

Note that measuring the 1-component, or transverse component of the recoil proton polarization, gives access to the interference term G_EG_M, which was inaccessible from an unpolarized cross section measurement.

2-component

The derivation for the 2-component is exactly identical. It involves the terms $W_{p,2}^{01}$ and L_{01}^{p} of the tensors, in particular:

$$L_{01}^{p} = 2ih\epsilon_{01\alpha\beta}k_{\alpha B}k'_{\beta B} = 2ih\left(k_{3B}k'_{2B} - k_{2B}k'_{3B}\right) = 0 \qquad (1.67)$$

since $k_{2B} = k'_{2B} = 0$. Therefore, **there is no normal component to the transferred polarization in elastic scattering.**

3-component

The same derivation applies to the longitudinal, 3-component, to get:

$$W_{p,3}^{\mu\nu}L_{\mu\nu}^{p} = -4hQ^2\sqrt{Q^2}\frac{G_M^2}{\sin\left(\theta_B/2\right)} \qquad (1.68)$$

The measurement of the longitudinal component of the recoil proton polarization is a measurement of the magnetic form factor G_M^2.

1.3.3   Recoil polarization formulas

Using Eq. 1.59, we can express the transferred polarization components, changing the notation $1 \leftrightarrow y$, $2 \leftrightarrow x$, $3 \leftrightarrow z$, applying the transformation from the Breit frame to the Lab frame defined in Appendix A, and rearranging the terms:

$$\sigma_{red}hP_x = 0$$
$$\sigma_{red}hP_y = -2h\sqrt{\tau(1+\tau)}\tan\frac{\theta_e}{2}G_E G_M$$
$$\sigma_{red}hP_z = h\frac{E+E'}{m}\sqrt{\tau(1+\tau)}\tan^2\frac{\theta_e}{2}G_M^2 \qquad (1.69)$$

where $\sigma_{red} = G_E^2 + (\tau/\epsilon)G_M^2$ was defined in Section 1.2.2. We can see from Eq. 1.69, that a simultaneous measurement of the transverse and longitudinal components of the polarization of the recoil proton results in the extraction of the ratio of the form factors G_E/G_M:

$$\frac{G_E}{G_M} = -\frac{hP_y}{hP_z}\frac{E+E'}{2m}\tan\frac{\theta_e}{2} \qquad (1.70)$$

Equation 1.70 shows that this method offers experimental advantages over the Rosenbluth separation:

- For a given Q^2, only a single measurement is necessary, if the polarimeter can measure both components at the same time. This greatly reduces the systematic errors associated with spectrometer motion and beam energy change.

- The extraction of a ratio makes unnecessary the knowledge of the beam polarization and of the analyzing power of the polarimeter.

- The measurement of the interference term $G_E G_M$ allows the characterization of the electric form factor with a much better accuracy than with a cross section measurement.

- There is no need to measure absolute cross sections, which therefore also reduces the systematic errors.

While the electric form factor can be extracted from this ratio using an independent measurement of G_M, by Rosenbluth separation for example, the value of the ratio, independently of G_M, is of considerable interest. In particular, this ratio is related to the ratio of the Pauli and Dirac form factors F_2/F_1. The theory of strong interaction at high energy, perturbative QCD, has asymptotic predictions of this ratio F_2/F_1, which can then be directly tested by this type of experiment, as will be seen later.

1.4 Experimental world data

Proton and neutron form factors have been measured for 50 years at different electron accelerators around the world. A good review of measurements of electromagnetic form factors of the nucleon can be found in Ref. [7].

1.4.1 Cross section experiments

Cross section measurements and Rosenbluth separation at low Q^2 uncovered the empirical dipole law and form factor scaling:

$$\frac{G_{Mp}}{\mu_p} \simeq G_{Ep} \simeq \frac{G_{Mn}}{\mu_n} \simeq G_D \tag{1.71}$$

where:

$$G_D = \left(1 + \frac{Q^2}{0.71 \text{GeV}^2}\right)^{-2} \tag{1.72}$$

corresponding to an exponential distribution of the charge and current, with a rms radius of 0.8 fm.

Magnetic form factors
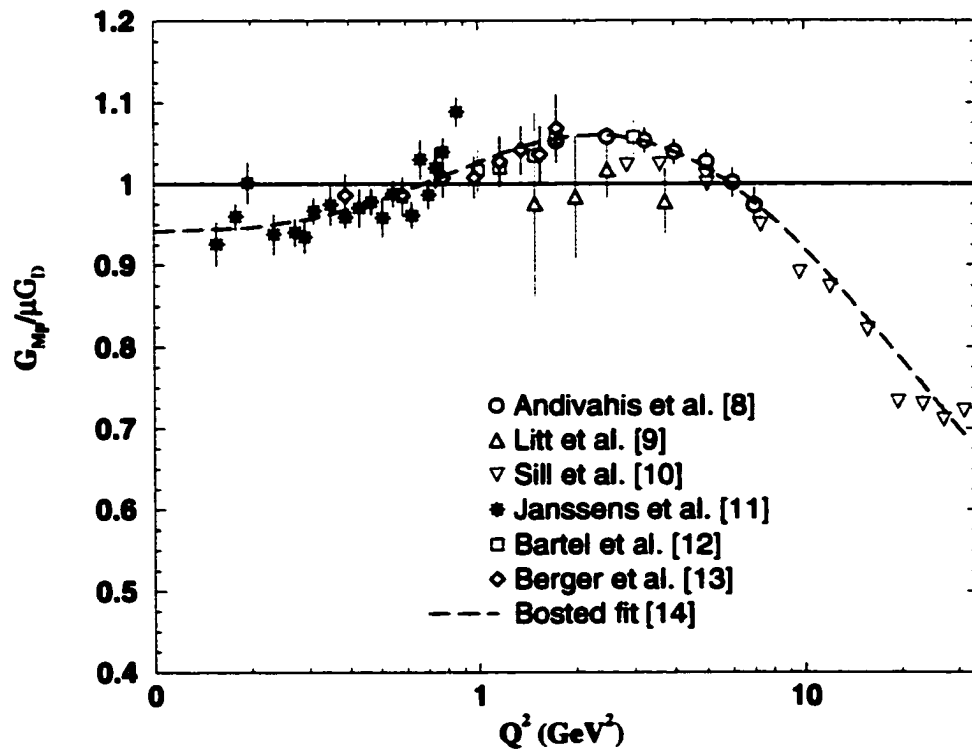
Figure 1.3: Measurement of $\mu_p G_{Mp}/G_D$ up to $Q^2 = 30$ GeV^2. The dashed line is the Bosted fit. See text for references.

Figure 1.3 shows a compilation of measurements of the magnetic form factor for the proton, divided by the dipole fit. The data presented here are from SLAC [8, 9, 10, 11], DESY [12] and Bonn [13]. Data from Ref. [10], up to $Q^2 = 31.2$ GeV^2, were taken in a Q^2 regime where the cross section was completely dominated by the magnetic term. Therefore, the two form factors could not be separated. Instead, G_{Mp} was extracted directly from the cross section measurement, assuming the form factor scaling $\mu_p G_{Ep}/G_{Mp} = 1$. These data were fit by Bosted [14], according to:

$$\frac{G_{Mp}}{\mu_p G_D} = \frac{1}{1 + 0.35Q + 2.44Q^2 + 0.50Q^3 + 1.04Q^4 + 0.34Q^5} \qquad (1.73)$$

The data follow the dipole shape reasonably well up to $Q^2 = 10$ GeV^2, but show a large deviation from this behavior at high Q^2.
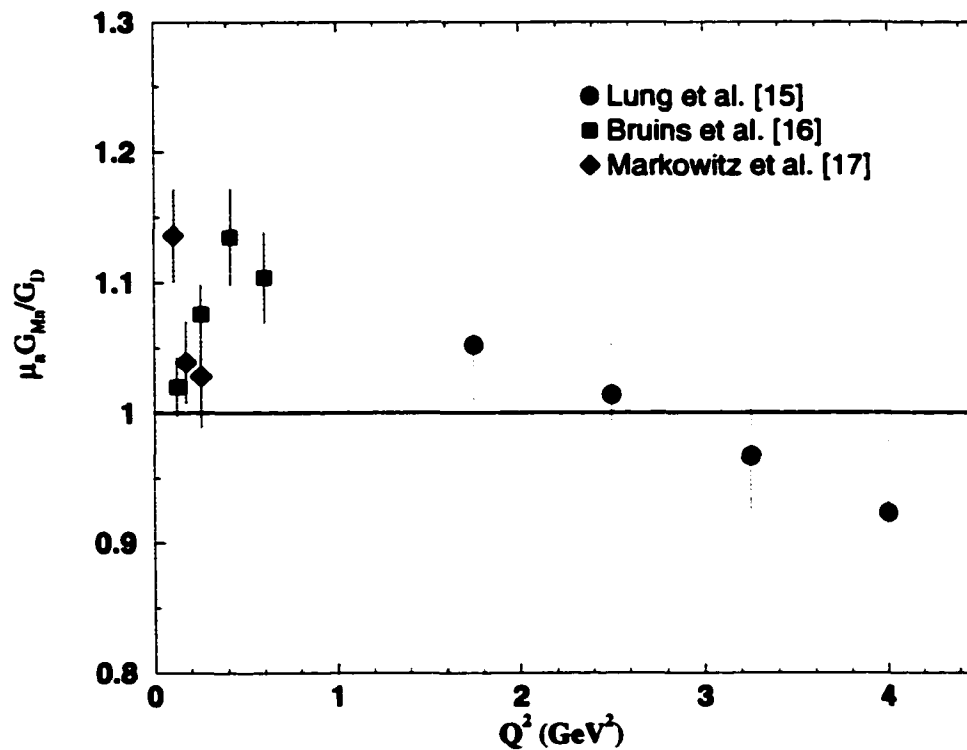
Figure 1.4: Measurements of $\mu_n G_{Mn}/G_D$ up to $Q^2 = 5$ GeV^2, by Rosenbluth separation.

The form factors of the neutron can be extracted from elastic and quasi-elastic scattering of electrons off a deuteron target. The neutron contribution must then be separated from the proton contribution, using a theoretical model. Figure 1.4 shows a compilation of Rosenbluth measurements of the neutron magnetic form factor, divided by the dipole fit. Data were taken at SLAC [15], Bonn [16] and Bates [17].

Experiment E94-017 in Hall B at Jefferson Lab measured the neutron form factors in electron-deuteron scattering from $Q^2 = 0.3$ to 7.5 GeV^2. The data are currently being analyzed.

Electric form factors
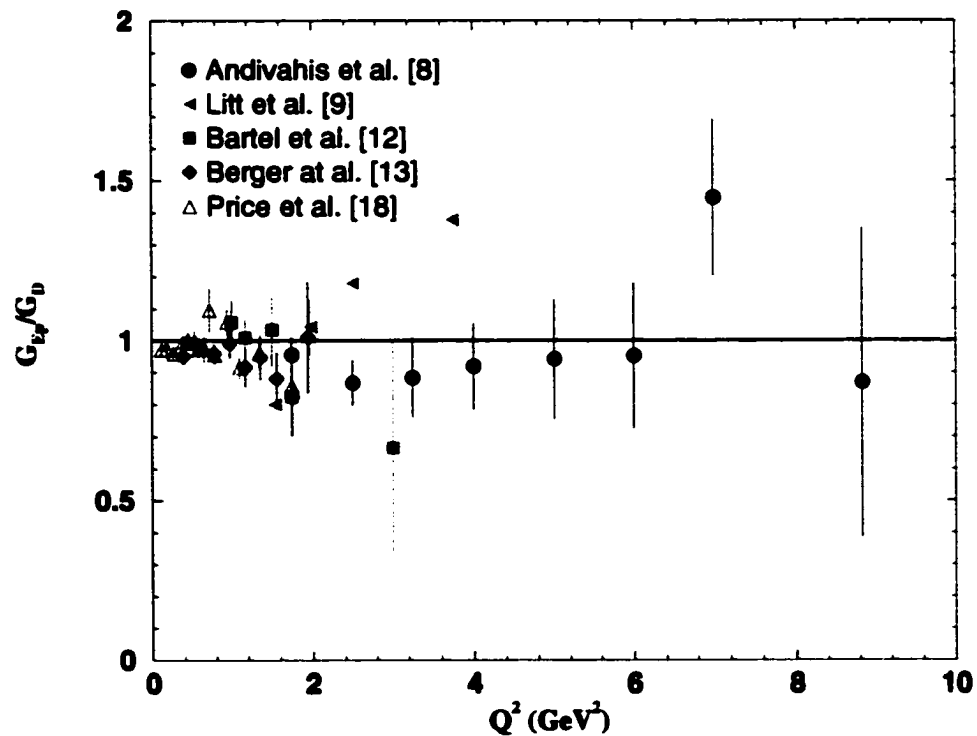
Figure 1.5: Results for G_{Ep}/G_D up to $Q^2 = 10$ GeV^2, by Rosenbluth separation.

For the proton, experiments presented in Fig. 1.3 (except the one of Ref. [10]) also measured the electric form factor, using the Rosenbluth separation technique. The results [8, 9, 12, 13, 18] are shown in Fig. 1.5. This technique is most powerful for $Q^2 < 2$ GeV^2, but above this value, it becomes increasingly difficult to measure the electric contribution, because it is kinematically dominated by the magnetic term. The results reported in Fig. 1.5 show large uncertainties and some discrepancy between data sets.

For the neutron, the extraction of G_{En} is very difficult with the Rosenbluth separation method. At low Q^2, G_{En} is close to zero, and as Q^2 increases, the electric contribution is dominated by the magnetic term.

1.4.2   Recoil polarization experiments
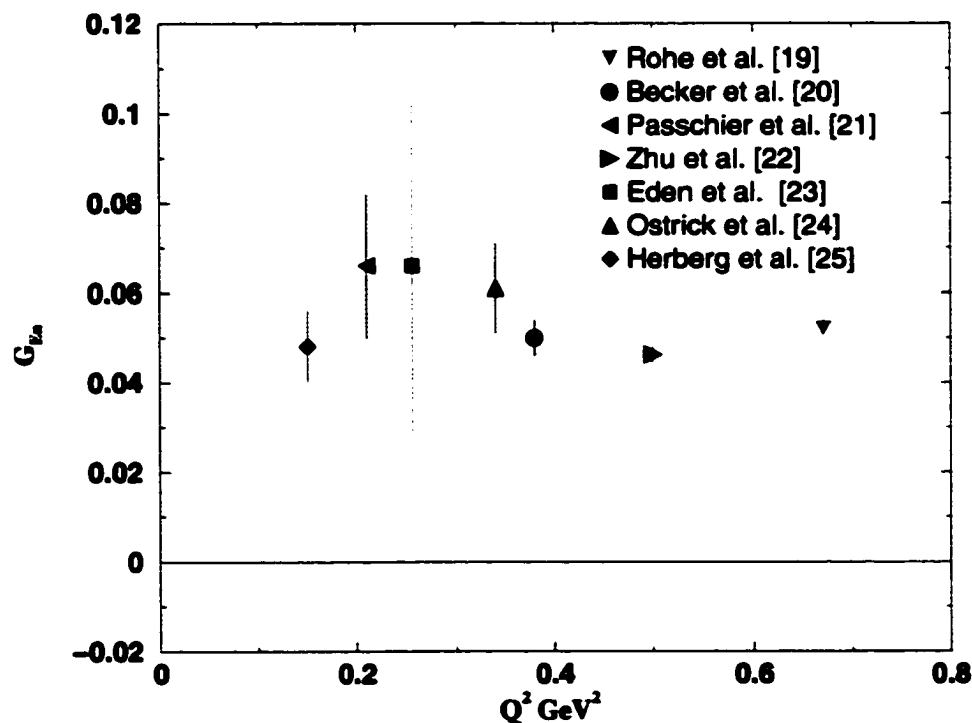
Figure 1.6: Results for G_{En} up to $Q^2 = 0.7$ GeV^2, by polarimetry methods.

The use of polarimetry to measure the neutron electric form factor has been greatly developed in the last decade. Precision measurements of G_{En} at low Q^2 have been achieved at Mainz using a polarized ^{3}He target [19, 20], and at NIKHEF [21] and JLab-Hall C [22] using a polarized ^{2}H target. Other measurements using a recoil neutron polarimeter were conducted at Bates [23] and Mainz [24, 25]. The results are presented in Fig. 1.6.
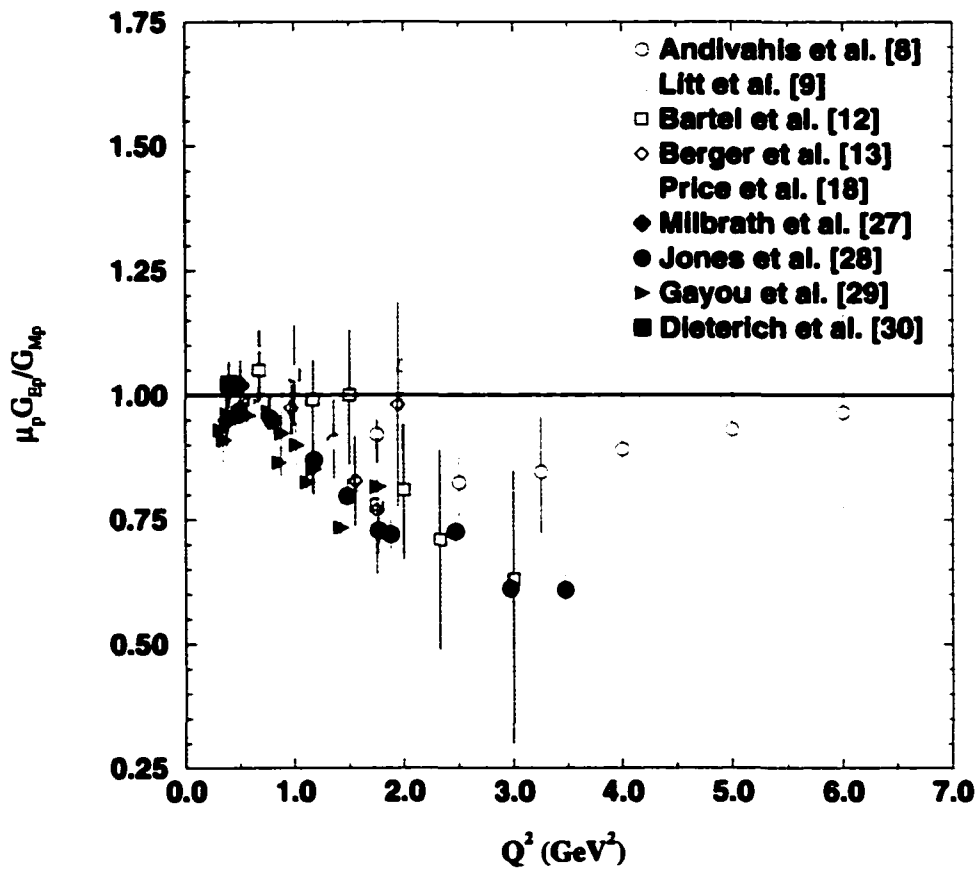
Figure 1.7: Measurements of $\mu_p G_{Ep}/G_{Mp}$ to $Q^2 = 7$ GeV^2, by Rosenbluth separation (empty symbols), and recoil polarization (full symbols).

For the proton, the first use of recoil polarimetry to measure the ratio of electric to magnetic form factors was done at Bates [26, 27], at $Q^2 = 0.38$ and 0.5 GeV^2,

proving the feasibility of the technique. Then the advent of Jefferson Lab, with its unique high luminosity and polarized beam allowed a precise measurement of this ratio to $Q^2 = 3.5$ GeV^2, in experiment E93-027 in Hall A [28]. Other measurements were conducted in Hall A at lower Q^2, as calibration measurements for other polarization experiments [29, 30]. The results are reported in Fig. 1.7. The JLab measurements [28] showed for the first time a clear deviation of the proton form factor ratio from unity, starting at $Q^2 \simeq 1$ GeV^2. The experiment presented here, E99-007, is the extension of E93-027 to higher Q^2. This deviation had early been suggested, with large uncertainties, by an experiment at DESY in 1973 to $Q^2 = 3.0$ GeV^2 [12], but this result was contradicted by later measurements [8, 9].

CHAPTER 2

Physics motivation

One of the goals of nuclear physics is to determine the role that quarks and gluons play in nuclei and nuclear structure. The Quantum ChromoDynamic (QCD) field theory emerges as the theory of the strong interaction. In this theory, quarks carry color charges (blue (B), red (R) or green (G)), and interact with each other exchanging massless particles, called gluons. The non-abelian character of the theory comes form the fact that gluons carry color charges too, so that they can interact with each other. One of the characteristics of QCD is confinement: no free quark has ever been observed, because quarks "gather" in a color-neutral system, such as a meson, made of a quark and an antiquark $(B\bar{B}, R\bar{R}$ or $G\bar{G})$ or a baryon made of three quarks (RBG). The second particular feature of QCD is asymptotic freedom. It comes from the fact that the coupling constant α_s depends on Q^2, according to [1, p.297]:

$$\alpha_s(Q^2) = \frac{\alpha_s(0)}{1 + \frac{\alpha_s(0)}{16\pi^2}\left(11 - \frac{2}{3}N_f\right)\ln\left(\frac{Q^2}{\Lambda_{QCD}^2}\right)} \tag{2.1}$$

where N_f is the number of quark flavors, and Λ_{QCD} is the QCD mass scale. This mass scale has been determined experimentally to be around 200 MeV. This behavior of the strong coupling constant, which is high at low Q^2 and low at high Q^2, leads to extremely complicated calculations of particular phenomena and quantities. In particular, in the low and intermediate momentum transfer regime, where the strong coupling constant is too large to allow a perturbative description, the calculation of nucleon form factors becomes an insurmountable task. However, several low Q^2 effective models have been developed, which try to describe the nucleon properties

30

in this kinematic region. All of them have parameters that are adjusted to fit the experimental data. The common way form factors can be calculated with these models requires expressing the hadronic current of the left-hand side of Eq. 1.11 in terms of the current of the constituents of the model, and relating this expression to the right-hand side of Eq. 1.11, which contains F_1 and F_2. Eq. 1.14 is used if the predicted form factors are the Sachs form factors G_E and G_M.

Several of these models are introduced in this chapter. First, some low Q^2 models are presented, such as the cloudy bag and the vector meson dominance models. Then relativistic constituent quark models, and other types of theories effective in the few GeV^2 region, such as the soliton or the diquark models are discussed. A lattice QCD approach is also introduced. Finally, the perturbative QCD predictions, effective at asymptotically high momentum transfer, are presented.

2.1 Low Q^2 models

We first discuss models which describe the nucleon form factors by assuming that the virtual photon couples not with the quarks inside the nucleon, but with mesons, which in turn interact with the nucleon. These models are expected to be valid at $Q^2 < 1 - 2$ GeV^2.

2.1.1 Cloudy bag model

The MIT bag model [31, 32, 33] describes the nucleon as three quark fields confined in a potential that maintains them within a finite sphere of radius R of order 0.8 to 1 fm. This model was later improved by adding a pionic field coupled to the quarks inside the bag [34], to improve the static properties of the nucleon (at $Q^2 = 0$). It also provides a convenient way to connect the model with πN and NN scattering data. The electromagnetic form factors were calculated in this cloudy bag model [35] using the quark and pion currents. The agreement with data is good

in the $Q^2 < 1$ GeV^2, given the simplicity of the model. In particular, there are no explicit vector meson contributions and one possible development would be to include $\pi\pi$ interactions [35].

2.1.2 Vector meson dominance model
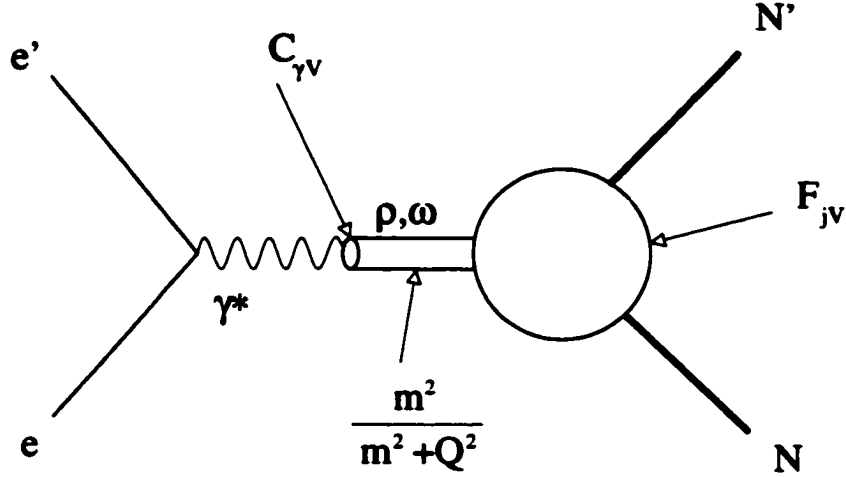
Figure 2.1: Photon-nucleon coupling in the VMD models.

In the vector meson dominance (VMD) picture, the virtual photon couples to the nucleon through vector mesons, as shown in Fig. 2.1, and the nucleon form factors are expressed in terms of photon-meson coupling strengths $C_{\gamma V}$ and meson-nucleon vertex form factors F_{jV}:

$$F_j^{is,iv}(Q^2) = \sum_i \frac{m_i^2 C_{\gamma Vi}}{m_i^2 + Q^2} F_{jVi}(Q^2) \qquad (2.2)$$

where the sum is over vector mesons of mass m_i, and is and iv correspond to the isoscalar and isovector electromagnetic currents respectively. The form factors are then given by:

$$2F_{jp} = F_j^{is} + F_j^{iv} \quad ; \quad 2F_{jn} = F_j^{is} - F_j^{iv} \qquad (2.3)$$

where $j = 1, 2$ and p and n denote the proton and neutron respectively.
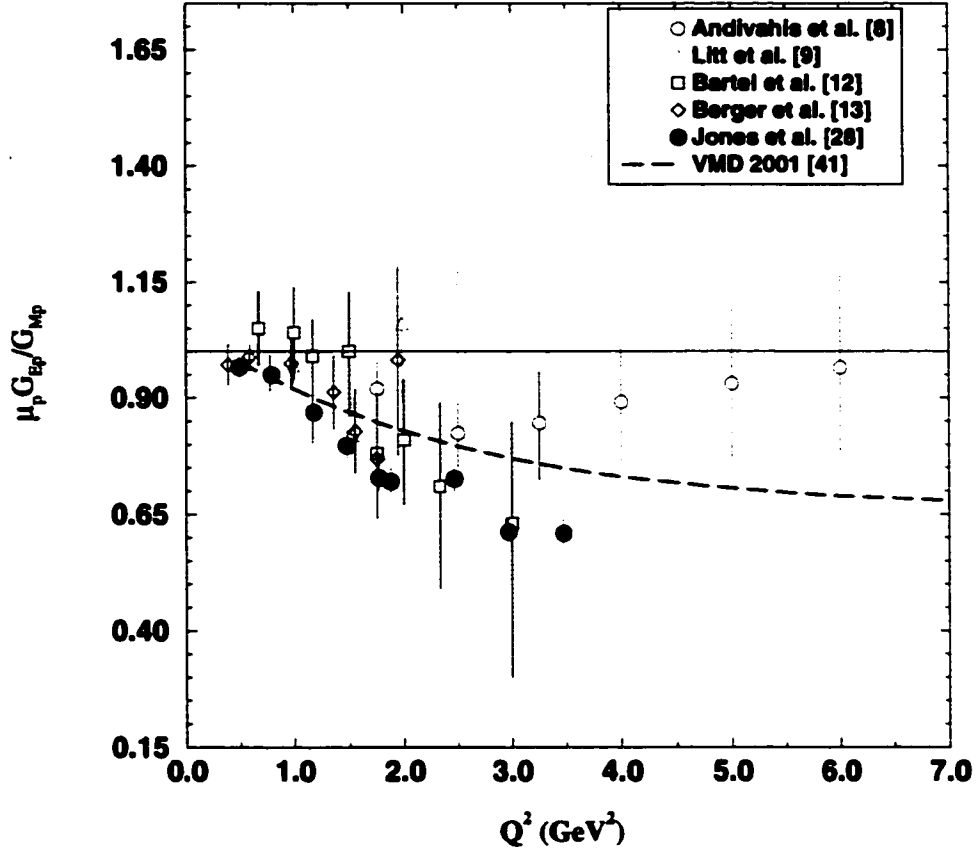
Figure 2.2: Ratio $\mu_p G_{Ep}/G_{Mp}$ to $Q^2 = 7$ GeV^2 calculated from VMD model including data from E93-027, compared with the data.

Early VMD models [36, 37] included the ρ, ω and ϕ and several phenomenological higher mass poles; these did give a fair description of the data at low Q^2. To extend the momentum transfer of the VMD description, in the early 90's, Gari and Krümpelmann [38, 39] fitted the existing data on the four nucleon form factors within the vector meson dominance model, restricting the VMD contributions to the ρ, ω and ϕ, but adding factors and terms which explicitly contained the asymptotic momentum transfer behavior of pQCD. In addition, the ρ contribution was modified by including the ρ width using a dispersion relation [40], and adding a ρ' (1450) contribution. The parameters which can be adjusted are the photon-meson coupling constants, the meson-nucleon form factors, the meson masses, the anomalous mag-

netic moments of the mesons and the asymptotic factors. In 2001, Lomon [41] used the same model, but extended the database with new data, and fitted five quantities: the four nucleon elastic form factors, plus the ratio $R_p = \mu_p G_{Ep}/G_{Mp}$, which was measured at JLab [28], to $Q^2 = 3.5$ GeV^2. The result of the fit for R_p is shown in Fig. 2.2. Note that this model offers a good parameterization of the nucleon form factors, but fails to describe the nucleon structure at higher Q^2, where terms that explicitly constrain the asymptotic behavior are added to account for the data.

2.2 Relativistic constituent quark models

The non-relativistic constituent quark model was developed to account for the meson and baryon mass spectrum (see Refs. [42, 43, 44] for a review). In this model, the nucleon is made of three constituent, or "dressed", quarks, and the dominant effects of the gluonic degrees of freedom are absorbed into the mass of these three quarks and an effective confining potential. However, to calculate electromagnetic form factors at high Q^2, in the $1 - 10$ GeV^2 region, it is necessary to include relativistic effects. Relativistic constituent quark models (rCQM) are based on relativistic quantum mechanics, as opposed to quantum field theory. The goal is to formulate a mechanics where the Hamiltonian acts on a suitable Hilbert space, similarly to the non-relativistic case.

This section first describes the three classes of Hamiltonian quantum dynamics defined by Dirac: the instant form, the light-front form and the point form. It then presents different calculations in rCQM, two formulated in the light-front form and one in the point form.

2.2.1 Different classes of relativistic quantum dynamics

Any relativistic quantum theory must respect Poincaré invariance, the Poincaré group being the group of Lorentz transformations and space-time translations. This

means, at the quantum level, that the theory must satisfy the commutation relations of the generators of the Poincaré group. Dirac [45] has given a general formulation of methods allowing for simultaneous compliance with the requirements of Special Relativity and Hamiltonian quantum mechanics. He distinguishes between three different classes of dynamics. The most intuitive one is the instant form, in which the state of a particle is defined by its three space coordinates at a given time t, e.g. on the hyper-surface $t = 0$, as shown on Fig. 2.3a. In the instant form, the Einstein mass relation $p_\mu p^\mu = m^2$ takes the form:

$$p^0 = \pm\sqrt{\vec{p}^2 + m^2} \tag{2.4}$$

which has two solutions for p^0, thus allowing quark-antiquark pair creation and annihilation in the vacuum, which complicates the theory. In this class, the ten generators of the Poincaré group are the energy of the system, the three components of the momentum and a six-components vector whose three components correspond to the total angular momentum and the three other components are more abstract mathematical objects.

a) b) c)
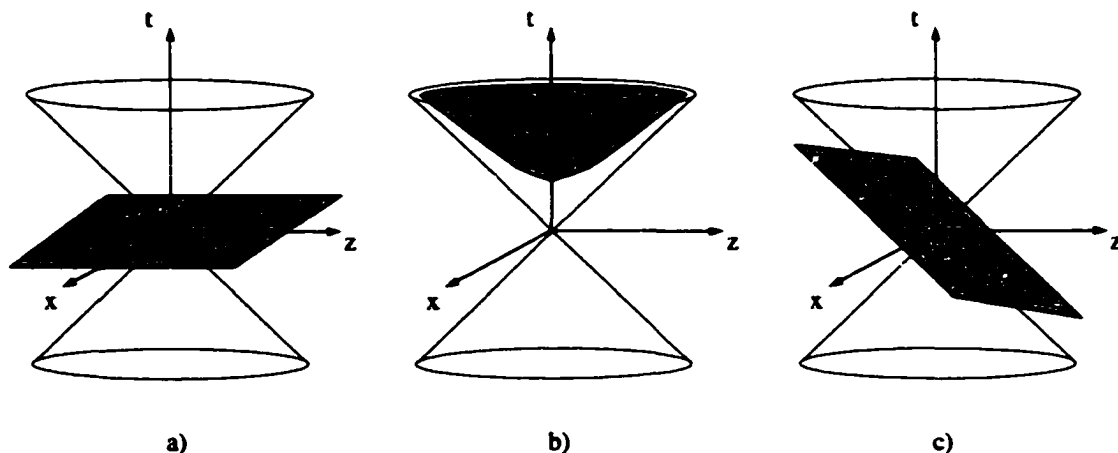
Figure 2.3: Three different classes of dynamics: a) instant form, where a state is defined on the $t = 0$ hyper-surface; b) point form, where a state is defined on a branch of a hyperboloid defined by $t^2 - \vec{x}^2 = \kappa^2$; c) light front form, where a state is defined on the $t + z = 0$ hyper-surface.

The second class developed by Dirac is the point form, where the dynamical variables refer to the physical conditions on some three-dimensional surface other than an instant. For example, one can take a branch of an hyperboloid defined by:

$$t^2 - \vec{x}^2 = \kappa^2 \tag{2.5}$$

where κ is a constant and $t > 0$, as shown in Fig. 2.3b.

The third class of dynamics is the light-front dynamics. It is illustrated in Fig. 2.3c. The hyper surface on which the physical system is described is defined by:

$$t + z = constant \tag{2.6}$$

Following the notation from Ref. [46], the four vector is given by $x = (x^+, x^-, x_\perp)$, where $x^\pm = \frac{1}{\sqrt{2}}(t \pm z)$ and $x_\perp = (x, y)$. Light-front vectors will be denoted here by boldface characters $\mathbf{x} = (x^+, x_\perp)$; they are covariant under kinematic Lorentz transformations [47]. The hyper-surface Eq. 2.6 is given by $x^+ = constant$.

The Einstein mass relation becomes in light-front dynamics:

$$p^- = \frac{p_\perp^2 + m^2}{2p^+} \tag{2.7}$$

If we view the $p^+ \equiv \mu$ component as a mass, we note an analogy with a non-relativistic expression of an Hamiltonian $H \equiv p^-$ of a particle on a two-dimensional surface [48]. So in the case of a system of several particles, this class of dynamics will allow us to easily separate between the motion of the center of mass of the system, and the relative motion of the particles in the system. The second advantageous feature of the light-front dynamics is that Eq. 2.7 is not quadratic in p^+ or p^-. Therefore this class does not allow negative energies, so that diagrams involving quarks created out of or annihilated into the vacuum do not contribute [49].

2.2.2 Schlumpf's relativistic constituent quark model

The relativistic constituent quark model (rCQM) presented here was first introduced by Berestetskii and Terent'ev [50, 51]. In this model, electromagnetic form factors of the nucleons have been developed by Schlumpf [52, 53], following the exploratory calculations of Chung and Coester [54]. The details of the calculations of this model can be found in Schlumpf's thesis [53], and are summarized in Appendix B, as an example of the construction of a nucleon wave function in the rCQM.

Schlumpf's wave function is calculated on the light-front. As was explained earlier, this procedure allows for a full separation of the center of mass motion from the internal relative motion of the quarks. The total wave function is the antisymmetric product of the momentum wave function. the flavor wave function, the spin wave function and the color wave function. The only parameters in this model are contained in the momentum distribution wave function; they are the constituent quark mass m_q, which is assumed to be point-like, and the confinement scale β. Schlumpf's parameters are $m_q = 267$ MeV and $\beta = 607$ MeV. These parameters were calculated in 1992, before the latest Rosenbluth separation measurement by Andivahis et al. [8] at SLAC, and the recoil polarization at Jefferson Lab by Jones et al. [28].

The "price to pay" for the easy non-relativistic-like treatment of the wave function in the light-front dynamics, comes from the spin. The light-front dynamics can also be seen as a Lorentz transformation to a frame boosted along the z-axis at a speed close to the speed of light, called the infinite momentum frame. Under such a transformation, the spins of the constituent quarks undergo a Melosh rotation $\mathcal{R}_M$ [55], represented by (for a two particle system):

$$\langle \lambda' | \mathcal{R}_M(\xi, q_\perp, m, M) | \lambda \rangle = \left[\frac{m + \xi M - i\vec{\sigma} \cdot (\vec{n} \times \vec{q})}{\sqrt{(m + \xi M)^2 + q_\perp^2}} \right]_{\lambda' \lambda} \tag{2.8}$$

where $\vec{n} = (0, 0, 1)$, λ and λ' are spin states, and m, M and ξ are mass parameters defined in Appendix B. These rotations, by mixing spin states, play an essential role in the calculation of the helicity-conserving and spin flip form factors F_1 and F_2, and contribute to the non trivial behavior of the ratio G_{Ep}/G_{Mp}, consistent with that observed in experiment E93-027 [28].

2.2.3 SU(6) symmetry breaking

Using another approach to the relativistic constituent quark model on the light front, Cardarelli *et al.* [56, 57, 58] have studied the consequences of the breaking of the SU(6) symmetry of the nucleon by the Melosh rotations. In their model they use the one-gluon exchange potential introduced by Capstick and Isgur [59] to calculate the observed deviation from SU(6) symmetry predictions: $G_{En}(Q^2) = 0$ and $G_{Mp}(Q^2)/G_{Mn}(Q^2) = -3/2$. They are also led to the conclusion that taking the Melosh rotations of the constituent quarks spins into account explains the deviation of $\mu_p G_{Ep}(Q^2)/G_{Mp}(Q^2)$ from unity. They compared calculations with point-like quarks with those that included quark form factors. They also demonstrated that the calculations of the form factors using the light-front +-component or using the y-component of the current are equivalent as far as $\mu_p G_{Ep}(Q^2)/G_{Mp}(Q^2)$ is concerned, even though the y-component calculation yields better results for $G_{Mp}(Q^2)/G_{Mn}(Q^2)$.

2.2.4 Point form spectator approximation

The first developments of point form rCQM came only recently in the literature. Klink [60] enumerates a number of features that distinguishes the point form dynamics from the other forms:

- because the operators that contain the dynamics (the four momentum operators) commute with each other, the theory is covariant, which means there

is a more direct connection with models motivated by quantum field theory,

- electromagnetic current operators at an arbitrary space-time point are related to the electromagnetic current operator at the space time origin by a translation from the origin generated by the interaction-dependent four momentum operators,

- spin and orbital angular momentum can be coupled together exactly as is done non-relativistically.

In this dynamics, Klink constructs a relativistic impulse approximation, called the point form spectator approximation (PFSA). Wagenbrunn *el al.* [61] uses this impulse approximation and a Goldstone boson exchange potential [62] to calculate the nucleon elastic form factors. The agreement with all form factors is quite good. The JLab results [28] were not used in fitting parameters of this model, but the ratio $\mu_p G_{Ep}/G_{Mp}$ starts deviating from unity starting at $Q^2 = 1$ GeV^2.

2.2.5 Results

Figure 2.4 compares the results of these calculations with recoil polarization data in the 1 to 6 GeV^2 region. It shows the ratio $\mu_p G_{Ep}/G_{Mp}$, measured by JLab [28] and previous Rosenbluth experiments [8, 9, 12, 13], The solid line corresponds to Schlumpf's rCQM described in Section 2.2.2. Note that the parameters used here are the ones calculated by Schlumpf in 1992, before the SLAC measurements by Andivahis *et al.* [8] (which disagree with the calculations), and well before the first polarization measurement at JLab [28]. The PFSA calculation does not include the JLab polarization results either. Figure 2.5 shows $G_{Mp}/\mu_p G_D$ from Refs.[8, 9, 10, 14], where G_D is the dipole fit, and the rCQM calculation by Schlumpf [52].
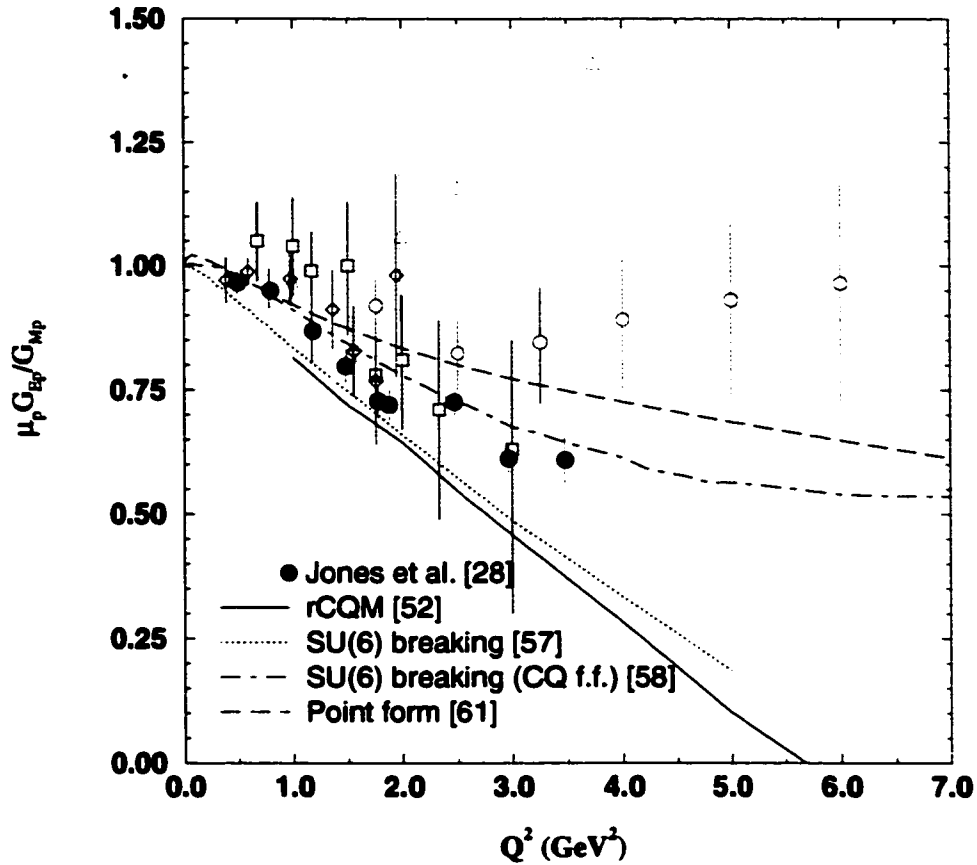
Figure 2.4: Form factor ratio $\mu_p G_E/G_M$ for the proton from JLab measurement (2000), and previous Rosenbluth measurements (empty symbols), compared with the fit calculated by Schlumpf in the rCQM (1992, solid line). Also shown are calculations using SU(6) breaking with point-like quarks (dotted line) and constituent quarks form factors (CQ f.f.. dot-dashed line). The point form calculation is also shown (dashed line). See text for references.

In conclusion, constituent quark models provide a good effective description of the nucleon structure. All developers of these models emphasize the importance of relativity. As suggested by a very naive description, in a non-relativistic image, the quarks being the carriers of the charge and current, there is no obvious reason for their distribution densities to be different, or equivalently, for the Q^2 dependence of the electric and magnetic form factors to be different. Indeed. what is observed at low Q^2 is that the ratio $\mu_p G_{Ep}/G_{Mp}$ is equal to unity. However, as Q^2 increases, the JLab data indicate a deviation of this ratio from unity [28], and CQMs have to incorporate relativistic effects, such as rotations affecting the quark spins undergoing

a Lorentz transformation, to account for this deviation.
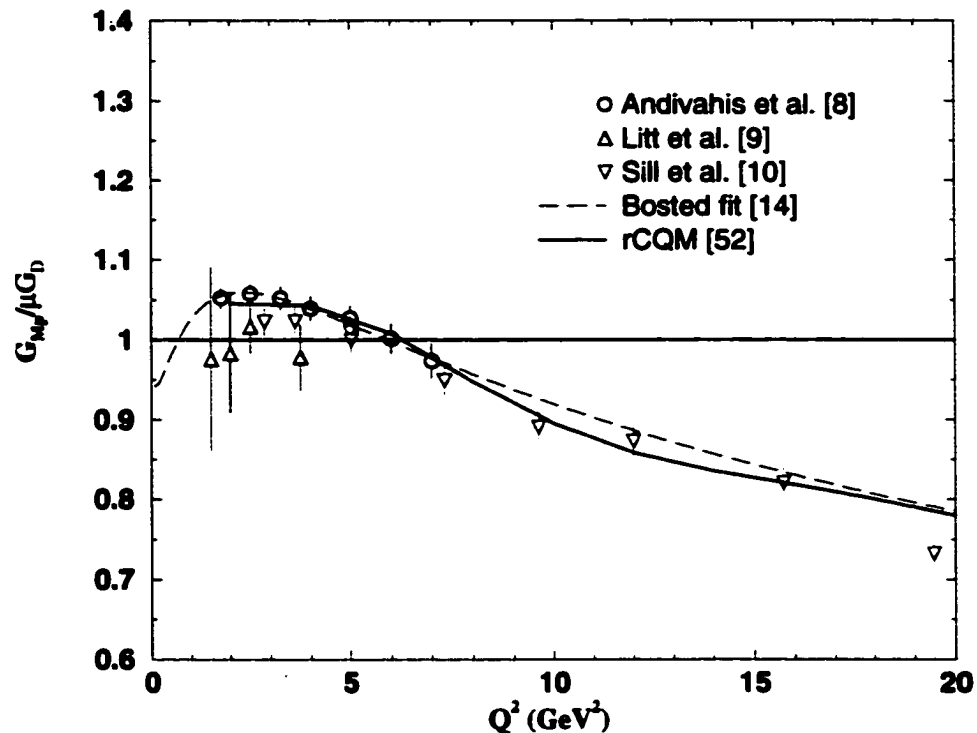
Figure 2.5: Magnetic form factor of the proton measured by Sill, Andivahis and Litt, and empirically fitted by Bosted (dashed line), compared with the fit calculated by Schlumpf in the rCQM (solid line) in the $2 < Q^2 < 20$ GeV^2 region. See text for references.

Many other types of models have been developed to describe the nucleon in the 1-10 GeV^2 range. For example, one can view the nucleon as a three quark bound state involving a spectator quark and a diquark correlation [63, 64]. Authors have also discussed the nucleon form factors in the soliton model, where the nucleon is described as a standard skyrmion [65, 66].

The formulation of QCD on a lattice is, at present, the only known way of obtaining low-energy properties of the theory in a direct way, without any model assumptions. This approach involves the calculation of the QCD action on a discretized space-time, with lattice spacing a. The path integral is then a very high

dimensional partition function, which is amenable to Monte-Carlo methods of statistical physics. The continuum is then obtained by letting $a \to 0$ with an extrapolation to $a = 0$ from finite a. Progress is slow in this field, and limited computer capabilities often lead to the neglect of some terms in the action, such as the fermion determinant. This approximation is known as the "quenched" approximation. Exploratory calculations of nucleon form factors on the lattice can be found in Ref. [67].

2.3 High Q^2 limit: perturbative QCD
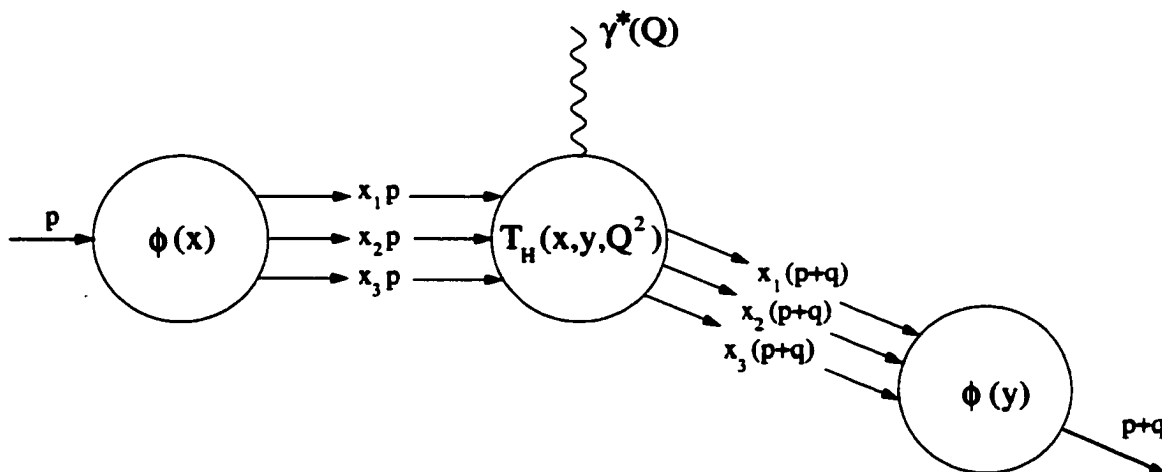
Figure 2.6: Electromagnetic interaction in hard elastic scattering.

We can see from Eq. 2.1 that the coupling constant decreases as Q^2 increases, in such a way that for high enough Q^2, namely $Q^2 >> \Lambda_{QCD}^2$, the coupling constant becomes small enough so that we can treat the reaction using perturbative methods, just as in QED. Based on simple and intuitive arguments, perturbative QCD (pQCD) makes predictions on the asymptotic behavior of the form factors [68].
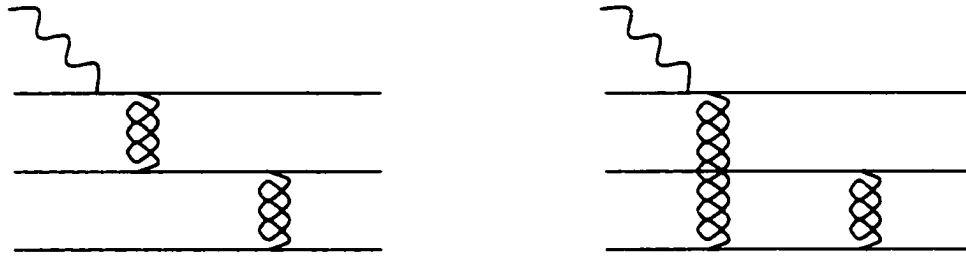
Figure 2.7: Example of Born diagrams contributing to the helicity-conserving form factor F_1. Other diagrams where the photon hits the other quarks must be added.

QCD describes the nucleon as being made up of elementary constituents, the quarks and gluons. Each constituent carries a fraction x_i of the total longitudinal momentum p of the nucleon. In pQCD, asymptotic freedom imposes that only the three valence quarks contribute to hard processes. In particular, for hard elastic scattering of electrons off a nucleon, the helicity-conserving form factor F_1 can be written as a convolution of process-independent distribution amplitudes $\phi(x)$ and the dynamics of hard-scattering quarks and gluons amplitude $T_H(x, y, Q^2)$ as shown in Fig 2.6:

$$F_1(Q^2) = \int_0^1 dx \int_0^1 dy \phi^*(y) T_H(x, y, Q^2) \phi(x) \qquad (2.9)$$

To leading order of $\alpha_s(Q^2)$, T_H is the sum of Born diagrams for $\gamma^* + 3q \rightarrow 3q$, as shown in Fig. 2.7. All particle masses and transverse momentum fluctuations of the quarks are negligible, compared to Q. The elasticity of the reaction is characterized by the fact that all quarks are collinear in both the initial and final states. Therefore, after one quark absorbs the transverse momentum of the photon, this momentum must be transferred to the other quarks, via gluons, requiring the introduction of two gluon propagators, therefore two factors of $\alpha_s(Q^2)/Q^2$. The falloff is intuitive, since the higher the Q^2, the less likely it is for the three quarks of the struck nucleon to remain collinear. This falloff can also be viewed as the probability for the quarks inside the nucleon to be within a distance of $1/Q$ of each other, so that the photon

interacts with the nucleon as a system [69]. This probability is proportional to $1/Q^2$ for the second quark to be next to the first, and $1/Q^2$ for the third quark to be next to the first two.

We can then establish a counting rule for hadrons, namely that the helicity conserving form factor has the following asymptotic behavior [70]:

$$F(Q^2 \to \infty) \propto \left(\frac{\alpha_s(Q^2)}{Q^2} \right)^{n-1} \tag{2.10}$$

where n is the number of constituents. In pQCD, the nucleon can be decomposed in a superposition of states $qqq + qqqq\bar{q} + qqqg + qqqgg + \cdots$, where q is a quark, $\bar{q}$ is an antiquark and g is a gluon. So we can see from Eq. 2.10 that, for baryons, all states with more constituents than the $3q$ state are suppressed by a factor of at least $\alpha_s(Q^2)/Q^2$. For the nucleon, $n = 3$, so that the pQCD prediction for $F_{1N}(Q^2)$ is:

$$F_{1N}(Q^2 \to \infty) \propto \frac{\alpha_s^2(Q^2)}{Q^4} \tag{2.11}$$

For the helicity non-conserving form factor, at leading order, chiral symmetry of pQCD requires that the amplitude for quark spin-flip processes is zero. However, second-order corrections, due to quark mass terms, of the order of $O(m/Q)$ have to be taken into account, so that hadron helicity-flip processes, represented by the factor QF_{2N} in the hadronic current, are suppressed by an additional factor $1/Q$ compared to the helicity-conserving term [68]. The pQCD prediction for F_{2N} is then:

$$QF_{2N}(Q^2 \to \infty) \propto F_{1N} \left(\frac{m}{Q} \right) \tag{2.12}$$

so that:

$$F_{2N}(Q^2 \to \infty) \propto \frac{\alpha_s^2(Q^2)}{Q^6} \tag{2.13}$$

The definition of the magnetic Sachs form factor:

$$G_M = F_1 + \tau \kappa F_2 \tag{2.14}$$

implies that, given the behavior of F_1 and F_2, the asymptotic behavior of G_M must also be:

$$G_M(Q^2 \to \infty) \propto \frac{\alpha_s^2(Q^2)}{Q^4} \tag{2.15}$$

This dependence has been observed experimentally for the proton [71, 10], for which the magnetic form factor has been measured to very high values of Q^2. Figure 2.8 shows $Q^4 G_{Mp}(Q^2)/\mu_p$ to $Q^2 = 31$ GeV^2.
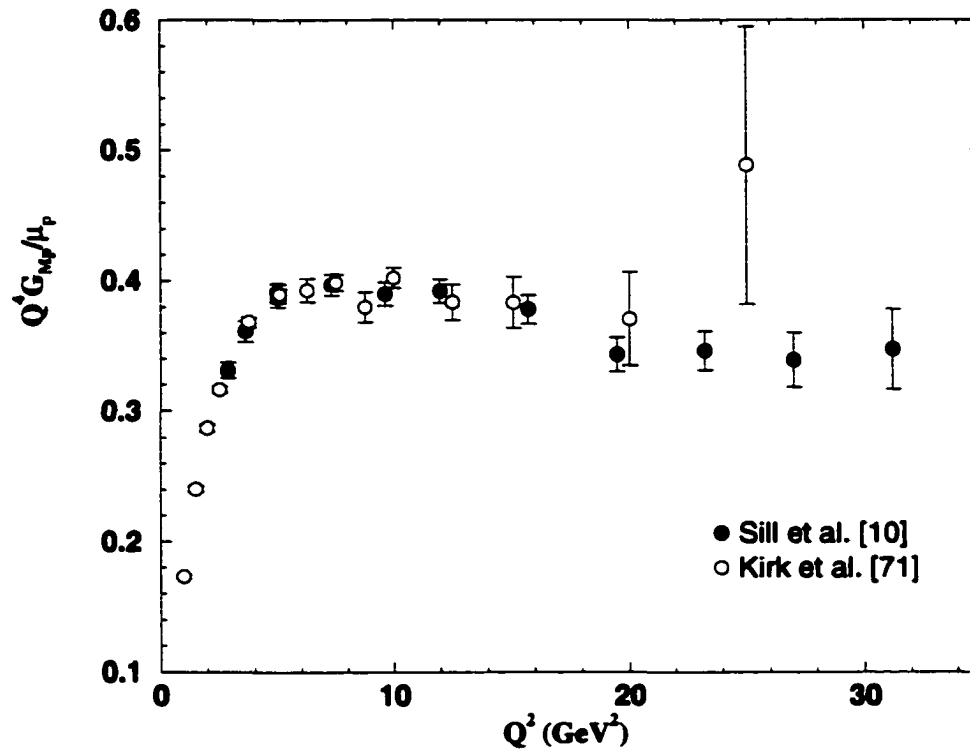
Figure 2.8: Data showing the asymptotic behavior of the proton magnetic form factor G_{Mp}.

The F_1 and F_2 Q^2 dependences Eqs. 2.11 and 2.13 lead to the prediction for the ratio F_2/F_1:

$$\frac{F_2}{F_1} \propto \frac{1}{Q^2} \tag{2.16}$$

This ratio is interesting because it is directly measurable in a recoil polarization experiment, since, following the definitions of the Sachs form factors, we have:

$$\frac{F_2}{F_1} = \frac{1 - \frac{G_E}{G_M}}{\kappa \left(\frac{G_E}{G_M} + \tau \right)}$$

(2.17)

where G_E/G_M is the quantity measured in these experiments. Therefore measuring this ratio at higher Q^2 provides a good test of pQCD and can signal onset of pQCD effects at low Q^2.

2.4 Form factors in the time-like region

So far we have discussed form factors in the space-like region only, where $Q^2 > 0$. The time-like region, defined by $Q^2 < 0$, and where the form factors are complex quantities, is experimentally accessible in colliders [72, 73, 74, 75, 76], in reactions such as $e^+ + e^- \leftrightarrow \bar{p} + p$. In this reaction, the time-like equivalent of Q^2 is the square of the total energy in the center of mass frame s. Data have been taken up to $s = 14$ GeV^2. The cross-section takes the following form [77]:

$$\frac{d\sigma}{d\cos\theta} = \frac{\pi \alpha^2}{8m^2 \tau \sqrt{\tau(\tau - 1)}} \left[\tau |G_M|^2 \left(1 + \cos^2\theta \right) + |G_E|^2 \sin^2\theta \right]$$

(2.18)

where θ is the angle between the electron and the antiproton is the center of mass frame. It is in principle therefore possible to extract the form factors by Rosenbluth separation, but the cross-section is so small that this procedure has not been applied yet. Two hypotheses have been tested: $G_E = 0$, and $|G_E| = |G_M|$. The first case is arbitrary, while the second one is strictly true at threshold, for $s = 4m^2$. Analysis show that the value for $|G_M|$ is nearly independent of this choice [78].

At low s, the time-like region might be interestingly described by vector meson exchange, as suggested by the measurement of time-like form factors for charged pions in $e^+ + e^- \leftrightarrow \pi^+ + \pi^-$. For this reaction, the threshold $s = 4m_\pi^2$ is low enough so that the masses of the mesons appear clearly on the spectrum, starting

with the ρ. Some predictions are also made for the asymptotic regime, at very high s. The Phragmén-Lindelöf theorem [79] constrains the form factors in the time-like region to have the same Q^2 behavior as its space-like counterpart, governed by quark counting rules and helicity conservation. Assuming that the time-like $|G_M|$ has reached an asymptotic behavior, as the data suggest, leads us to the conclusion that this regime has not been reached yet for the electric form factor, as the values of $|G_E|$ get more apart in time-like and space-like regions. However, these conclusions are dependent upon arbitrary assumptions, such as $|G_E| = |G_M|$, which can not be lifted until a careful separation of the form factors is done.

2.5 Conclusion

The only nucleon form factor which is well known up to Q^2 of 30 GeV^2 is the proton magnetic form factor, G_{Mp}. Yet, before we are able to have a complete theory of strong interactions, and later to test this theory, it is necessary to measure all other form factors, to Q^2's that reach the perturbative QCD regime. There is a gap in the theoretical understanding of the nucleon in the intermediate Q^2 region, where the vector meson exchange picture fails, but pQCD is not yet applicable. Various effective models, such as the relativistic constituent quark model, are continuously being developed, with more or less success, and solving this question is probably one of the most challenging goals that the nuclear physics community has currently set.

The JLab experiment E99-007 brings its contribution to this understanding, by providing the most precise measurement so far of the proton elastic form factor ratio to $Q^2 = 5.6$ GeV^2. For Q^2 up to about 12 GeV^2, the recoil polarization method could be applied at JLab using a 12 GeV beam, and is undoubtedly the best way to measure the proton's electric form factor.

CHAPTER 3

Experimental apparatus

In this experiment, electrons were elastically scattered off a hydrogen target to probe the internal structure of the proton. The polarized electron beam was produced and accelerated by the Continuous Electron Beam Accelerator Facility (CEBAF) at Jefferson Lab. This beam was sent to Hall A, where its energy was measured using the Arc and the eP method, and its high polarization was measured by Compton and Møller polarimeter. It was then scattered from a liquid hydrogen target. The recoil proton was detected in one of the two high resolution spectrometers (HRS), and its polarization was measured in the focal plane polarimeter (FPP). The elastic events were selected by requiring the electron to be detected in coincidence, either in the other HRS or in a large acceptance calorimeter. Details about all this equipment except the calorimeter can be found in Ref. [80] and the references therein.

3.1 The Continuous Electron Beam Accelerator

3.1.1 The injector and the accelerator

The Continuous Electron Beam Accelerator at the Thomas Jefferson National Accelerator Facility consists of two linear accelerators (linacs) that can deliver a high quality, polarized or unpolarized, 100% duty factor electron beam to three experimental halls at the same time. Energies can go up to 5.7 GeV at present, and intensities to 70 μA to Halls A and C at the same time (Hall B requires a tenth of a μA at most), or 120 μA in a single hall. Figure 3.1 shows a sketch of the accelerator.

48
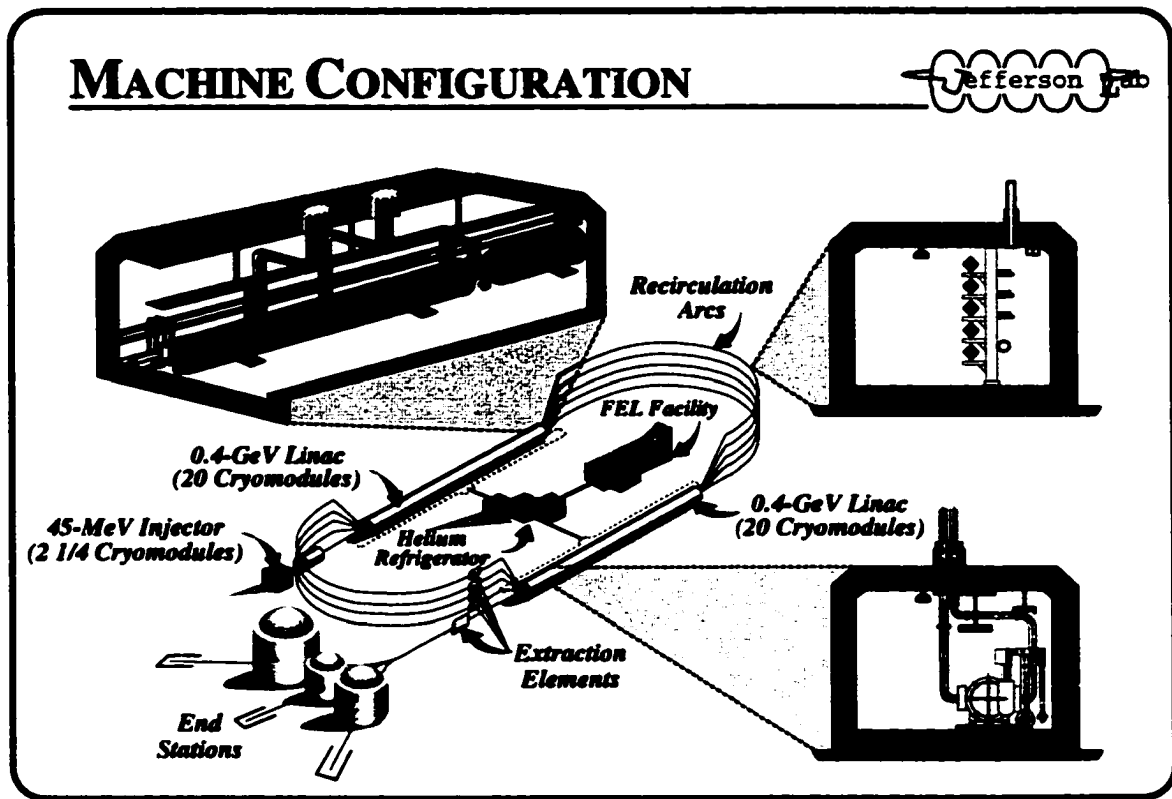
Figure 3.1: Sketch of the Continuous Electron Beam Accelerator at the Thomas Jefferson National Accelerator Facility.

The operation of the beam source is based on the excitation laser of electrons between states in the valence and the conduction bands of strained gallium arsenide (GaAs) using a Ti-sapphire. A mono-layer of cesium oxide lowers the vacuum level below the conduction band, so that electrons in the conduction band are released to the vacuum, producing a 100 keV electron beam. This beam is accelerated to 45 MeV (depending on the end-energy) in a set of cryomodules, to be fed to the race-track type accelerator. The beam first goes through the north linac. The linac consists of 20 cryomodules, providing a nominal total acceleration to 0.4 GeV. These cryomodules were improved over the years, and the accelerator is now able to accelerate the electrons to 0.58 GeV per linac. The beam is then recirculated in the

arc, and is accelerated again in the south linac, identical to the north linac. At this point it can either go to the recirculating arc for a second pass through the linacs, or go to one of the experimental halls. The maximum number of passes is five, corresponding to a maximum energy of 5.7 GeV, and the three halls can each request a different number of passes. The linac cavities use super-conductivity technology, to ensure that the heat produced by ohmic losses in the walls of the cavities during the continuous electron circulation is minimal. The average beam intensity delivered to Hall A during the experiment was 41 μA, with peaks at 70 μA. The number of passes was four.

The absorption of a right or left circularly polarized laser light preferentially produces electrons with a spin down or up respectively in the conduction band, thus longitudinally polarizing the beam, up to 80%. The laser light was circularly polarized using a Pockels cell. This birefringent crystal has a different optic index in two orthogonal directions, so that two orthogonal components of the electromagnetic field associated with the photon do not propagate with the same velocity through the crystal. The difference can be adjusted by varying the voltage applied to the cell, so that the relative phase between the two components is a quarter of the wavelength, producing a circularly polarized beam. A Wien filter can rotate the polarization angle of the electron to optimize the longitudinal polarization in all the halls that require a polarized beam, taking into account the precession of the electron spin in the recirculating arcs of the accelerator. The sign of the beam helicity was switched pseudo-randomly at a rate of 30 Hz, by switching the circular polarization of the laser. This was achieved by changing the voltage of the Pockels cell. In addition, at the request of the other halls, a half-wave plate was inserted or retracted at the injector about every 30 hours of beam time, changing the sign of the helicity. This did not affect our measurement, as this switch was taken into account in our analysis.

3.1.2 Beam energy measurements in Hall A

As shown in Eq. 1.70, in order to extract the form factor ratio from the polarization components ratio, it is necessary to precisely know the beam energy. Two devices in Hall A are dedicated to do this.

eP energy measurement
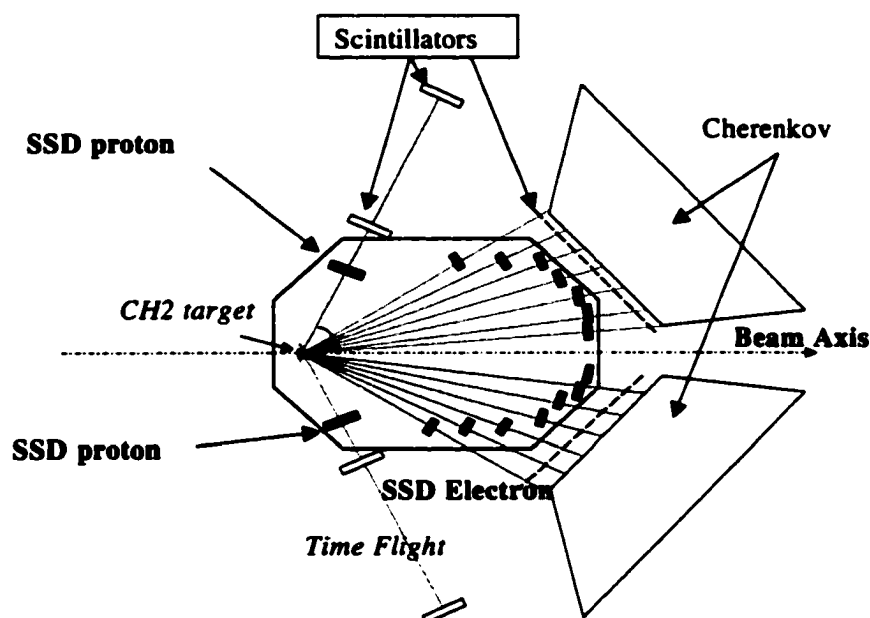
Figure 3.2: eP detector to measure the absolute electron beam energy in Hall A. The micro-strips (SSD) precisely measure the scattering angle of the electron and the proton, the scintillators are used to trigger the system, and the Čerenkov detectors serve for particle identification.

The eP method [81, 82], developed by the Clermont-Ferrand and Saclay groups, is a stand-alone device located 17 m upstream from the target. The electron beam scatters off a moving tape of CH_2. As shown in Fig. 3.2, the recoil proton is detected at a fixed angle, and the scattering angle of the electron is measured by detecting the electron in a set of silicon micro-strips (SSD), placed in the vertical plane.

Simultaneous measurements in both arms, symmetric around the beam axis, cancel asymmetries due to beam position and angle, to first order. At a fixed recoil proton angle, the elastic scattering angle of the electron is related to the incident electron energy by:

$$E_{beam} = M_p \frac{\cos\theta_e + \sin\theta_e / \tan\theta_p - 1}{1 - \cos\theta_p} + O(m_e^2 / E^2) \qquad (3.1)$$

The relative energy resolution of this method, typically less than 2×10^{-4}, is determined by the angular resolution of the micro-strips.

Arc energy measurement
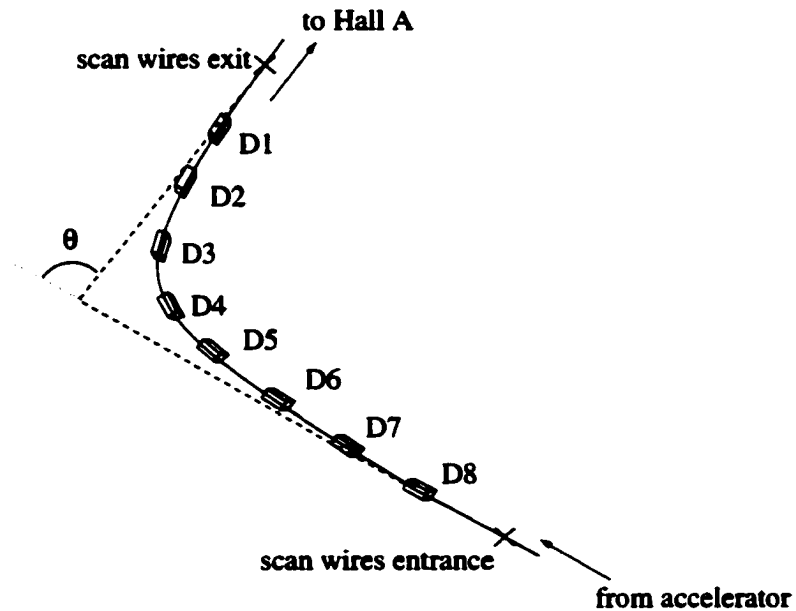
Figure 3.3: Arc method to measure the absolute electron beam energy in Hall A.

The Arc method [81, 83], developed by the Saclay group, measures the deflection angle θ, nominally 34.3 °, of the beam in the Hall A arc between the switch-yard and the hall entrance, based on a set of wire scanners, and the field integral $\int \vec{B} \cdot \vec{dl}$ in the bending elements (eight dipoles), based on a reference magnet (ninth dipole).

The electron momentum can then be calculated with a relative accuracy of less than 2×10^{-4}, according to:

$$p = c \frac{\int \vec{B} \cdot d\vec{l}}{\theta} \qquad (3.2)$$

where $c = 0.299792$ is the speed of light in units of GeV.rad/Tm. Figure 3.3 shows the principle of the method.

During the experiment, three energy measurements were taken. Two measurements were done in November 2000, with the eP and the Arc methods, and one measurement in December 2000 with the eP method, after a small energy change decided by the accelerator. Results are summarized in Table 3.1. The relative disagreement between the two methods has now been reduced to the 10^{-3} level. Note that the perfect agreement between the two measurements of November 6 in Table 3.1 is accidental.

Date	Method	Energy (MeV)	Uncertainty (MeV)
11-6	Arc	4606.7	1.5
11-6	eP	4606.7	0.6
12-1	eP	4588.5	0.8

Table 3.1: Absolute beam energy during the experiment.

3.1.3 Beam polarization measurements in Hall A

Even though in principle the beam polarization is not necessary to determine the ratio of the form factors, we monitored it to ensure it was high enough to achieve reasonable error bars. In addition, it is needed to obtain the analyzing power of the analyzer of the FPP. There are two polarimeters in Hall A, which measure the incident electron longitudinal polarization P_e.

Compton polarimeter

The Compton polarimeter [84, 85], developed by the Saclay group, is installed at the entrance of the hall. The polarized electron beam interacts with a laser beam of known circular polarization. This physical process $\vec{e}\vec{\gamma} \to e\gamma$ is described by Quantum ElectroDynamics (QED), which allows one to calculate the cross sections of the polarized electrons scattering off polarized photons as a function of their energies and scattering angle. The counting rate asymmetry is directly proportional to the laser and electron beam polarizations and the cross section asymmetry, as given in Eq. 3.3:

$$A_{exp} = \frac{N^+ - N^-}{N^+ + N^-} = A_c P_\gamma P_e \qquad (3.3)$$

where N^+ and N^- are the number of photons detected for the two states of the beam helicity, A_c is the asymmetry calculated by QED, and P_γ is the photon polarization, measured to be 99.3% ± 0.7%. The beam is deflected in a magnetic chicane, to separate the real electrons from the Compton photons, whose backward scattering angle is very small. A silicon strip detector is used to detect the scattered electron. A Fabry-Pérot Cavity, made of 2 multi-layer concave mirrors with very high reflectivity, amplifies the photon flux by a factor greater than 7000, to ensure a fast polarization measurement. The energy of the backward photons is measured by an electromagnetic calorimeter. This method of measuring the beam polarization is not intrusive, so that the polarization can be monitored at all times. A statistical error of 0.8% can be achieved in about an hour for the beam conditions of this experiment. The relative systematic errors have been reduced to the 1.1% level [85].

Møller polarimeter

The other Hall A polarimeter [86], developed by the University of Kentucky and the Kharkov Institute of Physics and Technology, is based on the Møller scattering of the polarized beam electrons off polarized atomic electrons in a magnetic foil

$\vec{e}^- + \vec{e}^- \rightarrow e^- + e^-$; its cross section depends on the beam and target polarizations P_e and P_{tgt} as:

$$\sigma \propto 1 + \sum_{i=X,Y,Z} (A_{ii} P_{tgt,i} P_{e,i}) \qquad (3.4)$$

where $i = X, Y, Z$ defines the projections of the beam and target polarizations. A_{ii} is the analyzing power, which depends only on the scattering angle in the center of mass frame θ_{cm}, and its maximum is at $\theta_{cm} = 90°$. The target polarization was measured to be 7.95% ± 0.26%. The Møller scattering events are detected in a magnetic spectrometer consisting of a sequence of three quadrupoles and one dipole. The relative systematic error on the Møller measurement is ~3%.
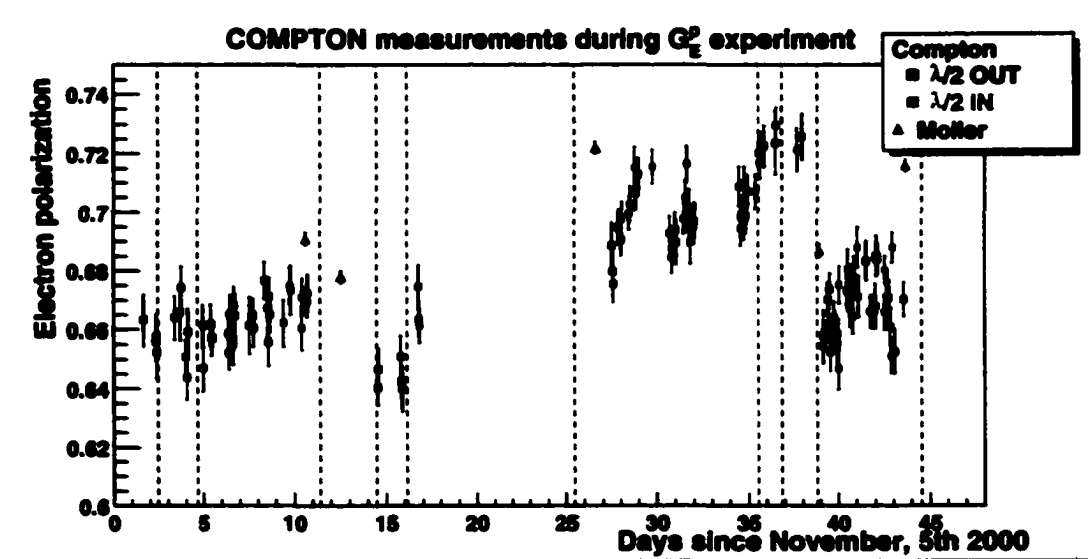
Figure 3.4: Results of Compton and Møller beam polarization measurements throughout the experiment. Dilution factor is not applied to Møller data (see text). Plot courtesy of S. Escoffier.

Figure 3.4 shows the beam polarization measured during the experiment. It was monitored every day by the Compton polarimeter except for five days in November. The results are shown with both statistical and systematic errors combined.

Five Møller measurements were done. They are shown with their statistical error only. Note that for the first four Møller measurements, a dilution correction must be applied due to leakage from the Hall C beam. This estimated correction results in an increase of the Møller result by about 6% (not included in the figure), and consequently the polarization measured by the two polarimeters differs by a significant amount, of the order of 6 to 7%, the Møller values being systematically higher than the Compton values . This difference, which is beyond the error quoted for the measurements, is not completely understood at this point. The people responsible for the Møller detector suspect they don't fully understand their systematic uncertainties, therefore suggest to take the Compton results as the reference for now.

3.2 The Hall A cryogenic hydrogen target

The electron beam was scattered off the standard Hall A liquid hydrogen target [87]. The target system consists of the scattering vacuum chamber, and the target loops ladder.

Scattering chamber

The scattering chamber consists of three sections. The lower section is fixed on the pivot of the Hall. It contains several ports for vacuum pumps, visual inspection and electrical feed-throughs. The second section is located at beam height, and has an inner diameter of 104 cm and aluminum wall thickness of 5 cm. It has a 15.2 cm vertical cutout on each side of the beam over the full angular range ($12.5° \leq \theta \leq 160°$). This exit window is covered with thin aluminum foils (0.38 mm). The middle section also has beam entrance and exit ports, which prevent the particles from interacting with any material except the target itself. The upper section has space to contain the cryogenic target plumbing system.

Cryogenic target

The target system is mounted inside the scattering chamber, on a ladder containing the cryogenic targets and a selection of dummy and solid targets, along with sub-systems for cooling, gas handling, temperature and pressure monitoring, target control and target motion. This ladder can be moved vertically from the counting house, to align the desired target on the beam-line.

The basic cryogenic target in the standard configuration has three independent loops: a liquid hydrogen (LH_2) loop, a liquid deuterium (LD_2) loop and a gaseous helium loop. Each loop has fans to force the liquid or gas to circulate through it. The LH_2 and LD_2 loops each consists of two target cells, of length 15 and 4 cm along the beam direction. Each aluminum cell has a diameter of 6.35 cm, an upstream window of 0.071 mm, and a downstream window of 0.102 mm. The side wall is 0.178 mm thick.

We used the 15 cm LH_2 loop for this experiment. The target coolant was supplied by the End Station Refrigerator (ESR). The ESR supplied coolant at 15 K, which was used by the target and returned at a little over 20 K. The target was operated at constant temperature of 19 K, and pressure of 25 psi, which gave a density of about 0.0723 g/cm^3. The temperature was stabilized with a high-power heater which compensated for beam intensity variation and a feedback circuit using temperature reading from a probe.

The beam spot size was so small, that it could cause local damage to the target cell at high beam current. To minimize this, the beam can be rastered, using dipole magnets in both vertical and horizontal directions. This raster can be used in sinusoidal or amplitude modulated mode, producing a square or a spherical shape respectively in the plane transverse to the beam axis. In the sinusoidal mode, which we used for this experiment, the magnets pairs are driven with a pure sine wave

with a relative phase of 90°, and frequencies that do not produce a closed Lissajous pattern. The square was approximately 4×4 mm^2, reducing the density fluctuation due to beam heating to a fraction of a percent.

3.3 The Hall A High Resolution Spectrometers

Hall A has two High Resolution Spectrometers (HRS) [88], which are identical in design. In this experiment, we used the left HRS to detect the recoil proton, and the right HRS to detect the scattered electron at the lowest Q^2.

3.3.1 The magnetic elements
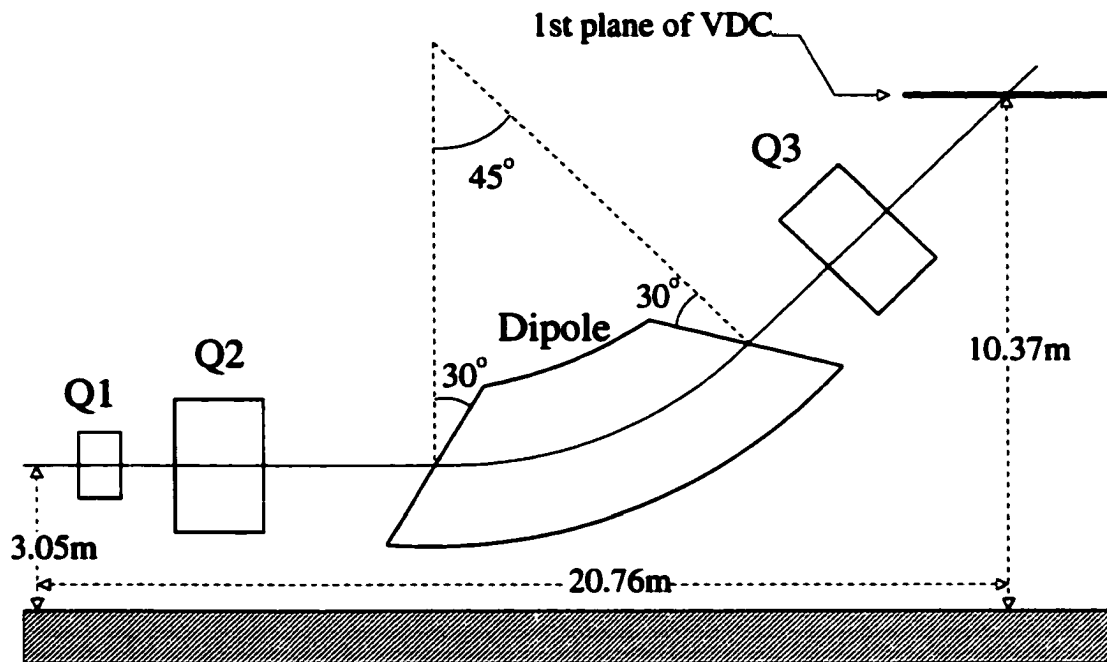
Figure 3.5: Layout of the High Resolution Spectrometer.

The High Resolution Spectrometer consists of two quadrupoles, one indexed dipole and one quadrupole, as shown in Fig. 3.5. An indexed dipole is a dipole where the field is not radially uniform, due to a trapezoidal cross sectional shape, as

shown in Fig. 3.6. The effect is to focus in the vertical plane. The first quadrupole is focusing in the vertical plane, while the second and third quadrupoles defocus in the vertical plane. All elements are super-conducting, refrigerated to 4.5 K by liquid helium provided by the ESR. This QQD_nQ configuration was chosen based on a number of considerations, including a momentum resolution at the 10^{-4} level, a large acceptance in both angle and momentum, a good angular and position resolution in the scattering plane and an extended target acceptance. The 45° vertical bend decouples, in first order, a measurement of the position along the target from a measurement of the momentum.

$$Q_1 \qquad D_n \qquad Q_2, Q_3$$
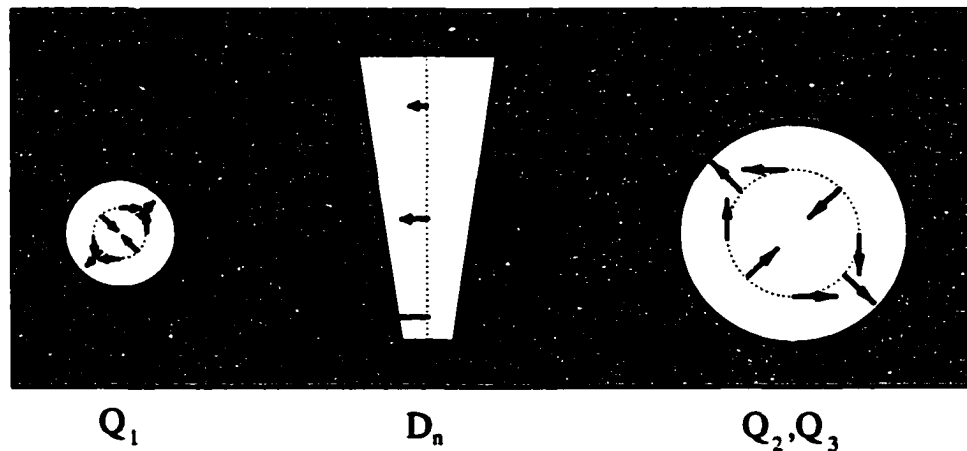
Figure 3.6: Cross sections of the quadrupoles and the indexed dipole of the HRS. The direction of the fields is given for a positively charged particle.

The size of the magnetic elements puts constraints on the size of the beam envelope: it can not exceed 0.25 m (0.80 m) in the dipole gap (width), and 0.3 m (0.6 m) diameter in the useful aperture of Q_1 (Q_2, Q_3). A 30° rotation of the dipole entrance and exit faces provides an additional radial focusing. The location of Q_3 after the dipole makes it possible to simultaneously have reasonably good horizontal

position and angular resolution.

The accurate knowledge of the fields inside the magnetic elements is of primary importance in this experiment, since the precession of the recoil proton spin generated by these fields is the main source of systematic errors. The field in the dipole was measured and monitored using two arrays of three NMR probes, providing a field range from 0.17 to 2.10 T, and giving field readings at the 10^{-5} level. Quadrupole fields were monitored using Hall probes and Gauss-meters. The setting of the fields was entirely automated from the counting house, where only the desired central momentum is specified. Some hysteresis effect in Q_2 and Q_3 due to the iron collar required these magnets to be cycled before any increase of the field setting.
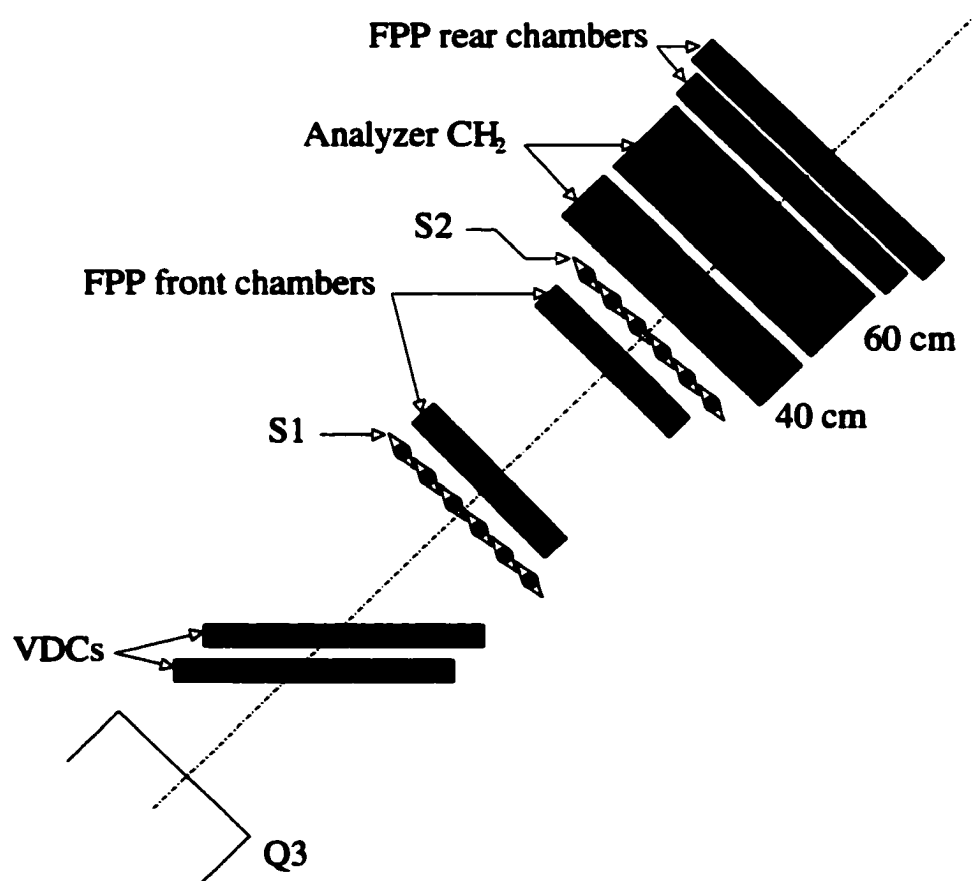
Figure 3.7: Layout of the detector package of the left HRS.

3.3.2 The Vertical Drift Chambers

The detector package of the left HRS is located at the focal plane of the spectrometer, downstream of Q_3. The standard package for the left arm contains two vertical drift chambers (VDC) for tracking purposes, two planes of scintillators, $S1$ and $S2$, for triggering and time of flight measurement, gas and aerogel Čerenkov detectors and a lead-glass pion rejector, for particle identification (PID), unused in this experiment, and the focal plane polarimeter (FPP) which will be the focus of the next section. Figure 3.7 shows a side view of the detector package we used for the experiment.

VDC design

Tracking information was provided by two VDCs [89], developed by the MIT group. They are bolted to an aluminum frame, which slides on Thompson rails attached to the spectrometer box beam. The rails and the VDCs are aligned to 100 μm accuracy to keep the VDCs flat and horizontal, and in the same location.
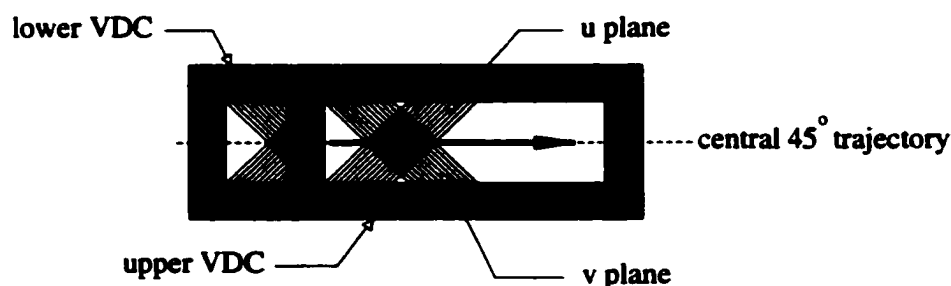
Figure 3.8: Top view of the VDC system.

Each VDC is composed of two wire planes in a standard uv configuration, respectively +45° and −45° with respect to the central particle trajectories, as shown in Fig. 3.8. There are a total of 368 gold-plated tungsten wires per plane.

The wire spacing is such that a track at 45° to the detector wire plane typically fires five wires of a plane, leading to a position resolution at the focal plane of $\sigma_{x,y} \sim 100$ μm. The chambers are vertically separated by 33.5 cm, to achieve an angular resolution of $\sigma_{\phi,\theta} \sim 0.5$ mrad. The VDCs use negative high-voltage for the cathode gold-plated mylar planes, and the signal wires are at virtual ground.

Read out system
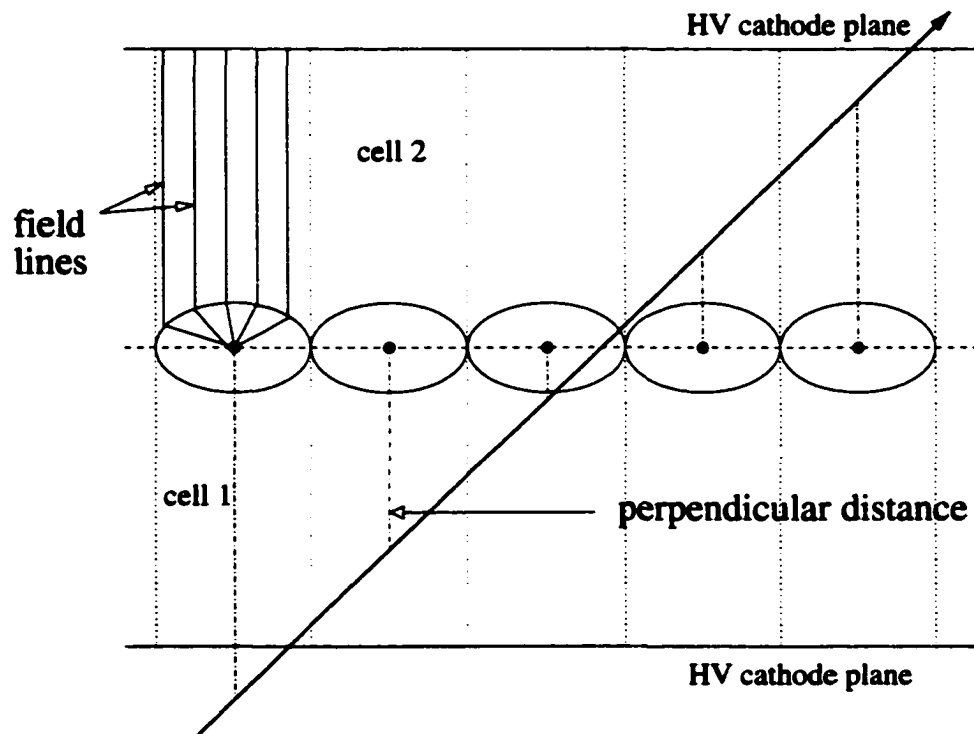
Figure 3.9: A trajectory in a VDC plane.

The chambers are flushed with a gas mixture of argon (62%) and ethane (38%) at a rate of 5 liters per hour. When a charged particle passes through the VDC, it ionizes the Ar gas atoms, and leaves behind a track of electrons and ions. The electrons start drifting towards the sense wires, with a constant drift velocity until they come near the sense wire, where there is a $1/r$ field gradient, as shown on

Fig. 3.9. Here they ionize more gas atoms, leading to an avalanche. This bunch of electrons is captured by the sense wire, and the negative analog signal is sent to a preamplifier/discriminator card. The logic signal output is then sent to a FastBus Lecroy multihit TDC module 1877. The time data from the TDCs are put into the data stream. The drift time information is combined with the drift velocity of the electrons to calculate the perpendicular distances from the track to each wire that fired.

3.4 The Focal Plane Polarimeter
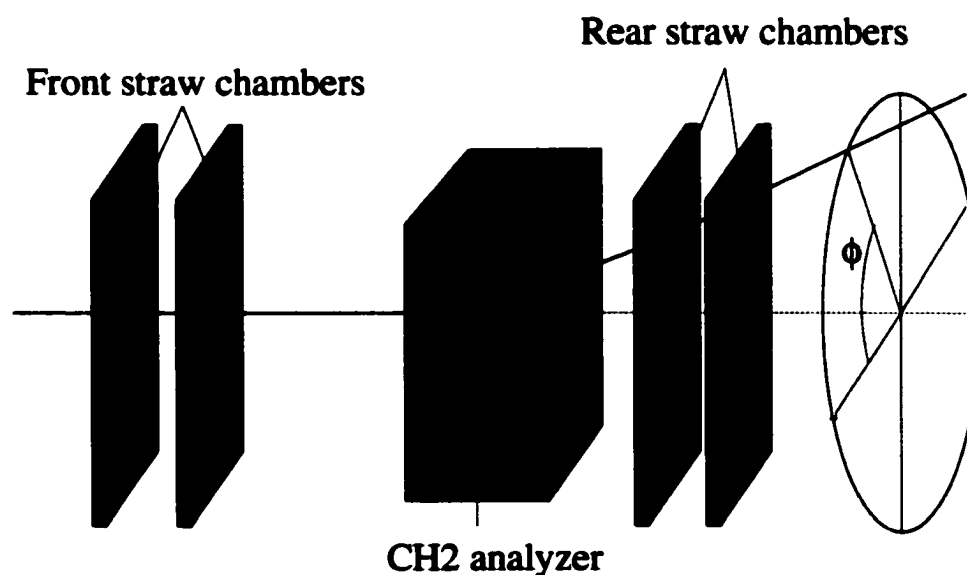
Figure 3.10: Layout of the Focal Plane Polarimeter.

The central piece of equipment in this experiment was the focal plane polarimeter (FPP) [90], developed by the College of William & Mary, Rutgers University, Norfolk State University and University of Georgia. It measures the polarization of the recoil proton. Following momentum analysis and focusing in the spectrometer, the protons are scattered in the focal plane region by an analyzer, as shown

in Fig 3.10. If the protons are polarized transverse to the momentum direction, an azimuthal asymmetry results from the spin-orbit interaction with the analyzing nucleus.

3.4.1 Analyzer
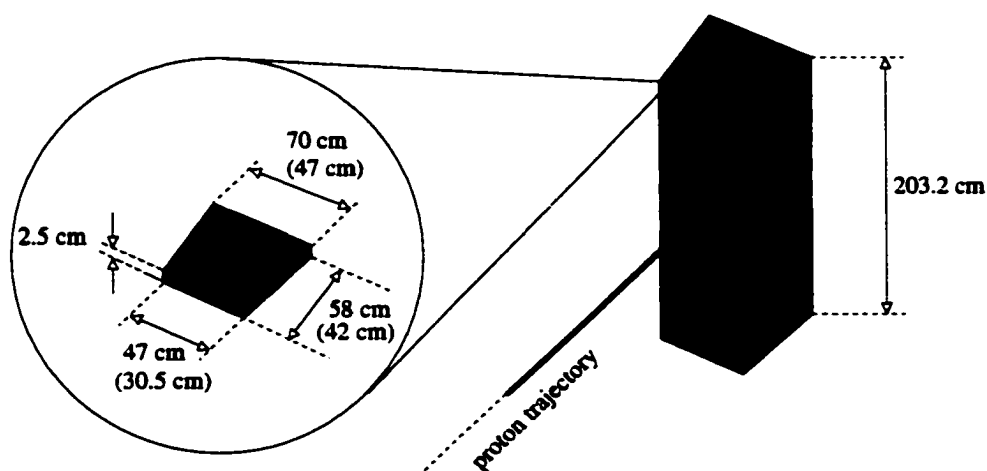
Figure 3.11: Stack of polyethylene plates for the analyzer. The dimensions on the plate are for the 58 cm (42 cm) stack.

The standard Hall A analyzer consists of four doors of carbon, for a maximum thickness of 51 cm. For cost, safety and efficiency reasons, carbon is ideal for measuring proton polarization with a momentum up to 2.4 GeV/c [91, 92]. However, for this experiment, the proton momentum was between 2.6 and 3.8 GeV/c. At this energy, the analyzing power of carbon, which contributes to the size of the asymmetry, and therefore to the size of the error bar, drops dramatically. Ideally, the best material would be hydrogen. But again for cost and safety reasons, it is not possible to install a tank of liquid hydrogen at the back of the detector stack. An intermediate solution was found by using a compound of carbon and hydrogen.

Polyethylene (CH_2) was chosen. A first stack of 80 2.5 cm-thick plates, 58 cm-long along the beam direction, cut to take the shape of the beam envelope, as shown on Fig. 3.11, was installed between the unused, opened, doors of carbon. A second stack, 42 cm-long along the beam direction could be inserted on a rail just upstream of the first stack. The thickness of analyzer is given in Table 3.2 for each kinematics.

Q^2 (GeV^2)	p_p (GeV/c)	T_p (GeV)	CH_2 thickness (cm)
3.5	2.641	1.865	58
4.0	2.922	2.131	100
4.8	3.359	2.550	100
5.6	3.808	2.984	100

Table 3.2: CH_2 thickness along the proton momentum at each kinematics. The four-momentum transferred squared Q^2, the proton momentum p_p and the proton kinetic energy T_p correspond to central values in the HRS.

3.4.2 Straw chambers

Accurately measuring scattering angles of the $CH_2(p, X)$ reaction, where X is a charged particle, implies detecting the proton tracks before and after the scattering. This is done in two sets of two straw chambers, before and after the analyzer, as shown in Fig. 3.10. The straw chambers are a set of cylindrical tubes of radius 0.5 cm, with a thin wire running along a central axis of each tube (straw), as shown on Fig. 3.12. The wire is at positive high voltage relative to the straw. Each tube is individually supplied with a gas mixture of Argon (62%) and Ethane (38%). Each chamber has six planes positioned normal to the spectrometer's nominal central trajectory. The incoming proton sees 3 v then 3 u planes in chamber 1; chamber 2 is identical. After scattering in the analyzer, the proton sees in the third chamber 2 u, 2 v and 2 x planes respectively. In chamber 4, it sees 3 u then 3 v planes. The dimensions of the chambers are given in Table 3.3. The rear chambers were made

large enough so that geometrical efficiency is close to 100% for events scattering at a polar angle less than 20°.
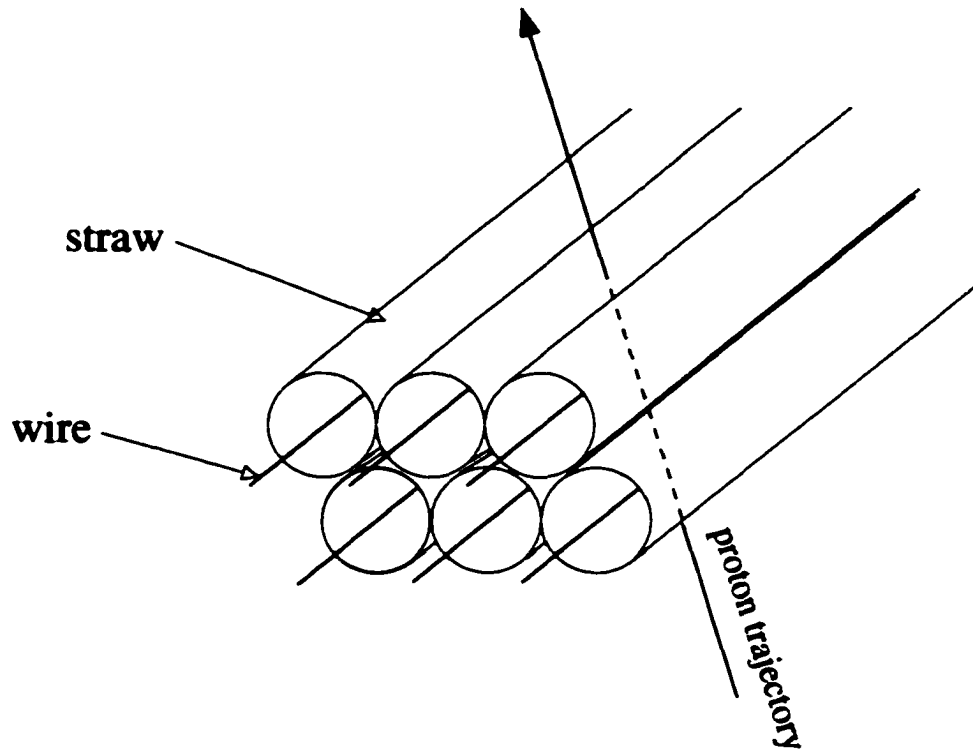
Figure 3.12: Six straws in two different planes of a FPP straw chamber. The proton trajectory is roughly perpendicular to these planes.

Chamber	Ch. 1	Ch. 2	Ch. 3	Ch. 4
Active length (cm)	209.0	209.0	267.5	292.2
Active width (cm)	60.0	60.0	122.5	140.6
Wire spacing (cm)	1.095	1.095	10.795	1.0795

Table 3.3: Dimensions of the FPP straw chambers.

3.4.3 Read out system

When a charged particle passes through the straw, it ionizes the Ar gas atoms, leaving behind a track of electrons. These electrons starts drifting towards the anode

wire, at a constant velocity of about 50 microns per second. When the electrons approach the wire, the strong $1/r$ field gradient gives them enough energy to ionize more atoms, creating an avalanche. This gives rise to a negative electrical signal. This analog signal is then sent to the read out board, where it is preamplified and discriminated to give a logic pulse.
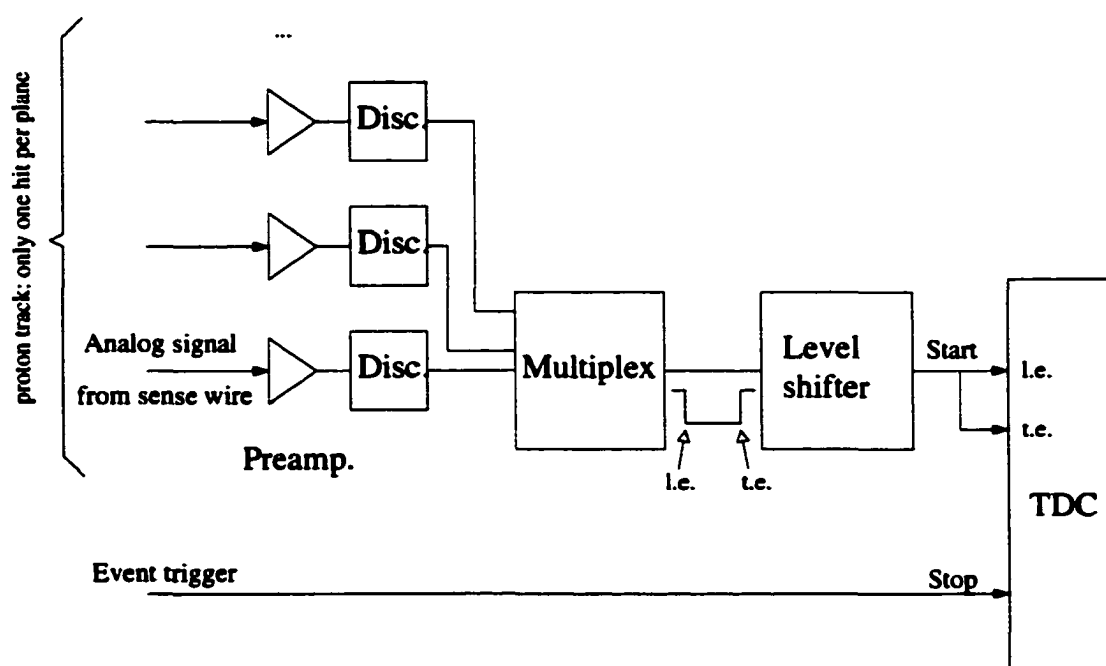
Figure 3.13: Block diagram for the logic of the FPP signal. (l.e.=leading edge, t.e.=trailing edge).

Because of the straw around each wire, which forms a physical ground, a proton track leaves a signal only in one wire of a plane. This allows to significantly reduce the amount of electronics associated to the FPP, by multiplexing the signal in groups of eight neighboring wires. Since for an event, it is likely that only one (or zero) wire fires per group, the entire group of eight is read by the same multiplexing chip. This chip is setup to give a logic pulse whose width depends on which wire fired. This

45 mV signal becomes a 800 mV signal in the level shifter, and is sent to the FastBus TDC modules, whose output is added to the data stream. The TDCs are multihit, recording two times: the arrival of the leading edge, and of the trailing edge of the logic signal. Offline reconstruction of the difference between these two times allows to identify the wire that fired. The time difference between the leading edge and the stop signal of the TDCs (the trigger), gives the drift time. The probability of a noise signal in another wire of the group at the exact same time than the particle signal being very small, there is no particular attention paid to these events. The block diagram for the logic is given in Fig 3.13.

3.5   The calorimeter

The calorimeter used to detect the scattered electron at the three highest Q^2 was assembled with lead-glass blocks from the standard total shower counter of the right arm, and from the standard pion rejector of the left arm. Since we did not need these detectors, we used their components to assemble our calorimeter on the floor.

3.5.1   Principle of calorimetry

Calorimeter

A calorimeter is usually used to detect photons or electrons and measure their total energy. When an electron hits the detector, it radiates a bremsstrahlung photon. This photon, if it has enough energy, can in turn interact electromagnetically with the atomic field of the material, and emit an electron-positron pair. The process repeats itself for each new particle, creating a shower, until the created photons are below the pair production threshold. The longitudinal development of the shower is characterized by the radiation length X_0, after which statistically a new generation starts. If the initial particle has an energy E_0, the next generation has two parti-

cles of average energy $E_0/2$. After n generations, there are 2^n particles with mean energy $E_0/2^n$. The cascade stops when particle energy is below the critical energy: $E_0/2^n \leq E_c$, which corresponds to the energy at which the energy lost by ionization is equal to the energy lost by radiation. The length of the shower is then given in terms of number of radiation lengths:

$$n = \frac{\ln\left(\frac{E_0}{E_c}\right)}{\ln 2} \qquad (3.5)$$

The transverse spread of the shower, characterized by the Molière radius, results from multiple scattering of the electrons that do not radiate, but have enough energy to travel far away from the axis.

For this experiment, the material chosen was lead-glass SF-5. It is a Čerenkov detector, meaning that photons detected do not come from bremsstrahlung but from Čerenkov radiation, which occurs when the incident electron travels at a velocity greater than the speed of light in the medium. Properties of lead-glass are summarized in Table 3.4.

Density	4.08 g/cm^3
Radiation length	2.54 cm
Molière radius	3.7 cm
Critical energy	~ 11.8 MeV

Table 3.4: Lead-glass SF-5 properties.

Photomultipliers

The photomultiplier is attached to the lead-glass block, and converts and amplifies the photon energy to an electrical signal that is digitized in ADCs and TDCs. The photomultiplier tubes (PMT) used in this experiment are Photonis XP2050. The principle is illustrated in Fig. 3.14. A window of borosilicate of diameter 130 mm

directs the photons to the semi-transparent photo-cathode, made of photo-emissive material (bialkali). An electro-optical system accelerates and focuses the electrons to the electron multiplier system. This system consists of ten dynodes covered with a layer of secondary emissive material. For each incident electron, the dynodes emit several secondary electrons; these electrons are accelerated to the next dynode, through an inter-dynode potential of typically 100 V. At the operating high voltage of 1900 to 2000 V, the electron gain was about 2×10^6. After the last dynode, the electron avalanche is collected on the anode, which produces an output signal.
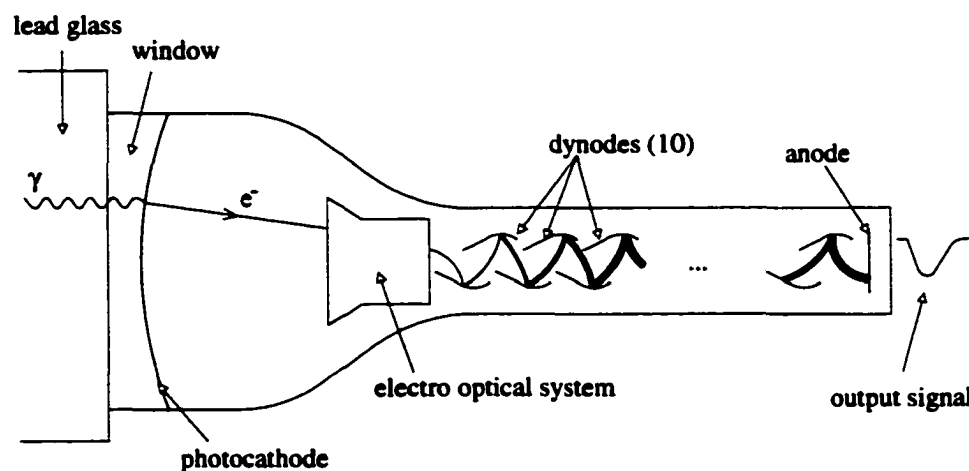
Figure 3.14: Principle of the photomultiplier tube.

3.5.2 The calorimeter design

Figure 3.15 shows a front and a side view of the calorimeter on its platform. The blocks of lead-glass, of cross-sectional area 15×15 cm^2, were carefully individually wrapped in one foil of aluminized mylar, and one foil of black paper, to avoid light leaks. Each block was then tested, and fine wrapping was performed in order to keep the current from noise drawn in the phototube under 100 nA. The blocks were then

put together in 9 columns and 17 rows. Most of the blocks, in green in Fig. 3.15, were 35 cm long, corresponding to 13.7 radiation lengths. 37 blocks, disposed on the edges of the calorimeter, were only 30 cm long, corresponding to 11.8 radiation lengths (in blue in Fig. 3.15). The highest electron energy, for this experiment, was 2.5 GeV. From Eq. 3.5 and Table 3.4, for this energy, the shower would stop after 7.7 X_0, which is shorter than the blocks. Therefore the entire shower was contained in the block. Because this detector was to be used temporarily, no purchase of additional blocks was made. However we were only able to obtain a total of 147 blocks, so that 6 blocks were missing to form a complete rectangle. Those were replaced by "dead blocks" (made of wood), at the corners of the detector (in red in Fig. 3.15). All six "dead blocks" should have been positioned on the side of the calorimeter far away from the beam, where the cross section is lowest, but a judgment error made us assemble a symmetric detector. Furthermore, the acceptance matching was only approximate, not taking into account the particular shape of the spectrometer acceptance. Overall, about 5% of the elastic events were lost due to acceptance mismatching. The active area of the calorimeter was 3.31 m^2.

The blocks were placed in the steel support frame (1), and held together using wooden plates (2). The front of the support was covered with a 2.54 cm-thick aluminum plate (3), to absorb very low energy particles. The ensemble was lifted by the top steel plate (4), using the Hall A crane, and put on the platform (5). Balance on the platform was maintained by the steel support legs (6). The ensemble could be put on wheels and moved with the help of the Hall A crane attached to the steel lifting frame (7). This was used to place the calorimeter at the correct distance to the target to match the solid angle at each kinematics. The vertical position of the calorimeter was surveyed by the JLab survey group. The middle of the ninth row, which was the nominal vertical middle of the calorimeter, was 3.9 cm below the beam line.
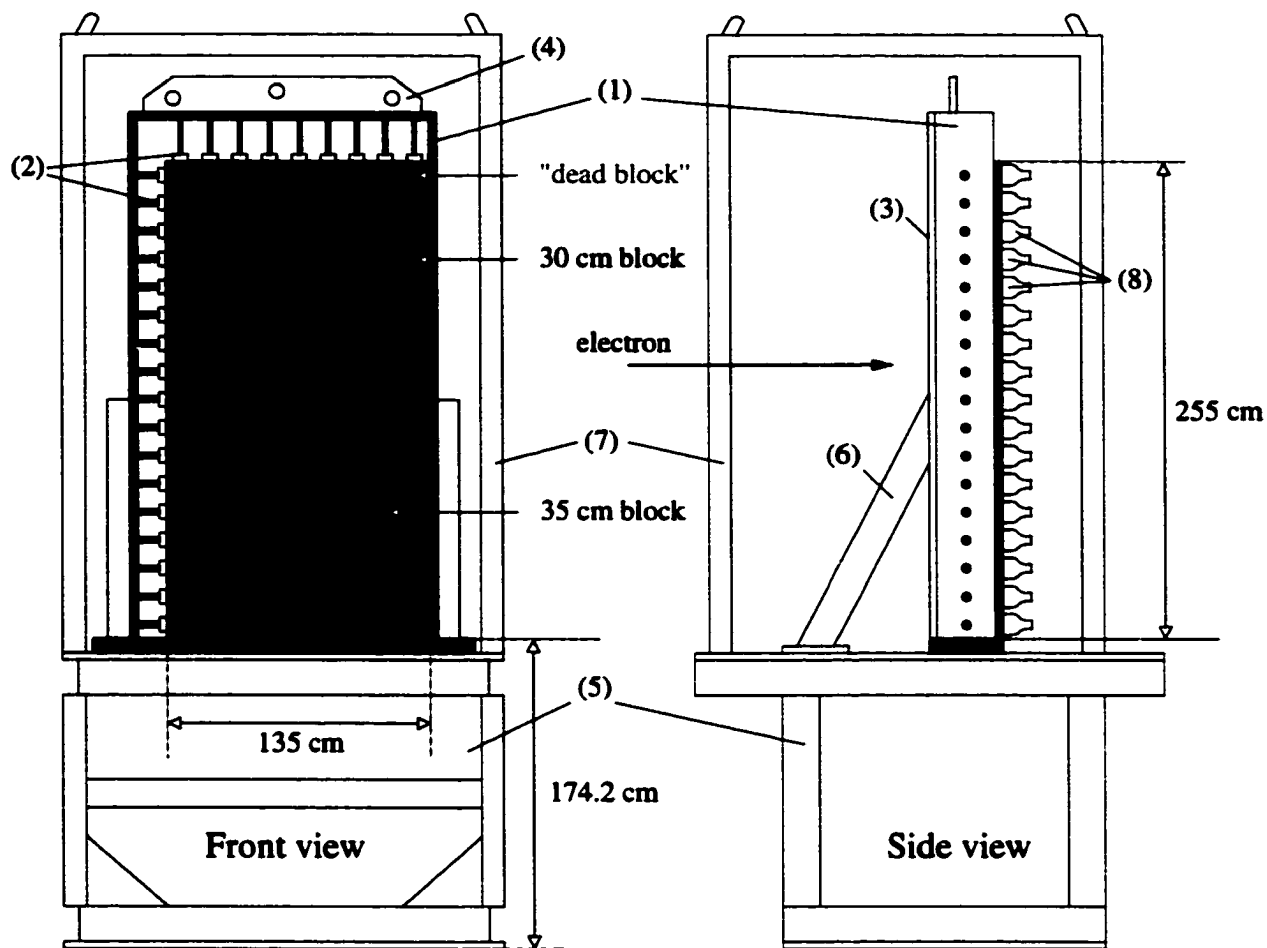
Figure 3.15: Design of the calorimeter used to detect the scattered electron. On the front view, a 2.54 cm thick aluminum plate was in front of the blocks, but is not shown on the figure for details.

3.5.3 The electronics

The light signal was collected in each block by a PMT ((8) in Fig. 3.15), which converted it to an electrical signal and amplified it. This signal was split at the base attached to the PMT, and sent into two different 36 m-long cables. One cable was connected to Lecroy 1881 ADC modules (borrowed from the right HRS

total shower counter and scintillators), where the amplitude signal was digitized. A trigger from the proton HRS sent a 200 ns gate to the ADCs, which recorded the charge accumulated within this gate. The other signal was sent to a discriminator. The discriminator was set at its minimum 10 mV threshold, and the 25 ns-wide output NIM signal was sent to multihit Lecroy 1877 TDC modules (borrowed from the right HRS VDCs). These TDCs were used in common stop mode: the clock was started by a signal in the block, and stopped by the left HRS single arm trigger. 15 blocks, uniformly distributed in the vertical direction, were connected, after the discriminator, to scalers, to analyze the event rate in the detector. A block diagram of the electronics for the calorimeter is shown on Fig. 3.16.
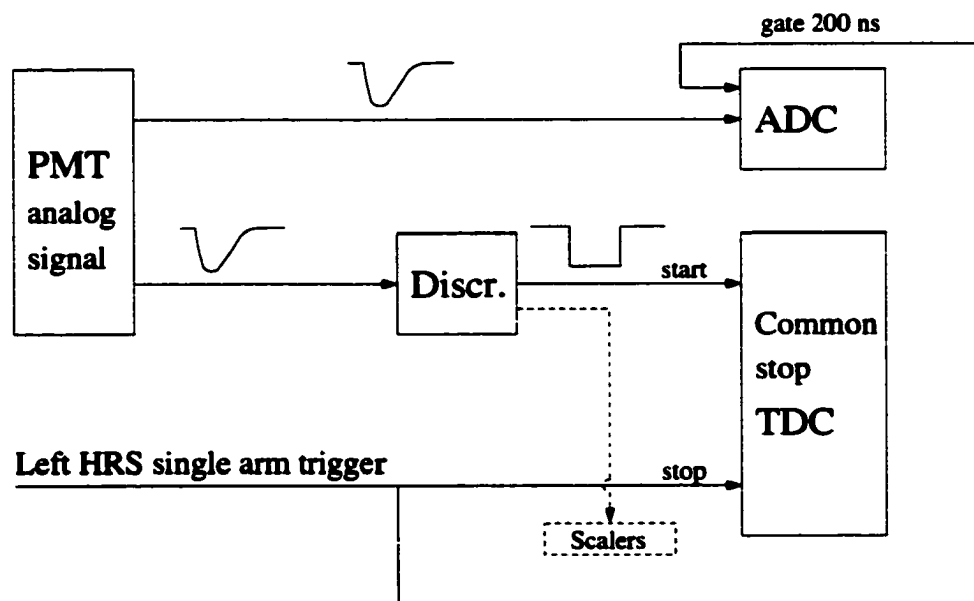
Figure 3.16: Block diagram for the logic of the calorimeter signal.

3.6 The data acquisition system

The standard data acquisition system in Hall A consists of two primary systems, one in each of the spectrometers, which are triggered by a passage of a particle

through two planes of scintillators, S_1 and S_2. In the case of a coincidence experiment, a "master" data acquisition system can be triggered by a coincidence of the two primary triggers.

3.6.1 The scintillators

The data acquisition system of a single HRS is triggered by the passage of a charged particle through two planes of 0.5 cm thin plastic scintillator, developed by the University of Regina [93]. Each plane ($S1$ and $S2$) consists of 6 overlapping paddles, each viewed by two photomultipliers, one at each end. The paddles are big enough to cover the entire beam envelope. The PMT signal is sent to an ADC to digitize the energy loss in the scintillator, and a TDC for time of flight measurement. The time resolution per plane is about 0.3 ns (1σ).

3.6.2 The triggering system
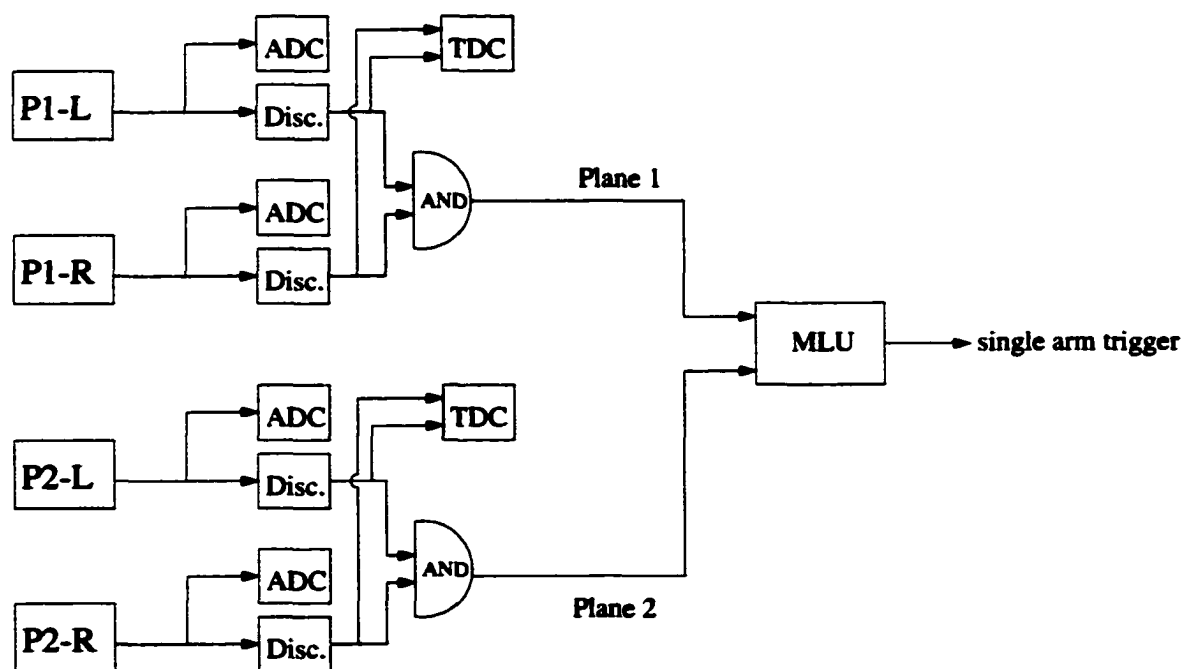
Figure 3.17: Simplified single arm trigger electronics for the HRS.

Single arm trigger

The trigger system is built from commercial CAMAC and NIM discriminators, delay units, logic units, and memory lookup units (MLU). For each paddle, the signal read by both PMTs is sent to an AND logic unit. The output signals for both planes of scintillators are analyzed by a MLU, and if a time coincidence and an approximate position correlation between the two planes is found, a single arm trigger is generated, and the event data go to the data stream. Figure 3.17 illustrates the single arm trigger system.

Trigger for E99-007
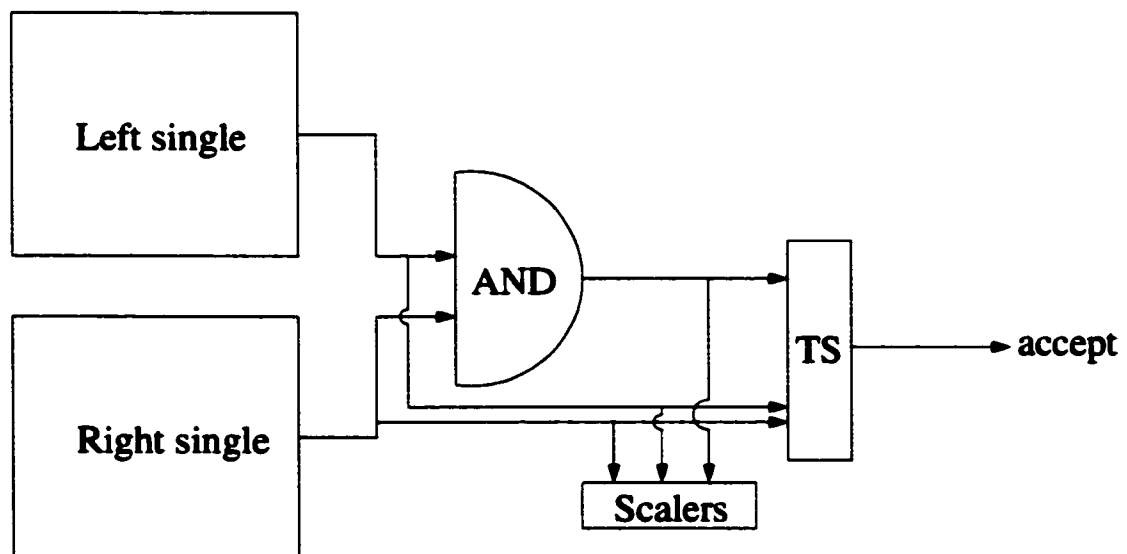
Figure 3.18: Coincidence trigger between the two HRSs.

There were two different situations during the experiment. First, at $Q^2 = 3.5$ GeV^2, the electron was detected in the right HRS. The right HRS has a trigger

system similar to the one of the left HRS, displayed in Fig. 3.17. For this point, there was an additional level of trigger. The two single arm signals were sent to an AND logic unit, and a coincidence between the two signals triggered the overall data acquisition system, as shown in Fig. 3.18. For such a configuration, all three types of trigger are analyzed, single left, single right and coincidence, their identification being handled by the trigger supervisor (TS).

For the three other kinematics, the electron was detected in the calorimeter, whose data were included in the left HRS data stream. When a proton was identified in the HRS, a 200 ns ADC gate was sent to every block of the calorimeter. In the offline analysis, we then looked for a TDC and an ADC signal in this gate. In this configuration, all protons in the HRS were analyzed, whether they come from an elastic reaction or not. So the trigger for these kinematics was a proton single arm trigger, and the coincidence analysis was done offline.

Table 3.5 summarizes the data taking, in November and December 2000. Data acquisition was divided in runs of 1 or 1.5 million triggers. Table 3.5 shows the time, charge accumulated and average current for each kinematics, and the total number of triggers.

Date	Q^2 (GeV^2)	Time (min)	Charge (C)	Beam current (μA)	Triggers
11/4-11/7	3.5	1686	4.150	41	48.6M
11/7-11/12	4.0	4693	10.829	38	80.7M
12/8-12/19	4.8	11310	31.210	46	178.4M
11/12-12/7	5.6	15912	35.955	38	294.3M

Table 3.5: Raw data collection.

CHAPTER 4

Analysis I: Selection of elastic events

This chapter starts with a presentation of the method used and the kinematics of the experiment. The first step of the analysis is to detect the recoil proton in the left high resolution spectrometer (HRS). The scintillator and the vertical drift chamber (VDC) data analysis will be described in the first part of this chapter, as well as the reconstruction of the proton coordinates at the target, and the selection of elastic events at $Q^2 = 3.5$ GeV^2 based on a coincidence in the two HRSs. The other kinematics required a larger acceptance detector for the scattered electron. The second part of this chapter will describe the calorimeter analysis, and the result of the selection. This first part of the analysis was done using the standard Hall A analyzer Fortran code ESPACE, modified to include the calorimeter.

4.1 E99-007 kinematics

The goal of this experiment was to measure the ratio of the electric to magnetic form factor of the proton, at four different kinematics, at $Q^2 = 3.5$, 4.0, 4.8 and 5.6 GeV^2. The kinematics of the experiment are presented in Table 4.1.

Q^2 (GeV^2)	E_{beam} (GeV)	E_e (GeV)	θ_e	p_p (GeV/c)	θ_p
3.5	4.6	2.73	30.6°	2.64	31.79°
4.0	4.6	2.47	34.5°	2.92	28.59°
4.8	4.6	2.04	42.1°	3.36	23.79°
5.6	4.6	1.61	51.4°	3.81	19.36°

Table 4.1: Kinematics of the experiment E99-007.

77

The first point, at $Q^2 = 3.5$ GeV^2, was an overlap point with experiment E93-027 [28]. It was taken in similar conditions, with the exception of the proton being detected in the left arm instead of the right arm, which required a swap of the detector packages, including the FPP, of the two spectrometers. This swap, which took the better part of the summer before the experiment, was motivated by the detection of the proton at momentum above 3.2 GeV/c, which is the limit of the right arm.

A crucial point in polarization experiments is to accumulate as much statistics as possible, because of the low efficiencies associated with hadron polarimeters, as will be discussed in Chapter 6. Since this experiment focused on elastic scattering, we wanted to detect the scattered electron to select elastic events. The left HRS, where the proton was detected, had an acceptance of 7.2 msr. If all elastic protons in this acceptance were to be included in the polarization analysis, we needed to detect all corresponding electrons. Two-body elastic kinematics constrained the solid angle in which these electrons could be contained. With a fixed beam energy around 4.6 GeV, the needed acceptance for the electron detector is given in Table 4.2.

Q^2 (GeV^2)	θ_e	θ_p	Jac	Ω_e (msr)
4.0	34.5°	28.59°	1.60	11.5
4.8	42.1°	23.79°	2.97	21.4
5.6	51.4°	19.36°	5.89	42.4

Table 4.2: Needed solid angle Ω_e for the electron detector. Jac= Ω_e/Ω_p is the jacobian of the reaction.

We can see that if we had detected the electron for the three high Q^2 points in the right HRS , which also has a 7.2 msr acceptance, we would have lost 5/6 of the events at $Q^2 = 5.6$ GeV^2. Therefore for these kinematics, we detected the scattered electron in the lead-glass calorimeter, whose distance to the target could be changed to match the acceptance at each kinematics, as shown in Table 4.3.

Q^2 (GeV^2)	Distance target-calorimeter (m)
4.0	17
4.8	12.5
5.6	9

Table 4.3: Distance target to calorimeter to match the electron solid angle at each kinematics.

4.2 HRS analysis

4.2.1 Scintillator analysis

Figure 4.1 shows ADC and TDC spectra for a scintillator paddle. The pulse height of the ADC signal is a measure of the amount of energy the particle has lost in the paddle. The trigger is defined using the timing information. A coincidence is required between the two PMTs on each side of a paddle, as well as with another paddle of the other scintillator plane that is located at a similar transverse position. The timing of the event is defined from the right PMT of the second plane.
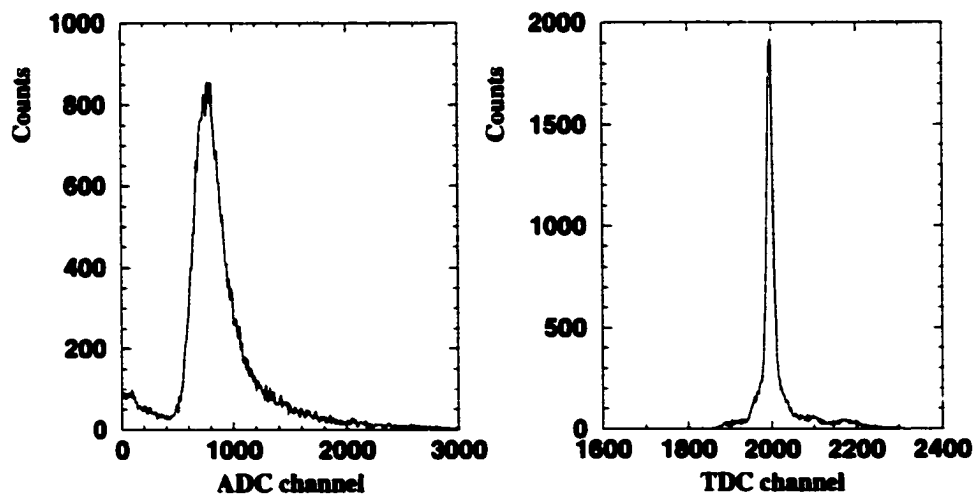
Figure 4.1: ADC and TDC spectrum for one side of a scintillator paddle.

4.2.2 VDC analysis

Drift time to drift distance conversion
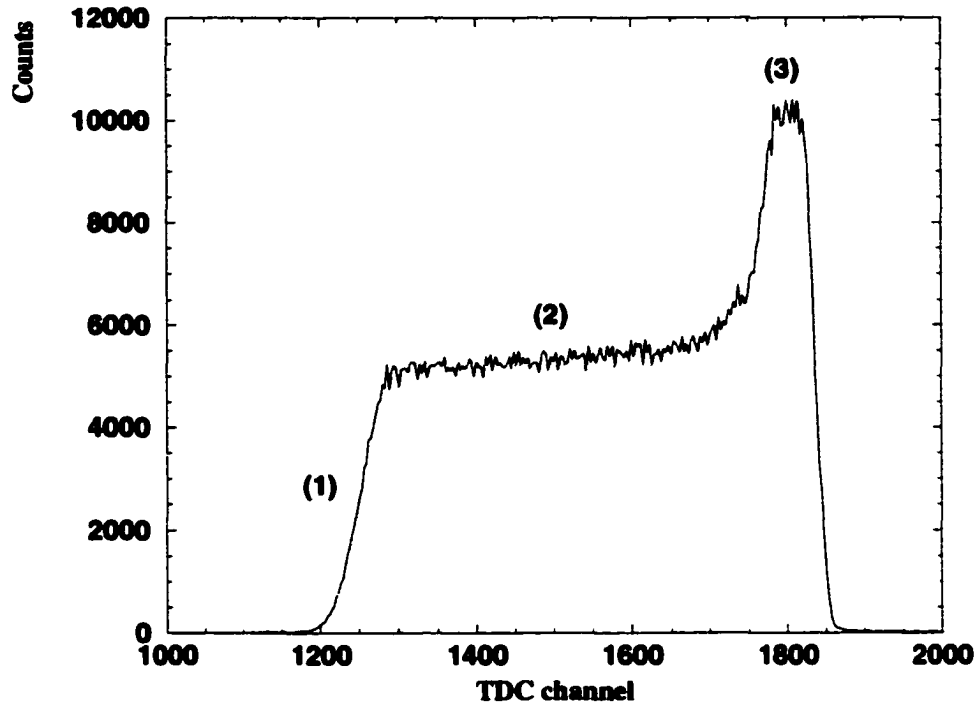
Figure 4.2: Drift time spectrum for U1 plane of VDC. The TDC's were used in common stop mode, so that the short drift times are at the left of the spectrum.

A complete description of the method can be found in Ref. [89]. Figure 4.2 shows the drift time spectrum for the U1 plane of the left VDC. The three regions apparent on the spectrum arise from geometric effects. The number of counts in the interval of the drift-time spectrum is given by:

$$\frac{dN}{dt} = \frac{dN}{ds}\frac{ds}{dt} \tag{4.1}$$

where s is the length of the path traveled by the drift electron. The drift velocity, ds/dt, is essentially constant, except very close to the wire. dN/ds is the effective flux through the drift line. In the region close to the cathode plane (region (1) in Fig. 4.2, corresponding to track (1) in Fig. 4.3), the probability dN/ds that a particle

fires the wire decreases, because the corresponding volume of the cell decreases, explaining the tail at the long drift-time end of the spectrum. In the uniform field region, both the drift velocity ds/dt and the effective flux dN/ds remain constant, giving rise to the plateau in region (2) of Fig. 4.2. The peak at the short drift-time end of the spectrum results from a combination of a dramatic increase of ds/dt, due to the avalanche effect, and the shape of dN/ds, which goes through a peak, in the quasi-radial field region, next to the sense wire.
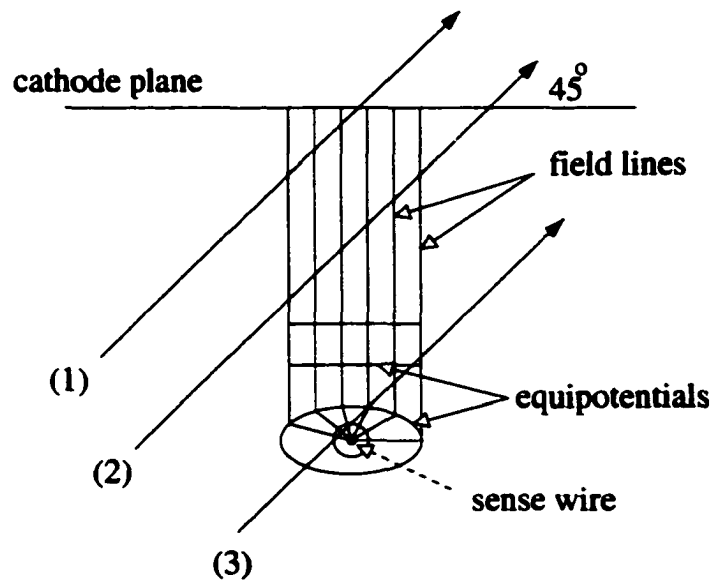
Figure 4.3: Drift cell in a VDC plane. Three tracks are shown, giving three different TDC signals. See text for details.

As shown in Fig. 4.4, a 45° track typically crosses five drift cells. In each cell in that track, the shortest time is determined by the arrival of the earliest electron, defining the geodetic (the electron path corresponding to the shortest drift time). A cluster is found when several adjacent wires have fired, with a possible gap of one wire. A hit pattern is defined by calculating the relative time t_0:

$$t_0 = |t_1 - t_2| - |t_4 - t_5| \qquad (4.2)$$

where t_i, $i = 1, 5$ are the drift times of the five fired wires. The best candidate for a track is the one with the lowest t_0. Using the knowledge of the drift velocity, the distance corresponding to this geodetic is calculated, and the corrected perpendicular distance is extracted. A linear fit of these five distances is performed to get the position of the cross-over point, for each wire plane.
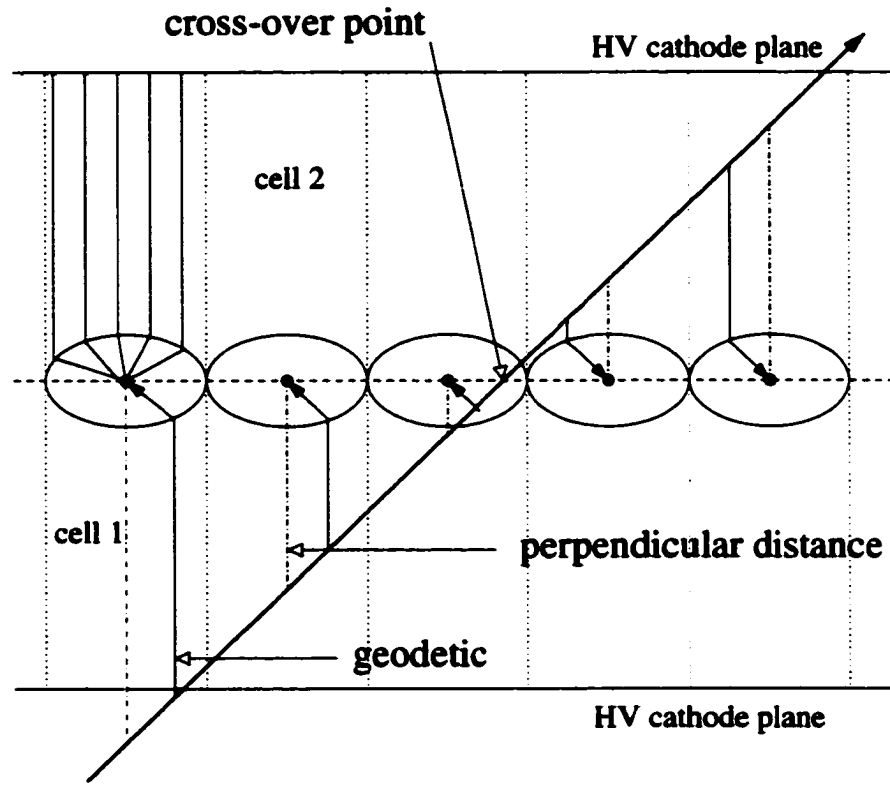
Figure 4.4: Typical track crossing five drift cells in a VDC plane. The cross-over point is found by fitting the trajectory determined from the perpendicular distances to the sense wires.

Determination of focal plane coordinates

The position of the cross-over point is defined for each of the four VDC planes, U1, V1, U2 and V2, as shown in Fig. 4.5. Taking advantage of the relatively large

distance between the two chambers, two angles η_1 and η_2 are calculated:

$$\tan \eta_1 = \frac{u_2 - u_1}{d_1}$$

$$\tan \eta_2 = \frac{v_2 - v_1}{d_1} \tag{4.3}$$

where $d_1 = 0.335$ m is the distance between the two u (and v) planes. The VDC coordinate system is defined on the U1 plane. Two coordinates u and v are defined, v being the projected v_1 position on the U1 plane:

$$u = u_1$$

$$v = v_1 - d_2 \tan \eta_2 \tag{4.4}$$

where $d_2 = 0.115$ m is the distance between the U and V planes in both chambers.
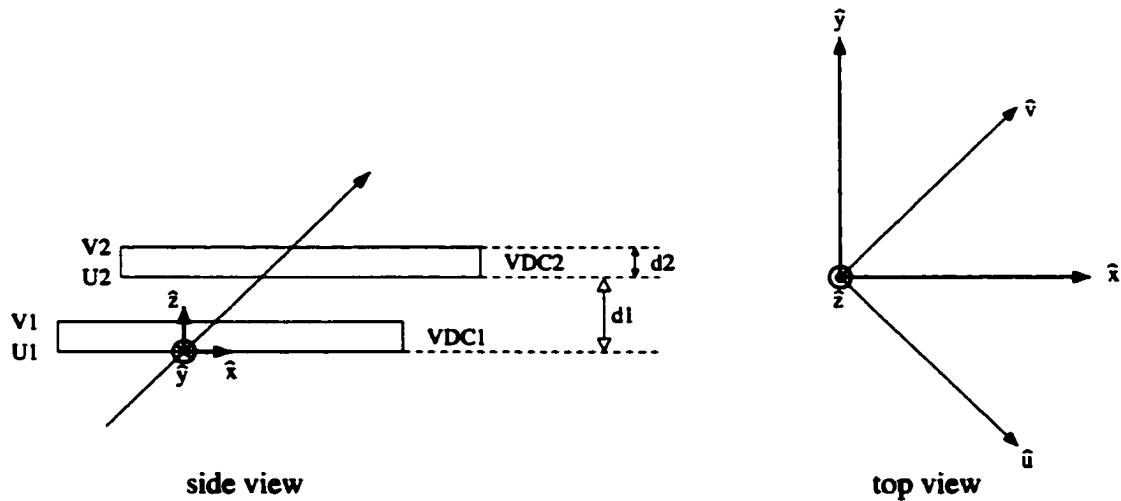
Figure 4.5: Side and top view of the VDC coordinate system and the detector hut coordinate system.

The track coordinates must then be expressed in the focal plane coordinate system, to be transported back to the target. The first step is a rotation to the detector hut coordinate system, by $45°$ around the z-axis, as shown in Fig. 4.5. The

transformation is:

$$x_{det} = \frac{1}{\sqrt{2}}(u + v)$$

$$y_{det} = \frac{1}{\sqrt{2}}(-u + v)$$

$$\tan\theta_{det} = \frac{1}{\sqrt{2}}(\tan\eta1 + \tan\eta2)$$

$$\tan\phi_{det} = \frac{1}{\sqrt{2}}(-\tan\eta1 + \tan\eta2) \tag{4.5}$$

The second step is the transformation to the transport system, obtained by rotating the detector hut coordinate system clockwise by the dipole bending angle $\rho_0 = 45.1°$ around its y-axis:

$$\theta_{trans} = \frac{\theta_{det} + \tan\rho_0}{1 - \theta_{det}\tan\rho_0}$$

$$\phi_{trans} = \frac{\phi_{det}}{\cos\rho_0 - \theta_{det}\sin\rho_0}$$

$$x_{trans} = x_{det}\cos\rho_0(1 + \theta_{trans}\tan\rho_0)$$

$$y_{trans} = y_{det} + \sin\rho_0\phi_{trans}x_{det} \tag{4.6}$$

4.2.3 Reconstruction of target coordinates

The target coordinates are calculated in the transport coordinate system at the target, shown in Fig. 4.6, where $\hat{z}$ lies along the spectrometer axis, $\hat{x}$ points vertically downwards and $\hat{y} = \hat{z} \times \hat{x}$. y_{tg} and ϕ_{tg} are the horizontal position and geometric angle respectively, θ_{tg} is the vertical geometric angle, and δ is the relative deviation from the central momentum p_0, defined as $p = p_0(1 + \delta)$.

We used the optics tensor of the spectrometer to calculate the target coordinates. The tensor is by now well known. It has been optimized many times since Hall A began operation. The optimization procedure is described in Ref. [94]. The tensor was determined using (ee') elastic scattering from a thin ^{12}C target, and a 49 holes sieve slit positioned before the entrance of Q_1. This tensor relates the focal plane

coordinates vector $(x_{fp}, y_{fp}, \theta_{fp}, \phi_{fp})$ to the target coordinate vector $(y_{tg}, \theta_{tg}, \phi_{tg}, \delta)$, where δ is the relative deviation from the central momentum. The x_{tg} position (vertical) at the target is obtained from the beam position monitor information, positioned on the beam-line close to the target. The δ and θ_{tgt} coordinates are then corrected for the x_{tg} displacement. Distances are in meters (m), angles are in radians (rad) and δ is in units of percent.
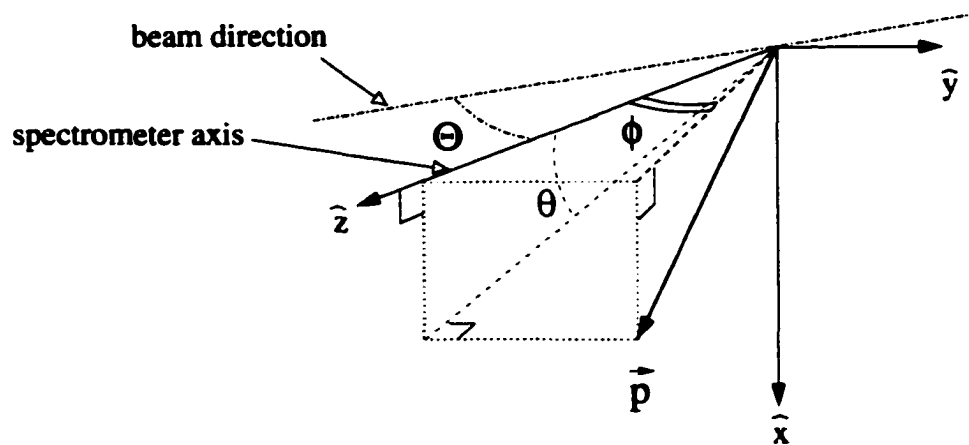
Figure 4.6: Transport coordinate system at the target. The z-axis is along the spectrometer axis.

In a first order approximation, we can relate the target quantities to the focal plane quantities by the following matrix:

$$
\begin{bmatrix} \delta \\ \theta \\ y \\ \phi \end{bmatrix}_{tg}
=
\begin{bmatrix}
\langle \delta|x \rangle & \langle \delta|\theta \rangle & 0 & 0 \\
\langle \delta|x \rangle & \langle \delta|\theta \rangle & 0 & 0 \\
0 & 0 & \langle y|y \rangle & \langle y|\phi \rangle \\
0 & 0 & \langle \phi|y \rangle & \langle \phi|\phi \rangle
\end{bmatrix}
\begin{bmatrix} x \\ \theta \\ y \\ \phi \end{bmatrix}_{fp}
\tag{4.7}
$$

The null matrix elements arise from the mid-plane symmetry of the spectrometer.

The optimization was performed to the fifth order in the development in focal plane coordinates. A set of tensors Y_{jkl}, T_{jkl}, P_{jkl} and D_{jkl} connects the focal plane

to the target coordinates:

$$y_{tg} = \sum Y_{jkl}\theta_{fp}^{j}y_{fp}^{k}\phi_{fp}^{l}$$

$$\theta_{tg} = \sum T_{jkl}\theta_{fp}^{j}y_{fp}^{k}\phi_{fp}^{l}$$

$$\phi_{tg} = \sum P_{jkl}\theta_{fp}^{j}y_{fp}^{k}\phi_{fp}^{l}$$

$$\delta_{tg} = \sum D_{jkl}\theta_{fp}^{j}y_{fp}^{k}\phi_{fp}^{l} \tag{4.8}$$

Here each tensor element Y_{jkl}, T_{jkl}, P_{jkl} and D_{jkl} is a polynomial in x_{fp}:

$$Y_{jkl} = \sum_{i=1}^{m} y_{ijkl}x_{fp}^{i}$$

$$T_{jkl} = \sum_{i=1}^{m} t_{ijkl}x_{fp}^{i}$$

$$P_{jkl} = \sum_{i=1}^{m} p_{ijkl}x_{fp}^{i}$$

$$D_{jkl} = \sum_{i=1}^{m} d_{ijkl}x_{fp}^{i} \tag{4.9}$$

These tensor elements are obtained by a χ^2 minimization procedure. The focal plane coordinate system, which is involved in Eq. 4.8, does not necessarily coincide with the transport coordinate system, due to various misalignments of the VDCs. The offsets are calculated during the optimization procedure, and are represented by the terms P_{000}, Y_{000} and T_{000}. The transformation from the transport to the focal plane coordinate systems is the following:

$$\theta_{fp} = \frac{\theta_{det} + T_{000}}{1 - \theta_{det}T_{000}}$$

$$\phi_{fp} = \frac{\phi_{det} - P_{000}}{\cos(\arctan T_{000}) - \theta_{det}\sin(\arctan T_{000})}$$

$$x_{fp} = x_{trans}$$

$$y_{fp} = y_{trans} - Y_{000} \tag{4.10}$$
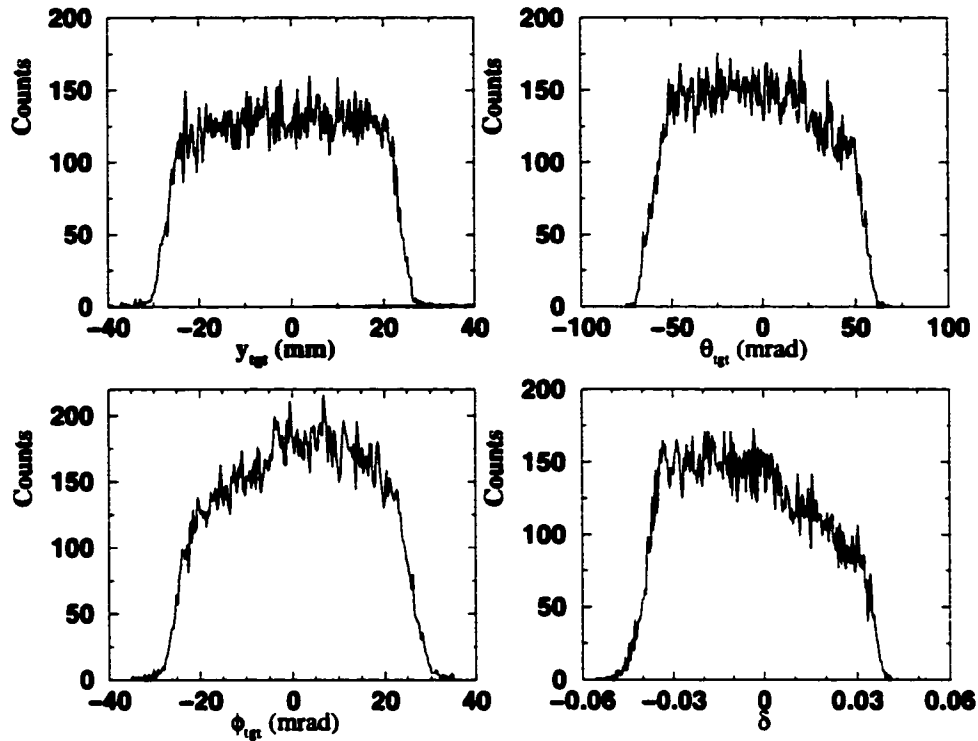
Figure 4.7: Distributions of the proton target coordinates at $Q^2 = 5.6$ GeV^2.

Figure 4.7 shows the target coordinates distributions for the $Q^2 = 5.6$ GeV^2 point, reconstructed from the focal plane coordinates and the tensor defined in Eq. 4.8.

4.2.4 Coincidence between proton and scattered electron

At $Q^2 = 3.5$ GeV^2, the scattered electron was detected in coincidence in the right HRS, which was analyzed in an identical way as the left HRS for the proton. Along with the beam energy measurements, the information on both particles was used to reconstruct the missing energy and the missing momentum of the reaction. For elastic kinematics, both these quantities must be zero. Figure 4.8 shows the E_{miss} vs. p_{miss} spectrum, and the cut applied to it. Events on the diagonal have a null missing mass, and are photons radiated from the scattered or the incident

electron. Events on the horizontal tail arise from multiple scattering in the target, and angular resolution.
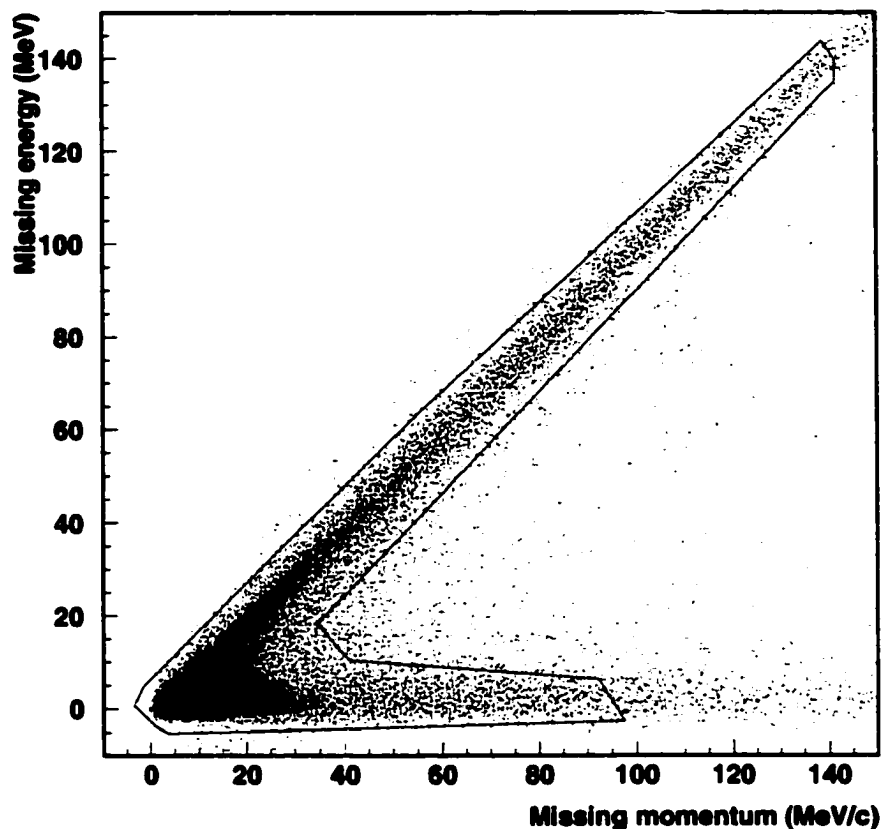
Figure 4.8: E_{miss} vs. p_{miss} spectrum at $Q^2 = 3.5$ GeV^2.

4.3 Calorimeter analysis

As explained earlier, for the higher Q^2 points, we couldn't use the other HRS to detect the electron, and therefore we could not use the coincidence trigger. Instead, the data acquisition system was triggered every time a proton was detected in the spectrometer. Figure 4.9 illustrates how much inelastic background was included in the spectrometer at $Q^2 = 5.6$ GeV^2. It shows the difference between the expected momentum of the proton from its recoil angle, beam energy and elastic kinematics,

and the momentum measured in the HRS. The expected momentum is given by:

$$p(\Theta) = \frac{2E\cos\Theta M_p(E + M_p)}{E^2(1 - \cos^2\Theta) + 2EM_p} \tag{4.11}$$

where Θ is the recoil angle of the proton with respect to the beam direction, E is the beam energy, corrected for energy loss in the target, and M_p is the proton mass. Θ is defined from the angles in the spectrometer coordinate system and the spectrometer angle:

$$\cos\Theta = \frac{\cos\theta_{spec} - \phi_{tgt}\sin\theta_{spec}}{\sqrt{1 + \theta_{tgt}^2 + \phi_{tgt}^2}} \tag{4.12}$$
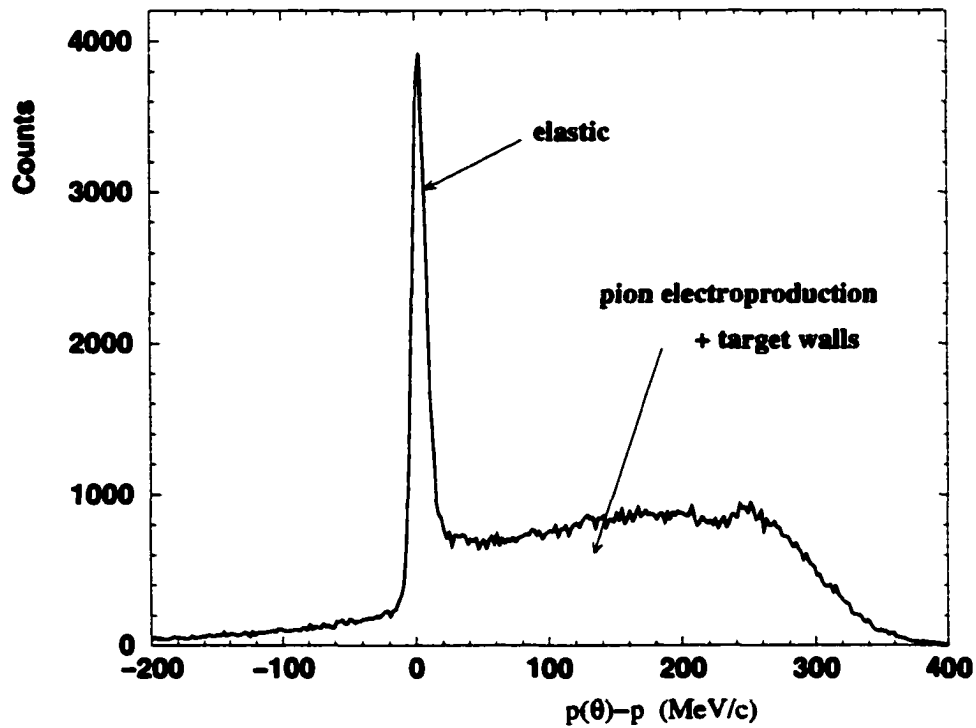
Figure 4.9: Difference between the expected (from proton scattering angle) and the measured proton momentum at $Q^2 = 5.6$ GeV^2. See text for details.

The elastic peak is seen on the spectrum in Fig. 4.9 around 0, as expected. The remaining background comes partly from scattering off the target walls, and mostly from pion electroproduction. Both can be eliminated by looking for the electron

at the angles ϕ_e and θ_e expected from two-body kinematics. The calorimeter was placed at this expected position, and its signal was collected each time a proton started the trigger.

4.3.1 Calorimeter test in April 2000

This method was tested in April 2000, using a prototype calorimeter of 45 blocks, in 5 rows and 9 columns. The blocks were the same as the ones used for E99-007, described in Section 3.5, and the energy deposition of the signal in each block was recorded in the same ADCs described in the same section. Table 4.4 shows the kinematics of the test at which solid angle matching was satisfied. The results of this test are presented in Ref. [95].

Q^2 (GeV^2)	E (GeV)	E' (GeV)	p_p (GeV/c)	θ_e	θ_p	Calo distance (m)
3.0	3.40	1.80	2.36	41.06°	30.04°	8.25

Table 4.4: Kinematic settings for the calorimeter test.

The trigger was a proton single-arm trigger, and signal clusters in the calorimeter were reconstructed solely from the ADC information. Events were selected based on the position and energy of the cluster with the most energy. It was observed that for each trigger, about 30% of the blocks had a hit, therefore that the background from non-elastic events was important.

To evaluate this background, for one run, we delayed the ADC gate, so that the signal collected by the ADC was not in the time window of the elastic events. In this run, no event was recorded under the elastic peak. To verify that a timing cut could suppress this background, two blocks were also connected to TDCs, which allowed us to measure the time between the trigger and the signal collection in

the calorimeter, ensuring that the signal corresponded to the same reaction as the trigger.

A run with a "dummy target", which consists only of the aluminum walls of the cryogenics cell, evaluated the target walls contribution under the elastic peak at the level of 10^{-4}.

The recoil proton polarization analysis was also performed, and the ratio $\mu_p G_{Ep}/G_{Mp}$ was extracted and compared with the result of E93-027. The value for the ratio was 0.62±0.048, while the value for E93-027 at $Q^2 = 5.6$ GeV^2 was 0.61±0.032 (statistical uncertainty only) [28]. This showed the equivalence between the elastic event selection methods, using the HRS and using a calorimeter.

It was therefore decided to proceed with a larger calorimeter for E99-007, which included TDC information for every block. Three software cuts were applied on the calorimeter data. A coincidence time cut ensured that the particle detected came from the same reaction as the proton that triggered the data acquisition system. An angular correlation cut between the position of the particle detected and the position of the proton in the HRS eliminated signals that were accidentally in time. An energy cut allowed us to discriminate some accidentals in the elastic peak of the two other cuts.

4.3.2 Raw signal analysis

TDC

Figure 4.10a is a typical histogram of the raw TDC signal for one block of the calorimeter. Several coincidence time peaks are seen; they are due to different TDC offsets for corresponding scintillator paddles that fired and stopped the calorimeter TDC. This offset was measured for each of the six paddles, and the TDC information was corrected accordingly. All blocks were also aligned in software for a peak in channel 1500, as shown in Fig. 4.10b. Analysis shows that this time selection cuts

the events that have scattered on the target walls.
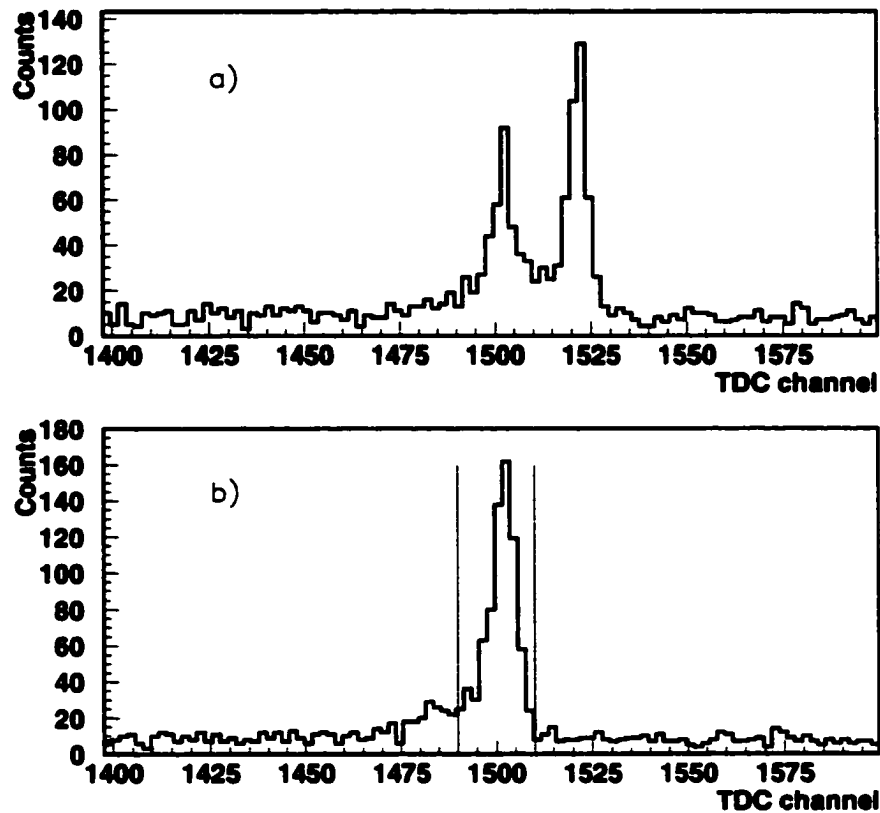
Figure 4.10: TDC spectrum corresponding to one block of the calorimeter a) raw, b) corrected for offset corresponding to scintillator paddle. 1 TDC channel ≡ 0.5 ns.

ADC

Figure 4.11a shows a typical raw ADC signal for one block of the calorimeter. The elastic events peak is seen at the end of the spectrum near channel 900. The ADCs were calibrated to convert the ADC signal into an energy measurement. The conversion takes the form:

$$E_i = C_i(ADC_i - P_i) \tag{4.13}$$

where i represents the block number, E_i is the energy, in MeV, deposited in this block, ADC_i is the channel number corresponding to that energy deposition, P_i is the

pedestal and C_i is the gain coefficient of the ADC. The pedestals were determined by hand from the raw spectrum of each block (420 on Fig. 4.11a, found after a zoom on the 300-700 channel region). The gain coefficients were calculated using the calibration method described in Appendix C. Since it was observed that this coefficients slowly drifted down with time, because of a slow drift of the high voltage, or of the temperature, a better precision was achieved by calibrating the ADCs for every run. Figure 4.11b shows an ADC spectrum corrected for pedestal and gain, where the horizontal axis is the energy deposition in the block in MeV.
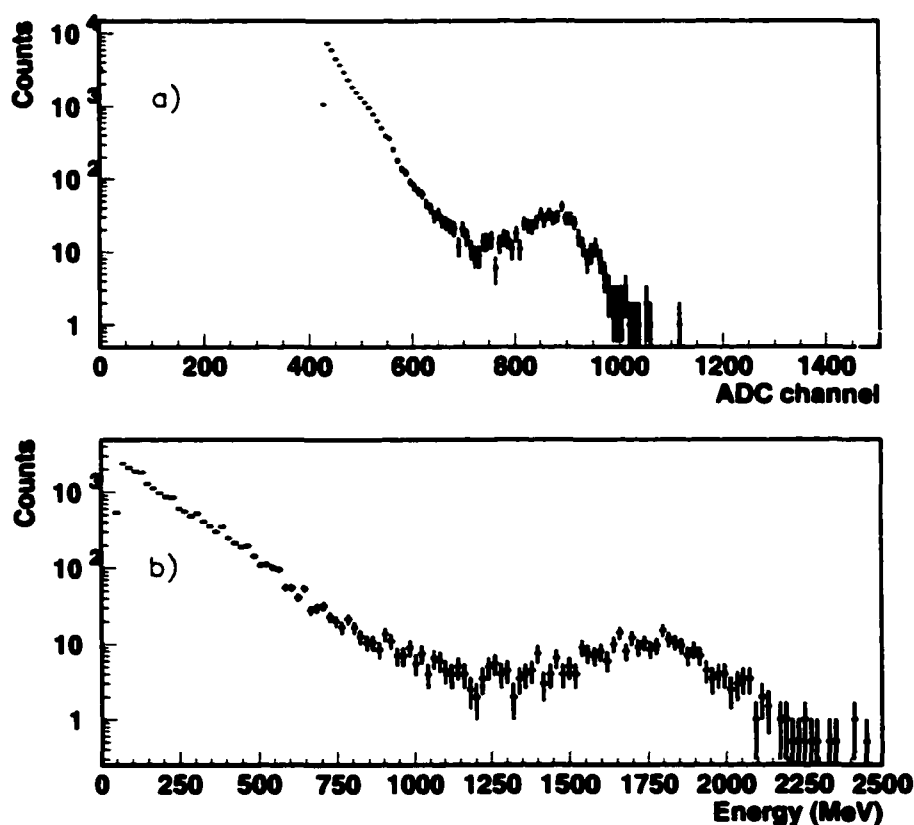
Figure 4.11: a) raw ADC spectrum corresponding to one block of the calorimeter, no hits are seen below the pedestal at 420; b) corrected ADC spectrum for pedestal and gain.

4.3.3 Event reconstruction algorithm

Figure 4.12 shows the diagram of the event selection algorithm, detailed in this section.
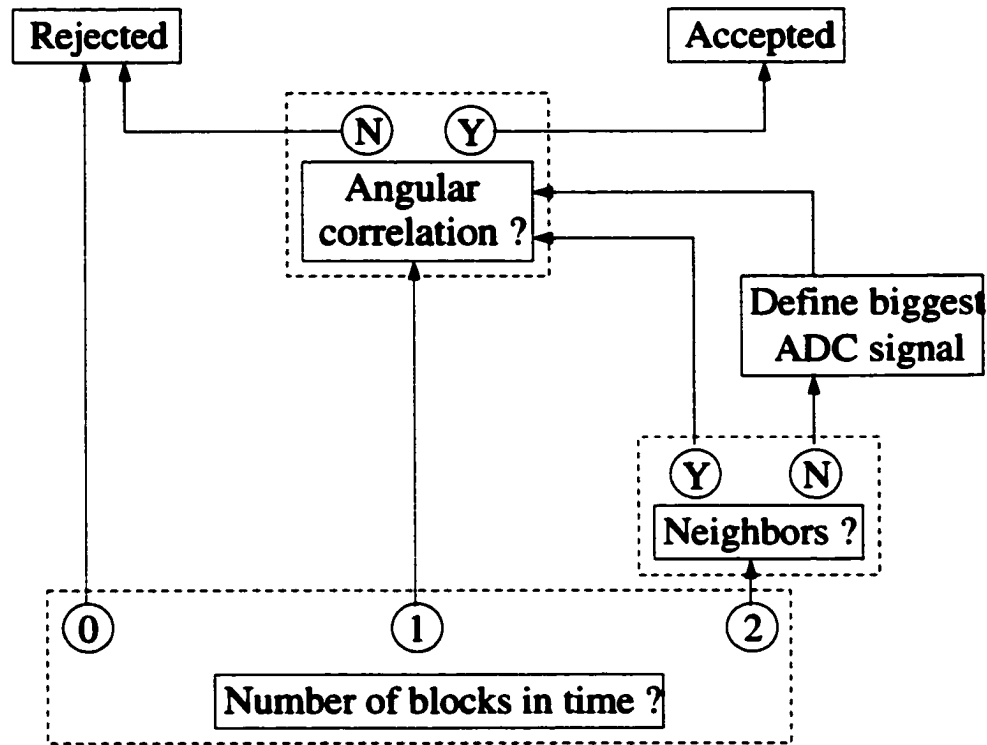
Figure 4.12: Diagram of the event selection algorithm.

Time selection

A time coincidence cut was defined on the TDC spectrum of each block, as shown on Fig. 4.10. The width of this cut for each kinematics is given in Table 4.5. For each trigger, the event reconstruction algorithm looked through the entire array of calorimeter blocks, for all blocks with one TDC hit inside the cut. Table 4.5 gives the number of such blocks per event. It shows that in a large number of cases, no

block was in time. It meant that either no particle hit the calorimeter, or the particle that hit it was not correlated in time with the proton that triggered the DAQ; **such events were identified as not elastic and rejected**. For a coincidence event, either one or two blocks were hit. If these two blocks were neighbors, they were identified as being the same particle, whose shower spread over two blocks. The energy of the particle was then given by the sum of the two corresponding ADCs. If they were not neighbors, then two clusters were identified, and the one with the biggest ADC signal was chosen as the best candidate for being an elastic electron.

Kinematics	Cut width (ns)	Number of blocks in time		
		0	1	2
4.0 GeV^2	8	44.7%	52.1%	3.2%
4.8 GeV^2	8	60.8%	37.8%	1.4%
5.6 GeV^2	10	69.1%	29.3%	1.6%

Table 4.5: Timing cut information for each kinematics. If the number of blocks in time is 0, the event is not elastic and rejected. Otherwise, angular correlation is investigated further.

We can see that for most events that had a signal in time in the calorimeter, only one block was hit within the time window. The elastic signal was typically of the order of 50 mV at the highest Q^2, five times higher than the threshold of the discriminator. This means that if the shower spread over two blocks, but only 20% or less of the energy was in the second block, this second block would not pass the threshold, as illustrated in Fig. 4.13. Table 4.5 shows that in 95% of the events, 80% of the shower is contained in only one block, due to the large size of the blocks. There was no calorimeter simulation done to predict these numbers, because what matters in our case was only that the electron was detected, therefore one signal was sufficient. But the lateral spread of the shower was confirmed by a recent experiment in Hall A, which used a calorimeter with smaller blocks. Because

in most cases only one block was used to reconstruct the cluster, the resolution of the calorimeter was $15/\sqrt{12} = 4.3$ cm in both directions, where 15 cm is the size of the blocks, but **there was no loss of elastic events corresponding to the fairly poor resolution due to the large size of the blocks**.
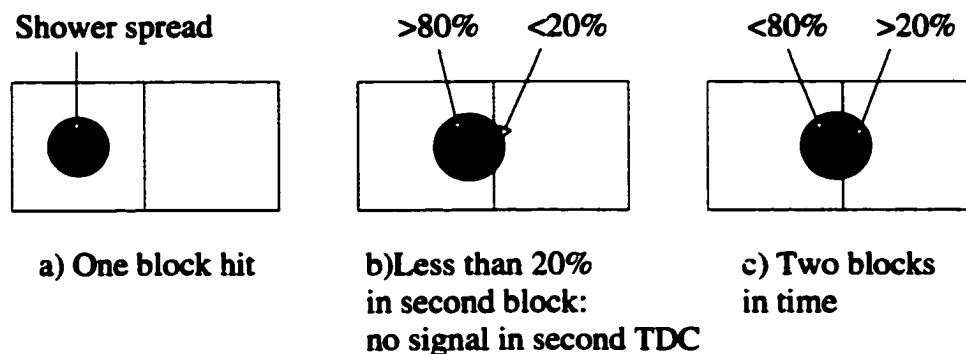
Figure 4.13: Shower spread over one or two blocks of the calorimeter.

More complete shower reconstruction could have been achieved, by using:

- smaller blocks, therefore improving the resolution,

- amplifiers, so that the small energy depositions would still pass the discriminator,

- or by taking into account the ADC signal of the neighbors, even if no TDC signal was recorded for these blocks.

The problem with the last two items is that they are not able to discriminate the small signals from spread showers, and the small signals from background. In fact, the last item was tested on a few runs, and the multiplicity of the clusters is given in Table 4.6. Since this algorithm also requires at least one block to be in time, the

same events were selected, and the result was not improved. Therefore the entire set of data was not reanalyzed this way.

Multiplicity of the cluster		
1	2	≥ 3
47.3%	35.5%	17.2%

Table 4.6: Fraction of events versus multiplicity of cluster in calorimeter, when taking into account the ADC signal in the neighbors of the block in time, for $Q^2 = 5.6$ GeV^2.

Angular correlation

As shown in Table 4.5, the timing cut removes a great part of the background, by rejecting all events without a signal in coincidence with the proton. These events, which are mostly from pion electroproduction, have a scattered electron, and two photons, products of the decay of π^0, somewhere outside the acceptance of the calorimeter. However, some of these π^0-production events might occasionally send a detectable signal in time in the calorimeter. Those contribute to the background under the peak in Fig. 4.10b, and must be rejected also. To discriminate between the elastic events and this background, an angular correlation cut was applied.

The expected position of the elastic scattered electron was calculated from the proton coordinates measured in the left HRS, assuming elastic kinematics. The details of this calculation are in Appendix D. The position of the candidate cluster detected in the calorimeter is assigned at the location of the center (X, Y) of the block if the cluster contains only one block, and at the average position defined as followed if the cluster contains several blocks:

$$x = \frac{\sum_i^{mult} E_i X_i}{\sum_i^{mult} E_i}$$

$$y = \frac{\sum_i^{mult} E_i Y_i}{\sum_i^{mult} E_i} \tag{4.14}$$

where *mult* is the multiplicity of the cluster. For the analysis, this multiplicity is the one defined in Table 4.5, only from timing information. The angular correlation is then made on the plot of the difference between the expected and the measured positions in both directions, which should have an elastic peak centered at ($dx = 0$, $dy = 0$). Figure 4.14 shows such a plot, at $Q^2 = 5.6$ GeV^2. The extent of the elastic peak, about 25 cm in the vertical direction and 15 cm in the horizontal direction, is a combined effect of the resolution of the HRS and the size of the blocks in the calorimeter. The polygon around the elastic peak shows the cut applied to the data.
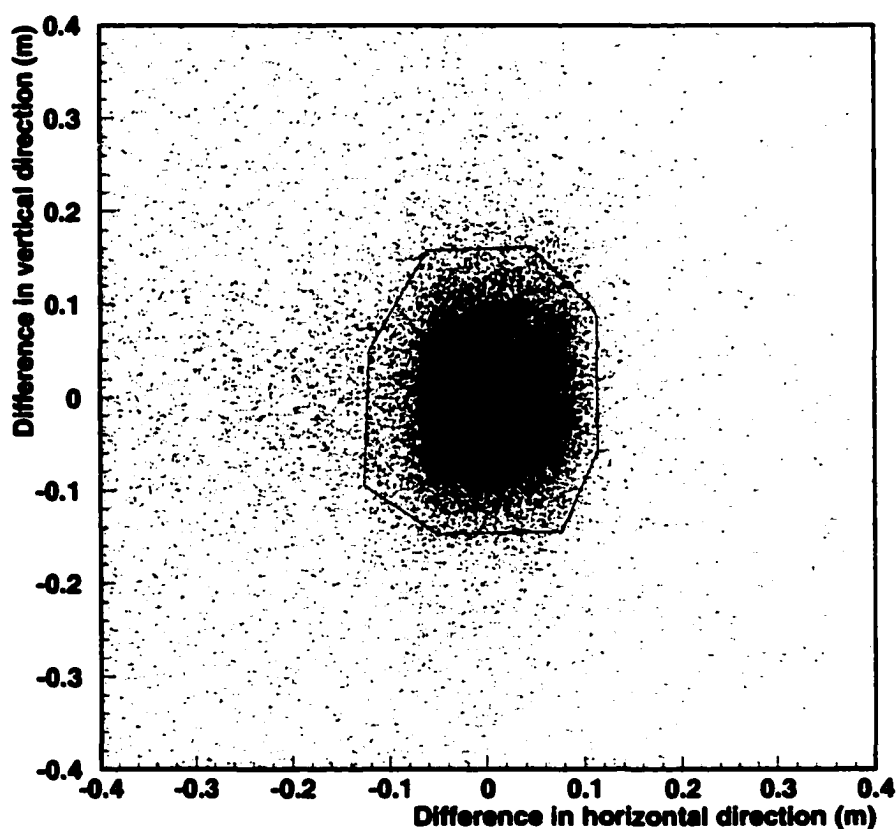
Figure 4.14: Angular correlation between the proton and the calorimeter signal. The differences are between the expected position of the elastic electron and the position of the cluster detected in the calorimeter. The polygon shows the 2D-cut made on the angular correlation.

<u>Energy cut</u>

Figure 4.15 shows the missing energy $E_{miss} = E_{beam} + m - \sqrt{p_p^2 + m^2} - E_{calo}$, after the timing and the angular correlation cuts. The energy resolution is 145 MeV (1σ), or 9%, at $Q^2 = 5.6$ GeV^2. Events at $E_{miss} > 1000$ MeV, corresponding to accidentals under the elastic peak with a small energy deposition in the calorimeter, are rejected.
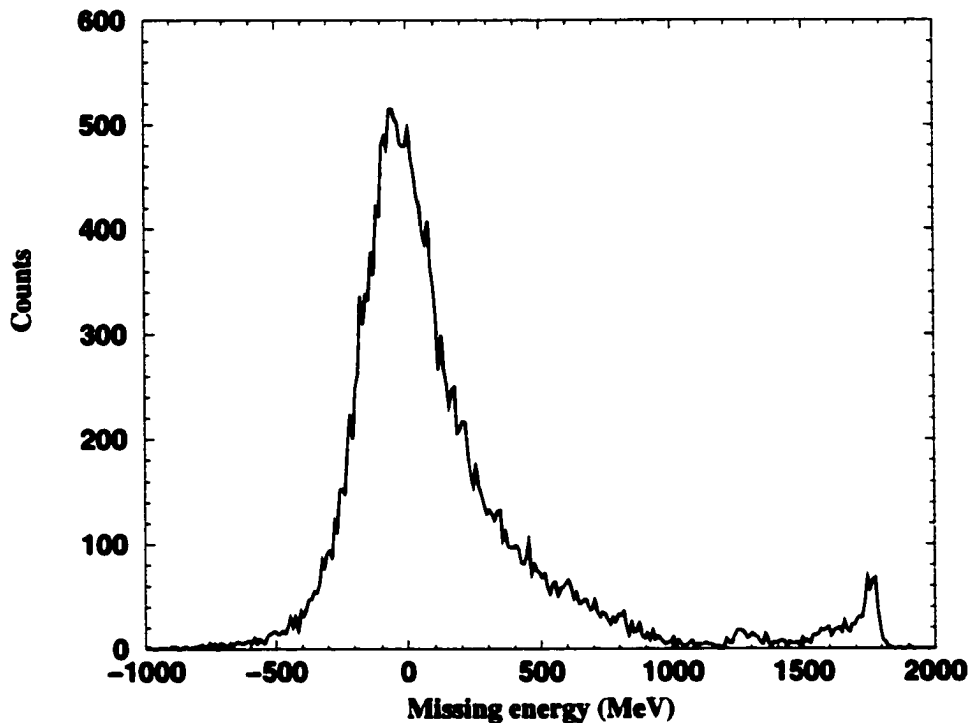
Figure 4.15: Missing energy of the reaction $E_{miss} = E_{beam} + m - \sqrt{p_p^2 + m^2} - E_{calo}$, after timing and position cuts. The energy resolution is 145 MeV, or 9%, at $Q^2 = 5.6$ GeV^2. Events with $E_{miss} > 1000$ MeV are rejected.

4.3.4 Result of selection of elastic events

Figure 4.16 shows how a very good selection of elastic events was achieved by these three software cuts on the calorimeter data. The dashed line represents the rejected data. It shows that most inelastic events have been rejected. The small

bump under the elastic peak shows the ~5% of elastic events that have been omitted by acceptance mismatching, as explained in Section 3.5.2. **This did not affect the result of the experiment, since the goal was to ultimately measure the polarization of elastic protons. Only the statistical uncertainty was affected by this minor loss of events.**
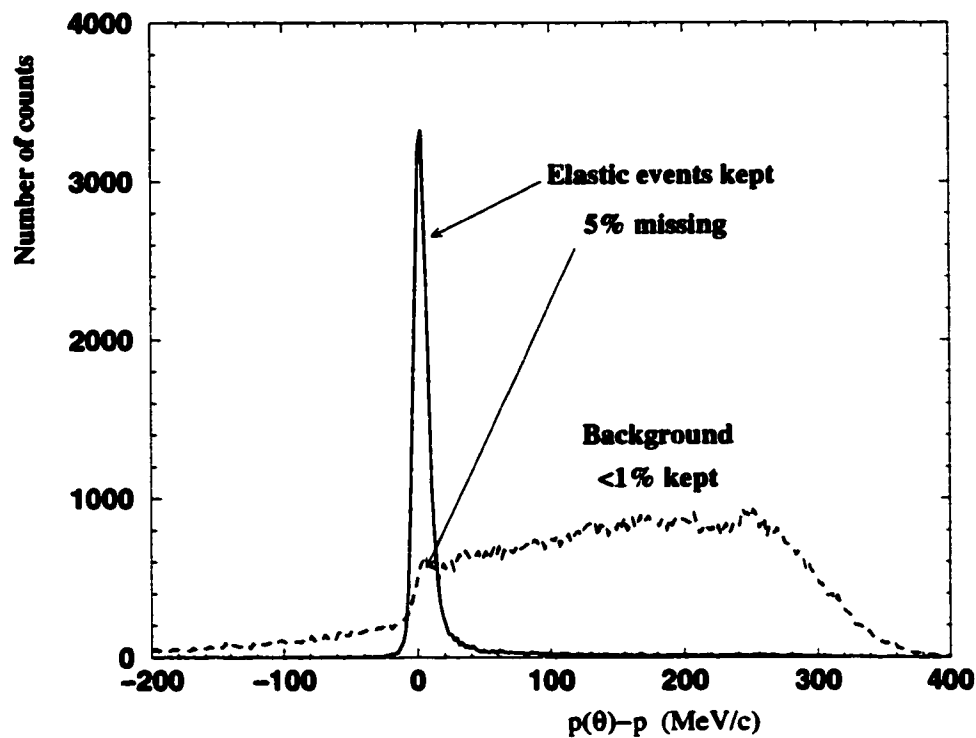
Figure 4.16: Same as Fig. 4.9, separated for events accepted by calorimeter selection (solid line) and rejected (dashed line).

4.3.5 Remaining background estimate

There is an unavoidable number of inelastic events that are accepted: those that happen to be accidentally in time and at the right place in the calorimeter. To evaluate their contribution, the dx vs. dy distribution outside the elastic peak in Fig. 4.14 has been extrapolated to the area under the peak. This is illustrated in Fig. 4.17, where the 2D-plot of Fig. 4.14 is projected on the vertical axis, representing

the difference distribution between the measured and the expected vertical position of the electron in the calorimeter. The dashed line shows this distribution, with the elastic peak centered at zero. The solid line represents the Gaussian extrapolation of the background under this elastic peak. The same extrapolation was also made on the horizontal difference distribution. The combination of the two gives an estimate of the fraction of events passing the angular position cut.
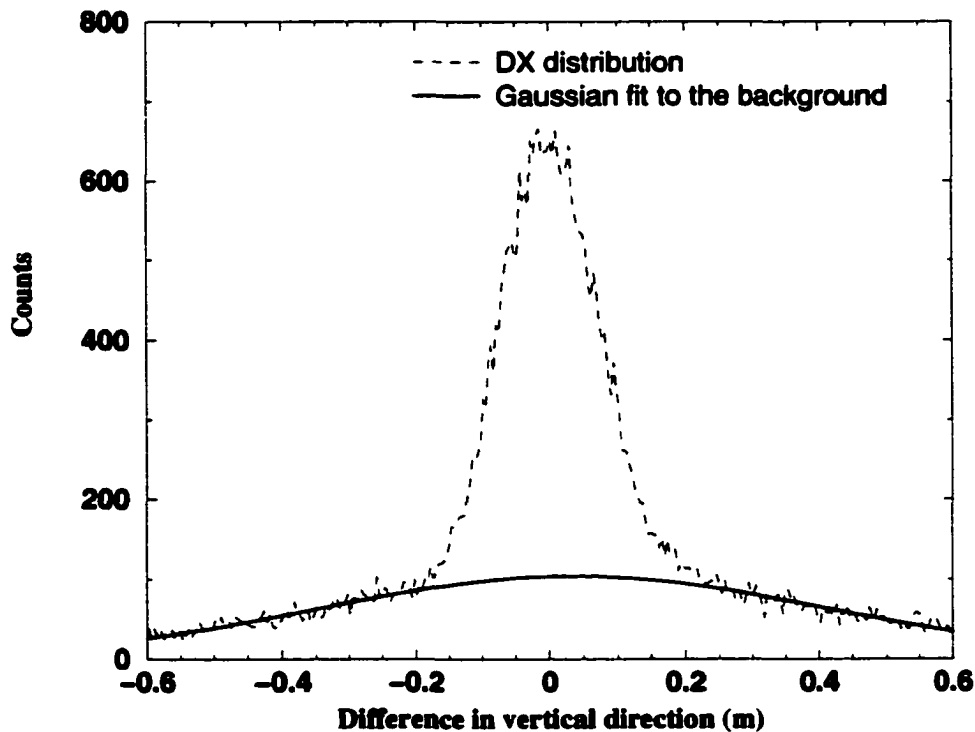
Figure 4.17: Projection on the vertical axis of Fig. 4.14 (dashed line) and Gaussian extrapolation of the background under the elastic peak (solid line). A similar extrapolation is made on the projection in the horizontal direction of Fig. 4.14.

Kinematics	Calo distance (m)	Calo angle	% of inelastic events
4.0 GeV^2	17	34.5°	0.7%
4.8 GeV^2	12.5	42.1°	0.4%
5.6 GeV^2	9	51.4°	1.4%

Table 4.7: Fraction of accepted events that are inelastic.

The fraction of the inelastic events remaining after the cuts is shown in Table 4.7; these events are then taken into account into the polarization analysis, as explained in Section 6.1.2 in Chapter 6.

CHAPTER 5

Analysis II: Extraction of polarization observables

Once elastic recoil protons have been identified, the polarization observables must be calculated to extract the form factor ratio. In this chapter, the distribution of the scattering of the proton in the analyzer of the focal plane polarimeter is analyzed. The code used to model the spin precession through the spectrometer, COSY, is presented. Both informations are then used to extract the components of the transferred polarization, and the form factor ratio.

5.1 Focal plane asymmetries

5.1.1 FPP event reconstruction

All the steps of the reconstruction of the scattering angles of the proton in the analyzer are described in Ref. [90, 96]. There is a total of four steps: identifying the wires that have fired, calculating the drift distances, reconstructing the tracks in the front and rear chambers, and determining the scattering angle. All steps are done in the ESPACE program, the standard Hall A analyzer.

Demultiplexing

As was noted in Section 3.4.3, the signals from the sense wires are multiplexed in groups of eight, to decrease the number of TDCs, by assigning a different pulse width to each straw within the group to identify which wire fired. The TDC signal has then to be demultiplexed in the analysis. The straw group, the leading edge and the trailing edge of the TDC signal are fed into ESPACE, which calculates two time differences: the difference between the trigger signal (that stops the TDC) and

103

the leading edge gives the drift time; the difference between the leading edge and the trailing edge identifies the straw number in the group.

Drift distance calculation

Once the drift time for each wire that fired has been determined. one must convert it into drift distance, which will allow us to reconstruct tracks in the chambers. First an offset is applied to the drift time spectrum, to correct for various delays in the electronics. Except very close to the anode wire, the drift distance is then proportional to the drift time, the longest drift time corresponding to the radius of the straw, 0.522 cm.

Near the anode wire, the electric field becomes strong enough for the secondary electron to ionize another gas atom, starting an avalanche. In this region. the drift velocity increases near the sense wire, and the drift distance is not proportional to the drift time anymore. The drift distance d is obtained from a fifth-order polynomial in drift time t:

$$d = \sum_{n=0}^{5} T(j,n)t^n \qquad (5.1)$$

where $T(j,n)$ are obtained from fitting the integrated drift time spectra for a plane j. These coefficients are all stored in a file read in by ESPACE.

Track reconstruction

Next the code analyzes the tracks in the chambers. Rear and front chambers are analyzed separately, to produce a rear and a front track. For each set of chambers. the u and v directions are also analyzed separately. The x planes in chamber 3 are not used. The first step is to identify hit clusters in the sets of u planes of each chamber. In this set, a cluster can have at most one hit per plane. The process is illustrated in Fig. 5.1, where darker straws have fired. The code looks at the top plane, and finds a hit in 12. It then looks on the second plane at the straws adjacent

to 12. It finds that 21 has fired. 12 and 21 start forming a cluster. It then looks at the third plane, at straws that are adjacent to 21 or 22 because they both are adjacent to 12, even though 22 has not fired). It finds 31, which it includes in the first cluster, since it touches 21, and it also finds 33, which forms another cluster with 12 through 22, even though 22 has not fired). The area around 12 is now all scanned, so the code starts looking at the rest of the first plane. It finds 15, and finds nothing else in this cluster on the next planes.
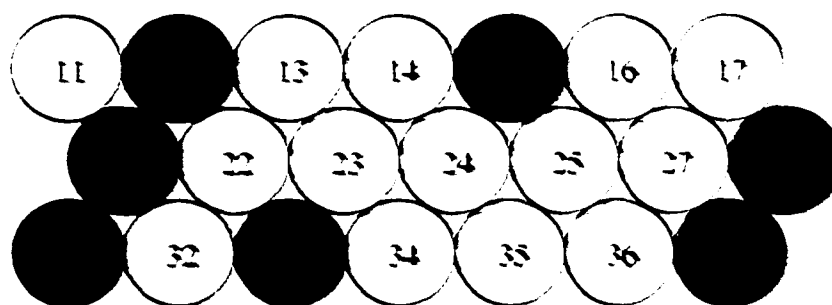
Figure 5.1: Illustration of the procedure to find clusters in a FPP chamber. The three layers represent the three planes (three a planes of chamber 1, for example, and the circle are cross-sectional cuts of the straws.

When the entire first plane has been scanned, it goes to the second plane. 21 is already included in a cluster, so it is discarded. A hit is found at 26, which forms a cluster with 37. When looking at the third plane, no hit is found that is not already included in a cluster, so the procedure is complete. The code has found a total of four clusters: (12,21,31), (12,33), (15) and (26,37).

The same procedure is applied to the second chamber. All combinations of pairs of clusters in both chambers are then considered. For each combination, several tracks are reconstructed, passing left or right of the sense wire of every fired straw, at a distance given by the drift distance (see Fig. 5.2). Straight lines are then fitted, and a χ^2 for each trajectory is calculated. Since it is easier for a cluster with very

few hits to give a very good χ^2, a weight is given to the χ^2 corresponding to the number of hits for the track. The track with the lowest χ^2 is then considered the good track. The procedure is repeated for the v direction.

4 possible tracks
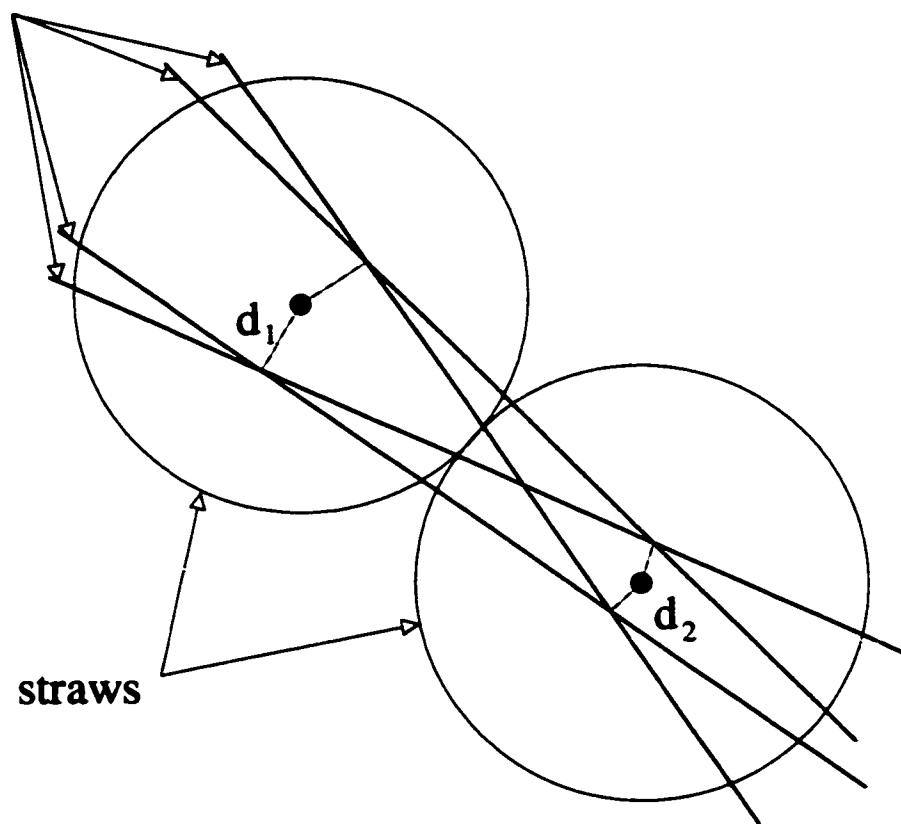
Figure 5.2: Track possibilities in the FPP: for two given straws and two given drift distances d_1 and d_2, four tracks can be reconstructed. The good track is the one with the lowest χ^2 when taking into account all planes of all chambers.

<u>Alignment</u>

To insure that the scattering angle in the analyzer is calculated correctly, the position of the chambers has to be known to the 100 μm level. This is very difficult to obtain from a survey, so we must use a software procedure to get a precise alignment

of the chambers. Several methods are available. The general idea of the one used in this experiment is to rotate the chambers in three dimensions so that trajectories of protons without any analyzer ("straight-throughs") coincide no matter what set of two chambers is used to determine the trajectory, and that these trajectories coincide with the trajectories calculated by the VDCs, using a minimization procedure. The alignment parameters are the offsets u_0, v_0, and z_0, and the rotation angles θ_{zu}, θ_{zv} and θ_{uv} for each chamber. First the position of the wires is determined by:

$$u_{pos} = d_{straw}(i_{straw} - 1) + u_0$$

$$v_{pos} = d_{straw}(i_{straw} - 1) + v_0 \tag{5.2}$$

where d_{straw} is the diameter of the straw and i_{straw} is the straw number in the plane. The code also takes into account that two adjacent planes are shifted by $d_{straw}/2$ with respect to each other (see Fig. 5.1). Second comes a rotation around the u-axis by the angle θ_{zv}:

$$u_1 = u$$

$$v_1 = v \cos \theta_{zv} + z_0 \sin \theta_{zv}$$

$$z_1 = -v \sin \theta_{zv} + z_0 \cos \theta_{zv} \tag{5.3}$$

then a rotation around the v_1-axis by the angle ψ:

$$\tan \psi = \tan \theta_{zu} \tan \theta_{zv}$$

$$u_2 = u_1 \cos \psi - z_1 \sin \psi$$

$$v_2 = v_1$$

$$z_2 = u_1 \sin \psi + z_1 \cos \psi \tag{5.4}$$

and finally a rotation around the z_2-axis by the angle θ_{uv}:

$$u_3 = u_2 \cos \theta_{uv} - v_2 \sin \theta_{uv}$$

$$v_3 = u_2 \sin \theta_{uv} + v_2 \cos \theta_{uv}$$

$$z_3 = z_2 \qquad\qquad (5.5)$$

For this experiment, the alignment procedure was slightly complicated:

- because of the detector configuration of the previous experiment, chamber 2 was not in the stack at the time we took straight-throughs, (the experiment prior to E99-007 did not use the FPP, and chamber 2 was removed to allow for other detectors to be installed)

- because the CH_2 analyzer was not a standard equipment, there was no automatic system to move it in and out of the stack (as there is for the carbon doors), so that the entire stack had to be pulled out before taking straight-throughs to remove the analyzer, and again before taking data to put the analyzer back in.

So straight-throughs were first taken with chambers 1, 3 and 4 in. Chambers 1 and 4 were aligned by comparing a track reconstructed from the two chambers and a VDC track. Chamber 3 could not be aligned at that time, because it was not pinned in place at its final position. After it was later pinned down, it was aligned by comparing a track from chambers 1 and 4, already aligned, and a track from chambers 1 and 3. Then chamber 2 was put in place at the same time as the CH_2. This required to move the detector stack out and back in the hut. The assumption was made that the relative position between the VDCs and chambers 1,3,4 did not change during this movement. Then chamber 2 was aligned by comparing a track from chambers 1 and 2 with a VDC track. Table 5.1 summarizes the alignment procedure.

Chamber(s) $\cdots$	is (are) aligned by comparing a track from $\cdots$	with a track from $\cdots$
1 and 4	chambers 1 and 4	VDC
3	chambers 1 and 3	chambers 1 and 4
2	chambers 1 and 2	VDC

Table 5.1: Summary of the FPP alignment procedure used in this experiment.

Scattering angle calculation

In the angle calculation algorithm, there is no cut applied on the distance between the front and the back track. The distribution of this distance is a normal distribution with a σ of 0.5 cm. Previous analysis show that different cuts on this quantity do not affect the quality of the result.
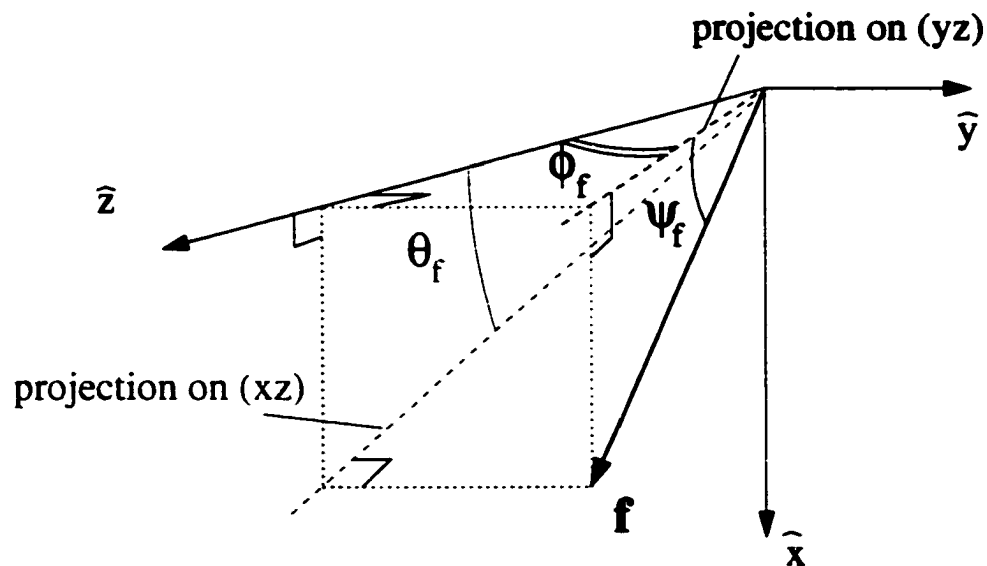
Figure 5.3: Cartesian angles for tracks in the FPP.

Figure 5.3 shows the Cartesian angles for the incident track $\vec{f}$ in the transport coordinate system: $\hat{z}$ is along the spectrometer axis at the focal plane, $\hat{x}$ is downwards perpendicular to $\hat{z}$ in the vertical plane, and $\hat{y} = \hat{z} \times \hat{x}$. θ_f and ϕ_f are the Cartesian angles: θ_f is the angle between the projection of the track on the (xz) plane and the z-axis, and ϕ_f is the angle between the projection on the (yz) plane

and the z-axis. In addition, we define ψ_f as the angle between the track and its projection on the (yz) plane. The relation between the angles is:

$$\tan \psi_f = \tan \theta_f \cos \phi_f \qquad (5.6)$$
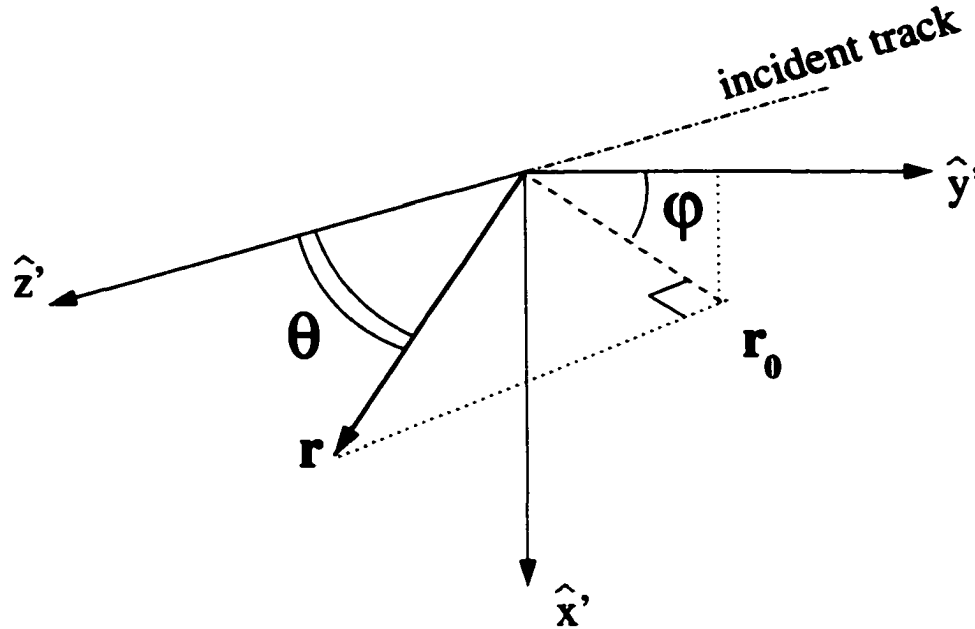
Figure 5.4: Spherical angles of the scattering in the FPP. Asymmetries in azimuthal angle φ are analyzed.

To determine the polar and azimuthal scattering angles, for each event, we must rotate the coordinate system so that its z-axis lies along the momentum of the incident track, and then express the scattered track in this new coordinate system. This rotation can be decomposed into two rotations: the first one is a rotation of the (yz) plane around the x-axis by an angle ϕ_f, and the second one is a rotation by an angle ψ_f so that the new z'-axis lies along the incident track. The new projection of the incident track f is then given by:

$$
\begin{bmatrix} f'_x \\ f'_y \\ f'_z \end{bmatrix} = \begin{bmatrix} 0 \\ 0 \\ 1 \end{bmatrix} = \begin{bmatrix} \cos\psi_f & 0 & -\sin\psi_f \\ 0 & 1 & 0 \\ \sin\psi_f & 0 & \cos\psi_f \end{bmatrix} \begin{bmatrix} 1 & 0 & 0 \\ 0 & \cos\phi_f & -\sin\phi_f \\ 0 & \sin\phi_f & \cos\phi_f \end{bmatrix} \begin{bmatrix} f_x \\ f_y \\ f_z \end{bmatrix} \qquad (5.7)
$$

Similarly, the new projection of the scattered track **r** is now:

$$
\begin{bmatrix} r'_x \\ r'_y \\ r'_z \end{bmatrix} = \begin{bmatrix} \cos\psi_f & 0 & -\sin\psi_f \\ 0 & 1 & 0 \\ \sin\psi_f & 0 & \cos\psi_f \end{bmatrix} \begin{bmatrix} 1 & 0 & 0 \\ 0 & \cos\phi_f & -\sin\phi_f \\ 0 & \sin\phi_f & \cos\phi_f \end{bmatrix} \begin{bmatrix} r_x \\ r_y \\ r_z \end{bmatrix} \qquad (5.8)
$$

We can now define the scattering angles (ϑ, φ), as the spherical angles of the scattered track in this new coordinate system, as shown on Fig. 5.4.
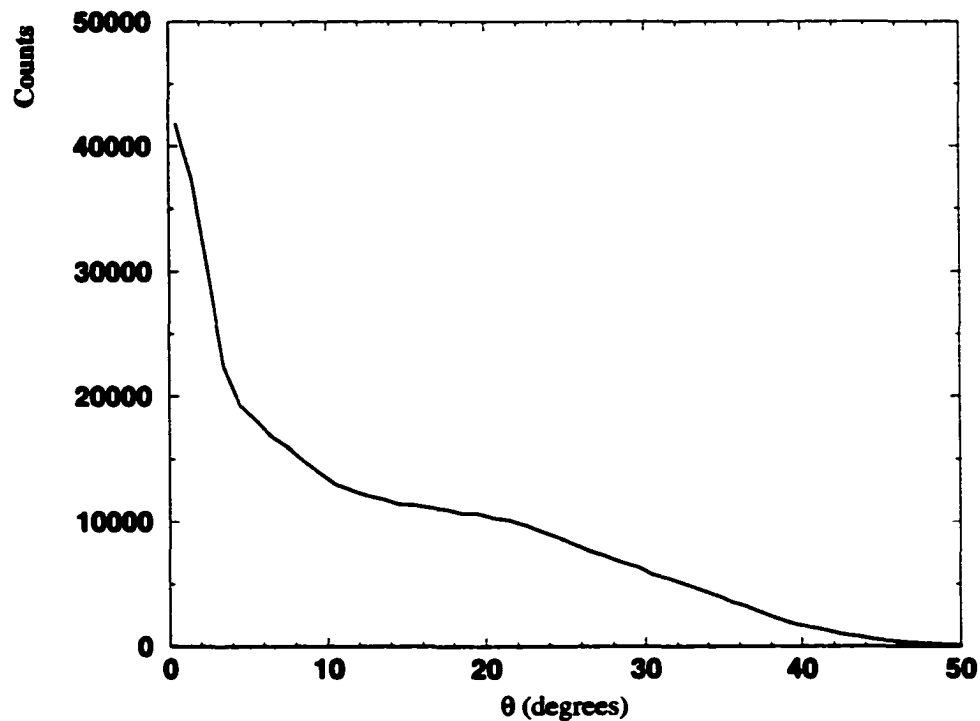
Figure 5.5: ϑ distribution in the FPP at $Q^2 = 5.6$ GeV^2. The peak at small angle is dominated by Coulomb scattering.

If r_0 is the projection of **r** on the $(x'y')$ plane:

$$
r_0^2 = r_x'^2 + r_y'^2 \qquad (5.9)
$$

$$
\vartheta = \tan^{-1}\left(\frac{r_0}{r_z'}\right) \qquad (5.10)
$$

$$\varphi = \tan^{-1}\left(\frac{r'_x}{r'_y}\right) \qquad (5.11)$$
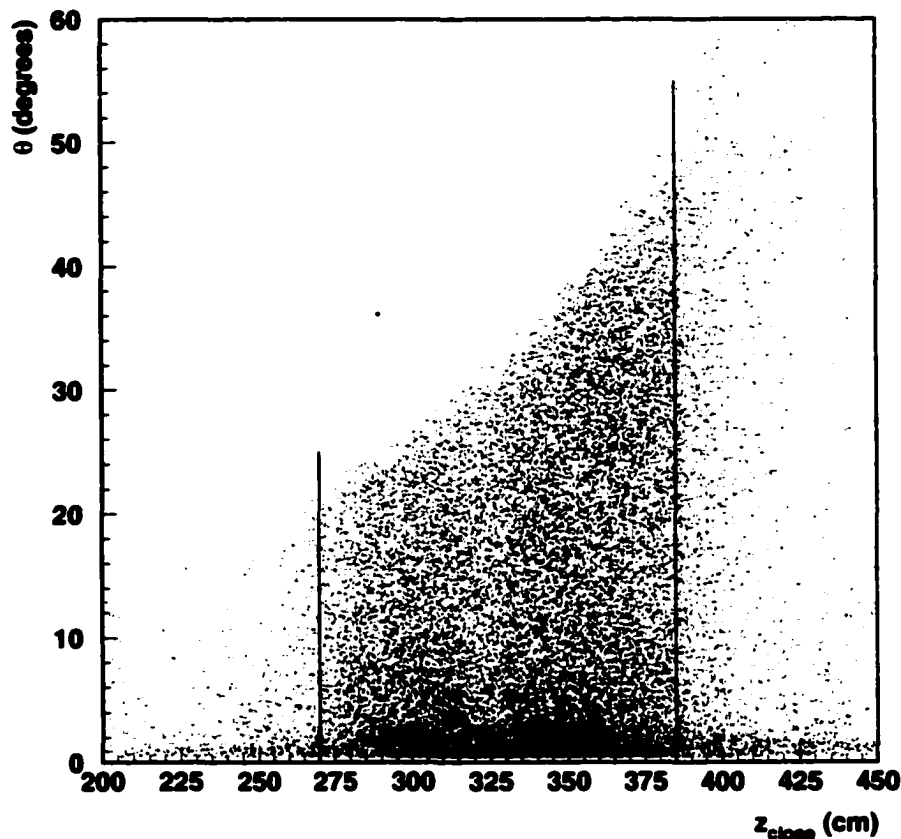
Figure 5.6: z_{close} vs. ϑ at $Q^2 = 5.6$ GeV^2. A cut is made at the edges of the block of CH$_2$.

Figure 5.5 shows the ϑ distribution of the scattering in the analyzer, at $Q^2 = 5.6$ GeV^2, where ϑ is the polar scattering angle of a particle X in the CH$_2(p, X)$ reaction. The last condition for the reconstructed angles to correspond to physical events is to ensure that the position z_{close} along the beam of the reconstructed vertex of the scattering is within the block of analyzer. Figure 5.6 shows the z_{close} position of the vertex versus the scattering angle ϑ. The edges of the CH$_2$ block can easily be seen, as well as the gap between the two analyzer plugs (around $z_{close} = 325$ cm). The "razor blade" shape of the distribution illustrates that large scattering angles

are detected only close to the rear chambers, because of their limited geometrical acceptance. A cut was made on this quantity: 270 cm$<$ z_{close} $<$ 385 cm, where the origin of z_{close} is in the U plane of the first VDC. This cut rejects about 16% of the events in the FPP. These events correspond to extra scattering of the proton in the detectors, including a second scattering in the CH_2 blocks possibly.

5.1.2 Angular distribution

Asymmetries
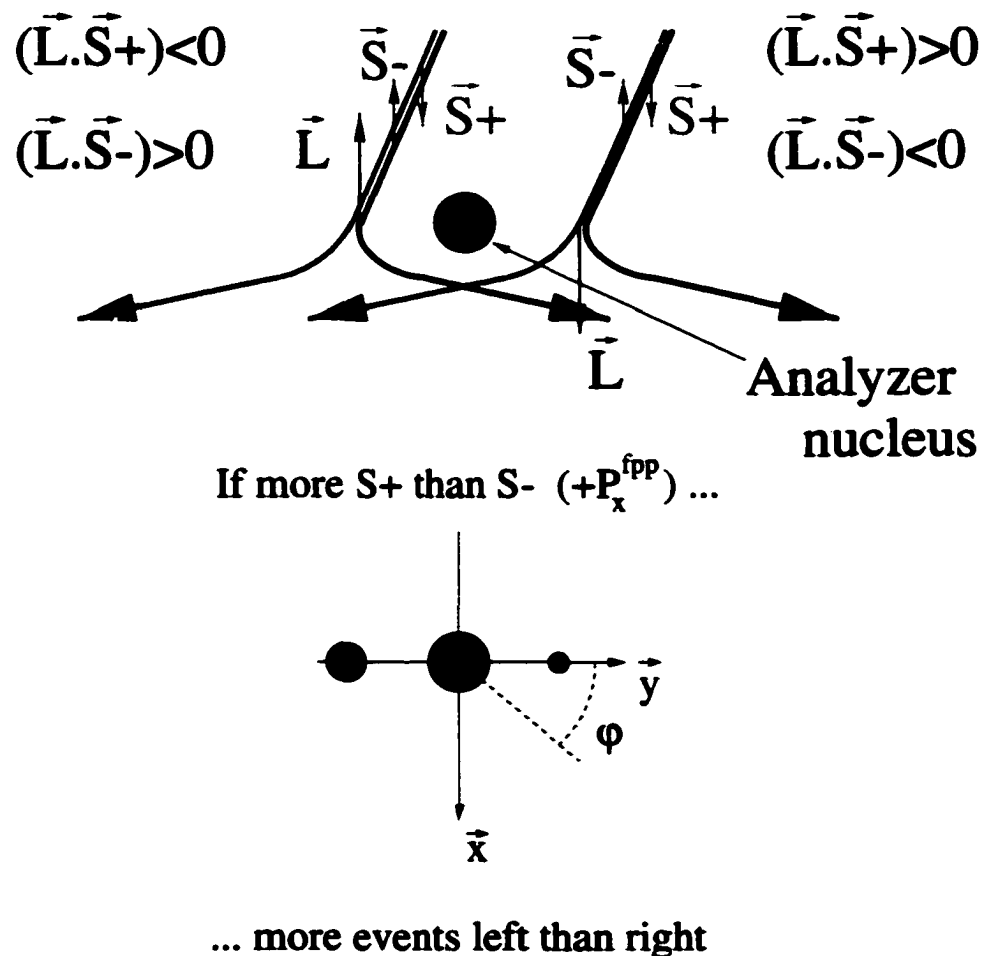
Figure 5.7: Polarimetry principle: a left-right asymmetry is observed if the proton is polarized vertically, as its strong interaction with the analyzer nucleus depends on its spin.

For a polarization measurement, the events of interest are those that have scattered on the analyzer via the strong interaction with a nucleus of an atom of the analyzer. As opposed to the Coulomb scattering, dominant at small angle $\vartheta < 4°$, as shown in Fig. 5.5, the strong interaction is sensitive to the direction of the spin of the incident proton, through a spin-orbit coupling. This is illustrated in Fig. 5.7, showing a left-right asymmetry in the scattering if the proton spin is preferentially up or down. The sign of the force between the incident particle and the analyzer nucleus is governed by the sign of the $\vec{L} \cdot \vec{S}$ scalar product, where $\vec{L}$ is the orbital angular momentum of the proton with respect to the analyzer nucleus, and $\vec{S}$ represents its spin. Therefore, as shown in Fig. 5.7, all particles with spins up are scattered to the left and all particles with spin down are scattered to the right. If there are more particles with spin up than spin down (corresponding to a polarization of the incident particle sample), we will observe an asymmetry in the scattering angle.

A left-right asymmetry corresponds to a polarization component in the vertical direction, P_x^{fpp}, and an up-down asymmetry corresponds to a polarization component in the horizontal direction, P_y^{fpp}. The angular distribution for a large sample of incident protons is then represented by a smooth sinusoidal curve:

$$f^{pol}(\vartheta, \varphi) = \frac{1}{2\pi} \left[1 + A_y(\vartheta, T_p) \left(P_y^{fpp} \sin \varphi - P_x^{fpp} \cos \varphi \right) \right] \qquad (5.12)$$

where $A_y(\vartheta, T_p)$ is the analyzing power of the reaction $A(p, N)X$; it represents the strength of the spin-orbit coupling of the nuclear scattering. Coulomb scattering has no analyzing power, since it involves no such coupling. For strong interaction scattering, this strength represents the sensitivity to the incident particle polarization. The analyzing power depends on the scattering polar angle ϑ and the proton kinetic energy T_p. The relevance of the ϑ dependence of the analyzing power is discussed in Section 5.3.2 at the end of this chapter.

To avoid non-physical asymmetries arising at the edges of the rear chambers due to their limited size, a "cone test" is applied. For a scattering angle ϑ, we ensure that the entire cone of angle ϑ around the incoming track is within the acceptance of the rear chambers. In Fig. 5.8, track 1 passes the cone test, while track 2 fails it and is rejected. This test eliminates 14% of the events. 85% of the rejected events have an angle $\vartheta > 20°$, since small scattering angles are more likely to pass the cone test.
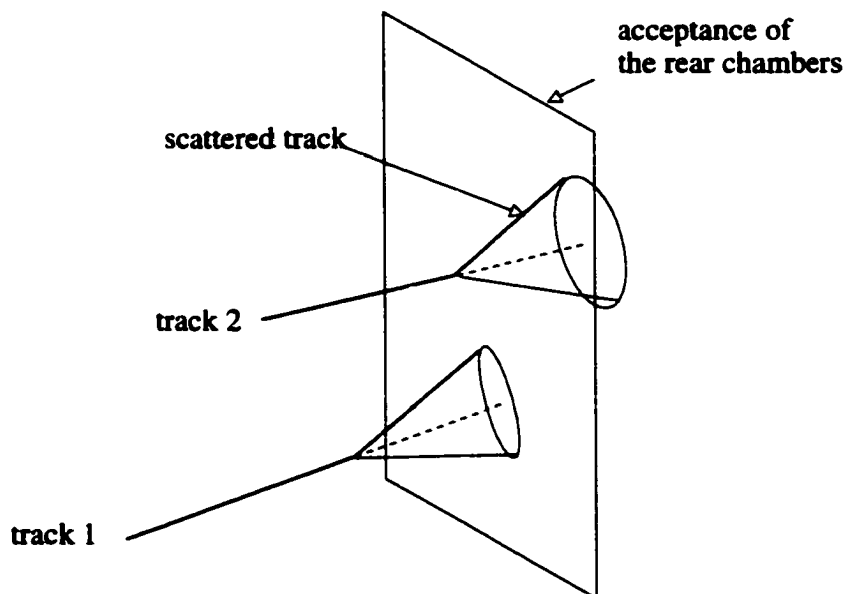
Figure 5.8: Cone test in the FPP. The cone of angle ϑ around track 1 is entirely within the rear chambers acceptance, while the one around track 2 is not.

False asymmetries

Equation 5.12 represents the azimuthal angle distribution in a perfect polarimeter. However, the complexity and size of the focal plane polarimeter introduce some false asymmetries, due to various physical misalignments of the chambers, and possible variations in the efficiency of individual straws. All these false asymmetries,

or instrumental asymmetries, have to be determined experimentally.

Including the false asymmetries, the actual experimental azimutal angle distribution is:

$$f(\vartheta, \varphi) = \frac{1}{2\pi}[1 + (a_0 - A_y P_x^{fpp})\cos\varphi + (b_0 + A_y P_y^{fpp})\sin\varphi$$

$$+ c_0 \cos 2\varphi + d_0 \sin 2\varphi] \qquad (5.13)$$

where (a_0, b_0, c_0, d_0) are parameters determined by fitting the experimental distribution. They are already minimized by the alignment procedure described earlier. These coefficients are measured by using ep elastic scattering. As was explained in Section 1.3.2, there is no induced polarization in elastic scattering. **This way, if we measure the angular distribution of the proton in the analyzer from an unpolarized electron beam, there should be no asymmetry, except for the instrumental ones.**

Two distributions like Eq. 5.13 can be defined separately, $f^+(\vartheta, \varphi)$ and $f^-(\vartheta, \varphi)$ for each of the two beam helicity states. The only contribution to the polarization terms in the distribution is the transferred, helicity-dependent polarization. Therefore, if the number of events and the beam polarization are the same for both helicity states, only the sign of P_x^{fpp} and P_y^{fpp} is different between the two distributions. Therefore if we sum the two distributions, we effectively get an unpolarized sample. and we can directly extract the false asymmetry terms by fitting this sum distribution. An example of the values of these terms are given in Table 5.2, corresponding to $Q^2 = 5.6$ GeV^2.

a_0 (cos φ)	$(-1.60 \pm 0.07) \times 10^{-2}$
b_0 (sin φ)	$(0.19 \pm 0.07) \times 10^{-2}$
c_0 (cos 2φ)	$(-0.69 \pm 0.07) \times 10^{-2}$
d_0 (sin 2φ)	$(0.86 \pm 0.07) \times 10^{-2}$

Table 5.2: False asymmetry terms at $Q^2 = 5.6$ GeV^2.

Difference distribution

If we now take the difference between the two distributions, the false asymmetry terms cancel out, and only the polarization transfer terms remain, which are the quantities of interest. Thus we don't even need to know the false asymmetries. The difference distribution has the simple form:

$$f^{diff}(\vartheta, \varphi) = f^+(\vartheta, \varphi) - f^-(\vartheta, \varphi) = \frac{1}{\pi} \left[A_y \left(P_x^{fpp} \cos \varphi - P_y^{fpp} \sin \varphi \right) \right] \qquad (5.14)$$

This distribution can easily be fitted to extract the polarization at the focal plane. Figure 5.9 shows such a difference distribution, at $Q^2 = 5.6$ GeV^2. The data have been separated in 20 equal bins in φ.
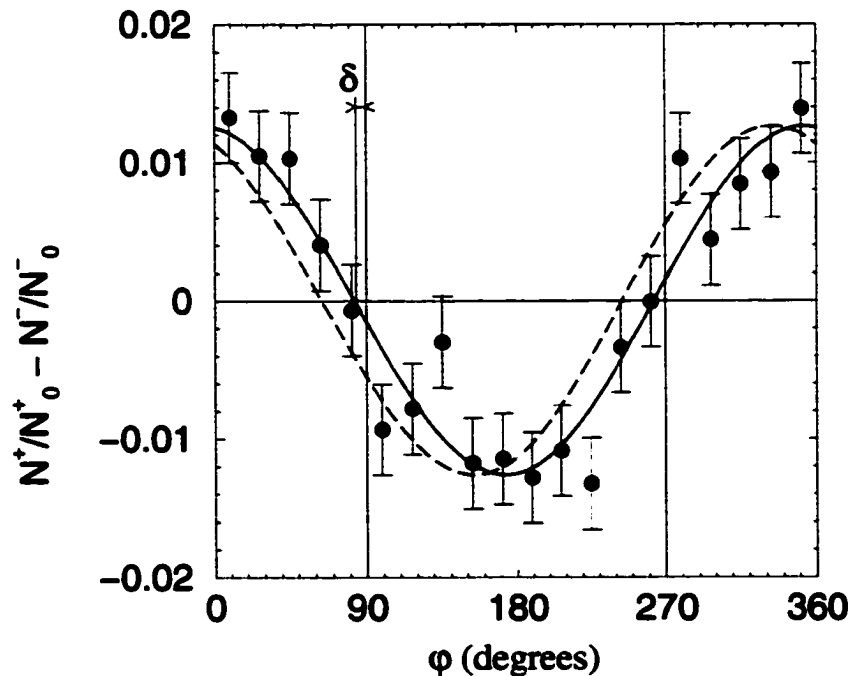
Figure 5.9: Difference distribution between the two helicity states, at $Q^2 = 5.6$ GeV^2. N_0^+ and N_0^- are the number of incoming protons from events with beam helicity positive and negative respectively. The solid curve represents the sinusoidal fit to the data ($\chi^2 = 0.97/$ndf). The dashed line corresponds to the shifted distribution assuming $\mu_p G_{Ep}/G_{Mp} = 1$ ($\chi^2 = 1.85/$ndf). See text for details.

Equation 5.14 can equivalently be rewritten:

$$f^{diff}(\vartheta, \varphi) = C \cos(\varphi + \delta) \qquad (5.15)$$

where:

$$C = \frac{1}{\pi} A_y \sqrt{(P_x^{fpp})^2 + (P_y^{fpp})^2}$$
$$\tan \delta = \frac{P_y^{fpp}}{P_x^{fpp}} \qquad (5.16)$$

In first approximation, P_y^{fpp} is equal to the transverse component at the scattering plane, which is proportional to the product $G_{Ep}G_{Mp}$. P_x^{fpp} being related to G_{Mp}^2, the phase shift δ is a measure of G_{Ep}/G_{Mp}. In Fig. 5.9, the solid curve represents the best sinusoidal fit to the data, with a χ^2 of 0.97 per degree of freedom. As small as it is, the phase shift, of about 7° at this kinematics, illustrates the amplitude of the electric form factor compared to the one of the magnetic form factor, and demonstrates the difficulty to measure it. Also represented in the figure (dashed curve) is a hypothetical distribution assuming $\mu_p G_{Ep}/G_{Mp} = 1$, as predicted by the dipole model. This curve corresponds to a χ^2 value of 1.85 per degree of freedom. The deviation from this curve is a direct evidence of the deviation from the dipole model at high Q^2.

5.2 Spin precession

5.2.1 Precession

The ratio G_{Ep}/G_{Mp} cannot be obtained so simply from the phase shift δ. The relation between the polarization components at the target and at the focal plane is complicated. The proton trajectory is bent in the magnet of the spectrometer, because of the existence of magnetic fields. The spin of the proton is also affected by these magnetic fields, as it precesses around the axis of the field.
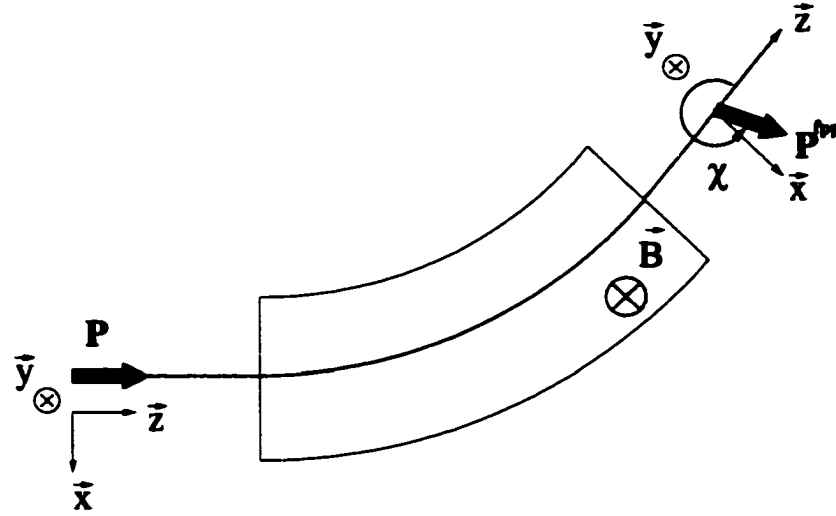
Figure 5.10: Dipole approximation of the model of the spectrometer: the dipole is perfect, with sharp edges and a uniform field.

Dipole approximation

If we first consider that the spectrometer consists only of a single perfect dipole, as shown in Fig. 5.10, then the spin precesses around the transverse field by an angle χ:

$$\chi = \gamma(\mu_p - 1)\Theta_{bend} \tag{5.17}$$

where $\gamma = 1/\sqrt{1-\beta^2}$, and Θ_{bend} is the bending angle of the trajectory, which is 45° for this spectrometer. The relation between the polarization components at the target and at the focal plane are:

$$\begin{pmatrix} P_x^{fpp} \\ P_y^{fpp} \\ P_z^{fpp} \end{pmatrix} = \begin{pmatrix} \cos\chi & 0 & \sin\chi \\ 0 & 1 & 0 \\ -\sin\chi & 0 & \cos\chi \end{pmatrix} \begin{pmatrix} P_x \\ P_y \\ P_z \end{pmatrix} \tag{5.18}$$

Note that the transverse component P_y does not precess, since it is parallel to the magnetic field.

As we have noted earlier, in the case of elastic scattering off a hydrogen target, there is no induced polarization.

$$\mathbf{P}^{ind} = 0 \qquad (5.19)$$

Furthermore, in the single photon exchange approximation of elastic ep scattering, as noted in Section 1.3.2, there is no normal part of the transferred polarization:

$$hP_x^{trans} = 0 \qquad (5.20)$$

Finally, the FPP can measure only the two components perpendicular to the momentum at the focal plane:

$$P_z^{fpp} = unknown \qquad (5.21)$$

So in the present case, Eq. 5.18 reduces to (from now on, $\mathbf{P}^{trans}$ will be noted $\mathbf{P}$):

$$\begin{pmatrix} P_x^{fpp} \\ P_y^{fpp} \end{pmatrix} = \begin{pmatrix} 0 & \sin\chi \\ 1 & 0 \end{pmatrix} \begin{pmatrix} hP_y \\ hP_z \end{pmatrix} \qquad (5.22)$$

Full precession matrix

However, in reality, the magnetic structure of the spectrometer is more complicated than that. The field is not uniform inside the dipole, it is distorted at the entrance and exit faces (fringe fields), and there are three quadrupoles, with field components in both x and y directions. But the matrix that relates the two polarizations is still a rotation matrix, taking the general form:

$$\begin{pmatrix} P_x^{fpp} \\ P_y^{fpp} \end{pmatrix} = \begin{pmatrix} S_{xy} & S_{xz} \\ S_{yy} & S_{yz} \end{pmatrix} \begin{pmatrix} hP_y \\ hP_z \end{pmatrix} \qquad (5.23)$$

The S_{ij} coefficients depend on the trajectory of the proton in the spectrometer: two protons recoiling at different angles at the target don't enter the first quadrupole at the same place, therefore they don't "see" the same magnetic fields along their trajectory, and their precession is different. To calculate those coefficients, a code is

used that models the spectrometer, and determines the fields from the shape of the elements and the currents in the excitation coils. For a given central momentum, the output of the code is a table of the expansion coefficients C_{ij}^{klmnp} of the rotation matrix, and the matrix is finally calculated for each event using the coordinates of the individual protons at the target:

$$S_{ij} = \sum_{k,l,m,n,p} C_{ij}^{klmnp} x^k \theta^l y^m \phi^n \delta^p \qquad (5.24)$$

5.2.2 COSY
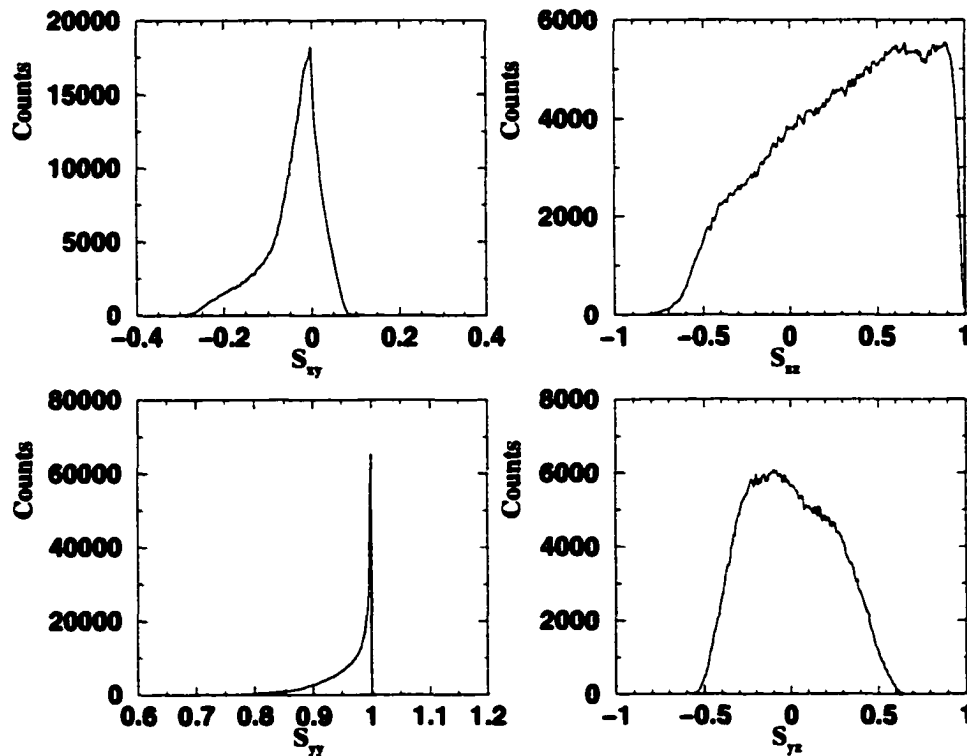
Figure 5.11: Distribution of the four spin transport coefficients of interest at $Q^2 = 5.6 \text{ GeV}^2$, for elastic events.

Several codes are available to calculate the spin precession matrix. In this experiment, as for most Hall A polarization experiments, COSY [97] was used.

COSY is a differential algebra-based code written by M. Berz of Michigan State University, for the simulation, analysis and design of particle optics systems. COSY takes as input the dimensions and positioning of the magnetic elements, such as the diameter of the quadrupoles, the bending angle of the dipole and its shape, $\cdots$, and the central momentum of the protons. An accurate calculation also requires a good description of the dipole fringe fields. The fringe fields were measured at the commissioning of the Hall, and those measurements were fed into COSY. The matrix was computed to order 5. The optical matrix elements generated by the code were compared with the one used by ESPACE as explained in Section 4.2.3. The reconstructed tracks were within 1 mrd of each other for the angles and 2 mm for the positions.

Figure 5.11 shows the distribution of the four coefficients of interest at $Q^2 = 5.6$ GeV^2. Note in particular that the S_{yz} term, which is 0 in the dipole approximation, covers in fact a rather large range at this high momentum. From Eq. 5.23 we have:

$$P_y^{fpp} = S_{yy}hP_y + S_{yz}hP_z \qquad (5.25)$$

In the dipole approximation, the (large) longitudinal component of the polarization at the target hP_z does not contribute to the transverse component at the focal plane P_y^{fpp}, but in fact this "corrective" term is big. This is due to the precession of the spin in the non-dispersive direction in the quadrupoles, which becomes important at high momentum, and is not taken into account in the dipole approximation.

5.2.3 Total rotation

The total rotation $\mathbf{S}$ presented in the previous section relates the polarization in the scattering frame $h\mathbf{P}$ to the polarization in the focal plane frame $\mathbf{P}^{fpp}$. The rotation matrix that COSY calculates is in the transport coordinate system. Therefore $\mathbf{S}$ also includes two small additional rotations, from the scattering plane to the

transport system at the target, and from the transport system to the focal plane frame at the FPP.

From scattering to transport
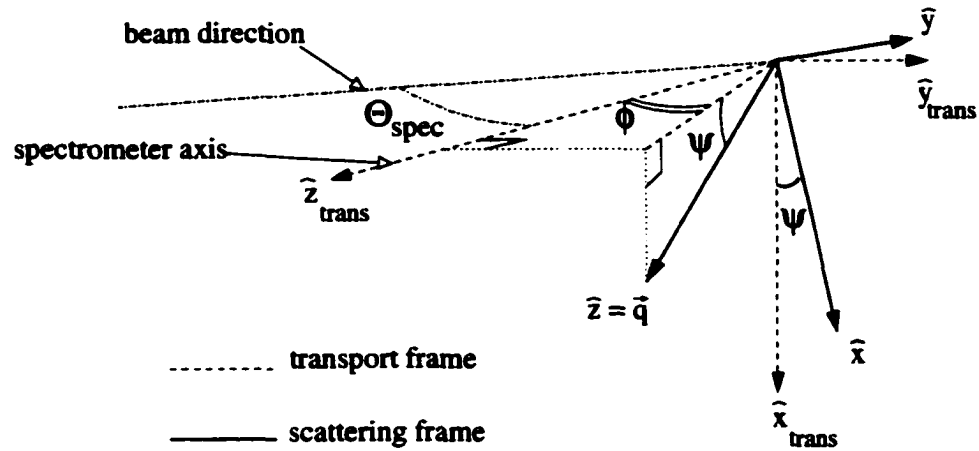
Figure 5.12: The scattering coordinate system (solid lines) is the CS where the polarization must be expressed; the transport coordinate system (dashed lines) is the one in which COSY does the calculation.

The scattering plane is defined as followed:

$$\hat{x} = \frac{\vec{k}_i \times \vec{k}_f}{|\vec{k}_i \times \vec{k}_f|}$$

$$\hat{y} = \hat{z} \times \hat{x} \qquad (5.26)$$

$$\hat{z} = \frac{\vec{k}_i - \vec{k}_f}{|\vec{k}_i - \vec{k}_f|}$$

where $\vec{k}_i$ and $\vec{k}_f$ are vectors along the incident and scattered electron momenta respectively. They must be expressed in the transport coordinate system. In the elastic case, if $\vec{q}$ is the vector along the momentum of the recoil proton:

$$\vec{q} = \vec{k}_i - \vec{k}_f$$

$$\vec{k}_f = \vec{k}_i - \vec{q} \qquad (5.27)$$

so that:

$$\vec{k}_i \times \vec{k}_f = \vec{k}_i \times \vec{k}_i - \vec{k}_i \times \vec{q} = \vec{q} \times \vec{k}_i \qquad (5.28)$$

So in the elastic case, Eq. 5.26 becomes:

$$\hat{x} = \frac{\vec{q} \times \vec{k}_i}{|\vec{q} \times \vec{k}_i|}$$
$$\hat{y} = \hat{z} \times \hat{x} \qquad (5.29)$$
$$\hat{z} = \frac{\vec{q}}{|\vec{q}|}$$

The rotation matrix from the scattering to the transport frame is given by column vectors $(\hat{x}, \hat{y}, \hat{z})$, where $\hat{x}$, $\hat{y}$ and $\hat{z}$ are expressed in the transport frame. For this we need to get $\vec{k}_i$ and $\vec{q}$ in this frame. In the lab frame, $\vec{k}_i$ is along the z-axis. So in the transport frame:

$$\vec{k}_i = \begin{pmatrix} 0 \\ -\sin\Theta_{spec} \\ \cos\Theta_{spec} \end{pmatrix} \qquad (5.30)$$

Let's now express $\vec{q}$ in the transport frame. If we define ψ as the angle between the momentum and its projection on the yz plane, as shown in Fig. 5.12. then $\vec{q}$ in the transport frame is given by:

$$\vec{q} = \begin{pmatrix} \sin\psi \\ \cos\psi\sin\phi \\ \cos\psi\cos\phi \end{pmatrix} \qquad (5.31)$$

The transformation from the scattering frame to the transport frame is then a complicated expression given by Eqs. 5.29, 5.30 and 5.31.

From transport to focal plane

This rotation is a transformation from the fixed transport frame. whose z-axis lies along the spectrometer axis, to a local frame, whose z-axis is along the proton

momentum at the focal plane. If ψ_{fp} is again defined as the angle between the momentum and its projection on the yz plane, the transformation consists of a rotation by an angle ϕ_{fp} around the x-axis, followed by a rotation by an angle ψ_{fp} around the new y-axis, in a way similar to the one shown in Fig. 5.3.

$$
\begin{pmatrix} P_x^{fpp} \\ P_y^{fpp} \\ P_z^{fpp} \end{pmatrix} = \begin{pmatrix} \cos\psi_{fp} & -\sin\psi_{fp}\sin\phi_{fp} & -\sin\psi_{fp}\cos\phi_{fp} \\ 0 & \cos\phi_{fp} & -\sin\phi_{fp} \\ \sin\psi_{fp} & \cos\psi_{fp}\sin\phi_{fp} & \cos\psi_{fp}\cos\phi_{fp} \end{pmatrix} \begin{pmatrix} P_x^{transport} \\ P_y^{transport} \\ P_z^{transport} \end{pmatrix}
$$

$$(5.32)$$

5.3 Extraction of polarization observables

We now need to use all this information (scattering in the analyzer and precession through the spectrometer) to extract the polarization of the recoil proton in the scattering plane. In the elastic case, two components at the focal plane are measured, and we want to calculate two components at the target. It is possible to solve exactly the system of Eq. 5.23. A code has been written for this purpose by G. Quéméner of the Institut des Sciences Nucléaires de Grenoble, France[1], and the method is described in detail in Refs. [98]. However, in the general case of polarization measurements in Hall A, three components at the target have to be extracted out of only two components at the focal plane. Therefore the system can not be solved exactly. Instead, a general polarization code has been written by Steffen Strauch, of George Washington University[2], based on parameter estimates, using a maximum-likelihood procedure. The two methods are equivalent for the elastic scattering reaction. The second one has been used in this experiment, and will be described in this section.

---

[1]at the time at the College of William and Mary
[2]at the time at Rutgers University

5.3.1 Maximum-likelihood technique

Construction of the likelihood function

In a sample of protons with a polarization (P_x^{fpp}, P_y^{fpp}), the probability that a proton i scatters in the analyzer with angles (ϑ_i, φ_i) is given, from Eq. 5.12:

$$F_i(\vartheta_i, \varphi_i) = \frac{1}{2\pi}\left[1 + \left(a_0 - A_y(\vartheta_i)P_x^{fpp}\right)\cos\varphi_i + \left(b_0 + A_y(\vartheta_i)P_y^{fpp}\right)\sin\varphi_i\right] \quad (5.33)$$

where a_0 and b_0 are the $\cos\varphi$ and $\sin\varphi$ terms of the instrumental asymmetries (the higher order terms are neglected: since they do not have a physical asymmetry counterpart, they do not directly affect the polarization measurement). Such a probability can be defined for each proton scattered in the analyzer. We can now express the probability for the experimental angular distribution, as the product of all the individual probabilities:

$$F = \prod_{i=1}^{N_p}\left\{\frac{1}{2\pi}\left[1 + \left(a_0 - A_y(\vartheta_i)P_x^{fpp}\right)\cos\varphi_i + \left(b_0 + A_y(\vartheta_i)P_y^{fpp}\right)\sin\varphi_i\right]\right\} \quad (5.34)$$

Let's now use the spin matrix and Eq. 5.23, to express this probability as a function of the polarization at the target, which is the likelihood function:

$$L(hP_y, hP_z) = \prod_{i=1}^{N_p}\{\frac{1}{2\pi}[1 + (a_0 - \epsilon_i A_y(\vartheta_i)(S_{xy,i}hP_y + S_{xz,i}hP_z))\cos\varphi_i$$
$$+ (b_0 + \epsilon_i A_y(\vartheta_i)(S_{yy,i}hP_y + S_{yz,i}hP_z))\sin\varphi_i]\} \quad (5.35)$$

where N_p is the total number of accepted events, and $\epsilon_i = \pm 1$ represents the sign of the beam polarization for the event i. Note that without losing any generality in the method, we have restricted the demonstration to the elastic case, where there is no induced polarization and no normal component. If we regroup the terms differently, Eq. 5.35 becomes:

$$L(hP_y, hP_z) = \prod_{i=1}^{N_p}\frac{1}{2\pi}(1 + \lambda_{0,i} + \lambda_{y,i}hP_y + \lambda_{z,i}hP_z) \quad (5.36)$$

with:

$$\lambda_{0,i} = a_0 \cos \varphi_i + b_0 \sin \varphi_i$$

$$\lambda_{y,i} = \epsilon_i A_y(\vartheta_i) \left(S_{yy,i} \sin \varphi_i - S_{xy,i} \cos \varphi_i \right) \tag{5.37}$$

$$\lambda_{x,i} = \epsilon_i A_y(\vartheta_i) \left(S_{yz,i} \sin \varphi_i - S_{xz,i} \cos \varphi_i \right)$$

The λ's take the sign of the beam helicity.

Estimation of parameters

In this likelihood function, hP_y and hP_z are parameters, which must be adjusted to maximize the probability function. They must satisfy:

$$\frac{\partial \ln L}{\partial hP_y} = 0$$

$$\frac{\partial \ln L}{\partial hP_z} = 0 \tag{5.38}$$

where the logarithm is taken to transform the product into a sum. The system 5.38 is a system of coupled nonlinear equations, which admits no algebraic solution. However it can be linearized, as demonstrated in Ref. [99], using:

$$\ln(1 + x) = x - \frac{x^2}{2} + o(x^3) \tag{5.39}$$

In this case, Eq. 5.38 becomes, using $x = \lambda_{0,i} + \lambda_{y,i} hP_y + \lambda_{z,i} hP_z$ in Eq. 5.36 and dropping the $o(x^3)$ terms in Eq. 5.39:

$$\begin{pmatrix} \sum_i \lambda_{y,i}(1 - \lambda_{0,i}) \\ \sum_i \lambda_{z,i}(1 - \lambda_{0,i}) \end{pmatrix} = \begin{pmatrix} \sum_i \lambda_{y,i}\lambda_{y,i} & \sum_i \lambda_{y,i}\lambda_{z,i} \\ \sum_i \lambda_{z,i}\lambda_{y,i} & \sum_i \lambda_{z,i}\lambda_{z,i} \end{pmatrix} \begin{pmatrix} hP_y \\ hP_z \end{pmatrix} \tag{5.40}$$

where the λ's depend only on scattering angles, spin matrix coefficients and analyzing power. Note that because of the presence of ϵ_i in $\lambda_{y,i}$ and $\lambda_{z,i}$, the false asymmetries $\lambda_{0,i}$ cancel to first order in the resolution of the system. If we call $\mathbf{B}$

the vector on the left hand-side, and $\mathbf{M}$ the correlation matrix, we have:

$$\mathbf{B} = \mathbf{M} \cdot \begin{pmatrix} hP_y \\ hP_z \end{pmatrix}$$

$$\begin{pmatrix} hP_y \\ hP_z \end{pmatrix} = \mathbf{M}^{-1} \cdot \mathbf{B} \tag{5.41}$$

The statistical error is given by:

$$\Delta(hP_y) = \sqrt{(M^{-1})_{yy}}$$

$$\Delta(hP_z) = \sqrt{(M^{-1})_{zz}} \tag{5.42}$$

and the correlation factor between the two is:

$$\rho = \frac{(M^{-1})_{yz}}{\sqrt{(M^{-1})_{yy}(M^{-1})_{zz}}} \tag{5.43}$$

The ratio of the form factors is then given by:

$$\mu_p \frac{G_{Ep}}{G_{Mp}} = Kr \tag{5.44}$$

where $a = hP_y$, $b = hP_z$ and $r = \frac{a}{b}$ for simplification, and K is the kinematic factor from Eq. 1.70:

$$K = -\mu_p \frac{E_e + E_{e'}}{2m} \tan \frac{\theta_e}{2} \tag{5.45}$$

For the statistical error, we define:

$$\frac{dr}{da} = K\frac{1}{b}$$

$$\frac{dr}{db} = -K\frac{a}{b^2} \tag{5.46}$$

which leads to:

$$\Delta\left(\frac{G_{Ep}}{G_{Mp}}\right) = \sqrt{\left(\frac{dr}{da}\right)^2 (\Delta a)^2 + \left(\frac{dr}{db}\right)^2 (\Delta b)^2 + 2\rho \frac{dr}{da}\Delta a \frac{dr}{db}\Delta b} \tag{5.47}$$

5.3.2 The analyzing power problem

Relevance of the analyzing power

So far, the analyzing power A_y has been treated as if it was known, and actually is required as an input parameter of the code. As noted earlier, it depends only on ϑ and T_p. However, because of the limited range of energies accepted in the spectrometer, we will consider that at a given ϑ, A_y is constant over that range of energy. Therefore, for our purpose, we will consider that the analyzing power depends only on ϑ. In the ideal case, the analyzing power would be known, from calibration or from other data. This experiment used polyethylene for the first time at this energy, and its analyzing power was largely unknown. However, because the result is a ratio of two polarization components that are measured simultaneously, the knowledge of the analyzing power is unnecessary, since it eventually cancels out. In that respect, the values of hP_y and hP_z extracted in Eq. 5.41 may not be the actual values of the transferred polarization. depending on what analyzing power is used an input of the code, but their ratio is really the ratio of the polarization components. As far as the determination of $\mu_p G_{Ep}/G_{Mp}$ is concerned, the value entered for A_y is irrelevant, even though the code is set up in such a way that we have to enter a value.

It is important though to take into account certain properties of the analyzing power, to minimize the error bar. As shown in Eqs. 5.46 and 5.47, the minimum of the error bar is reached when hP_y and hP_z are maxima. Taking the ϑ dependence of the analyzing power into account gives more weight to events scattered at angles corresponding to high analyzing power, leading to large amplitudes, and less weight to events scattered at angles corresponding to low analyzing power, such as small angles dominated by Coulomb scattering, leading to small amplitudes. This ϑ dependence can be known by looking at the ϑ dependence of the asymmetries

at the focal plane. Figure 5.13 shows the $A_y P_y^{fpp}$ distribution as a function of ϑ at $Q^2 = 5.6$ GeV^2. Since P_y^{fpp} is a physical quantity related to the proton, independent of ϑ, only A_y contributes to the ϑ-dependence shown in Fig. 5.13. In the analysis code, the scattering angle ϑ was separated into 12 bins, and each bin was given a value for the analyzing power proportional to the distribution shown in Fig. 5.13.
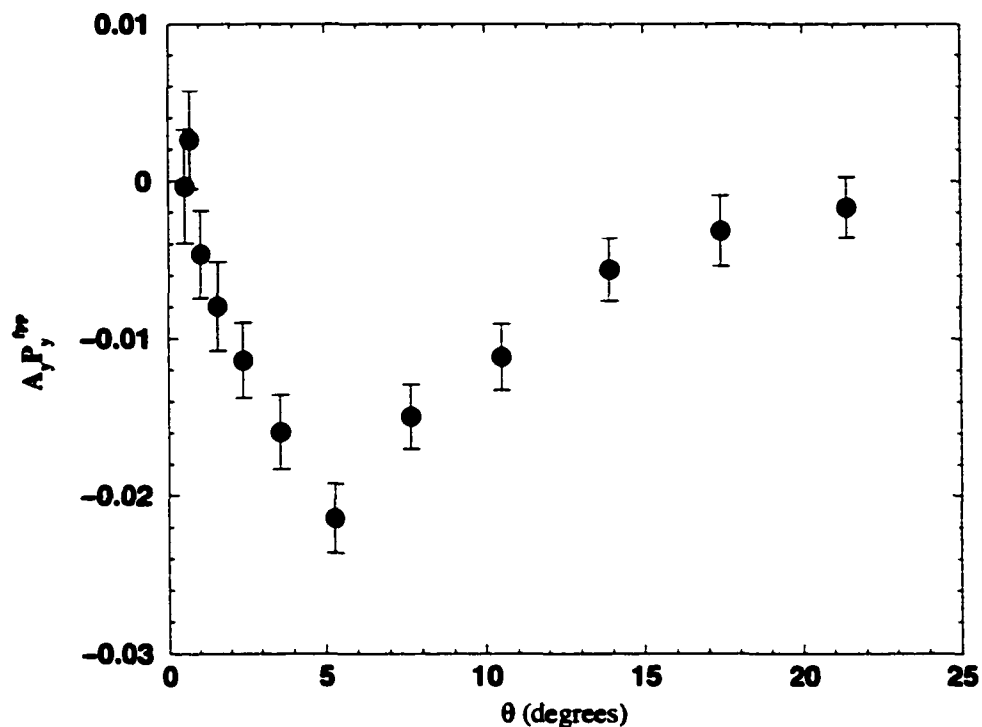
Figure 5.13: ϑ dependence of the amplitude $A_y P_y^{fpp}$ at the focal plane at $Q^2 = 5.6$ GeV^2.

The proportionality factor is not important, since it is only the relative weight of the events that matters. Table 5.3 illustrates the independence of the polarization ratio on the analyzing power value entered as input of the code. It also demonstrates its impact on the statistical error. The ratio is independent of the A_y value, but the error is improved on the second line.

	hP_y	hP_z	hP_y/hP_z
$A_y = 1$	-0.0015 ± 0.0007	0.0249 ± 0.0012	-0.0602 ± 0.0252
$A_y(\vartheta)$	-0.0395 ± 0.0129	0.6491 ± 0.0227	-0.0608 ± 0.0197

Table 5.3: Impact of the analyzing power value entered as input of the code on the polarization ratio and the statistical error. The $Q^2 = 5.6$ GeV^2 data have been analyzed with $A_y = 1$, and with $A_y(\vartheta)$ dependence discussed in the text.

Analyzing power calibration

Even though the absolute value of the analyzing power is irrelevant to the extraction of the form factors ratio, the calibration of this quantity is a byproduct of this type of measurement, and is of great interest for future experiments using the FPP at high momentum. Since we measure two quantities simultaneously, P_z^{fpp} and P_y^{fpp}, two independent variables can be calculated. The first is G_{Ep}/G_{Mp}, and the second is the analyzing power.

First we can note that using Eq. 1.69 that relates the recoil proton polarization components to the proton form factors, we can write the proton polarization components as a function of the form factor ratio only, independent of the beam polarization and the analyzing power:

$$P_y = \frac{-2\sqrt{\tau(1+\tau)}\tan\frac{\theta_e}{2}G_E G_M}{G_E^2 + (\tau/\epsilon)G_M^2} = \frac{-2\sqrt{\tau(1+\tau)}\tan\frac{\theta_e}{2}\frac{G_E}{G_M}}{\left(\frac{G_E}{G_M}\right)^2 + (\tau/\epsilon)}$$

$$P_z = \frac{\frac{E+E'}{m}\sqrt{\tau(1+\tau)}\tan^2\frac{\theta_e}{2}G_M^2}{G_E^2 + (\tau/\epsilon)G_M^2} = \frac{\frac{E+E'}{m}\sqrt{\tau(1+\tau)}\tan^2\frac{\theta_e}{2}}{\left(\frac{G_E}{G_M}\right)^2 + (\tau/\epsilon)} \tag{5.48}$$

If $A_y = 1$ is taken as an input of the code, the output quantity hP_z is really the product hA_yP_z, for each bin of ϑ. Since we know P_z from Eq. 5.48 and G_E/G_M, and h from beam polarization measurement, we can easily extract A_y. The tedious algebra leads to:

$$A_y = \alpha\frac{a^2}{b} + \beta b$$

$$\Delta A_y = \sqrt{\left(\frac{dA_y}{da}\right)^2 (\Delta a)^2 + \left(\frac{dA_y}{db}\right)^2 (\Delta b)^2 + 2\rho\frac{dA_y}{da}\Delta a\frac{dA_y}{db}\Delta b} \tag{5.49}$$

with:

$$\frac{dA_y}{da} = 2\alpha\frac{a}{b}$$

$$\frac{dA_y}{db} = -\alpha\left(\frac{a}{b}\right)^2 + \beta \tag{5.50}$$

and:

$$\alpha = \frac{E_e + E_{e'}}{h4m\sqrt{\tau(1+\tau)}}$$

$$\beta = \frac{\tau\left[1 + 2(1+\tau)\tan^2\left(\frac{\theta_e}{2}\right)\right]}{h\frac{E_e+E_{e'}}{m}\sqrt{\tau(1+\tau)}\tan^2\left(\frac{\theta_e}{2}\right)} \tag{5.51}$$

ρ is defined in Eq. 5.43, and, again, $a = hA_yP_y$ and $b = hA_yP_z$ are the output of the code, with $A_y = 1$ as input. Note that the calibration of the analyzing power requires the knowledge of the beam polarization h. The results of this calibration are given in Section 6.1.1 in the next chapter.

CHAPTER 6

Results

The results of the analysis described in Chapter 5 are presented, including a discussion of the statistical errors, the radiative effects and the systematic errors.

6.1 Results

6.1.1 Statistical uncertainties

The statistical uncertainty on the ratio $\mu_p G_{Ep}/G_{Mp}$ is the result of the propagation of the uncertainty on the amplitude of the asymmetries at the focal plane $A_y P_x^{fpp}$ and $A_y P_y^{fpp}$, which are directly proportional to the number N of events that contribute to the amplitude, i.e events for which we can reconstruct a track, and which have scattered via the strong interaction in the analyzer.

$$\Delta(A_y P_x^{fpp}) = \Delta(A_y P_y^{fpp}) = \sqrt{\frac{2}{N}} \qquad (6.1)$$

This number takes into account the efficiency of the polarimeter. First there might be some inefficiencies in the straws of the chambers. Second, the chambers do not detect neutrons, which can be ejected from the analyzer nucleus when the incoming proton interacts with it. At a given scattering angle ϑ, we can define the efficiency of the chamber as:

$$\epsilon(\vartheta) = \frac{N_{eff}(\vartheta)}{N_0} \qquad (6.2)$$

where N_0 is the number of incoming protons, and $N_{eff}(\vartheta)$ is the number of outgoing tracks that passed the cone test and scattered with a polar angle ϑ. $N_{eff}(\vartheta) = N_0 \epsilon(\vartheta)$ is the effective number of events which participate in the measurement of

133

the asymmetry. Not all of these events actually contribute to the asymmetry: only those interacting via strong interactions do. Furthermore, their sensitivity to the spin-orbit coupling of the nuclear interaction varies depending on the scattering angle. Therefore, the effective number of events has to be multiplied by the square of the analyzing power, $A_y^2(\vartheta)$. We can then write the number of contributing events at the angle (ϑ):

$$N(\vartheta) = N_0 \epsilon(\vartheta) A_y^2(\vartheta) \tag{6.3}$$

The total number of contributing events is obtained by integrating over the angle (ϑ):

$$N = N_0 \int_{\vartheta_{min}}^{\vartheta_{max}} \epsilon(\vartheta) A_y^2(\vartheta) d\vartheta = N_0 \cdot \text{COM} \tag{6.4}$$

The quantity:

$$\text{COM} = \int_{\vartheta_{min}}^{\vartheta_{max}} \epsilon(\vartheta) A_y^2(\vartheta) d\vartheta \tag{6.5}$$

is called the coefficient of merit and is a characteristic of the polarimeter. It is related to the statistical uncertainty via:

$$\Delta(A_y P_x^{fpp}) = \Delta(A_y P_y^{fpp}) = \sqrt{\frac{2}{N}} = \sqrt{\frac{2}{N_0 \text{COM}}} \tag{6.6}$$

FPP efficiency

Figure 6.1 shows the differential efficiency of the polarimeter at the four different kinematics of this experiment. The three curves at high energy show a saturation in energy, corresponding to a total $p(CH_2,p)X$ cross section energy independent above 2 GeV/c. However, the curve at the lowest kinetic energy is lower than the others, because for this point a thickness of only 58 cm was used, therefore lowering the efficiency.
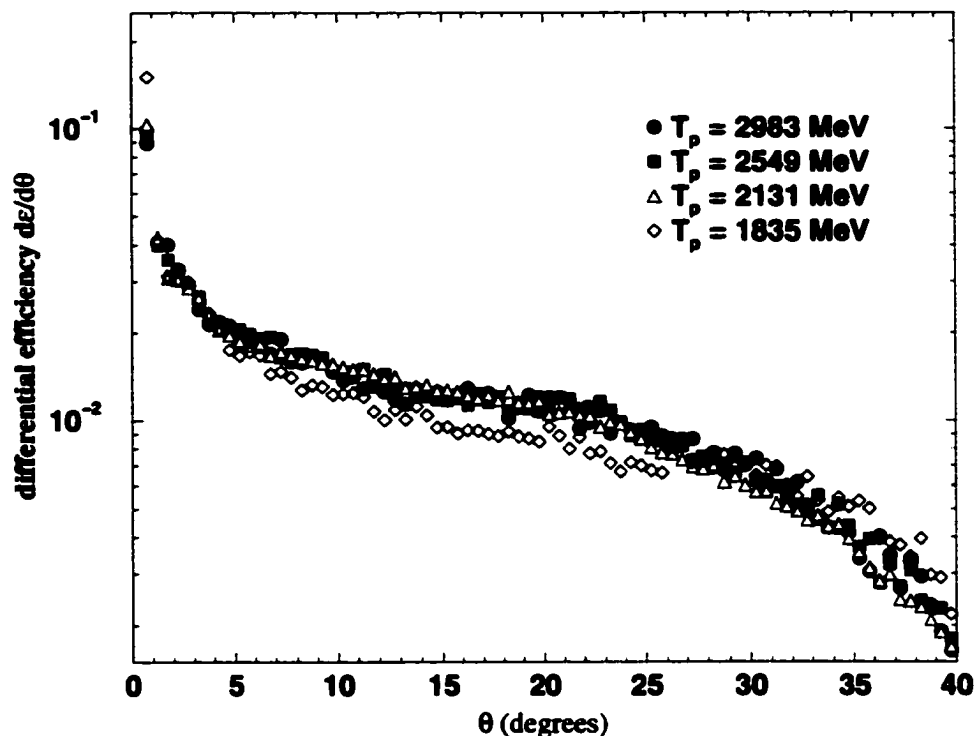
Figure 6.1: Differential efficiency of the FPP at the four kinetic energies of the experiment.

Analyzing power

The analyzing power was measured, as described in Section 5.3.2. The beam polarization h used in this calibration is the value measured by the Compton polarimeter, averaged over three periods: a value of $|h| = 0.71$ for the data taken in November, $|h| = 0.74$ for data taken in December at $Q^2 = 5.6$ GeV^2, and $|h| = 0.71$ for the data taken in December at $Q^2 = 4.8$ GeV^2. The results are reported in Fig. 6.2. As expected, the shape of the analyzing power is similar to the shape of the $A_y P_y^{fpp}$ in Fig. 5.13, since only the analyzing power contributes to the ϑ dependence (the difference in the sign comes from $P_y^{fpp} < 0$). The analyzing power peaks around 6 to 8°, and decreases rapidly at very small angles and angles larger than 25°. In the analysis, angles below 0.5° were rejected, because this approximately corresponds to the resolution of the reconstruction of the scattering angle. Events between 0.5 and 4° were kept, even though this region is mostly dominated

by Coulomb scattering: including these Coulomb events, with no analyzing power, does not affect the result, and allows to keep the increasing proportion of nuclear scattering events with significant analyzing power. The dependence of the analyzing power upon the proton kinetic energy is less important than the one observed for Carbon at lower energy [98].
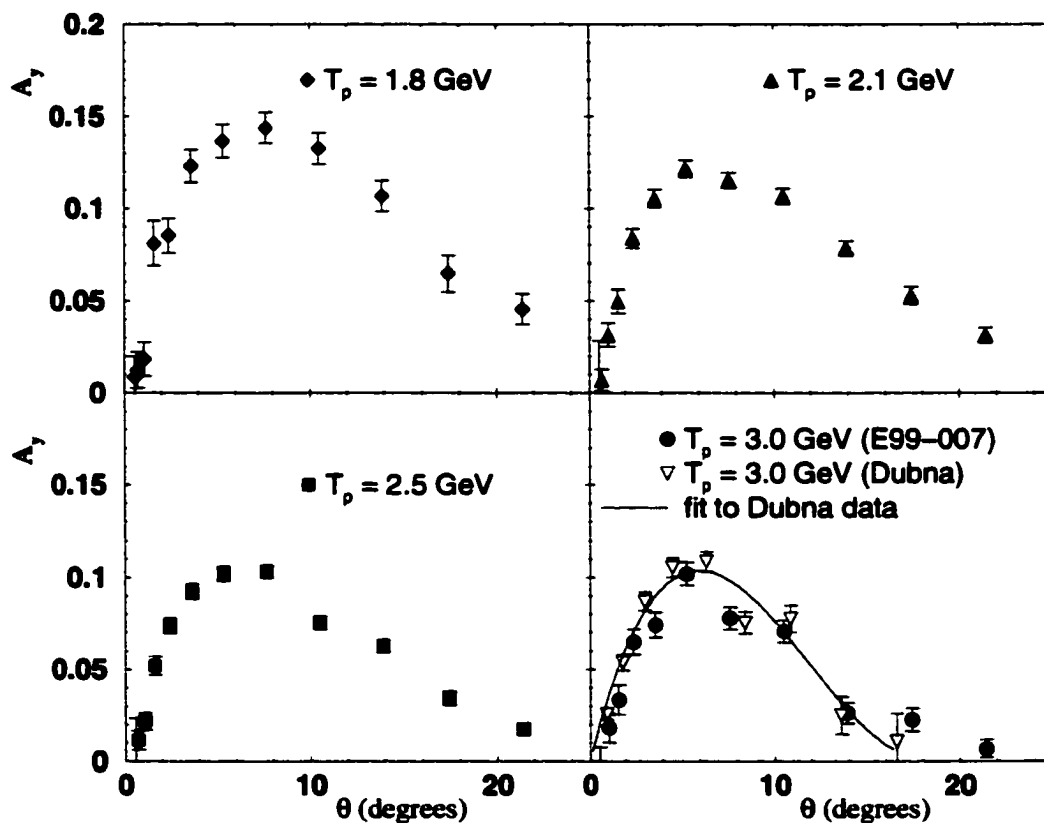
Figure 6.2: Angular distribution of the analyzing power of CH_2 at the four kinetic energies of the experiment. At the highest energy, the data are compared with a calibration run at Dubna.

The highest Q^2 data from this experiment are compared with preliminary results of a analyzing power calibration run at the Dubna Synchrophasotron in June and October 2001, with a proton beam of known polarization. The results presented here for this calibration run are averaged over different thicknesses of analyzer, rang-

ing from 40 to 85 cm. The analyzing power dependence on the CH_2 thickness was very small.

Figure of merit

The coefficient of merit of the polarimeter is calculated for all four kinematics from the data presented in Fig. 6.1 and 6.2, from Eq. 6.5. It is presented in Table 6.1. It shows the rather poor sensitivity of a polarimeter to the polarization of the incoming proton sample. This is why polarization experiments require so much statistics and beam time.

Q^2 (GeV^2)	T_p (MeV)	CH_2 thickness (cm)	COM
3.5	1835	58	$(3.6 \pm 0.6) \times 10^{-3}$
4.0	2131	100	$(2.9 \pm 0.3) \times 10^{-3}$
4.8	2549	100	$(2.0 \pm 0.2) \times 10^{-3}$
5.6	2983	100	$(1.9 \pm 0.2) \times 10^{-3}$

Table 6.1: Coefficient of merit (COM) of the FPP for the experiment.

6.1.2 Polarization results

This section describes the results for the polarization analysis. First it presents the output of the analysis code hP_y and hP_z, computed with analyzing power input from Fig. 6.2. Then it describes the correction to the polarization due to inelastic background, and gives the final corrected result.

Raw results

The results of the polarization analysis at the target are given in Table 6.2, with their statistical error, where the last column is proportional to the ratio $\mu_p G_{Ep}/G_{Mp}$, according to Eq. 1.70. The polarizations given in Table 6.2 are the overall polar-

izations of the accepted data, including the inelastic background discussed in Section 4.3.5.

Q^2 (GeV^2)	hP_y	hP_z	$\frac{hP_y}{hP_z}$
3.5	-0.0843 ± 0.0104	0.4407 ± 0.0125	-0.1914 ± 0.0241
4.0	-0.0717 ± 0.0077	0.4860 ± 0.0081	-0.1474 ± 0.0160
4.8	-0.0596 ± 0.0083	0.5931 ± 0.0098	-0.1005 ± 0.0140
5.6	-0.0395 ± 0.0129	0.6491 ± 0.0227	-0.0608 ± 0.0197

Table 6.2: Polarization transfer results with statistical uncertainties, at the target.

Inelastic background

A correction has to be made to the ratio hP_y/hP_z given in Table 6.2. Since the polarization of background events is different from the polarization of elastic events, its contribution must be evaluated, and the ratio must be corrected for it. To achieve this, the polarization of the rejected events (protons that don't have an electron detected where expected) was obtained. The assumption was made that this polarization was independent of the position of the undetected particle, so that the polarization of the background under the elastic peak was the same as the polarization of rejected events. The corrected polarization is then calculated using:

$$N_{cor} = N_{obs} - N_{inel}$$

$$N_{cor}hP_{y,cor} = N_{obs}hP_{y,obs} - N_{inel}hP_{y,inel}$$

$$N_{cor}hP_{z,cor} = N_{obs}hP_{z,obs} - N_{inel}hP_{z,inel} \tag{6.7}$$

where obs corresponds to the total number of events within the calorimeter cuts (polarizations shown in Table 6.2), cor stands for the corrected polarizations and inel for the inelastic background. The fraction of inelastic events N_{inel}/N_{obs} was given in Table 4.7 in Section 4.3.5.

Table 6.3 presents the polarization of the background and the corrected polarization.

Q^2 (GeV^2)	$hP_{y,obs}$	$hP_{y,inel}$	$hP_{y,cor}$	$hP_{z,obs}$	$hP_{z,inel}$	$hP_{z,cor}$
4.0	-0.0717	0.0135	-0.0723	0.4860	0.3026	0.4872
4.8	-0.0596	0.0908	-0.0602	0.5931	0.3227	0.5942
5.6	-0.0395	0.1141	-0.0417	0.6491	0.3480	0.6534

Table 6.3: Value of hP for inelastic background, and corrected values.

This leads to a correction on the ratio of 0.6% at 4.0 GeV^2, 0.8% at 4.8 GeV^2 and 4.8% at 5.6 GeV^2. Because this estimation of the background contribution relies on several assumptions, such as the uniformity of the background polarization, or the extrapolation of the inelastic population under the elastic peak, only half the correction was applied to the ratio, with a 100% uncertainty that was included in the systematic uncertainties. The corrected ratio is given in Table 6.4.

Q^2 (GeV^2)	$\mu_p G_{Ep}/G_{Mp}$ ± stat. ± inel. err.
3.5	0.571 ± 0.072
4.0	0.481 ± 0.052 ± 0.002
4.8	0.379 ± 0.053 ± 0.002
5.6	0.275 ± 0.087 ± 0.007

Table 6.4: $\mu_p G_{Ep}/G_{Mp}$ results with statistical uncertainties, including the correction due to the inelastic background and its error.

Transferred polarization

From the ratio $r = \mu_p G_{Ep}/G_{Mp}$, we can calculate the transferred polarization components, from Eq. 5.48:

$$P_y = \frac{-2\sqrt{\tau(1+\tau)}\tan\left(\frac{\theta_e}{2}\right) r}{r^2 + \tau\left[1 + 2(1+\tau)\tan^2\left(\frac{\theta_e}{2}\right)\right]}$$

$$P_z = \frac{\frac{E_e+E_{e'}}{m}\sqrt{\tau(1+\tau)}\tan^2\left(\frac{\theta_e}{2}\right)}{\tau^2+\tau\left[1+2(1+\tau)\tan^2\left(\frac{\theta_e}{2}\right)\right]}$$ (6.8)

The results are reported in Table 6.5. Not that this result is completely independent of the beam polarization and the analyzing power. It is directly extracted from the form factor ratio.

Q^2 (GeV^2)	P_y	P_z
3.5	-0.1179 ± 0.0139	0.6162 ± 0.0049
4.0	-0.1016 ± 0.0106	0.6894 ± 0.0027
4.8	-0.0801 ± 0.0110	0.7969 ± 0.0018
5.6	-0.0537 ± 0.0173	0.8833 ± 0.0015

Table 6.5: Physical transferred polarization results calculated from the ratio $\mu_p G_{Ep}/G_{Mp}$, with statistical uncertainties.

6.2 Radiative corrections
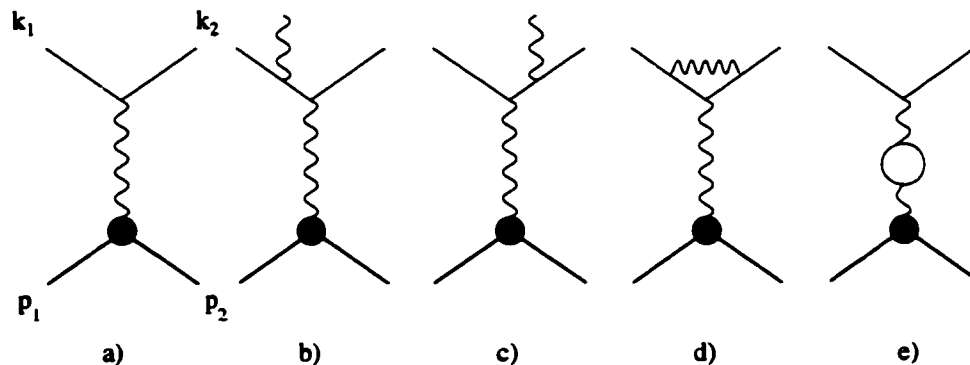
Figure 6.3: Feynman diagrams contribution to the Born and the radiative corrections cross sections. a) elastic scattering; b) and c) radiative processes; d) additional photon exchange; e) vacuum polarization.

No radiative corrections have been applied to the ratio presented here. The reason is that no full calculation exists of polarization observables in ep scattering.

An important contribution, that includes the one-photon exchange radiative corrections shown in Fig. 6.3, has been made by A. Afanasev *et al.* [100]. They calculate radiative corrections to asymmetries of elastic ep scattering for experiments in which events are selected entirely on the basis of the hadronic kinematics. In particular, $Q^2 = -(p_2 - p_1)^2$, where p_2 and p_1 are the final and initial proton 4-momenta respectively, does not depend on the photon momentum, so that the integration over this photon momentum (required to get to G_{Ep} and G_{Mp} which depend only on Q^2) can be performed analytically. Figure 6.3 shows the diagrams that have been calculated. The relative correction on the polarization ratio is no bigger than 1% .

Other contributions are model dependent and can not be uniquely calculated. First is the virtual Compton scattering on the proton [101], which is driven by the amplitude of the process $\gamma^* + p \to \gamma + p$ with very complicated spin structure and with different mechanisms, such as pion exchange in t-channel and Δ exchange in s-channel, as shown in Fig. 6.4. The corresponding relative correction to the polarization ratio is estimated at the 1-3% level. Contributions from two-photon exchange are also model dependent, as they rely on the structure of the hadron. These processes generate an induced (helicity-independent) normal component. They are also expected to modify the ratio by 1-2% [102].
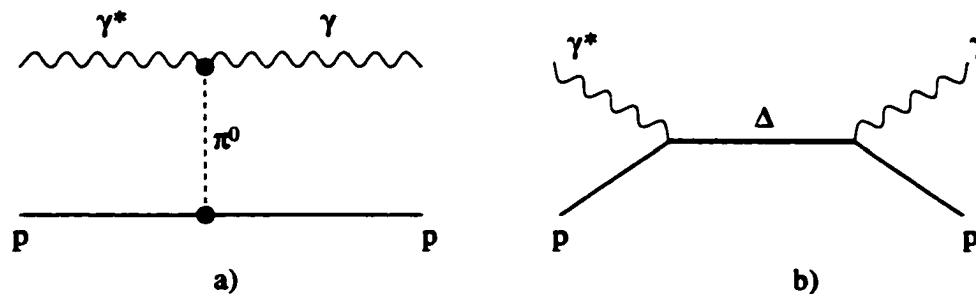
Figure 6.4: Examples of mechanism for $\gamma^* + p \to \gamma + p$: a) pion exchange in t-channel b) Δ exchange in s-channel.

6.3 Systematic errors

As we have seen earlier, measuring transfer polarization in the FPP eliminates false asymmetries in the scattering of the proton in the analyzer, which could be sources of uncertainties. Also measuring simultaneously the two polarization components and taking their ratio, cancel most systematic errors one has to deal with when measuring Rosenbluth cross-sections and changing the angles of the detectors and the beam energy. The biggest source of systematic error in this experiment is in the precession of the spin in the spectrometer. Smaller contributions from uncertainties in scattering angles in the analyzer exist. The errors associated to the uncertainty on the beam energy or the proton momentum are negligible.

6.3.1 Scattering angles in the FPP

The accuracy of the measurement of the polarization at the focal plane depends of course on the accuracy with which the scattering angles are measured in the FPP. The chambers resolution, with a physical alignment and its correction in software at the level of 100 μm, is about 1 mrd, both in the polar and azimuthal scattering angles ϑ and φ. To estimate the systematic error on $\mu_p G_{Ep}/G_{Mp}$ associated to it, we shift separately these angles by the conservative value of 2 mrd in the analysis code, and observe the shift in the ratio. The result is presented in Table 6.6.

Q^2 (GeV^2)	ϑ (+2 mrd)	φ (+2 mrd)
3.5	+0.0014	+0.0051
4.0	+0.0008	+0.0063
4.8	+0.0014	+0.0061
5.6	+0.0007	+0.0029

Table 6.6: Shift observed on the ratio $\mu_p G_{Ep}/G_{Mp}$ when shifting the FPP scattering angles.

6.3.2 Precession

The main source of systematic errors is the precession of the spin of the proton in the spectrometer, where both errors on the precession angles and in the model used to compute the precession itself contribute.

Precession angles

The precession is described by the rotation matrix that relates the polarization at the target to the polarization at the focal plane.

$$
\begin{pmatrix} P_x^{fpp} \\ P_y^{fpp} \end{pmatrix} = \begin{pmatrix} S_{xy} & S_{xz} \\ S_{yy} & S_{yz} \end{pmatrix} \begin{pmatrix} hP_y \\ hP_z \end{pmatrix}
\tag{6.9}
$$

In first approximation, Eq. 6.9 can be written:

$$
\begin{pmatrix} P_x^{fpp} \\ P_y^{fpp} \end{pmatrix} = \begin{pmatrix} 0 & \sin\chi_\theta \\ \cos\chi_\phi & \sin\chi_\phi \end{pmatrix} \begin{pmatrix} hP_y \\ hP_z \end{pmatrix}
\tag{6.10}
$$

where:

$$
\chi_\theta = \gamma\mu_p\left(\theta_{fp} - \theta - 45°\right) = \gamma\mu_p\Theta_{bend}
$$

$$
\chi_\phi = \gamma\mu_p\left(\phi_{fp} - \phi\right) = \gamma\mu_p\Phi_{bend}
\tag{6.11}
$$

are the precession angles in the dispersive and non dispersive planes respectively. Equation 6.10 shows that these angles have to be reconstructed accurately, as the target vertical and horizontal angles θ and ϕ respectively are part of the input to COSY.

Dispersive plane To estimate the error on χ_θ, we could benefit from the fact that at $Q^2 = 5.6$ GeV^2, $\chi_\theta = -360°$ is within the range of the precession angle, as shown in Fig. 6.5. This means that for $\chi_\theta = -2\pi$, $P_x^{fpp} = 0$. Figure 6.6 shows P_x^{fpp} vs. χ_θ, where the solid line is a sinusoidal fit to P_x^{fpp}. In the small box the region of

the zero crossing at $\chi_\theta = -2\pi$ is magnified. The dashed lines show the uncertainty on the fit, which is the uncertainty on the precession angle. The plot also shows S_{xx} calculated from COSY (small dots), which is approximately $\sin \chi_\theta$.
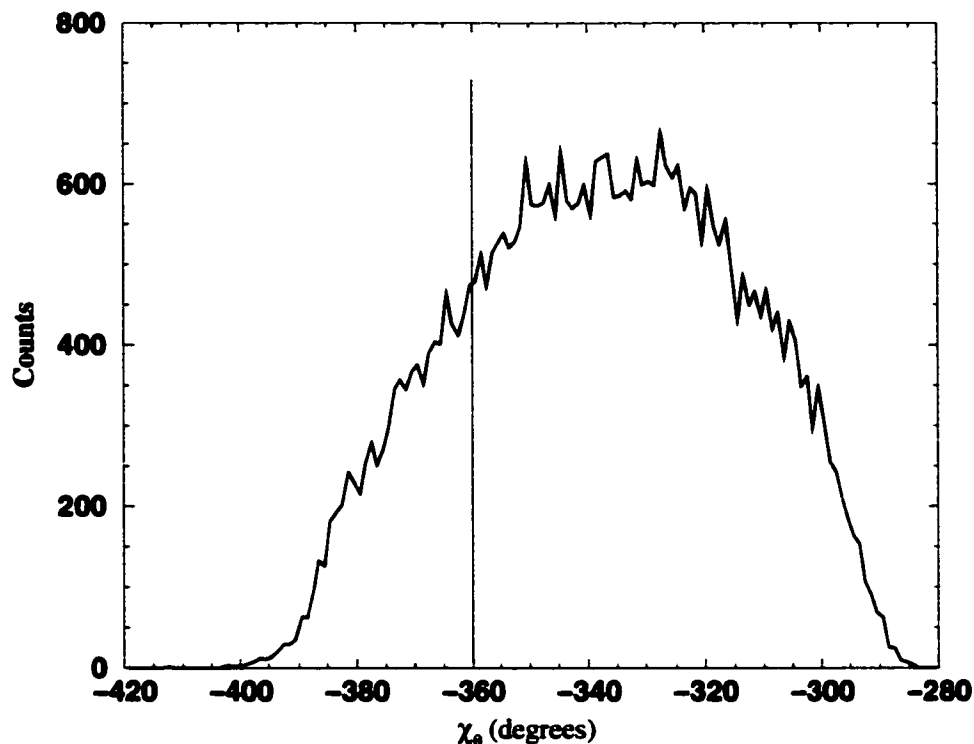
Figure 6.5: χ_θ distribution at $Q^2 = 5.6$ GeV^2.

The uncertainty on the precession angle is about 40 mrd, which corresponds to 5.5 mrd uncertainty on the bending angle. Such a variation on the bending angle was used as input of the code, in order to study the systematic error associated to this, and the corresponding shift of the ratio was observed. Results are reported in Table 6.7. The change of sign of the effect is explained by the fact that the precession angle passes $270°$ around $Q^2 = 4.0$ GeV^2, where the slope of $\sin \chi_\theta$ flips its sign.
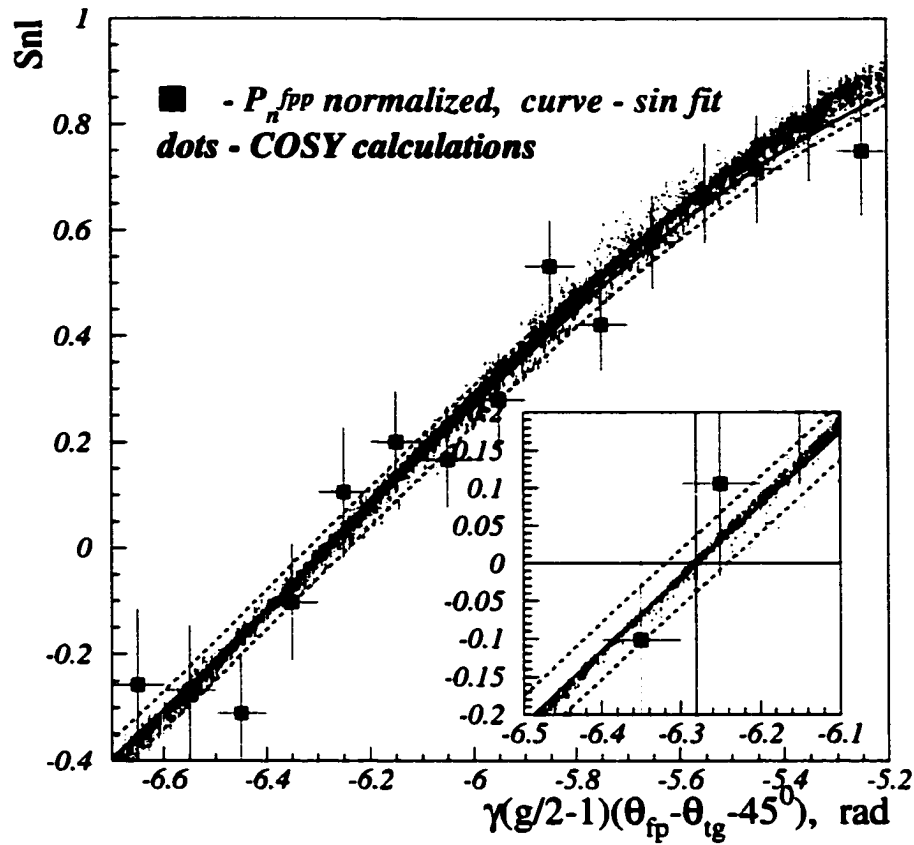
Figure 6.6: P_x^{fpp} vs. χ_θ at $Q^2 = 5.6$ GeV^2. The crossing of 0 of P_x^{fpp} at $\chi_\theta = -2\pi$ shows the accuracy with which the precession angle in the dispersive plane is reconstructed.

Non dispersive plane The precession in the non dispersive plane is described by:

$$P_y^{fpp} = S_{yy}hP_y + S_{yz}hP_z \qquad (6.12)$$

where the second term is zero in the dipole approximation. However, with increasing proton momentum, the range of the precession angle in the non dispersive plane increases rapidly, and can reach 30° at $Q^2 = 5.6$ GeV^2 for extreme rays, as shown on Fig. 6.7. In this case, this second term becomes important, and variations in $S_{yz} \sim \sin \chi_\phi$ because of uncertainties in χ_ϕ lead to large uncertainties on the final

Q^2 (GeV^2)	Θ_{bend} (+5.5 mrd)
3.5	+0.0046
4.0	-0.0001
4.8	-0.0026
5.6	-0.0043

Table 6.7: Shift observed on the ratio $\mu_p G_{Ep}/G_{Mp}$ when shifting the precession angle in the dispersive plane.

result. A 1.4 mrd error on the bending angle Φ_{bend} (corresponding to the uncertainty on the angle between the VDC plane and the dipole axis) leads to a 0.045 absolute error on $\mu_p G_{Ep}/G_{Mp}$ at $Q^2 = 5.6$ GeV^2.
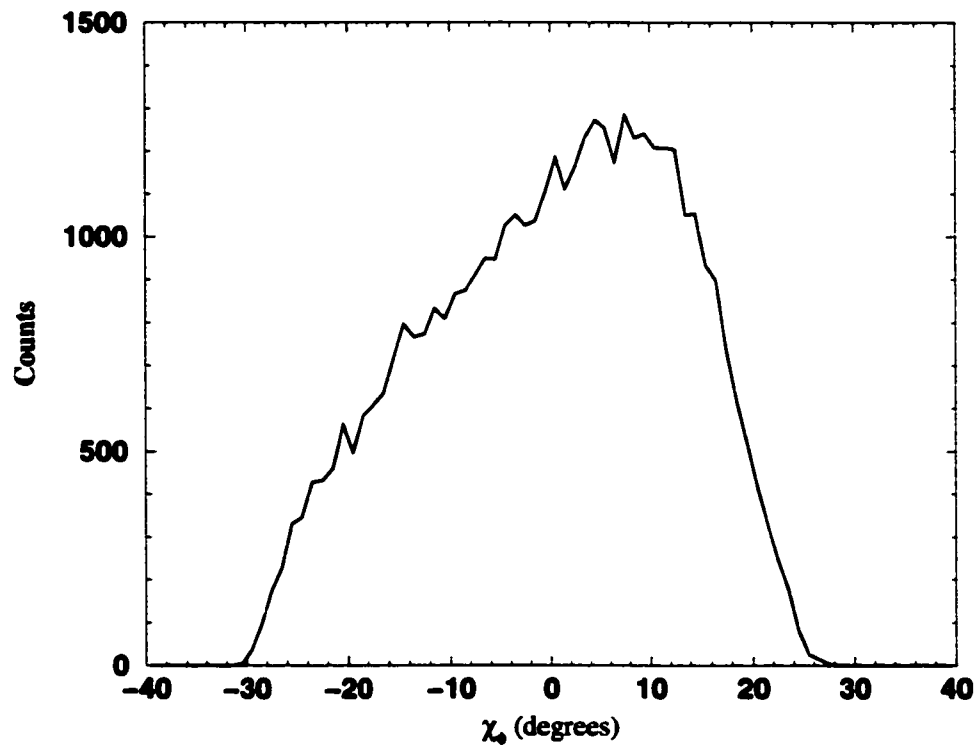
Figure 6.7: χ_ϕ distribution at $Q^2 = 5.6$ GeV^2.

This source of uncertainty was greatly reduced by making a careful measurement of the horizontal misalignment of the quadrupoles in the spectrometer, in April 2001. The detailed results of this study are in Ref [103]. A brief description

of the method is given here. Measurements were performed with six different tunings of the elements of the spectrometer, of elastic scattering off a carbon target of a 0.836 GeV beam, at 15°. The first setting was the nominal tune $(Q_1Q_2DQ_3)$ of the spectrometer, and the next two were only the dipole and one quadrupole $(Q_2D$ and $DQ_3)$. The tuning of the energized quadrupole was chosen to obtain a point-to-parallel focusing in the transverse (y) direction. The Q_1D configuration was not taken into account, because the different holes of the sieve slit could not be separated, as well as the elastic peak from the excitation peaks. The last three settings were a "reduced field" by 30% in one quadrupole at a time $(0.7Q_1Q_2DQ_3$, $Q_10.7Q_2DQ_3$ and $Q_1Q_2D0.7Q_3)$. For each of these six settings, the displacement of the image of the central hole of the sieve slit was studied, by looking at the displacement of the peak of the y_{fp} and ϕ_{fp} distributions at the focal plane. These quantities moved by up to 2 mm and 1.2 mrd respectively, from one tuning to another; the origin of these displacements must be due to misalignments of the quadrupoles. To account for this displacements, offsets s_i and rotations of angle a_i $(i = 1, 3)$ about the middle entrance point of each quadrupole were introduced in the optics matrix. The measured peak positions at the focal plane are then given by:

$$\phi_{fp} = \phi_0 + \langle\phi|y\rangle y_{tgt} + \langle\phi|\phi\rangle\phi_{tgt} + \sum_{i=1}^{3}\langle\phi|s_i\rangle s_i + \sum_{i=1}^{3}\langle\phi|a_i\rangle a_i$$

$$y_{fp} = y_0 + \langle y|y\rangle y_{tgt} + \langle y|\phi\rangle\phi_{tgt} + \sum_{i=1}^{3}\langle y|s_i\rangle s_i + \sum_{i=1}^{3}\langle y|a_i\rangle a_i \qquad (6.13)$$

where $\langle\phi|s_i\rangle = d\phi/ds_i$, $\langle\phi|a_i\rangle = d\phi/da_i$, $\langle y|s_i\rangle = dy/ds_i$, $\langle y|a_i\rangle = dy/da_i$, and ϕ_0 and y_0 are coordinate and angle offsets of the VDCs with respect to the dipole axis. y_0 was surveyed at the commissioning of the Hall. ϕ_{tgt} and y_{tgt} are related by:

$$\phi_{tgt} = \frac{y_s - y_{tgt}}{z_s} \qquad (6.14)$$

where y_s and z_s are the coordinates of the central hole of the sieve slit, known to 0.1 mm from a survey. The equations Eq. 6.13 can be written for each setting,

resulting in a system of 12 equations, where y_{tgt}, ϕ_0, a_i and s_i $(i = 1,3)$ are eight parameters. These parameters are calculated using the linear least squares method.

The result is that the observed displacements at the focal plane of the image of the central hole can be explained by offsets and rotations less than 0.5 mm and 0.8 mrd respectively of Q_1 and Q_2, and less than 2.5 mm and 3 mrd of Q_3. This is in agreement with the stated precision of the quadrupole positioning. Optics matrices calculated from both codes COSY and TRANSPORT were used, and they give similar results. Assuming a conservative error of 3 mm on the surveyed y_0, the analysis results in a systematic uncertainty on the total bending angle in the non dispersive plane Φ_{bend} of 0.3 mrd, to be compared with 1.4 mrd, which was the value of this uncertainty before the misalignment study. The resulting error on $\mu_p G_{Ep}/G_{Mp}$ is given in Table 6.8. At $Q^2 = 5.6$ GeV^2, this uncertainty was divided by more than 3 with this study.

Q^2 (GeV^2)	Error associated to χ_ϕ
3.5	$\pm$ 0.0013
4.0	$\pm$ 0.0011
4.8	$\pm$ 0.0061
5.6	$\pm$ 0.0123

Table 6.8: Error on the ratio $\mu_p G_{Ep}/G_{Mp}$ corresponding to the uncertainty on the precession angle in the non dispersive plane.

Model uncertainty

Another source of systematic error related to the precession lies in the model itself that calculates the precession matrix in the COSY code. A way to estimate the uncertainties related to various approximations or assumptions that are made within that model, such as the modeling of the fringe fields, is to use it to calculate the same precession matrix, but in different ways.

The standard way is to measure focal plane coordinates in the VDCs, use ES-PACE to reconstruct the target coordinates, model the spectrometer in its $(Q_1 Q_2 D Q_3)$ configuration with COSY and use the target coordinates to calculate the precession matrix TGT $\rightarrow$ FP for each event. An alternative way to do it is to model the spectrometer in a reverse configuration $(Q_3 D Q_2 Q_1)$, and use directly the focal plane coordinates to calculate a precession matrix FP $\rightarrow$ TGT, and inverse it. Another possibility is to use COSY as optics model to reconstruct the target coordinates instead of ESPACE. A summary of the ways used is in Fig. 6.8. Table 6.9 gives the variation of the ratio $\mu_p G_{Ep}/G_{Mp}$ from one way to another.
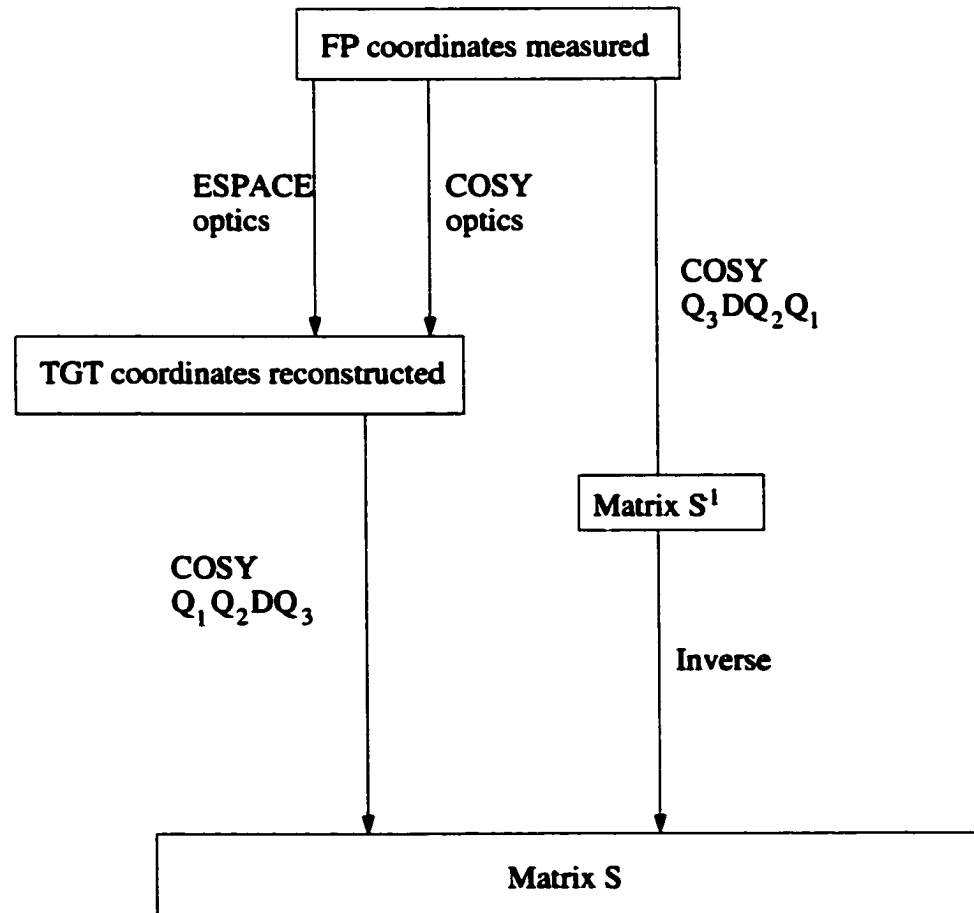
Figure 6.8: Three different ways to calculate the precession matrix using COSY.

Q^2 (GeV^2)	Variation due to different COSY configurations
3.5	± 0.0004
4.0	± 0.0004
4.8	± 0.0012
5.6	± 0.0127

Table 6.9: Variation of the ratio $\mu_p G_{Ep}/G_{Mp}$ corresponding to different ways to calculate the precession matrix with COSY.

Conclusion on the precession
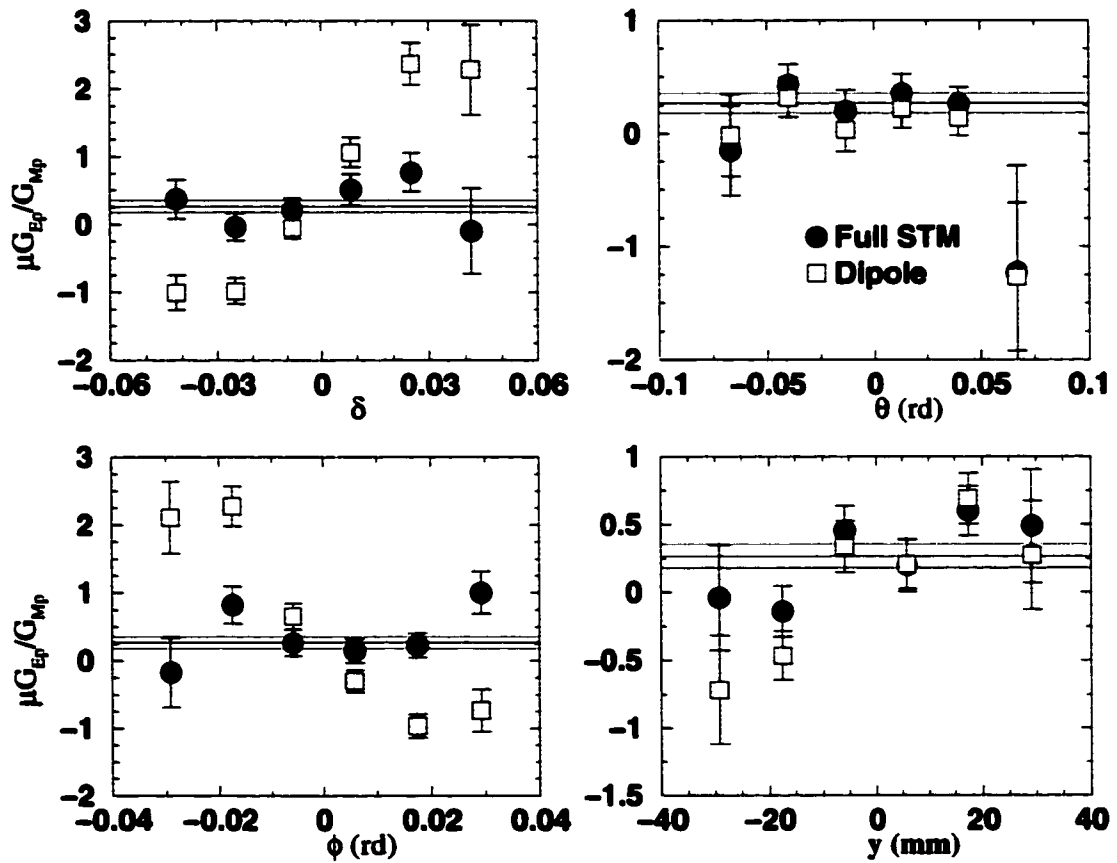
Figure 6.9: Dependence of $\mu_p G_{Ep}/G_{Mp}$ on the proton target quantities, for the full precession matrix calculated by COSY, compared to the dipole approximation, at $Q^2 = 5.6$ GeV^2.

If the precession is handled correctly, the ratio $\mu_p G_{Ep}/G_{Mp}$ should not depend

on the target quantities $(\theta, y, \phi, \delta)$. Figure 6.9 shows the dependence of the ratio on these quantities, when calculated with the dipole approximation, and with a full precession matrix calculated by COSY. It illustrates the correction that COSY brings to a crude approximation like the single dipole: Table 6.10 compares the χ^2 of a constant fit to the target variable dependence of the ratio for the two methods.

Variable	δ	θ	ϕ	y
Dipole	28.10	1.74	27.67	5.55
Full STM	1.40	0.97	2.09	2.02

Table 6.10: $\chi^2/n.d.f.$ for a constant fit of the dependence of the ratio $\mu_p G_{Ep}/G_{Mp}$ on the target quantities, for the single dipole approximation, and the full precession matrix.

6.3.3 Total systematic error
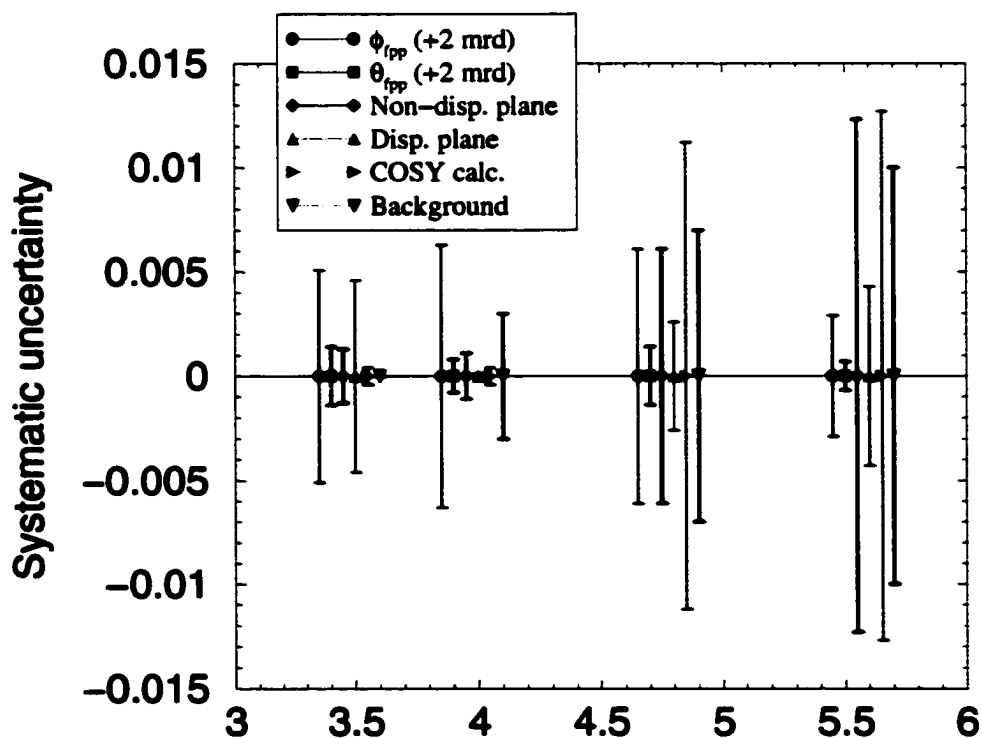
Figure 6.10: Comparison of all contributions to the systematic uncertainty, for each kinematics.

The uncertainties quoted in Tables 6.6, 6.7, 6.8 and 6.9, as well as the one associated with the inelastic background contribution in Table 6.4, are compared in Figure 6.10, for each Q^2 point. While the uncertainties associated with the polarimeter and the reconstruction of the scattering angle are roughly energy-independent, the contributions due to the precession increase with the proton momentum, because of the relativistic γ factor involved in the precession.

All these contributions are added quadratically to give the total systematic error. The final result, with statistical and systematic uncertainty is given in Table 6.11.

Q^2	$\mu_p G_{Ep}/G_{Mp}$	stat. uncert.	syst. uncert.
3.50	0.571	± 0.072	± 0.007
3.97	0.481	± 0.052	± 0.008
4.75	0.379	± 0.053	± 0.011
5.54	0.275	± 0.087	± 0.028

Table 6.11: Final results for the ratio $\mu_p G_{Ep}/G_{Mp}$ with statistical and systematic uncertainties. The first column is the Q^2 averaged over the spectrometer acceptance.

Figure 6.11 shows the result of this experiment combined with the ones of E93-027 presented earlier, which was the same experiment at lower Q^2. The two measurements at $Q^2 = 3.5$ GeV^2 overlap very well. The striking feature is the improvement of the total systematic uncertainty, shown in a band at the top of the figure, which was reduced by a factor of six at this overlap point. The reason for this is a much better understanding of the precession, partly thanks to the alignment study performed on the HRS. The data from E93-027 will be eventually reanalyzed and the systematic uncertainties reevaluated.

The data of the two experiments can be linearly fitted. The expression for this fit, over the range $0.5 < Q^2 < 5.6$ GeV^2 is:

$$\mu_p \frac{G_{Ep}}{G_{Mp}} = 1 - 0.13 \left(Q^2 - 0.04 \right)$$

(6.15)

Note that this is an empirical fit to the data, not motivated by any physical considerations.
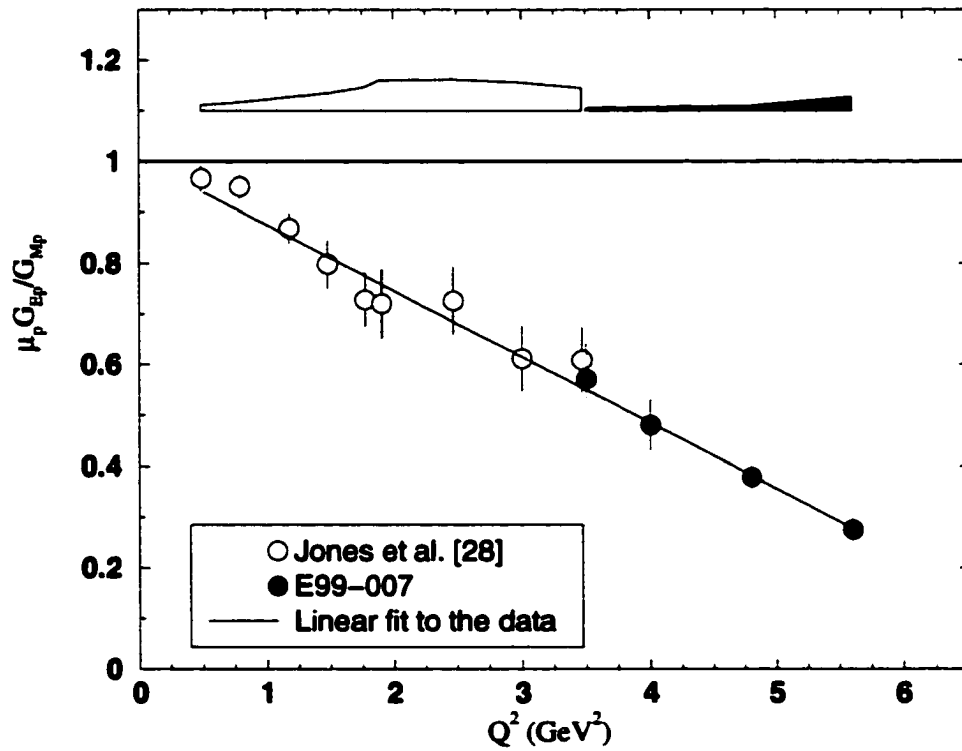
Figure 6.11: Final result of E99-007 combined with E93-027. The error bars are statistical only; systematic are shown as a band on top of the figure. The linear fit has no physical motivation.

6.4 G_{Mp} Rosenbluth reanalysis

As explained in Section 1.4.1, the form factors G_{Ep} and G_{Mp} have been measured by Rosenbluth separation over the last 35 years. This method separates the

two contributions from the electric and magnetic terms to the unpolarized elastic ep scattering cross-section. A global analysis of all these experiments led to a fit of the form factors [14]. This fit, which approximately results in $\mu_p G_{Ep}/G_{Mp} = 1$ over a large range of Q^2, gives systematically more weight to the electric term relatively to the magnetic term, than Eq. 6.15 for our data does. Therefore, in a reanalysis of the cross-section data, a constraint on $\mu_p G_{Ep}/G_{Mp}$ imposed by Eq. 6.15 should systematically give a lower value for the magnetic term, thus to G_{Mp}.
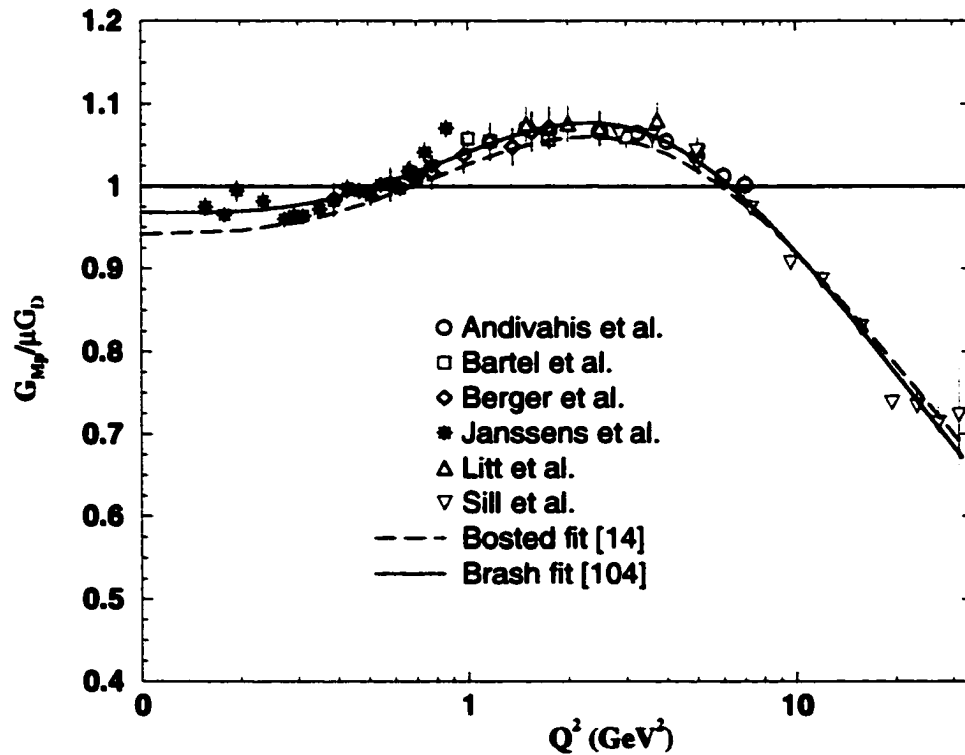
Figure 6.12: Reanalysis of the magnetic form factor data using the constraint of Eq. 6.15. The new fit (solid line) is compared to the previous one (dashed line).

Such an analysis has been done by E. Brash *et al.* [104]. The result is presented in Fig. 6.12. It shows $G_{Mp}/\mu_p G_D$ as a function of Q^2, where G_D is the dipole parameterization. The experimental points are the reevaluated values of the magnetic form factor. The solid line represents the new fit to these data, compared with the old one (dashed line). The constraint of Eq. 6.15 results in an increase of 1.5-3% of G_{Mp}.

CHAPTER 7

Discussion and perspectives

This last chapter discusses the results presented in the previous chapter. The experimental data are compared with other data and with theoretical predictions. The chapter concludes with a presentation of future experiments of nucleon form factors at Jefferson Lab.

7.1 Comparison with other experimental data

As shown on Fig. 7.1, experiment E99-007 measured for the first time a very clear deviation of the ratio $\mu_p G_{Ep}/G_{Mp}$ from unity, up to $Q^2 = 5.6$ GeV^2, as was expected from the earlier, but similar experiment E93-027 to $Q^2 = 3.5$ GeV^2. Only one experiment, NE11 at SLAC [8], had measured the electric form factor to such high momentum transfer, and the new measurements are in clear disagreement with these results with these data. It is worthwhile to note that at the same Q^2, the experiment NE11 of SLAC used two different spectrometers (1.6 and 8 GeV/c spectrometers) to measure the cross section at different values of $1/\epsilon$ (see Section 1.2.2). In particular, the acceptance of the 1.6 GeV/c spectrometer was not fully understood, and cross section measurements from this spectrometer were renormalized to cross section measurements from the 8 GeV/c spectrometer. Using the non-renormalized values for the 1.6 GeV/c spectrometer yields results comparable with the ones of E99-007. This illustrates the fact that in this range of Q^2, a pure Rosenbluth separation technique results in systematic uncertainties and normalization factors that are very difficult to control. These problems are not present in recoil polarization

156

experiments, where the main source of systematic uncertainties is in the precession of the proton spin in the spectrometer.
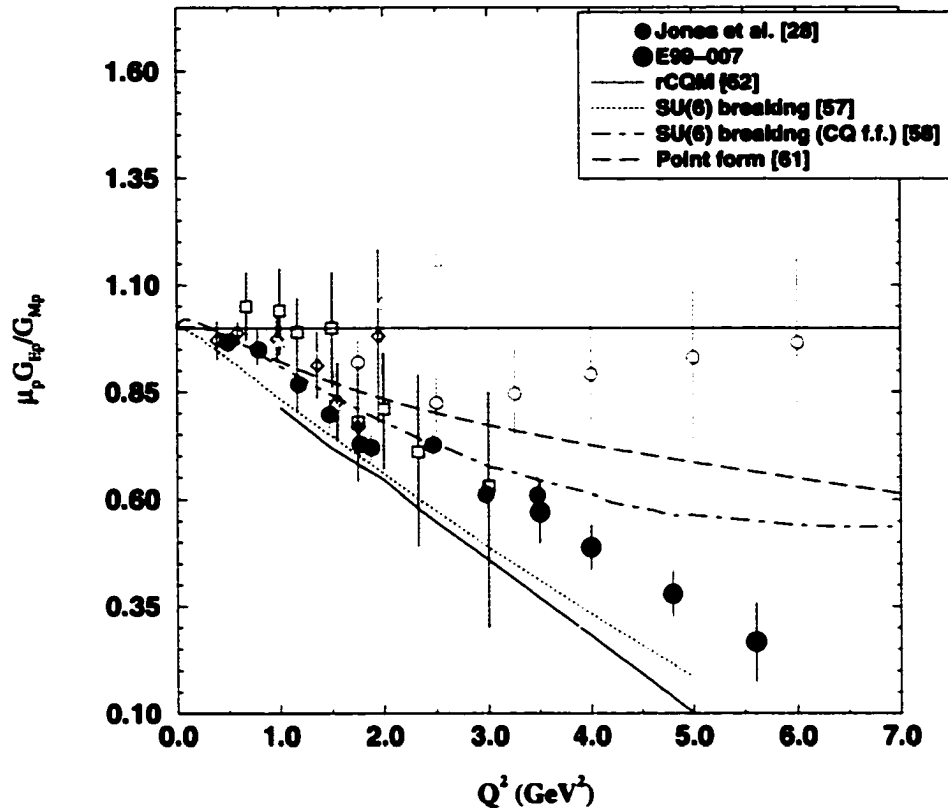
Figure 7.1: Comparison of new data with previous data and theoretical calculations.

7.2 Comparison with theoretical models

7.2.1 Constituent quark models

Also shown in Fig. 7.1 are the same theoretical curves as in Fig. 2.4. As explained earlier, these curves, from relativistic constituent quark model (rCQM) calculations, have parameters to be adjusted to fit hadrons properties measured experimentally. The curves shown here were obtained before the new data from experiment E99-007, and therefore their parameters have not been adjusted. Even

if the theoretical curves do not lie on the experimental points, it is interesting to note that the rCQM predict the deviation of G_{Ep}/G_{Mp} from unity. The degree of disagreement between the model and the data is reasonable, because so many plausible effects, such as configuration mixing involving quark and gluon degrees of freedom and a Q^2 variation of the constituent quark masses, are ignored [105].

7.2.2 Vector meson dominance
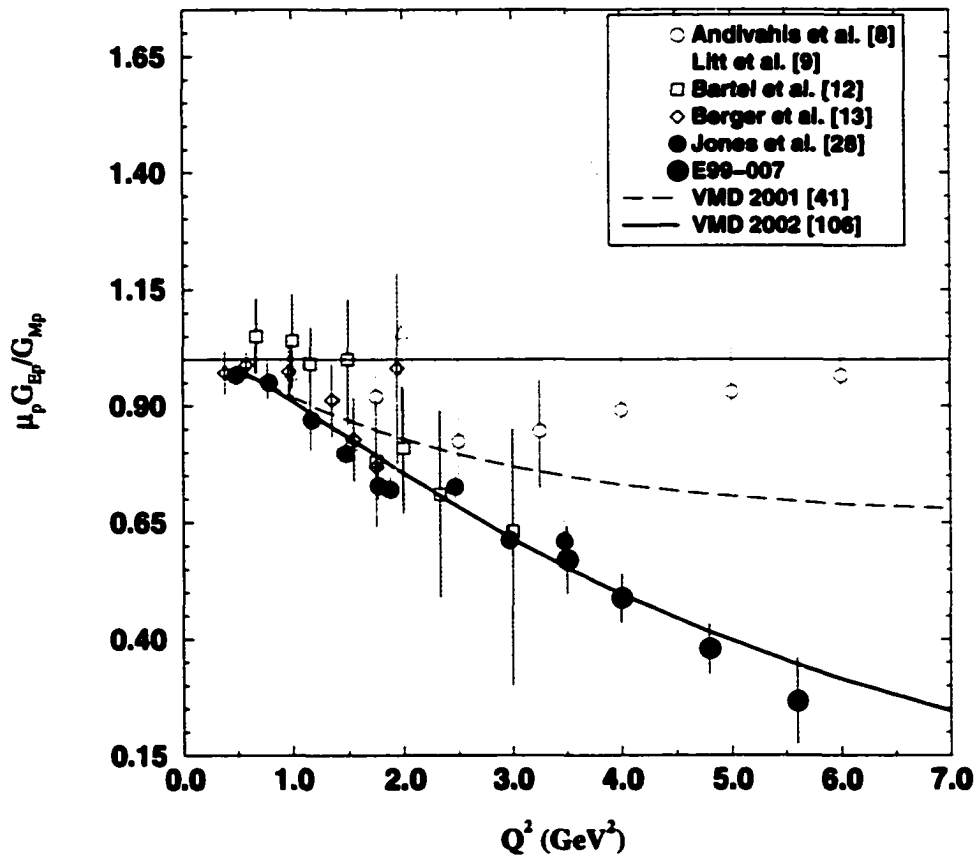
Figure 7.2: Ratio $\mu_p G_{Ep}/G_{Mp}$ to $Q^2 = 7$ GeV^2 calculated from VMD model including data from E93-027 (dashed line) and including data from E99-007 (solid line).

In 2002, Lomon again refined his fit of the nucleon form factor in the Gari and Krümpelmann type VMD model, including the data from E99-007, and preliminary results from Jlab Hall C experiment E93-038 which measured G_{En}. He also rejected

some G_{Ep} results that were in strong disagreement with the rest of the data. The new fit for R_p is shown in Fig. 7.2 (solid line), compared to the 2001 fit presented in Chapter 2 (dashed line). The new fit is remarkably close to the data. It describes very well in general the latest measurements of all form factors, including those at higher momentum transfer [106].

This model, in its attempt to bridge the gap between the low Q^2 mesonic behavior and the asymptotic pQCD regime, does not provide a realistic description of the nucleon structure, since it requires some artificial parameters to describe the asymptotic regime. However, it is a very effective parameterization of the nucleon form factors, which may be used in calculations of more complex systems, such as the deuteron form factors.

7.3   Perturbative QCD prediction

Figure 7.3 compares the new Jlab results and the pQCD scaling prediction, that F_2/F_1 should go as Q^{-2}, as explained in Section 2.3 in Chapter 2. The quantity $Q^2 F_2/F_1$ is plotted for experiments E93-027, E99-007, and previous Rosenbluth measurements. While earlier measurements in this range of Q^2 from experiment NE11 at SLAC [8] showed scaling behavior, the polarization measurements contradict it, but rather suggest that the asymptotic regime is not reached yet. There is no reason to believe that such a regime should be reached as this momentum transfer. For the magnetic form factor, the $\alpha_s^2(Q^2)/Q^4$ behavior starts only around 6-8 GeV^2, as shown in Fig. 2.8.

However, motivated by a work from Ralston et al. [107], who discussed a different approach to pQCD which explicitly includes quark orbital angular momentum, it is interesting to look at the ratio QF_2/F_1, where $Q = \sqrt{Q^2}$. Figure 7.4 shows the ratio QF_2/F_1 for experiments E93-027, E99-007, and previous Rosenbluth measurements. A plateau is clearly reached starting at $Q^2 = 2$ GeV^2.
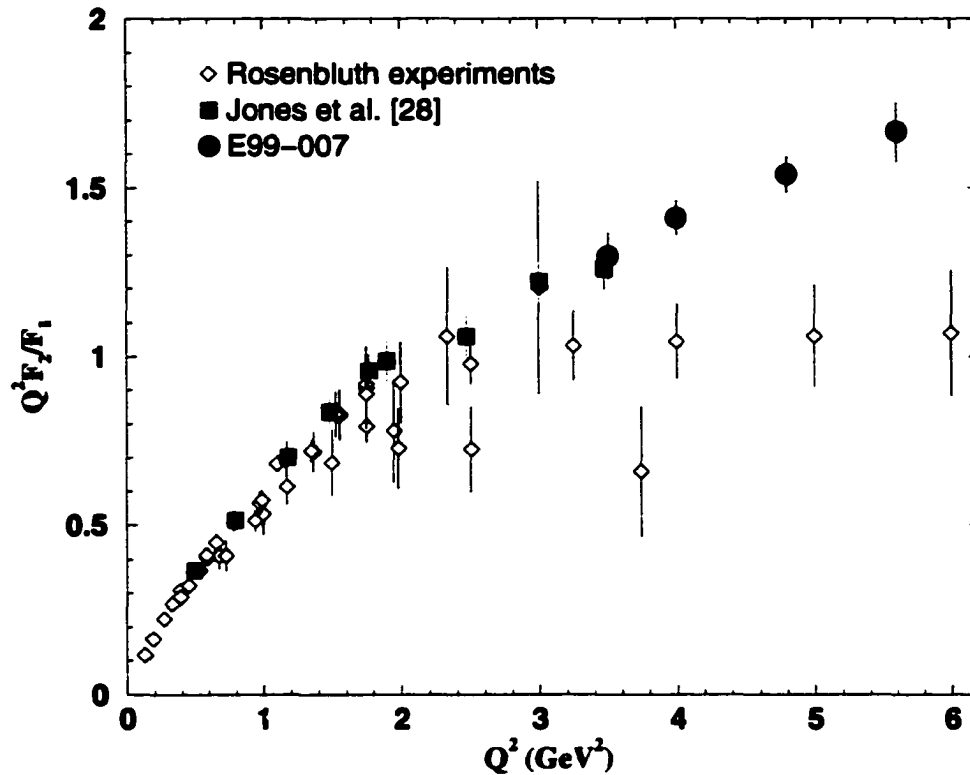
Figure 7.3: Ratio $Q^2 F_2/F_1$ to $Q^2 = 6.2$ GeV^2 for experiments E93-027, E99-007 and previous Rosenbluth separation results.

Ralston *et al.* have an interpretation of this plateau within the pQCD framework. They keep the argument that quark spin flip is forbidden in pQCD, but they reject the argument that hadron helicity flip, represented by the term QF_2 in the current, comes from corrective terms in m/Q due to quark mass. Instead, they suggest that the orbital momentum of the quarks facilitates the proton spin flip by transferring a unit of orbital momentum in the quark [108]. In this approach, power counting of the transverse separation of the quarks $b \sim 1/Q$ leads to $F_2/F_1 \rightarrow 1/Q$ [107].

Another interpretation for this behavior has been suggested by Frank and Miller [105]. Opposite to the idea that this is a pQCD behavior, they work in

the relativistic constituent quark model on the light front, described in Chapter 2.
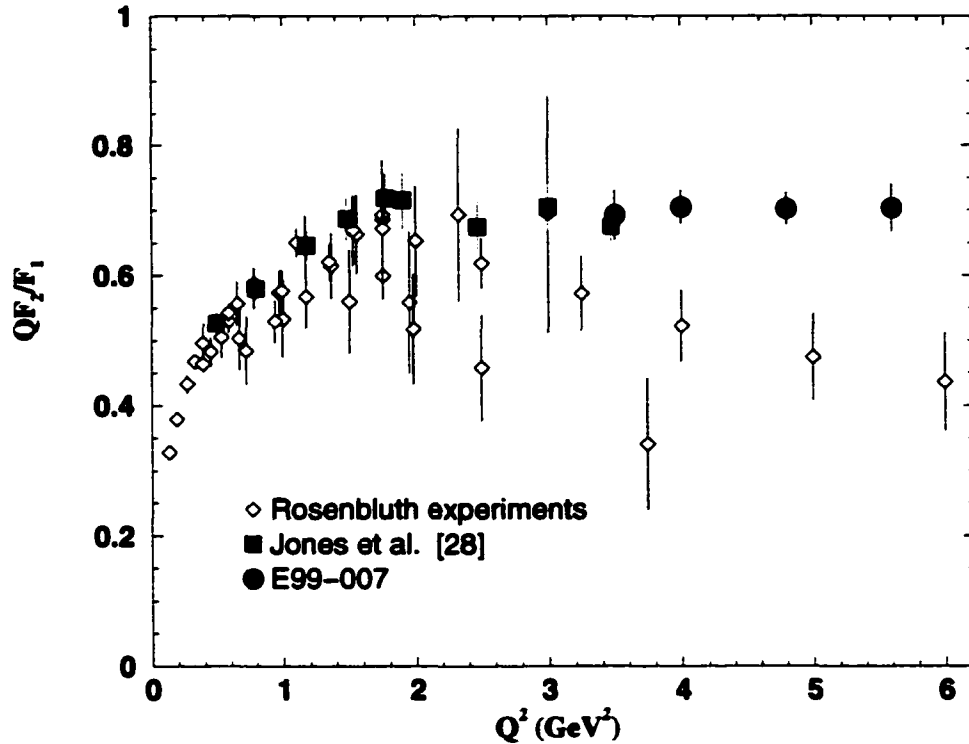
Figure 7.4: Ratio QF_2/F_1 to $Q^2 = 6.2$ GeV^2 for experiments E93-027, E99-007 and previous Rosenbluth separation results.

Light front dynamics offers a framework in which the center of mass motion and the relative motion of the quarks in the nucleon are completely separated, so that the nucleon wave function is frame independent. The relativistic effect is represented in the Melosh rotations imposed on the light front spinors, which have the following representation:

$$\langle \lambda' | \mathcal{R}_M(\xi, q_\perp, m, M) | \lambda \rangle = \left[\frac{m + \xi M - i\vec{\sigma} \cdot (\vec{n} \times \vec{q})}{\sqrt{(m + \xi M)^2 + q_\perp^2}} \right]_{\lambda'\lambda} \tag{7.1}$$

There are two terms in the numerator: the first one, $m + \xi M$, conserves the nucleon spin, and corresponds to the Dirac from factor F_1, while the second one, $\vec{\sigma} \cdot (\vec{n} \times \vec{q})$,

allows spin flip and is associated to the Pauli form factor QF_2. Both terms contain the same power of Q (the momentum transfer is contained in M), so that QF_2/F_1 is a constant. In the light front description, there is no reason to expect light front helicity conservation, because the non-perturbative wave function is a mixture of different light front helicity states, due to the Melosh rotations.

This statement is not in contradiction with pQCD, which involves a different, perturbative, wave function of the nucleon. As Q^2 becomes asymptotically large, the non-perturbative wave function effects might disappear, and perturbative effects may take over.

7.4 Future experiments

We discuss now the form factor program at Jefferson Lab for the future. The regain of interest for nucleon form factors is certainly visible in the fact that in the last two years, three proposals for measuring proton and neutron from factors were accepted by the Program Advisory Committee, with approval rating A.

7.4.1 Super-Rosenbluth

The next experiment is a G_{Ep}/G_{Mp} measurement by a "super-Rosenbluth" method [109]. Scheduled in Hall A for May 2002, it will measure unpolarized elastic scattering cross sections from the proton, simultaneously at a Q^2 fixed of 0.5 GeV^2 with one spectrometer, where G_{Ep}/G_{Mp} is known with a good accuracy, and another (higher) Q^2 with the other spectrometer. Taking the ratio of the simultaneous measurements and repeating this measurements at different values of ϵ, by varying the beam energy, allows a precision measurement of G_{Ep}/G_{Mp} up to relatively high Q^2. The simultaneous measurement at low Q^2 provides a good luminosity monitor, so that the measurement is insensitive to measured charge and target thickness. Also the detection of protons, instead of electrons as in the previous Rosenbluth

separation experiments, leads to a reduced cross section dependence upon the beam energy and scattering angle, therefore should result in a better handling of the systematic errors. Figure 7.5 shows the expected errors for this measurement at the three proposed kinematics. The error bar on the ratio depends on the ratio G_{Ep}/G_{Mp} itself, so the points were arbitrarily put on the Jlab data fit line from Eq. 6.15, with the uncertainty corresponding to this value.
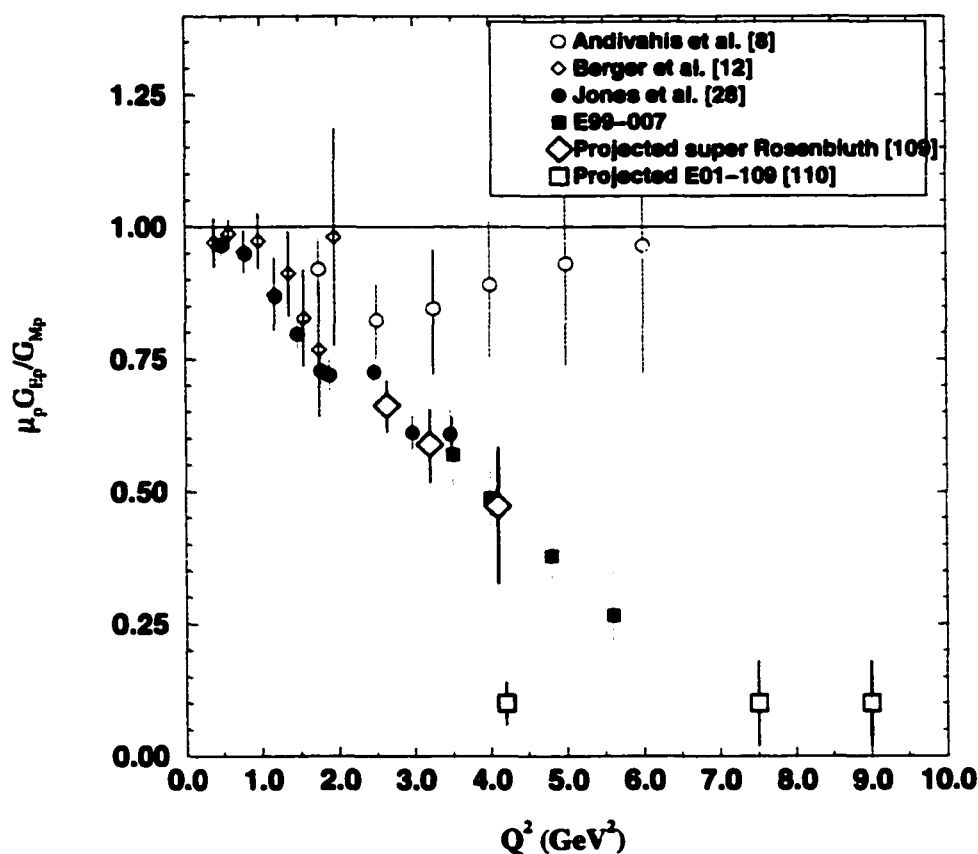
Figure 7.5: Expected errors for "super-Rosenbluth" experiment and Hall C proposal. The "super Rosenbluth" points were arbitrarily put on the Jlab data fit line from Eq. 6.15.

7.4.2 Experiment E01-109

The third phase of the Jlab recoil polarimetry measurement of G_{Ep}/G_{Mp} will take place in Hall C, using the High Momentum Spectrometer (HMS). Experiment

E01-109 will measure $\mu_p G_{Ep}/G_{Mp}$ up to $Q^2 = 9$ GeV^2, using a 6 GeV electron beam [110]. The principle is very similar to the one described in this thesis. The experiment requires the construction of a focal plane polarimeter, to be mounted in the HMS, and a large solid angle calorimeter for electron detection. At $Q^2 = 9$ GeV^2, with a beam energy of 6 GeV, the required solid angle for the electron detector is 135 mrd. The calorimeter will consist of $\sim$1700 3.9×3.9 cm^2 lead-glass blocks. The projected uncertainties are shown in Fig. 7.5. These uncertainties use the coefficient of merit obtained in a calibration of the CH$_2$ analyzing power up to 5.3 GeV/c.

Proposals are now developing to measure $\mu_p G_{Ep}/G_{Mp}$ up to $Q^2 = 12$ GeV^2, using the HMS also, with the upgraded 12 GeV beam, provided that the analyzing power has a reasonable value at such high momentum. There is no question that recoil polarimetry, together with the high luminosity, high polarization CEBAF electron beam, provides an ideal tool to measure electric form factors.

7.4.3 Other form factors

On the front of other form factors, G_{En} is certainly the form factor that inspires the most efforts. Hall C is currently analyzing experiments E93-026 [111] and E93-038 [112], which measured the neutron electric form factor in the reactions $\vec{d}(\vec{e}, e'n)p$, and $d(\vec{e}, e'\vec{n})p$, respectively, at Q^2 between 0.5 and 1.5 GeV^2. At the last Jlab Program Advisory Committee meeting in January 2002, no less than three groups proposed to measure G_{En}. One proposal, E02-013, was accepted, with approval rating A, and will measure G_{En} at $Q^2 = 2.4$ and 3.4 GeV^2, in the $^3\vec{H}e(\vec{e}, e'n)p$ reaction, using the BigBite detector to detect the electron and scintillator bars to detect the neutron.

Conclusion

In conclusion, electric to magnetic form factor ratios for the proton obtained from recoil polarization measurements, between $Q^2 = 3.5$ and 5.6 GeV^2, were presented in this thesis. This experiment mostly used standard Hall A equipment, whose central piece was the Focal Plane Polarimeter in the proton High Resolution Spectrometer. The FPP allowed us to measure the transverse and longitudinal components of the recoil proton polarization in the $H(\vec{e}, e'\vec{p})$ reaction. The ratio of these components is proportional to the form factor ratio. The main source of systematic uncertainties, when measuring this polarization ratio, is the precession of the proton spin in the spectrometer. Careful alignment studies of the magnetic elements of the HRS allowed us to reduce the systematic uncertainties at a level much below the statistical uncertainties.

Solid angle matching requirements made the construction of a large acceptance calorimeter necessary, to detect the electron in coincidence. This calorimeter was assembled in the summer preceding the experiment, and allowed a very good selection of elastic events.

The main result of the measurement, published in Physical Review Letters [113], is that the ratio $\mu_p G_{Ep}/G_{Mp}$ continues the linear decrease with increasing Q^2 already observed in the first phase E93-027. The deviation of this ratio from unity shows a different behavior of the electric charge and magnetization distribution as we probe the proton to smaller distance, i.e. at higher four-momentum transfer. Even though previous measurements of the form factors may have led one to think that

G_{Ep}/G_{Mp} was a constant, there is no physical ground for such an assumption. In a non-relativistic picture, a naive interpretation of the polarization experiments results is that the electric charge distribution extends further out that the magnetization distribution. However, all models of the proton lead to a deviation from a constant by taking into account relativistic effects, which is natural in the range of kinematics that is explored here. The linearity of the deviation has yet to be explained. An extrapolation of the observed slope predicts a crossing of zero of the ratio at $Q^2 = 7.7$ GeV^2.

The predictions of perturbative QCD and quark counting rules do not apply in this range of kinematics yet, as might be expected. However, the measurement uncovers an unexpected scaling of the ratio QF_2/F_1, starting at $Q^2 = 2$ GeV^2. This elegant behavior should also find an physical meaning in terms of the proton constituents.

The increase of activity around the nucleon form factors due to the construction of new accelerators such as Jefferson Lab, also stimulates the development of numerous theoretical models. These models attempt to bridge the gap of understanding of the nucleon structure between the low Q^2 region, where the nucleon can be described in terms of mesonic degrees of freedom, and the asymptotically high Q^2 regime, where perturbative QCD should prevail. Several types of models exist, including vector meson dominance, soliton, diquark, cloudy bag, constituent quark models, $\cdots$ Some were described here with more or less detail, and their results compared to the experimental data. It is important to notice that all proposed models so far are effective theories, with parameters that can be adjusted to fit the data. There is no complete theory of the nucleon structure in particular, and of the strong interaction in general, that can explain all data in the low and intermediate Q^2 region. Maybe fast developments of computational capabilities will allow theories such as Lattice QCD to offer such a complete description.

The results of this experiment are of great interest, since it accurately measured fundamental quantities related to the most abundant strongly interacting system in the universe. Knowledge of the proton form factors is a key to the study of more complex systems, such as nuclei, and less simple processes, like real and virtual Compton scattering, form factor modification due to nuclear medium, strange form factors, $\cdots$

APPENDIX A

Breit frame

A.1 Proton kinematics in the Breit frame

By definition in elastic scattering, the Breit frame, also called the "brickwall frame", is the frame where the momenta of the initial and final nucleon are equal and opposite:

$$\vec{p}_B = -\vec{p}'_B = -\frac{\vec{q}_B}{2} \tag{A.1}$$

It follows that:

$$E_{pB} = E'_{pB} \tag{A.2}$$

so that, in elastic scattering:

$$\omega_B = E_{pB} - E'_{pB} = 0 \tag{A.3}$$

The particular value of the four-momentum transfer in the Breit frame is:

$$Q^2 = -q_B^2 = \vec{q}_B^2 \tag{A.4}$$

A.2 Electron kinematics in the Breit frame

A.2.1 Kinematics

Obviously, Eq. A.3 imposes

$$E_B = E'_B$$
$$\vec{k}_B^2 = \vec{k}'^2_B$$
$$\vec{k}_B = \vec{q}_B + \vec{k}'_B \tag{A.5}$$

168

Let's define the coordinate system, where the scattering takes place in the (13) plane, and the photon three-momentum is along the 3-axis. In this coordinate system, the three-momentum of the electron obeys

$$
\begin{aligned}
k_{B1} &= k'_{B1} = \frac{|\vec{q_B}|}{2}\cot\left(\frac{\theta_B}{2}\right) = \frac{\sqrt{Q^2}}{2}\cot\left(\frac{\theta_B}{2}\right) \\
k_{B2} &= k'_{B2} = 0 \\
k_{B3} &= -k'_{B3} = \frac{|\vec{q_B}|}{2} = \frac{\sqrt{Q^2}}{2}
\end{aligned}
\tag{A.6}
$$

This coordinate system is represented in Fig. A.1.
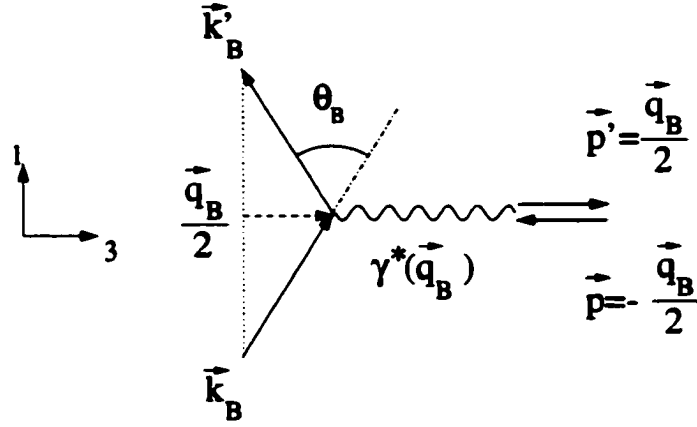
Figure A.1: Elastic scattering in the Breit coordinate system.

A.2.2 Relation between the scattering angle in the Breit and the Lab frames

We want to express the scattering angle θ_B in the Lab frame. Let's first notice that the Breit frame is moving along the 3-axis, so that the 1 and 2 components of the electron momentum are left unchanged by the Lorentz transformation:

$$
\begin{aligned}
k_1 &= k_{1B} = k'_1 = k'_{1B} = \frac{\sqrt{Q^2}}{2}\cot\frac{\theta_B}{2} \\
k_2 &= k_{2B} = k'_2 = k'_{2B} = 0
\end{aligned}
\tag{A.7}
$$

Since the $\vec{q}$ is along the 3-axis, we can write

$$k_3^2 = \frac{\left(\vec{k}\cdot\vec{q}\right)^2}{\vec{q}^2} = \frac{\left(\vec{k}\cdot\vec{k}-\vec{k}\cdot\vec{k'}\right)^2}{\vec{q}^2} = \frac{(E^2)^2 + (EE'\cos\theta_e)^2 - 2E^2 EE'\cos\theta_e}{\vec{q}^2} \quad (A.8)$$

and use it to get

$$\begin{aligned}
k_1^2 &= \vec{k}^2 - k_3^2 = \frac{\vec{k}^2\vec{q}^2 - \left(\vec{k}\cdot\vec{q}\right)^2}{\vec{q}^2}\\[2mm]
&= \frac{\left[(E^2)^2 + E^2 E'^2 - 2E^2 EE'\cos\theta_e\right] - \left[(E^2)^2 + (EE'\cos\theta_e)^2 - 2E^2 EE'\cos\theta_e\right]}{\vec{q}^2}\\[2mm]
&= \frac{E^2 E'^2\left(1 - \cos^2\theta_e\right)}{\vec{q}^2}\\[2mm]
&= \frac{E^2 E'^2\sin^2\theta_e}{\vec{q}^2}\\[2mm]
&= \frac{4E^2 E'^2}{\vec{q}^2}\sin^2\frac{\theta_e}{2}\cos^2\frac{\theta_e}{2}\\[2mm]
&= \frac{(Q^2)^2}{4\vec{q}^2}\cot^2\frac{\theta_e}{2} \quad (A.9)
\end{aligned}$$

where, again, the electron mass is neglected, and the relation

$$Q^2 = 4EE'\sin^2\frac{\theta_e}{2} \quad (A.10)$$

was used. Since $q = p' - p$ and $p^2 = p'^2 = m^2$, we can write

$$\begin{aligned}
p'^2 &= (q+p)^2 = q^2 + 2q\cdot p + p^2\\[2mm]
q^2 &= -2q\cdot p = -2\omega m\\[2mm]
\omega &= -\frac{q^2}{2m} = \frac{Q^2}{2m} \quad (A.11)
\end{aligned}$$

which leads, using $Q^2 = -\left(\omega^2 - \vec{q}^2\right)$, to

$$\vec{q}^2 = Q^2\left(1 + \frac{Q^2}{4m^2}\right) = Q^2(1+\tau) \quad (A.12)$$

which we can plug into Eq.A.9 to get

$$k_1^2 = \frac{Q^2}{4(1+\tau)}\cot^2\frac{\theta_e}{2} \quad (A.13)$$

to be compared to Eq. A.7, to get the relation

$$\cot^2\frac{\theta_B}{2} = \frac{\cot^2\frac{\theta_e}{2}}{1+\tau} \quad (A.14)$$

APPENDIX B

Schlumpf's relativistic constituent quark model

The Einstein mass relation becomes in light-front dynamics:

$$p^- = \frac{p_\perp^2 + m^2}{2p^+} \qquad (B.1)$$

If we view the $p^+ \equiv \mu$ component as a mass, we note an analogy with a non-relativistic expression of an Hamiltonian $H \equiv p^-$ of a particle on a two-dimensional surface [48]. So in the case of a system of several particles, this class of dynamics will allow us to easily separate between the motion of the center of mass of the system, and the relative motion of the particles in the system. The second advantageous feature of the light front dynamics is that Eq. B.1 is not quadratic in p^+ or p^-. Therefore this class does not allow negative energies, so that diagrams involving quarks created out of or annihilated into the vacuum do not contribute [49].

B.1 Hamiltonian

The analogy with non-relativistic mechanics makes it easy to construct the Hamiltonian of a system of several particles.

B.1.1 Two-particles state

For a system of two non-interacting particles, we can introduce the total momentum $\mathbf{p}_A = (p_A^+, p_{A\perp})$ and the relative momentum $q_\perp$ defined as

$$\mathbf{p}_A = \mathbf{p}_1 + \mathbf{p}_2$$
$$\frac{q_\perp}{\mu_A} = \frac{q_{1\perp}}{\mu_1} + \frac{q_{2\perp}}{\mu_2} \qquad (B.2)$$

171

with

$$\frac{1}{\mu_A} = \frac{1}{\mu_1} + \frac{1}{\mu_2} \qquad \text{(B.3)}$$

The Hamiltonian can then be written (up to constants), separating the center of mass motion and the relative motion:

$$H_A = \frac{p_{A\perp}^2}{2(\mu_1 + \mu_2)} + \frac{q_\perp^2}{2\mu_A} + \frac{m_1^2}{2\mu_1} + \frac{m_2^2}{2\mu_2} = \frac{p_{A\perp}^2 + M_{12}^2}{2(\mu_1 + \mu_2)} \qquad \text{(B.4)}$$

where

$$M_{12}^2 = \frac{q_\perp^2}{\xi(1-\xi)} + \frac{m_1^2}{\xi} + \frac{m_2^2}{1-\xi} \qquad \text{(B.5)}$$

with

$$\xi = \frac{\mu_1}{\mu_1 + \mu_2} = \frac{p_1^+}{p_1^+ + p_2^+} \qquad \text{(B.6)}$$

This Hamiltonian looks like a one-particle Hamiltonian in which the mass m is replaced by the effective mass M_{12} of the system, depending on the relative variables.

B.1.2 Three-particles state

It is easy to construct the three-particle state, if we consider it as a two-particles system consisting of the previous system A and a new particle 3. The Hamiltonian is then

$$H = H_1 + H_2 + H_3 = H_A + H_3 \qquad \text{(B.7)}$$

We introduce the total momentum $\mathbf{P} = (P^+, P_\perp)$ and the relative momentum of the system $K_\perp$

$$\mathbf{P} = \mathbf{p}_A + \mathbf{p}_2 = \mathbf{p}_1 + \mathbf{p}_2 + \mathbf{p}_3$$
$$\frac{K_\perp}{\mu} = \frac{q_\perp}{\mu_A} + \frac{q_{3\perp}}{\mu_3} \qquad \text{(B.8)}$$

In complete analogy with Eq. B.4, we have

$$H = \frac{P_\perp^2}{2(\mu_1 + \mu_2 + \mu_3)} + \frac{K_\perp^2}{2\mu} + \frac{M_{12}^2}{2\mu_A} + \frac{m_3^2}{2\mu_3} = \frac{P_\perp^2 + M_0^2}{2(\mu_1 + \mu_2 + \mu_3)} \qquad \text{(B.9)}$$

where

$$M_0^2 = \frac{K_\perp^2}{\eta(1-\eta)} + \frac{M_{12}^2}{\eta} + \frac{m_3^2}{1-\eta} \qquad (B.10)$$

with

$$\eta = \frac{\mu_A}{\mu_A + \mu_3} = \frac{p_A^+}{p_A^+ + p_2^+} = \frac{p_1^+ + p_2^+}{P^+} \qquad (B.11)$$

It is convenient to define here a few variables:

$$E_{1,2} = \sqrt{\vec{q}^2 + m_{1,2}^2} \quad , \quad E_3 = \sqrt{\vec{K}^2 + m_3^2} \quad , \quad E_{12} = \sqrt{\vec{K}^2 + M_{12}^1} \qquad (B.12)$$

where $\vec{q} = (q_1, q_2, q_3)$ and $\vec{K} = (K_1, K_2, K_3)$, so that

$$\xi = \frac{E_1 + q_3}{E_1 + E_2}$$

$$\eta = \frac{E_{12} + K_3}{E_{12} + E_3} \qquad (B.13)$$

Using these variables, the mass operator is now simply:

$$M = E_{12} + E_3 \quad , \quad M_{12} = E_1 + E_2 \qquad (B.14)$$

We can now switch on interactions, replacing the free mass operator M_0 by an effective mass operator $M = M_0 + W$, where W is a confinement interaction. M acts on the space of the relative variables $(q_\perp, \xi, K_\perp, \eta)$. The three-particles system, by analogy with non-relativistic mechanics, must satisfy the "Schrödinger equation"

$$i\frac{\partial}{\partial x^+}\Psi = H\Psi \qquad (B.15)$$

B.2   Nucleon wave function

Ψ can be separated into center of mass motion and relative motion, and the relative part ψ must be eigenfunction of the mass operator:

$$M\psi = m\psi \qquad (B.16)$$

The wave function ψ depends on $q_\perp$, ξ, $K_\perp$, η and spin variables. The variables ξ and η describe the distribution of the "mass", or the variable P^+.

The wave function ψ can be decomposed in three parts: $\psi = \Phi\chi\phi$, where Φ, χ and ϕ represent the flavor, spin and momentum distributions respectively. The product ψ is symmetric, and the color wave function (not explicit here) is antisymmetric.

B.2.1 Angular momentum

χ must be eigenfunction of the angular momentum operators $\vec{j}^2$ and j_3, obeying:

$$\vec{j}^2\chi = \frac{3}{4}\chi$$

$$j_3\chi = \frac{1}{2}\chi \tag{B.17}$$

The angular momentum $\vec{j}$ commutes with the mass operator M, which is necessary and sufficient for Poincaré invariance of the bound state. The angular momentum can generally be expressed as a sum of orbital and spin contributions

$$\vec{j} = i\vec{\nabla}_p \times \vec{p} + \sum_{j=1}^{3}\mathcal{R}_{Mj}\vec{s}_j \tag{B.18}$$

where $\vec{s}_j$ is the spin of the quark j. $\mathcal{R}_M$ is a Melosh rotation acting on the quark spins, which projects them to the infinite momentum-frame. The representation of this rotation (for a two-particles system) is given by [55]:

$$\langle\lambda'|\mathcal{R}_M(\xi, q_\perp, m, M)|\lambda\rangle = \left[\frac{m + \xi M - i\vec{\sigma}\cdot(\vec{n}\times\vec{q})}{\sqrt{(m+\xi M)^2 + q_\perp^2}}\right]_{\chi'\lambda} \tag{B.19}$$

where $\vec{n} = (0, 0, 1)$ and λ and λ' are spin states. This rotation is a purely relativistic effect, and is the "price" to pay for the non-relativistic treatment of the wave function. To derive the angular momentum in terms of relative coordinates, we can proceed by steps as in the previous section. Let's first consider the system of two particles:

$$\vec{j}_{12} = i\vec{\nabla}_q \times \vec{q} + \mathcal{R}_M(\xi, q_\perp, m_1, M_{12})\vec{s}_1 + \mathcal{R}_M(1 - \xi, -q_\perp, m_2, M_{12})\vec{s}_2 \tag{B.20}$$

and iterate by adding a third particle:

$$\vec{j} = i\vec{\nabla}_K \times K + \mathcal{R}_M(\eta, K_\perp, M_{12}, M)\vec{j}_{12} + \mathcal{R}_M(1 - \eta, -K_\perp, m_3, M)\vec{s}_3 \qquad (B.21)$$

The orbital contribution does not contribute for the ground state baryon octet, so that

$$\vec{j} = \sum_{i=1}^{3} \mathcal{R}_i \vec{s}_i \qquad (B.22)$$

The explicit expressions of the three Melosh rotation matrices are given in Ref. [52]

$$\mathcal{R}_1 = \frac{1}{\sqrt{a^2 + K_\perp^2}\sqrt{c^2 + q_\perp^2}} \begin{pmatrix} ac - q_R K_L & -aq_L - cK_L \\ cK_R + aq_R & ac - q_L K_R \end{pmatrix}$$

$$\mathcal{R}_2 = \frac{1}{\sqrt{a^2 + K_\perp^2}\sqrt{d^2 + q_\perp^2}} \begin{pmatrix} ad + q_R K_L & -aq_L - dK_L \\ dK_R - aq_R & ad + q_L K_R \end{pmatrix}$$

$$\mathcal{R}_3 = \frac{1}{\sqrt{b^2 + K_\perp^2}} \begin{pmatrix} b & K_L \\ -K_R & b \end{pmatrix} \qquad (B.23)$$

where $a, b, c, d, q_{(R,L)}$ and $K_{(R,L)}$ are given by

$$a = M_{12} + \eta M \quad , \quad b = m_3 + (1 - \eta)M$$

$$c = m_1 + \xi M_{12} \quad , \quad d = m_2 + (1 - \xi)M_{12}$$

$$q_R = q_1 + iq_2 \quad , \quad q_L = q_1 - iq_2 \qquad (B.24)$$

$$K_R = K_1 + iK_2 \quad , \quad K_L = K_1 - iK_2$$

We can now express the total proton wave function by:

$$\psi = \frac{-1}{\sqrt{3}}(uud\chi^{\lambda_3} + udu\chi^{\lambda_2} + duu\chi^{\lambda_1})\phi \qquad (B.25)$$

where

$$\chi_\uparrow^{\lambda_3} = \frac{1}{\sqrt{6}}(\downarrow\uparrow\uparrow + \uparrow\downarrow\uparrow - 2\uparrow\uparrow\downarrow)$$

$$\chi_\downarrow^{\lambda_3} = -\frac{1}{\sqrt{6}}(\uparrow\downarrow\downarrow + \downarrow\uparrow\downarrow - 2\downarrow\downarrow\uparrow) \qquad (B.26)$$

and $\chi^{\lambda 2}$ and $\chi^{\lambda 1}$ are the appropriate permutations of $\chi^{\lambda 3}$. The spin wave function of the i-th quark is given by:

$$\uparrow = \mathcal{R}_i \begin{pmatrix} 1 \\ 0 \end{pmatrix} \quad \text{and} \quad \downarrow = \mathcal{R}_i \begin{pmatrix} 0 \\ 1 \end{pmatrix} \tag{B.27}$$

B.2.2 Momentum wave function

The momentum wave function ϕ can be chosen as a function of M to fulfill the requirements of spherical and permutation symmetry. The S-state orbital function $\phi(M)$ is approximated by either

$$\phi(M) = M \exp\left[-\frac{M^2}{2\beta_G^2}\right] \tag{B.28}$$

or

$$\phi(M) = \frac{N'}{(M^2 + \beta^2)^\gamma} \tag{B.29}$$

The first function is the conventional choice used in spectroscopy, but it has a too strong fall-off for large values of Q^2. So we will use the power law form, with the parameters determined by Schlumpf [52]: the constituent quark mass $m_i = 0.267$ GeV, the confinement scale $\beta = 0.607$ GeV, and $\gamma = 3.5$.

B.3 Electromagnetic current matrix

The electromagnetic current in elastic scattering can be expressed using Eq. 1.11:

$$\langle \psi', \lambda' | J^\mu | \psi, \lambda \rangle = \bar{v}(p', \lambda') \left[\gamma^\mu F_1(Q^2) + \frac{i\sigma^{\mu\nu} Q_\nu}{2m} \kappa F_2(Q^2) \right] v(p, \lambda) \tag{B.30}$$

In the constituent quark model, where the three quarks do not have an internal structure, the current is calculated from the three diagrams shown in Fig. B.1, and is expressed by:

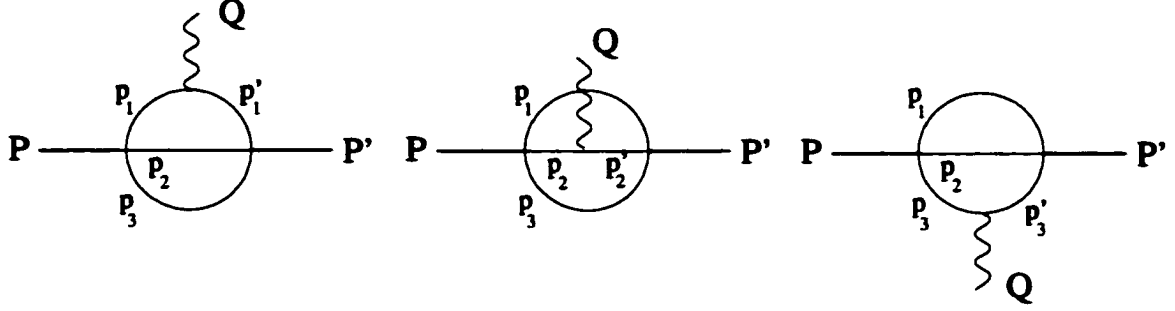$$J^\mu = \sum_{i=1}^{3} \bar{q}_i e_i \gamma^\mu q_i \tag{B.31}$$

Figure B.1: The absorption of momentum by the quarks.

where e_i is the charge and q_i the spinor of the i-th quark. We can use the $+$ component of the current in light front dynamics to express the form factors F_1 (helicity conserving) and F_2 (non helicity conserving), so that no $q\bar{q}$ pair is created:

$$F_1(Q^2) = \frac{1}{2P^+}\langle\psi',\uparrow\,\big|J^+\big|\,\psi,\uparrow\rangle$$

$$Q_\perp\kappa F_2(Q^2) = -\frac{2m}{2P^+}\langle\psi',\uparrow\,\big|J^+\big|\,\psi,\downarrow\rangle \tag{B.32}$$

The wave function can be expressed in a light front "Breit frame", in which the photon has the light front momentum $\vec{Q} = (0, Q_\perp)$. In this case, the absorption of this photon is expressed via:

$$q'_\perp = q_\perp \quad , \quad K'_\perp = K_\perp - \eta Q_\perp \tag{B.33}$$

Finally, in this model, the expressions for the nucleon form factors are:

$$F_1(Q^2) = \frac{N_c}{(2\pi)^6} \int \frac{d^2q_\perp d\xi}{\xi(1-\xi)} \frac{d^2K_\perp d\eta}{\eta(1-\eta)} \sqrt{\frac{E'_3 E'_{12} M}{E_3 E_{12} M'}}$$

$$\times \phi^\dagger(M')\phi(M) \sum_{i=1}^{3} e_i \langle\chi_\uparrow^{\lambda i}|\chi_\uparrow^{\lambda i}\rangle \tag{B.34}$$

and

$$Q_\perp\kappa F_2(Q^2) = -2m\frac{N_c}{(2\pi)^6} \int \frac{d^2q_\perp d\xi}{\xi(1-\xi)} \frac{d^2K_\perp d\eta}{\eta(1-\eta)} \sqrt{\frac{E'_3 E'_{12} M}{E_3 E_{12} M'}}$$

$$\times \phi^\dagger(M')\phi(M) \sum_{i=1}^{3} e_i \langle\chi_\uparrow^{\lambda i}|\chi_\downarrow^{\lambda i}\rangle \tag{B.35}$$

where the primed quantities refer to the transformation Eq. B.33.

APPENDIX C

Calorimeter calibration

The correspondence between the ADC channel corresponding to a block and the energy deposited in this block is given by:

$$E_i = C_i(ADC_i - P_i) \tag{C.1}$$

where P_i is the pedestal, read off the raw spectrum, and C_i is the gain coefficient, whose determination is the purpose of this calibration procedure.

The calibration takes advantage of the over-determination of the exclusive elastic reaction. We select events whose information from the left HRS is sufficient to ensure that this event is elastic. For these events, the energy E'_{elas} of the scattered electron can be predicted using energy conservation:

$$E_{beam} + m = \sqrt{p_p^2 + m^2} + E'_{elas} \tag{C.2}$$

We can then establish a correspondence between the energy deposited (supposed to be E'_{elas}), and the ADC read-out.

The calibration program makes different cuts on the data to select elastic events:

• A cut on the quantity shown in Fig. 4.9 and defined in Section 4.3, the difference between the expected (from scattering angle) and the measured proton momentum, is made:

$$-10 < p(\Theta) - p_p < 20 \tag{C.3}$$

where the unit is MeV/c.

178

- The position of the block hit X_{block}, Y_{block} is roughly compared with the position X_{exp}, Y_{exp} of the electron in the calorimeter expected from elastic kinematics, given the proton energy and angles

$$-40 < X_{block} - X_{exp} < 40$$
$$-30 < Y_{block} - Y_{exp} < 30 \qquad (C.4)$$

in cm.

Additional cuts were made on the quality of the calorimeter signal:

- The amplitude of the raw signal should be reasonably large: the ADC channel should be above 500 for most blocks, and above 1000 for the 25 blocks that have a high PMT gain coefficient (some blocks were newer).

- Only one block should be hit in time

Once the events have been selected, the ADC gain coefficients are estimated using a χ^2 minimization procedure. The quantity to minimize is:

$$\chi^2 = \sum_{i=1,N} \left[(C_j(ADC_j - P_j))_i - E'_{elas,i} \right]^2 \qquad (C.5)$$

where N is the number of calibration events, and j is the block that had a hit in the i-th event. The calorimeter was calibrated for each run using the 300,000 first events of the run. An example of the result of the calibration is given in Fig. C.1. It shows the gain coefficient of every block for run 1318 (taken during the $Q^2 = 5.6$ GeV^2 setting).
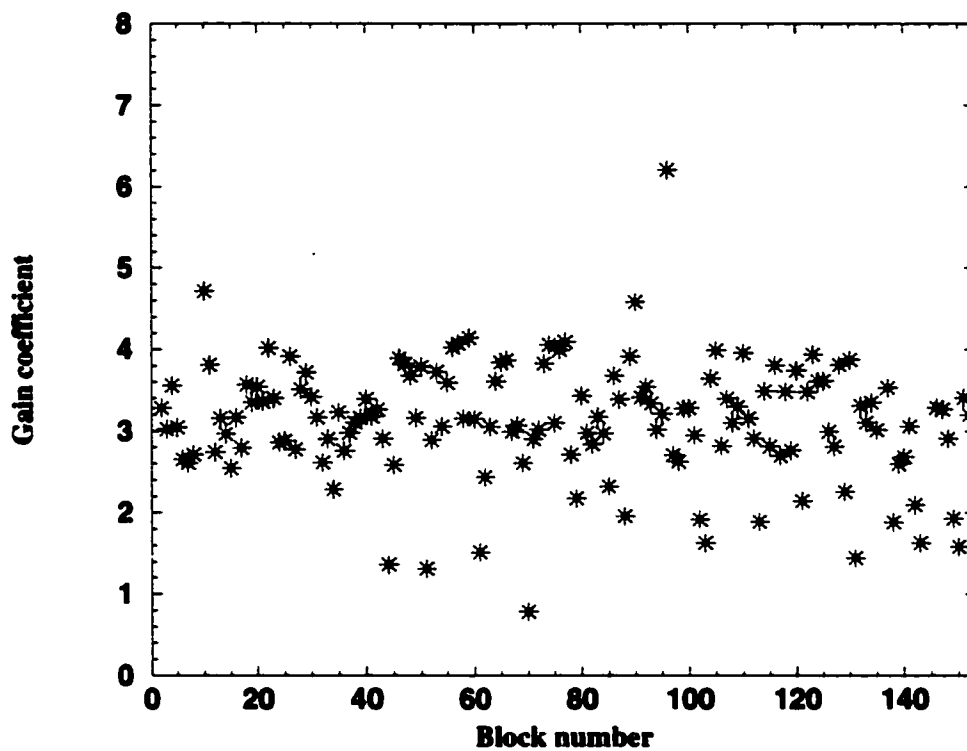
Figure C.1: Value of the gain coefficient after calibration for each block.

APPENDIX D

Angular correlation calculation in the calorimeter

The angular correlation analysis to select elastic events calculates the distance in horizontal and vertical directions, between the position of the shower in the calorimeter, and the position where it is expected from the proton energy and angles in the right HRS, assuming the reaction is elastic. We describe here the calculation of the expected x and y position of the electron in the calorimeter, where $x = 0$ at the middle of the central column and $y = 0$ at beam height.

We start from the angles of the proton in the spectrometer coordinate system, express them in the Lab frame, apply energy-momentum conservation at the vertex to calculate the expected angles of the electron in the Lab frame, and use the vertex position information and the distance target-calorimeter to transport this electron to the detector.

D.1   From spectrometer to Lab

Figure D.1 defines the angles ϕ and θ in both coordinate systems. ϕ is the angle between the projection p_2 of the momentum vector $\vec{p}$ on the yz plane and the z axis (horizontal angle), while θ is the angle between the projection p_1 of $\vec{p}$ on the xz plane and the z axis (vertical angle). The spectrometer frame is rotated with respect to the Lab frame around the x-axis by an angle Θ, which is the spectrometer setting angle. In the following, the particle index p refers to the proton, the particle index e refers to the electron, the frame index $spec$ refers to the spectrometer frame and the frame index $calo$ refers to the calorimeter. The absence of frame index refers to the Lab.

181
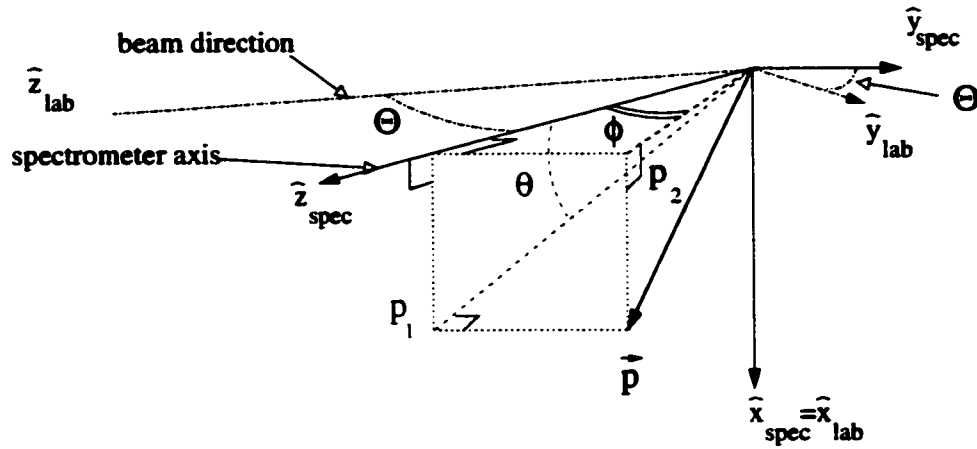
Figure D.1: The Lab and the spectrometer coordinate system.

The relation between the angles of the proton in the spectrometer and the Lab frames is:

$$\phi_p = \phi_{p,spec} + \Theta_p$$

$$\theta_p = \arctan\left(\frac{\tan\theta_{p,spec}}{\cos\Theta_p}\right) \tag{D.1}$$

The three components of $\vec{p}$ in the Lab frame are, from Fig.D.1:

$$p_x = p_1 \sin\theta_p$$

$$p_y = p_2 \sin\phi_p \ .$$

$$p_z = p_1 \cos\theta_p = p_2 \cos\phi_p \tag{D.2}$$

The latest gives

$$p_2 = p_1 \frac{\cos\theta_p}{\cos\phi_p} \tag{D.3}$$

and using normalization:

$$p^2 = p_x^2 + p_y^2 + p_z^2 = p_1^2 \left[1 + \cos^2\theta_p \tan^2\phi_p\right] \tag{D.4}$$

we can express the components in terms of $p = |\vec{p}|$:

$$p_x = p\frac{\sin\theta_p}{\sqrt{1+\cos^2\theta_p\tan^2\phi_p}}$$

$$p_y = p\frac{\cos\theta_p\tan\phi_p}{\sqrt{1+\cos^2\theta_p\tan^2\phi_p}}$$

$$p_z = p\frac{\cos\theta_p}{\sqrt{1+\cos^2\theta_p\tan^2\phi_p}} \tag{D.5}$$

D.2 Reaction at the target

D.2.1 Vertical angle

We can also define the same components for the electron momentum. Let us express conservation of energy-momentum in elastic 2-body kinematics at the vertex. First defining

$$\lambda_e = \sqrt{1+\cos^2\theta_e\tan^2\phi_e} \tag{D.6}$$

$$\lambda_p = \sqrt{1+\cos^2\theta_p\tan^2\phi_p} \tag{D.7}$$

we can write, neglecting the mass of the ultra-relativistic electron:

$$E+m = E' + \sqrt{p^2+m^2} \tag{D.8}$$

$$0 = p\frac{\sin\theta_p}{\lambda_p} + E'\frac{\sin\theta_e}{\lambda_e} \tag{D.9}$$

$$0 = p\frac{\cos\theta_p\tan\phi_p}{\lambda_p} + E'\frac{\cos\theta_e\tan\phi_e}{\lambda_e} \tag{D.10}$$

$$E = p\frac{\cos\theta_p}{\lambda_p} + E'\frac{\cos\theta_e}{\lambda_e} \tag{D.11}$$

The unknowns we are heading for are θ_e and ϕ_e, which are both explicitly in the equations and contained in λ_e. θ_p, ϕ_p and λ_p are known.

We can use Eq. D.9 to express E'/λ_e:

$$\frac{E'}{\lambda_e} = -\frac{p\sin\theta_p}{\lambda_p}\frac{1}{\sin\theta_e} \tag{D.12}$$

and rewrite Eq. D.11:

$$E = \frac{p}{\lambda_p}\left(\cos\theta_p - \sin\theta_p \cot\theta_e\right) \qquad (D.13)$$

which can be solved for θ_e:

$$\theta_e = \arctan\left(\frac{p\sin\theta_p}{p\cos\theta_p - E\lambda_p}\right) \qquad (D.14)$$

D.2.2 Horizontal angle

Knowing θ_e, we can now easily use Eqs. D.12, D.6 and D.14 to express ϕ_e:

$$\phi_e = \arctan\sqrt{\left(\frac{E'^2\lambda_p^2}{(p\cos\theta_p - E\lambda_p)^2} - \frac{1}{\cos^2\theta_e}\right)} \qquad (D.15)$$

D.3 From Lab to calorimeter

D.3.1 Angles

We can now define the calorimeter coordinate system, with a z-axis pointing horizontally from the target center (in the $\hat{z}_{Lab}\hat{z}_{spec}$ plane), and a x-axis common with the Lab and spectrometer frames. The relation between the electron angle in the calorimeter frame and the Lab frame is:

$$\phi_{e,calo} = \phi_e - \Theta_e$$

$$\theta_{e,calo} = \arctan\left(\tan\theta_e \cos\Theta_e\right) \qquad (D.16)$$

Note that $\Theta_e < 0$, because the calorimeter is on the right side of the beam.

D.3.2 Vertex coordinates in the calorimeter frame

Let us express the coordinates (x_{tg}, y_{tg}, z_{tg}) of the vertex in the calorimeter coordinate system, in terms of the coordinates (X_{tg}, Y_{tg}, Z_{tg}) in the Lab. They are obtained by performing a rotation of Θ_e around the x-axis:

$$x_{tg} = x_{tg}$$

$$y_{tg} = Y_{tg} \cos \Theta_e - Z_{tg} \sin \Theta_e$$

$$z_{tg} = Y_{tg} \sin \Theta_e + Z_{tg} \cos \Theta_e \qquad \text{(D.17)}$$

If we call D the distance between the target center and the entrance face of the calorimeter, then the coordinates (x,y) of the electron on the calorimeter are given by:

$$x = x_{tg} + (D - z_{tg}) \tan \theta_e$$

$$y = y_{tg} + (D - z_{tg}) \tan \phi_e \qquad \text{(D.18)}$$

BIBLIOGRAPHY

[1] J. D. Walecka. *Theoretical Nuclear and Subnuclear Physics*. Oxford University Press, 1995.

[2] M. P. Rekalo and E. Tomasi-Gustafsson. Polarization effects in elastic electron-proton scattering. *Internal report DAPNIA/SPHN*, 02-34, 2002.

[3] R. G. Sachs. *Phys. Rev.*, 126:2256, 1962.

[4] N. Dombey. *Rev. Mod. Phys.*, 41:236, 1969.

[5] M. E. Peskin and D. V. Schroeder. *An Introduction to Quantum Field Theory*. Addison Wesley, 1995.

[6] M. N. Rosenbluth. *Phys. Rev.*, 79:615, 1950.

[7] G. G. Petratos. *Nucl. Phys. A*, 666& 667:61c, 2000.

[8] L. Andivahis et al. *Phys. Rev. D*, 50:5491, 1994.

[9] J. Litt et al. *Phys. Lett. B*, 31:40, 1970.

[10] A. F. Sill et al. *Phys. Rev. D*, 48:29, 1993.

[11] T. Jannsens et al. *Phys. Rev.*, 142:922, 1966.

[12] W. Bartel et al. *Nucl. Phys. B*, 58:429, 1973.

[13] Ch. Berger et al. *Phys. Lett. B*, 35:87, 1971.

[14] P. E. Bosted. *Phys. Rev. C*, 51:409, 1995.

[15] A. Lung et al. *Phys. Rev. Lett.*, 70:718, 1993.

[16] E. E. W. Bruins et al. *Phys. Rev. Lett.*, 75:21, 1995.

[17] P. Markovitz. *Phys. Rev. C*, 48:R5, 1993.

[18] L. E. Price et al. *Phys. Rev. D*, 4:45, 1971.

[19] D. Rohe et al. *Phys. Rev. Lett.*, 83:4257, 1999.

[20] J. Becker et al. *Eur. Phys. J. A*, 6:329, 1999.

[21] I. Passchier et al. *Phys. Rev. Lett.*, 82:4988, 1999.

[22] H. Zhu et al. eprint nucl-ex/0105001.

[23] T. Eden et al. *Phys. Rev. C*, 50:R1749, 1994.

[24] M. Ostrick et al. *Phys. Rev. Lett.*, 83:276, 1999.

[25] C. Herberg et al. *Eur. Phys. J. A*, 5:131, 1999.

[26] B. Milbrath et al. *Phys. Rev. Lett.*, 80:452, 1998.

[27] B. Milbrath et al. *Phys. Rev. Lett.*, 82:2221(E), 1999.

[28] M. K. Jones et al. *Phys. Rev. Lett.*, 84:1398, 2000.

[29] O. Gayou, K. Wijesooriya, et al. *Phys. Rev. C*, 64:038202, 2001.

[30] S. Dieterich et al. *Phys. Lett. B*, 500:47, 2001.

[31] A. Chodos, R. L. Jaffe, K. Johnson, C. B. Thorn, and V. F. Weisskopf. *Phys. Rev. D*, 9:3471, 1974.

[32] A. Chodos, R. L. Jaffe, K. Johnson, and C. B. Thorn. *Phys. Rev. D*, 10:2599, 1974.

[33] T. A. DeGrand, R. L. Jaffe, K. Johnson, and J. Kiskis. *Phys. Rev. D*, 12:2060, 1975.

[34] A. W. Thomas. *Adv. Nucl. Phys.*, 13:1, 1984.

[35] D. H. Lu, A. W. Thomas, and A. G. Williams. *Phys. Rev. C*, 57:2628, 1998.

[36] F. Iachello, A. Jackson, and A. Lande. *Phys. Lett. B*, 43:191, 1973.

[37] G. Höhler. *Nucl. Phys. B*, 114:505, 1976.

[38] M. F. Gari and W. Krümpelmann. *Phys. Lett. B*, 274:159, 1992.

[39] M. F. Gari and W. Krümpelmann. *Phys. Lett. B*, 282:483(E), 1992.

[40] P. Mergell, U. G. Meissner, and D. Drechsel. *Nucl. Phys. A*, 596:367, 1996.

[41] E. L. Lomon. *Phys. Rev. C*, 64:035204, 2001.

[42] S. Godfrey. *Nuovo Cim. A*, 102:1, 1989.

[43] W. Lucha, F. F. Schöberl, and D. Gromes. *Phys. Rep.*, 200:127, 1991.

[44] J.-M. Richard. *Phys. Rep.*, 212:1, 1992.

[45] P. A. M. Dirac. *Rev. Mod. Phys.*, 21:392, 1949.

[46] M. R. Miller, B. K. Jennings, and G. A. Miller. *Phys. Rev. C*, 54:920, 1996.

[47] P. L. Chung et al. *Phys. Rev. C*, 37:2000, 1988.

[48] L. Susskind. *Phys. Rev.*, 165:1535, 1968.

[49] S. Weinberg. *Phys. Rev.*, 150:1313, 1966.

[50] V. B. Berestetskii and M. V. Terent'ev. *Sov. J. Nucl. Phys.*, 24:547, 1976.

[51] V. B. Berestetskii and M. V. Terent'ev. *Sov. J. Nucl. Phys.*, 25:347, 1977.

[52] F. Schlumpf. *Phys. Rev. D*, 47:4114, 1993.

[53] F. Schlumpf. *Relativistic constituent quark model for baryons*. PhD thesis, Universität Zürich, 1992. eprint hep-ph/9211255.

[54] P. L. Chung and F. Coester. *Phys. Rev. D*, 44:229, 1991.

[55] H. J. Melosh. *Phys. Rev. D*, 9:1095, 1974.

[56] F. Cardarelli, E. Pace, G. Salmè, and S. Simula. *Phys. Lett. B*, 357:267, 1995.

[57] F. Cardarelli, E. Pace, G. Salmè, and S. Simula. *Nucl. Phys. A*, 666&667:33c, 2000.

[58] F. Cardarelli and S. Simula. *Phys. Rev. C*, 62:065201, 2000.

[59] S. Capstick and N. Isgur. *Phys. Rev. D*, 34:2809, 1986.

[60] W. H. Klink. *Phys. Rev. C*, 58:3587, 1998.

[61] R. F. Wagenbrunn, S. Boffi, W. H. Klink, W. Plessas, and M. Radici. *Phys. Lett. B*, 511:33, 2001.

[62] L. Ya. Glozman, W. Plessas, K. Varga, and R. F. Wagenbrunn. *Phys. Rev. D*, 58:094030, 1998.

[63] J. C. R. Bloch, C. D. Roberts, S. M. Schmidt, A. Bender, and M. R. Frank. *Phys. Rev. C*, 60:062201, 1999.

[64] J. C. R. Bloch, C. D. Roberts, and S. M. Schmidt. *Phys. Rev. C*, 61:065207, 2000.

[65] G. Holzwarth. *Z. Phys. A*, 356:339, 1996.

[66] G. Holzwarth. *Nucl. Phys. A*, 666&667:24c, 2000.

[67] M. Göckeler, R. Horsley, D. Pleiter, P. E. L. Rakow, and G. Schierholz. e-print hep-ph/0108105.

[68] G. P. Lepage and S. J. Brodsky. *Phys. Rev. D*, 22:2157, 1980.

[69] G. Sterman and P. Stoler. *Hadronic form factors and perturbative QCD*, in *Annual Review of Nuclear and Particle Science*. Annual Review Inc., 1997.

[70] S. J. Brodksy and G. R. Farrar. *Phys. Rev. D*, 11:1309, 1975.

[71] P. N. Kirk et al. *Phys. Rev. D*, 8:63, 1973.

[72] M. Ambrogiani et al. *Phys. Rev. D*, 60:032002, 1999.

[73] T. A. Armstrong et al. *Phys. Rev. Lett.*, 70:1212, 1993.

[74] A. Antonelli et al. *Phys. Lett. B*, 334:431, 1994.

[75] G. Bardin et al. *Nucl. Phys. B*, 411:3, 1994.

[76] D. Bisello et al. *Nucl. Phys. B*, 224:379, 1983.

[77] A. Zichichi et al. *Nuovo Cimento*, 24:170, 1962.

[78] E. Tomasi-Gustafsson and M. P. Rekalo. *Phys. Lett. B*, 504:291, 2001.

[79] E. C. Titchmarsh. *Theory of functions*. Oxford Univ. Press, London, 1939.

[80] B. Anderson et al. *Nucl. Instr. Meth. in Phys. Res.* In preparation.
http://www.jlab.org/~kees/nim.ps.

[81] J. Berthot and P. Vernin. *Nucl. Phys. News.*, 9:12, 1990.

[82] O. Ravel. *Mesure absolue de l'énergie du faisceau d'électrons de TJNAF par diffusion élastique p(e,e′)p*. PhD thesis, Université Blaise Pascal, Aubière, France, 1997.

[83] D. Marchand. *Mesure absolue de l'énergie du faisceau d'électrons de CEBAF par une méthode magnétique*. PhD thesis, Université Blaise Pascal, Aubière, France, 1997.

[84] N. Falleto et al. *Nucl. Instr. Meth. in Phys. Res. A*, 459:412, 2001.

[85] S. Escoffier. *Mesure de la polarisation du faisceau d'électrons de TJNAF par diffusion Compton pour les expériences N-Delta et GepII*. PhD thesis, Paris XI, France, 2001.

[86] http://www.jlab.org/~moller/index.html.

[87] Jlab cryotarget system. *Nucl. Instr. Meth. in Phys. Res.* In preparation.
http://hallaweb.jlab.org/equipment/targets/cryotargets/Halla_tgt.html.

[88] http://hallaweb.jlab.org/equipment/hrs.htm.

[89] K.G. Fissum et al. *Nucl. Instr. Meth. in Phys. Res. A*, 474:108–131, 2001.

[90] L. Bimbot et al. *Nucl. Instr. Meth. in Phys. Res.* In preparation.
http://hallaweb.jlab.org/equipment/detectors/fpp.html.

[91] B. Bonin et al. *Nucl. Instr. Meth. in Phys. Res. A*, 288:379, 1990.

[92] N. E. Cheung et al. *Nucl. Instr. Meth. in Phys. Res. A*, 363:561, 1995.

[93] http://hallaweb.jlab.org/equipment/detectors/trig.html.

[94] N. Liyanage. *A study of $^{16}O(ee'p)$ reaction at deep missing energies.* PhD thesis, Massachussets Institute of Technology, 1999.

[95] O. Gayou. Electron calorimeter for E99-007. *Hall A Status Report,* 2000. http://hallaweb.jlab.org/publications/Talks/StatusReport/StatusReport2000.ps.

[96] K. Wijesooriya. *First $(\vec{e}, e'\vec{p})$ measurement of polarization transfer in a complex nucleus: ^{16}O.* PhD thesis, College of William and Mary, 1999.

[97] K. Makino and M. Berz. Cosy infinity version 8. *Nucl. Instr. Meth. in Phys. Res. A,* 427:338, 1999.

[98] G. Quéméner, M. K. Jones, C. F. Perdrisat, and V. Punjabi. *Nucl. Phys. A,* 654:543, 1999.

[99] D. Basset et al. *Nucl. Instr. Meth. in Phys. Res.,* 166:515, 1979.

[100] A. Afanasev et al. *Phys. Rev. D,* 64:113009, 2001.

[101] M. P. Rekalo and E. Tomasi-Gustafsson. Radiative corrections to polarization observables for elastic e+A scattering. *Internal report DAPNIA/SPHN,* 01-14, 2001.

[102] A. Afanasev. Private communication.

[103] L. Pentchev and J. J. Lerose. Quadrupole alignment studies in the HRSs. *Jlab-TN-01-052,* 2001.

[104] E. J. Brash, A. Kozlov, Sh. Li, and G. M. Huber. 2001. submitted to Phys. Rev. C; e-print hep-ex/0111038.

[105] G. A. Miller and M. R. Franck. eprint nucl-th/0201021.

[106] E. L. Lomon. eprint nucl-th/0203081.

[107] J. P. Ralston, P. Jain, and R. V. Buniy. In *Intersections between Particle and Nuclear Physics,* page 302. AIP, 2000.

[108] P. Jain and J. P. Ralston. In *Future directions in Particle and Nuclear Physics at MultiGeV Hadron Beam Facilities,* 1993. eprint hep-ph/9305250.

[109] R. Segel and J. Arrington. New measurement of G_E/G_M of the proton. *Jlab Proposal,* E01-001, 2001.

[110] C. F. Perdrisat, E. J. Brash, M. K. Jones, and V. Punjabi. Measurement of G_{Ep}/G_{Mp} to $Q^2 = 9$ GeV^2 via recoil polarization. *Jlab Proposal*, E01-109, 2001.

[111] D. Day. The charge form factor of the neutron. *Jlab Proposal*, E93-026, 1993.

[112] R. Madey, B. Anderson, and S. Kowalski. The electric and magnetic form factor of the neutron in the $d(e, e'n)p$ reaction. *Jlab Proposal*, E93-038, 1993.

[113] O. Gayou et al. *Phys. Rev. Lett.*, 88:092301, 2002.

VITA

Olivier Gayou

Olivier Gayou was born in Bagneux, near Paris, France. He did his undergraduate studies at the Université Blaise Pascal, in Clermont-Ferrand. and received a Maitrise de Physique (Bachelor) in 1997. He started graduate studies in the same university, and received a Diplôme d'Etudes Approfondies (DEA) in 1998. He was accepted the next year in the graduate program at the Physics Department of the College of William and Mary, and started a joint PhD with the Université Blaise Pascal. He received a Masters degree in 2000, and defended his PhD dissertation on April 10, 2002. He accepted a Postdoctoral Associate position at the Massachusetts Institute of Technology.